UNIVERSITY OF CALIFORNIA

Santa Barbara

Enhancing Bioelectrochemical Conversion: Molecular Modifications for Amplified Transmembrane Electron Transfer

A dissertation submitted in partial satisfaction of the

requirements for the degree Doctor of Philosophy

in Materials

by

Nathan Daniel Kirchhofer

Committee in charge:

Professor Guillermo C. Bazan, Chair

Professor Frederick W. Dahlquist

Professor Cyrus R. Safinya

Professor H. Tom Soh, Stanford University

June 2016

The dissertation of Nathan Daniel Kirchhofer is approved.

_____

Frederick W. Dahlquist

_____

Cyrus R. Safinya

_____

H. Tom Soh

_____

Guillermo C. Bazan, Committee Chair

March 2016

Enhancing Bioelectrochemical Conversion: Molecular Modifications for Amplified Transmembrane Electron Transfer

Nathan Daniel Kirchhofer

ACKNOWLEDGEMENTS

For all of the opportunity and privilege that has been conferred to me, and for the endless love and support I have received, I am forever grateful and indebted to my family. My mother, Linda Kirchhofer, instilled me with generosity and artistry. My father, Dr. Mark Kirchhofer, cultivated my attention to detail and intensity. My sister, Emily Kirchhofer, made me mentally and physically stronger by looking up to me, depending on me, and pushing my limits in the way only a sibling can. My family is exceptional at communication, be it for learning, arguing, exploring meaning, or expressing and perceiving emotions, and these attributes have carried over into all aspects of my life in ways I cannot fully articulate.

I am grateful to my friends for the continuing adventures—in the loosest sense of the term—that broaden my perspective and deepen our friendships. Work is a large part of life, and yet work is not life. It is perhaps the intermittent breaks from our serious obligations that provide the most contrast and new ideas and new energy and refreshment, and these breaks are best in the company of friends. I think of the people over the years with whom I have run trails, homebrewed beer, cycled mountains, tasted delicious wines, enjoyed single-origin coffees, skied ragged peaks, surfed, gazed at the stars, traveled the world, played team sports, attended concerts, roadtripped, cooked delicious meals, played music, camped in the wilderness, and even simply sat and talked over a cup of tea. I cannot name them all here. I would not exchange those adventures for anything.

I am grateful to the Ultimate community for many reasons. Chasing around a flying plastic disc attracts a certain type of individual that is self-motivated, team-oriented, emotionally intelligent, intellectual, intense, good-spirited, and involved. Some of my closest friendships and many of the opportunities I have had have arisen from relationships with people I have competed with on the pitch. By virtue of the sport being self-refereed, the competition and intensity of Ultimate is inherently paralleled by equality and humility, and these aspects continuously carry over into the way I comport myself. Much like science, Ultimate transcends many cultural and ideological borders, for which I am deeply thankful.

I am grateful to the scientific community as a whole for advancing humanity and our quality of life, for providing a framework to pursue interesting and meaningful problems as well as peer-review results, and for exposing me to uncountable different cultural and ideological perspectives through collaboration and travel. Science—and more broadly, education—is a powerful antidote to intolerance and misunderstanding in our increasingly globalized world. Scientific inquiry transcends many real and perceived borders, and I am proud to be part of that process. I thank the faculty and staff at the outstanding institutions I have attended throughout my academic career: Carl Sandburg Elementary School; Newton Middle School; Arapahoe High School; University of Colorado at Boulder; University of California Santa Barbara. I am nothing without the combined efforts of so many others. I extend a special thank you to my colleagues during my tenure at UCSB: The advisement of Profs. Gui Bazan and Rick Dahlquist is irreplaceable; the synthetic accomplishments of Dr. Logan Garner, Xiaofen Chen, Zach Rengert, and Dr. Cheng-Kang Mai enabled me to explore materials modifications of bioelectronic interfaces; collaborators at the Navy Research Labs, University of Utah, and Nanyang Technological University taught me a great deal; the Institute for Collaborative Biotechnologies provided research funding; UCSB's Technology Management Program educated me in business basics; microscopy specialists, instrument managers, and other UCSB staff made everything click along the way.

VITA OF NATHAN DANIEL KIRCHHOFER
March 2016

EDUCATION

Bachelor of Arts in Physics (*magna cum laude*) and Mathematics, University of Colorado at Boulder, May 2008
Certificate in Management Practice, University of California, Santa Barbara, June 2015 (commencement speaker)
Doctor of Philosophy in Materials, University of California, Santa Barbara, March 2016

PROFESSIONAL EMPLOYMENT

August – December 2005: Undergraduate Learning Assistant, Department of Physics, University of Colorado at Boulder
May 2006 – August 2007: Undergraduate Lab Assistant, Kapteyn-Murnane Group, JILA (CU Boulder/NIST)
June 2008 – July 2010: Research Associate, Genomics, OPX Biotechnologies, Inc., Boulder, CO, USA
September 2010 – March 2016: Graduate Research Assistant, Department of Materials, University of California, Santa Barbara
January – March 2011 and September – December 2015: Graduate Teaching Assistant, Department of Chemistry and Biochemistry, University of California, Santa Barbara

PUBLICATIONS

"Improving charge collection in Escherichia coli–carbon electrode devices with conjugated oligoelectrolytes," *Physical Chemistry Chemical Physics*, 2013, 15, 5867-5872

"Conjugated oligoelectrolytes increase power generation in *E. coli* microbial fuel cells," *Advanced Materials*, 2013, 25(11), 1593-1597.

"Comparison of flavins and a conjugated oligoelectrolyte in stimulating extracellular electron transport from Shewanella oneidensis MR-1," *Electrochemistry Communications*, 2014, 41, 55-58.

"The conjugated oligoelectrolyte DSSN+ enables exceptional coulombic efficiency via direct electron transfer for anode-respiring Shewanella oneidensis MR-1—a mechanistic study," *Physical Chemistry Chemical Physics*, 2014, 16(38), 20436-20443.

"The photobioelectrochemical activity of thylakoid bioanodes is increased via photocurrent generation and improved contacts by membrane-intercalating conjugated oligoelectrolytes," *Energy & Environmental Science*, 2015, 8(9), 2698-2706.

"A molecular protein prosthetic for disabled bacteria." *Submitted*, 2016.

"Conjugated oligoelectrolytes accelerate syntrophic anaerobic exchange of reducing equivalents." *In preparation*, 2016.

"Amplification of bacterial anode respiration by a self-doped p-type pH-neutral conjugated polyelectrolyte." *In preparation*, 2016.

"Biofilm as a redox conductor: a systematic study of moisture and temperature dependence of its electrical properties." *In preparation*, 2016.

AWARDS

1st Place, Best Student Podium Presentation, Day 1, North American Regional Meeting of the International Society for Microbial Electrochemistry and Technology (NA-ISMET 4), The Pennsylvania State University, State College, PA, USA. May 13–15, 2014.

2nd Place, New Venture Competition Finals, Tech-Driven Track, Technology Management Program, University of California, Santa Barbara, USA. May 21, 2015.

Runner Up, Best Student Poster Presentation, 12th International Symposium on Functional π–Electron Systems (Fπ–12), University of Washington, Seattle, WA, USA. July 19–24, 2015.

FIELDS OF STUDY

Major Field: Materials for Bioelectronics

Studies in Bacterial Transmembrane Electron Transfer Mechanisms with Professors Guillermo C. Bazan and Frederick W. Dahlquist

Studies in Photobioelectrocatalysis with Professors Guillermo C. Bazan and Shelley D. Minteer

Studies in Syntrophic Intercellular Electronic Communication with Professors Frederick W. Dahlquist and Guillermo C. Bazan

Studies in Chemical Modification of Biotic-Abiotic Electron Transfer with Professors Guillermo C. Bazan, Frederick W. Dahlquist, and Thuc-Quyen Nguyen

ABSTRACT

Enhancing Bioelectrochemical Conversion: Molecular Modifications for Amplified Transmembrane Electron Transfer

by

Nathan Daniel Kirchhofer

In Bioelectronics—the confluence of Biology and Electronics—living biological entities are interfaced with electrical components for applications in bioenergy conversion and catalysis, biosensing, medical diagnostics and drug delivery, neural and tissue interrogation, and more. Improving the contacts at biotic-abiotic charge transfer interfaces is therefore of fundamental importance for improving these various bioelectrochemical systems. Here, specific attention is drawn to chemically modifying electrically insulating lipid bilayer membrane interfaces so that biologically-derived electrons may be more readily collected at an electrode. This research is of fundamental scientific interest from a biophysical perspective as well as immense practical importance for bioelectrochemical conversion technologies that interconvert organic fuels and electrical current.

Consider *microbial* bioelectrochemical conversion systems wherein certain bacterial species are commonly employed that have the evolved capacity to directly produce electrical current as a metabolic product. A unifying feature of these species is that they construct conductive membrane-bound redox-protein/cofactor nanostructures for transmembrane electron transport. Drawing inspiration from this molecular functionality, one may envision

and synthesize organic semiconducting molecules designed for biological/membrane affinity. The implementation of these materials in living devices for the purpose of amplifying biological transmembrane electron transport is the subject of this dissertation.

p-Phenylenevinylene-based conjugated oligoelectrolytes (PPV-COEs) are a class of organic semiconducting molecules designed for membrane modification. Early experiments indicated that PPV-COEs will spontaneously intercalate into lipid bilayer membranes and improve biocurrent outputs, suggesting that PPV-COEs act as transmembrane "molecular wires" for electron transmission. In order to test this hypothesized mechanism, the model lactate-consuming electrogenic bacterium *Shewanella oneidensis* MR-1 was cultivated and modified with PPV-COEs in microbial three-electrode electrochemical reactors (M3Cs). Because *S. oneidensis* MR-1 utilizes direct electron transfer (DET) and mediated electron transfer (MET) at distinct potentials, perturbations to the DET and MET current signals in M3Cs provide a view into the mechanism of PPV-COE biocurrent amplification. Results indicate that PPV-COEs statistically improve the coulombic efficiency of *S. oneidensis* MR-1 lactate-to-current conversion from 51 ± 10% to an exceptional 84 ± 7% (P = 0.0098) by amplifying the native bacterial DET pathway and increasing colonization of the electrode, but PPV-COEs do not appear to act as "molecular wires."

PPV-COEs were next applied to an anaerobic, obligately-crossfeeding (syntrophic) cultures of *Pelobacter acetylenicus* and *Acetobacterium woodii* and then to photobioelectrochemical devices based on photosynthetic green plant thylakoid membranes, and these were biochemically and electrochemically characterized. In the former experiments, it was found that PPV-COEs improve reaction rates and intercellular exchange of electron equivalents as a function of molecular length, while in the latter, interfacial

contacts and photocurrent were improved as a function of molecular structure and charge distribution; however, direct "molecular wiring" of the organisms to each other and thylakoids to electrodes were again ruled out. Two primary considerations rationalize this result: (a) mismatch of the PPV-COE frontier orbital energies with biological frontier orbital energies and the electrode Fermi energy and (b) the absence of direct electrode contacts.

Following this mechanistic insight, a similar experimental approach was extended to two different materials systems. First, a COE with membrane affinity containing a redox-active ferrocene moiety, DSFO+, was synthesized and applied to M3Cs. The frontier orbitals of DSFO+ are energetically aligned with physiological potentials, so DSFO+ catalytically couples to biocurrent production *via* ferrocene redox activity, remarkably also enabling partial recovery of biocurrent production in non-electrogenic mutant strains of *S. oneidensis* MR-1. Second, a set of four conjugated polyelectrolytes (CPEs) with systematic variations in backbone structure, pendant ionic functionalities, and the ability to remain doped at neutral pH in aqueous media were synthesized and applied in M3Cs. The self-doped p-type anionic derivative CPE-K is highly conductive and statistically significantly increases steady-state biocurrent output from *S. oneidensis* MR-1 by 2.7 ± 0.7-fold relative to unmodified controls (P = 0.002). Important structure-property relationships are revealed in these experiments suggesting that anionic pendant groups and the ability to be doped in aqueous media are necessary for CPE biocurrent enhancement. By absorbance spectroscopy, it appears that *S. oneidensis* MR-1 may de-dope (neutralize) CPE-K, allowing the electrode to re-dope (re-oxidize) it, creating an electronic extension of the electrode. This helps explain the increase in electrode cell colonization from CPE-K. These results provide a foundation for continued improvement of biotic-abiotic contacts with organic semiconductors in Bioelectronic devices.

TABLE OF CONTENTS

LIST OF FIGURES AND SCHEMES

LIST OF TABLES

Chapter I. Introductory Remarks

I.A. Research Context

The first recognition that physiological processes are inherently electrical may most readily be traced to the pioneering experiments of Luigi Galvani in the late 1700s at the University of Bologna. In 1791, Galvani reported that the leg muscle tissue of a dissected frog could be actuated by applying a voltage across the tissue to pass current through it.[1] As can be seen in Fig. I.1, that voltage was generated by forming a wire arc from sections of zinc and copper (which have an intrinsic 1.1 V reduction potential difference[2]) and bringing these into contact with the frog. Electrically stimulated contraction of muscles became known as "galvanism," and the field of Electrophysiology was born.

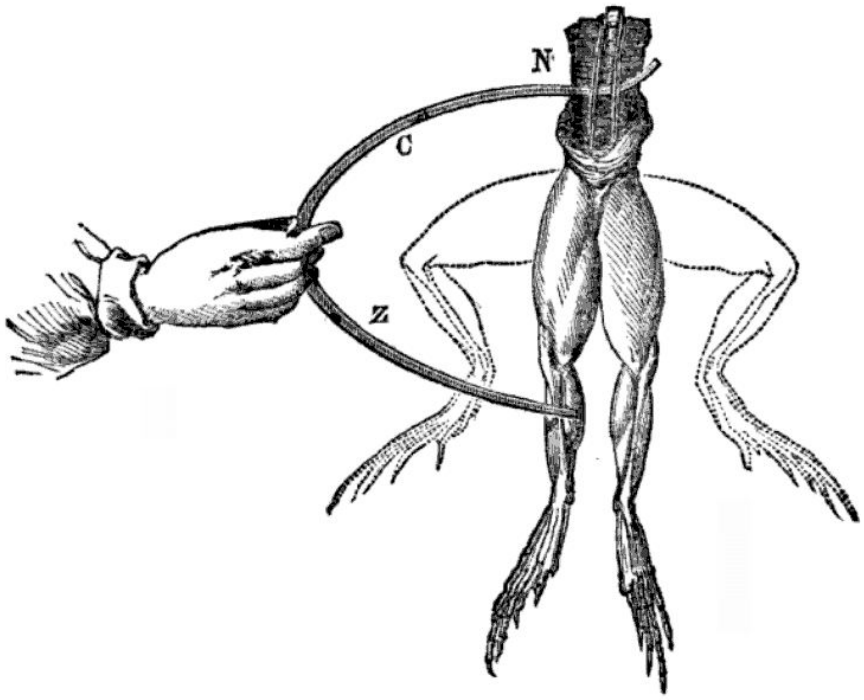

Figure I.1. In biological "galvanism," now known as electrophysiology, muscles will contract when an electrical potential is applied to drive current through the tissue. (N) Exposed nerve tissue in a dissected frog. (C) Copper and (Z) Zinc fragments of the wire arc supplying the voltage for tissue stimulus. (This image is reproduced from the Internet, and it is free of known restrictions under copyright law, including all related and neighboring rights.)

A century later, in 1911, M.C. Potter published a manuscript[3] describing bioelectrochemical experiments with yeast and other microorganisms that bolstered Galvani's observations and provided some simple tenets of electrophysiology—namely that "*… any physiological process accompanied by chemical changes involves an associated electrical change*," and that "*… differences in electrical potential are connected both with respiration and carbon assimilation*." This perhaps represents the conceptual "founding" of the field of Bioelectronics—the confluence of Biology and Electronics, a natural specialization of Electrophysiology—that deals broadly with the challenge of interfacing electrical components with biological materials for purposes of bioelectrocatalysis,[4] electromicrobiology,[5] waste treatment, renewable energy and global sustainability, remote power, biosensing,[6] biomedical applications,[7] neural and tissue interrogation,[8] and, most generally, electrical signal transmission at biological-electronic interfaces.

In the last two decades, Bioelectronics has emerged as a relevant field of exploration for addressing growing interest in the above avenues of research. In 1999 in particular, one key insight emerged: certain microorganisms act as electrocatalysts,[*] meaning they have the capacity to convert organic compounds into electricity, or biocurrent, by respiring on an electrode in the absence of oxygen.[9,10] A small number of these so-called "electrogenic"[†] bacteria[11–14] have been identified, and electrode respiration is a fortuitous side-effect of their

[*] It is worth noting that, by definition, bacteria are not true catalysts—that is, materials that increase the rate of a reaction (lower the activation energy or overpotential) without themselves undergoing chemical changes—because they subsume carbon and electron equivalents and vital energy from the oxidation of the organic material.[12,40–42] Enzymes within the bacteria are, however, true catalysts.

[†] Electrogenic bacteria have also been referred to as "exoelectrogens," "electrochemically active" bacteria, "anode-respiring" bacteria, and "electricigens," as seen in these references. For this dissertation, these terms are treated as synonymous and should be considered equivalent when reading.

evolved ability to colonize (directly attach to) and respire on oxidized minerals such as iron oxide, which is enabled by their enzymatic specificity and electron transfer efficiency.

Many researchers find inspiration from this remarkable molecular mechanism and seek to improve our ability to harvest and increase biocurrent output for the applications mentioned above. Towards achieving scalable improvements to biocurrent harvesting, it is hard to argue that one strategy is "the best," as many different approaches have merit and may be used in tandem: Engineering of device architectures enables higher power output (lower internal resistance) as well as larger device working volumes; design of new materials[15] for reactors and electrode coatings/functionalizations allows for faster reaction rates, encapsulation of electrocatalysts, and the prevention of biofouling; genetic and metabolic engineering enables heterologous expression of electroactive molecular machinery (proteins, cofactors, *etc.*) in natively non-electrogenic bacteria such as *Escherichia coli*[16,17] or diversion of metabolic electron equivalents towards electricity to alter the balance of products from bioconversion.[18]

One under-developed approach is the use of synthetic organic semiconductors and redox-active molecules that directly modify the electrocatalytic biological-electrical charge transfer interface. In July 2010, the seminal paper showcasing this strategy with membrane-intercalating *p*-phenylenevinylene-based conjugated oligoelectrolytes (PPV-COEs) was published by the Bazan labs,[19] and two months later, I began my dissertation research in the same group on the same project. Those first results were promising, as it appeared that membrane-intercalated PPV-COEs could function as transmembrane molecular wires[20,21] to enable electrons to tunnel or hop[22–25] through the insulating cell membrane.

I.B. A Brief Synopsis of Results by Chapter

The first research goals were therefore to (a) mechanistically understand the effect of

PPV-COEs and (b) test the molecular wire hypothesis in a rigorous, quantitative way. Microbial three-electrode electrochemical cells (M3Cs)[26] as well as a variety of electrochemical, metabolic, and spectroscopic characterization techniques were employed in an attempt to unravel the story. These experiments are presented in Chapters II–IV of this dissertation, and the mechanistic insights gained are extrapolated to new materials for bioelectronic modification in M3Cs in chapters V and VI.

In Chapter II, mechanistic experiments using the electrochemically well-understood electrogenic bacterium *Shewanella oneidensis* MR-1 help illuminate that amplification of native biological direct electron transfer (DET) processes is the origin of enhanced biocurrent from PPV-COE modification,[27] rather than PPV-COE molecular wire behavior. In Chapter III, by employing PPV-COEs of varying length in an anaerobic, obligately crossfeeding (syntrophic), ethanol-consuming, H_2-exchanging co-culture of *Pelobacter acetylenicus* GhAcy 1 and *Acetobacterium woodii* WB1, the possibility of overriding interspecies H_2 diffusion in favor of direct interspecies electron transfer (DIET) *via* PPV-COE molecules was examined. Therein, PPV-COEs do indeed accelerate the syntrophic metabolism; however, they appear to do this by limiting diffusion length *via* increased coaggregation between and *P. acetylenicus* and *A. woodii* without inducing DIET. In Chapter IV, a systematic series of PPV-COEs of varying molecular length and charge distribution are used to modify photobioelectrochemical anodes constructed with extracted sub-cellular photosynthetic thylakoid membranes from green plants. These experiments statistically demonstrate that both the photocurrent and electrical contacts of thylakoids are significantly improved by micromolar additions of COEs, and structure-property relationships are revealed.[28] Again, electrochemical characterization seems to indicate that electron transfer

through PPV-COEs is ruled out.

At this point, after accounting for (a) the mismatch of PPV-COE frontier orbital energies with those of relevant biological compounds and electrode Fermi levels, (b) the lack of covalent contacts of PPV-COEs with biological or electrode surfaces, and (c) the mounting experimental evidence discussed above, it is apparent that PPV-COEs do not act as molecular wires for transmembrane electron transport. It is therefore of interest to consider molecules with the frontier orbital energies, conductivity, and biocompatibility appropriate for physiological charge transport.

In Chapter V, we present the rational designed and synthesis of DSFO+, a ferrocene-based COE designed for membrane affinity that possesses an electrochemically-addressable, biologically-relevant redox potential. When applied to *S. oneidensis* MR-1 in M3C devices, DSFO+ catalytically couples to electrogenic metabolism and acts as a respiratory "protein prosthetic" enabling enhanced biocurrent harvesting. Of note are the exceptional capabilities of DSFO+ to (a) rescue catalytic biocurrent production in two mutant strains of *S. oneidensis* MR-1 lacking the electrogenic character of the wild-type strain and (b) increase the current output of individual bacterial cells, in contrast to the decreased per-cell current output induced by all other tested materials modifications to date.

In Chaper VI, in view of the affinity of CPEs for biological entities,[29] a set of four conjugated polyelectrolyte (CPE) derivatives are employed in M3Cs poised at 0.3 V vs. Ag/AgCl with *S. oneidensis* MR-1 to evaluate the possibility of amplifying biocurrent outputs. Of particular relevance in the tested set is the self-doped, p-type, pH-neutral, anionic derivative CPE-K.[30] It remarkably enables a statistically significant 2.7 ± 0.7-fold increase in steady-state biocurrent density relative to unmodified controls, as well as correlated increases

in collected charge and substrate turnover. Comparison to other tested CPEs suggests that both the anionic pendant groups and dopable backbone present on CPE-K are necessary to amplify the biocurrent output, implicating bacteria-CPE electrostatic repulsion as a positive interaction for the amplification of biocurrent in this system. Voltammetry indicates that CPE-K amplifies the DET component of *S. oneidensis* MR-1 electron transfer, consistent with increases in bacterial colonization of the electrode (a phenomenon that increases the DET signal). Optical characterization indicates that *S. oneidensis* MR-1 will also de-dope (neutralize) the CPE-K backbone, signifying that CPE-K may act as a cyclically doped conductive extension of the electrode, helping rationalize the observed trends.

I.C. Notes on Chapter Structure

In this dissertation, each chapter is written so that it stands on its own, meaning that acronyms, references, *etc*. are defined as necessary in each chapter for clarity. Wherever possible, the same acronyms have been used to describe the same concepts across chapters so that the dissertation may also be read by jumping between sections. At the beginning of each chapter, the indexing of references is reset to 1, and references are indexed continuously in the order they are presented through the main text and Appendices so as to avoid unnecessary duplication of citations.

I.D. Copyright Permissions

Each of the five remaining chapters of this dissertation has been derived predominantly from a published manuscript. In all cases, the figures, captions, tables, and text accompanying those elements have been used with permission from the original publishing agent, as follows:

- Chapter II is derived from Kirchhofer, N. D. *et al.* The conjugated oligoelectrolyte DSSN+ enables exceptional coulombic efficiency *via* direct electron transfer for anode-respiring *Shewanella oneidensis* MR-1—a mechanistic study. *Phys. Chem. Chem. Phys.* 16, 20436–43 (2014). – Reproduced by permission of the PCCP Owner Societies.
- Chapter III is derived from Kirchhofer, N. D., Dahlquist, F. W., Bazan, G. C. Conjugated oligoelectrolytes accelerate syntrophic anaerobic exchange of reducing equivalents. *In preparation*, 2016. – To allow for publication of this manuscript and permissions for its use to be granted, publication of this dissertation was embargoed.
- Chapter IV is derived from Kirchhofer, N. D., Rasmussen, M. A., Dahlquist, F. W., Minteer, S. D. & Bazan, G. C. The photobioelectrochemical activity of thylakoid bioanodes is increased *via* photocurrent generation and improved contacts by membrane-intercalating conjugated oligoelectrolytes. *Energy Environ. Sci.* 8, 2698–2706 (2015). – Reproduced by permission of The Royal Society of Chemistry.
- Chapter V is derived from Kirchhofer, N. D., Rengert, Z. D., Dahlquist, F. W., Nguyen, T.-Q., Bazan. G. C. A molecular protein prosthetic for disabled bacteria. *Submitted,* 2016. – To allow for publication of this manuscript and permissions for its use to be granted, publication of this dissertation was embargoed.
- Chapter VI is derived from Kirchhofer, N. D., Mai, C.-K., McCuskey, S. R., Dahlquist, F. W., Bazan, G. C. Amplification of bacterial anode respiration by a self-doped p-type pH-neutral conjugated polyelectrolyte. *In preparation*, 2016. – To allow for publication of this manuscript and permissions for its use to be granted, publication of this dissertation was embargoed.

I.E. References

1. Galvani, L. De bononiensi scientiarum et artium instituto atque academia Comentarrii. **7,** 363–418 (1791).
2. Bard, A. J. & Faulkner, L. R. *Electrochemical Methods: Fundamentals and Applications*. (2001).
3. Potter, M. C. Electrical effects accompanying the decomposition of organic compunds. *Proc. R. Soc. Lond. B* **84,** 260–276 (1911).
4. Hill, H. A. O. & Higgins, I. J. Bioelectrocatalysis. *Philos. Trans. R. Soc. A Math. Phys. Eng. Sci.* **302,** 267–273 (1981).
5. Lovley, D. R. Electromicrobiology. *Annu. Rev. Microbiol.* **66,** 391–409 (2012).
6. Magliulo, M., Manoli, K., Macchia, E., Palazzo, G. & Torsi, L. Tailoring Functional Interlayers in Organic Field-Effect Transistor Biosensors. *Adv. Mater.* 1–24 (2014).
7. Park, S., Kang, Y. J. & Majd, S. A Review of Patterned Organic Bioelectronic Materials and their Biomedical Applications. *Adv. Mater.* **27,** 7583–7619 (2015).
8. Green, R. & Abidian, M. R. Conducting Polymers for Neural Prosthetic and Neural Interface Applications. 1–18 (2015).
9. Kim, B.-H., Kim, H.-J., Hyun, M.-S. & Park, D.-H. Direct electrode reaction of Fe(III)-reducing bacterium, Shewanella putrefaciens. *J. Microbiol. Biotechnol.* **9,** 127–131 (1999).
10. Kim, H. J., Hyun, M. S., Chang, I. S. & Kim, B. H. A fuel cell type lactate biosensor using a metal reducing bacterium, Shewanella putrefaciens.pdf. *J. Microbiol. Biotechnol.* **9,** 365–367 (1999).
11. Debabov, V. G. Electricity from microorganisms. *Mikrobiologiia* **77,** 149–157 (2008).
12. Logan, B. E. Exoelectrogenic bacteria that power microbial fuel cells. *Nat. Rev. Microbiol.* **7,** 375–81 (2009).
13. Borole, A. P. *et al.* Electroactive biofilms: Current status and future research needs. *Energy Environ. Sci.* **4,** 4813 (2011).
14. Lovley, D. R. Bug juice: harvesting electricity with microorganisms. *Nat. Rev. Microbiol.* **4,** 497–508 (2006).
15. Du, J., Catania, C. & Bazan, G. Modification of Abiotic–Biotic Interfaces with Small Molecules and Nanomaterials for Improved Bioelectronics. *Chem. Mater.* **26,** 686–697 (2013).
16. Jensen, H. M. *et al.* Engineering of a synthetic electron conduit in living cells. *Proc. Natl. Acad. Sci. U. S. A.* **107,** 19213–8 (2010).
17. Goldbeck, C. P. *et al.* Tuning Promoter Strengths for Improved Synthesis and Function of Electron Conduits in Escherichia coli. *ACS Synth. Biol.* **2,** 150–9 (2013).
18. Flynn, J. M., Ross, D. E., Hunt, K. A., Bond, D. R. & Gralnick, J. A. Enabling Unbalanced Fermentations by Using Engineered Electrode-Interfaced Bacteria. *MBio* **1,** 1–8 (2010).
19. Garner, L. E. *et al.* Modification of the optoelectronic properties of membranes via insertion of amphiphilic phenylenevinylene oligoelectrolytes. *J. Am. Chem. Soc.* **132,** 10042–52 (2010).
20. Arrhenius, T. S., Blanchard-Desce, M., Dvolaitzky, M., Lehn, J. M. & Malthete, J. Molecular devices: Caroviologens as an approach to molecular wires-synthesis and incorporation into vesicle membranes. *Proc. Natl. Acad. Sci. U. S. A.* **83,** 5355–5359

(1986).
21. Davis, W., Svec, W., Ratner, M. & Wasielewski, M. Molecular-wire behaviour in p-phenylenevinylene oligomers. *Nature* **396,** 60–63 (1998).
22. Lloveras, V. *et al.* Tunneling versus hopping in mixed-valence oligo-p-phenylenevinylene polychlorinated bis(triphenylmethyl) radical anions. *J. Am. Chem. Soc.* **133,** 5818–33 (2011).
23. Choi, S. H. & Frisbie, C. D. Enhanced hopping conductivity in low band gap donor-acceptor molecular wires Up to 20 nm in length. *J. Am. Chem. Soc.* **132,** 16191–201 (2010).
24. Lu, Q. *et al.* From tunneling to hopping: a comprehensive investigation of charge transport mechanism in molecular junctions based on oligo(p-phenylene ethynylene)s. *ACS Nano* **3,** 3861–8 (2009).
25. Ho Choi, S., Kim, B. & Frisbie, C. D. Electrical resistance of long conjugated molecular wires. *Science* **320,** 1482–6 (2008).
26. Marsili, E., Rollefson, J. B., Baron, D. B., Hozalski, R. M. & Bond, D. R. Microbial biofilm voltammetry: direct electrochemical characterization of catalytic electrode-attached biofilms. *Appl. Environ. Microbiol.* **74,** 7329–37 (2008).
27. Kirchhofer, N. D. *et al.* The conjugated oligoelectrolyte DSSN+ enables exceptional coulombic efficiency via direct electron transfer for anode-respiring Shewanella oneidensis MR-1-a mechanistic study. *Phys. Chem. Chem. Phys.* **16,** 20436–43 (2014).
28. Kirchhofer, N. D., Rasmussen, M. A., Dahlquist, F. W., Minteer, S. D. & Bazan, G. C. The photobioelectrochemical activity of thylakoid bioanodes is increased via photocurrent generation and improved contacts by membrane-intercalating conjugated oligoelectrolytes. *Energy Environ. Sci.* **8,** 2698–2706 (2015).
29. *Conjugated Polyelectrolytes: Fundamentals and Applications*. (John Wiley & Sons, 2013).
30. Mai, C. K. *et al.* Facile doping of anionic narrow-band-gap conjugated polyelectrolytes during dialysis. *Angew. Chemie - Int. Ed.* **52,** 12874–12878 (2013).
31. Zhou, H. *et al.* Conductive Conjugated Polyelectrolyte as Hole-Transporting Layer for Organic Bulk Heterojunction Solar Cells. *Adv. Mater.* **26,** 780–785 (2014).
32. Li, Y. *et al.* Electronic Properties of Conjugated Polyelectrolyte/Single-Walled Carbon Nanotube Composites. *Adv. Mater.* **26**, 4697-4703 (2014).
33. Zhou, H. *et al.* Polymer Homo-Tandem Solar Cells with Best Efficiency of 11.3%. *Adv. Mater.* **27,** 1767–1773 (2015).
34. Mai, C.-K. *et al.* Electrical properties of doped conjugated polyelectrolytes with modulated density of the ionic functionalities. *Chem. Commun.* **51,** 17607–17610 (2015).
35. Choi, H. *et al.* Conjugated polyelectrolyte hole transport layer for inverted-type perovskite solar cells. *Nat. Commun.* **6,** 7348 (2015).
36. Zhou, H. *et al.* Solution-Processed pH-Neutral Conjugated Polyelectrolyte Improves Interfacial Contact in Organic Solar Cells. *ACS Nano* **9,** 371–377 (2015).
37. Mai, C. *et al.* Side-Chain Effects on the Conductivity, Morphology, and Thermoelectric Properties of Self-Doped Narrow-Band-Gap Conjugated Polyelectrolytes. *J. Am. Chem. Soc.* **136**, 13478-13481 (2014).
38. Mai, C.-K. *et al.* Varying the ionic functionalities of conjugated polyelectrolytes leads to both p- and n-type carbon nanotube composites for flexible thermoelectrics. *Energy*

Environ. Sci. **8,** 2341–2346 (2015).
39. Feng, G., Mai, C.-K., Zhan, R., Bazan, G. C. & Liu, B. Narrow band gap conjugated polyelectrolytes for photothermal killing of bacteria. *J. Mater. Chem. B* **3,** 7340–7346 (2015).
40. Rabaey, K. & Rozendal, R. A. Microbial electrosynthesis - revisiting the electrical route for microbial production. *Nat. Rev. Microbiol.* **8,** 706–16 (2010).
41. Franks, A. E. & Nevin, K. P. Microbial Fuel Cells, A Current Review. *Energies* **3,** 899–919 (2010).
42. Logan, B. E. & Rabaey, K. Conversion of wastes into bioelectricity and chemicals by using microbial electrochemical technologies. *Science.* **337,** 686–90 (2012).

Chapter II. Mechanistic Understanding of the Effect of a Conjugated Oligoelectrolyte (COE) on Bacterial Anode Respiration by Modification of the Model Electrogenic Organism *Shewanella oneidensis* MR-1

II.A. Abstract

Shewanella oneidensis MR-1 was cultivated on lactate with poised graphite electrodes (*E* = +0.2 V vs. Ag/AgCl) as electron acceptors in order to explore the basis for sustained increases in anodic current output following addition of the lipid-intercalating conjugated oligoelectrolyte (COE) 4,4'-bis(4'-(*N*,*N*-bis(6"-(*N*,*N*,*N*-trimethylammonium)hexyl)amino)-styryl)stilbene tetraiodide (DSSN+). Microbial cultures injected with DSSN+ exhibit a ~2.2-fold increase in charge collected, a ~3.1-fold increase in electrode colonization by *S. oneidensis*, and a ~1.7-fold increase in coulombic efficiency from 51 ± 10% to an exceptional 84 ± 7% without obvious toxicity effects. Direct microbial biofilm voltammetry reveals that DSSN+ rapidly, sustainably increases cytochrome-based direct electron transfer and subsequently increases flavin-based mediated electron transfer. Control experiments indicate that DSSN+ does not contribute to current in the absence of bacteria.

II.B. Broader Impact

The conversion of organic carbon substrates to electricity by electrogenic bacteria such as *Shewanella oneidensis* MR-1 is of relevance for its potential utility in wastewater treatment, environmental remediation, and power generation for remote sensing. However, direct conversion of organic carbon to electricity remains slow and inefficient with respect to other bioconversion processes. The efficiency of the process is usually measured by the coulombic efficiency of the system, which is the percentage of the theoretical maximum charge that the

system produces from a given quantity of substrate. This contribution demonstrates that modifying anodic *S. oneidensis* with the conjugated oligoelectrolyte DSSN+ induces exceptional coulombic efficiency in conversion of lactate to electricity as well as striking increases in anodic current, or electron transfer rate. Voltammetric analysis provides direct, quantitative evidence that DSSN+ primarily boosts direct electron transfer to an electrode. This is a vital conceptual steppingstone in designing synthetic modifications of biotic-abiotic electronic interfaces.

II.C. Introduction

Shewanella oneidensis MR-1 is a dissimilatory metal-reducing bacterium capable of respiring on a variety of soluble and insoluble acceptors.[1–4] This species is capable of anaerobic growth[5] by transporting electrons across its outer membrane *via* the MtrCAB-OmcA porin-cytochrome complex[6] to respire on exogenous metal oxides and electrodes, producing usable electrical current in the latter case. From the standpoint of bioelectricity production, which has applications in, for example, improving wastewater treatment or autonomous remote sensing systems, it is desirable to increase the coulombic efficiency (CE) as much as possible, and this challenge is under study in bioelectronics[7] and electromicrobiology.[8–10]

Key extracellular electron transport (EET) processes proposed[11] for *S. oneidensis* include (1) direct electron transfer (DET) to solid-state acceptors *via* terminal membrane-bound cytochromes MtrC and OmcA,[12–20] and (2) mediated electron transfer (MET) by secreted flavin-based molecules that shuttle electrons between cytochromes and exogenous acceptors,[16,21–25] as well as increase the electron transfer rate as bound flavin semiquinone.[26–28] These EET processes are electrochemically distinguishable in characteristic redox potential

ranges of –0.4-0 V (MET) and 0-0.2 V (DET)[11] which provides a crucial mechanistic backdrop for assessing perturbations to EET. A bottleneck exists for DET in the final electron transfer step to the solid acceptor[16] because MtrC and OmcA must come into intimate contact with the surface. Flavins may alleviate this barrier by coming into diffusive contact with MtrC and OmcA.[27–29] Finally, a third respiratory process has been discussed involving electrically conductive biosynthesized "nanowires" that transport electrons *via* DET over long distances,[30–35] and this mechanism remains under investigation.[36,37]

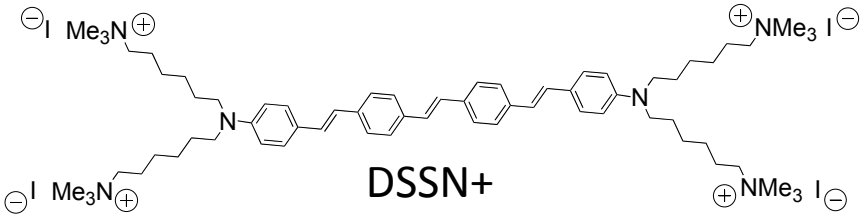

Figure II.1. The molecular structure of the conjugated oligoelectrolyte DSSN+.

Conjugated oligoelectrolytes (COEs), such as 4,4'-bis(4'-(*N,N*-bis(6"-(*N,N,N*-trimethylammonium)hexyl)amino)-styryl)stilbene tetraiodide (DSSN+) displayed in Fig. II.1, have recently drawn attention for their ability to increase current production in microbial fuel cells with *S. cerevisiae*,[38] *E. coli*,[39,40] and wastewater,[41] as well as current-driven substrate turnover in *S. oneidensis* microbial electrosynthesis cells.[42] Optical characterization indicates that DSSN+ intercalates into membranes perpendicular to their surface.[38,39,42,43] Additional studies indicate that intercalated DSSN+ can promote fluorescence resonance energy transfer[44] and transmembrane ion conductance[45] with minimal membrane perturbation.[46] Most recently, studies with *S. oneidensis* MR-1 indicate that supplemented flavin provides a higher-magnitude current boost than DSSN+, and yet DSSN+ does appear to decrease charge

transfer resistance independently of flavin.[47] However, detailed understanding of the mechanism of EET enhancement was not provided in that study, nor was any quantitative correlation made to device efficiency or biomass. These essential, missing elements are presented here.

In this chapter, the impact of DSSN+ addition to *S. oneidensis* EET is examined through use of 3-electrode batch-type membraneless bioelectrochemical reactors. The resulting data provide direct evidence that rapid, sustainable increases in anodic respiratory current and the exceptionally-high CE from DSSN+ addition arise from (1) an increase in cytochrome-based DET redox current and (2) an increase in biofilm formation on the electrode, which together also increase the flavin-based MET redox current over time.

In this work, triplicate unmodified control reactors (hereafter referred to as "Type 1") are statistically compared to identically prepared triplicate test reactors that receive 5 μM DSSN+ during operation (hereafter referred to as "Type 2"). For each reactor, chronoamperometry (CA), cyclic voltammetry (CV), and differential pulse voltammetry (DPV) were conducted. For clarity throughout the text, the same single representative experiment is presented in figures to showcase the discussed behavior of the reactors. Average parameters from triplicate reactors are presented in Table II.1 and additional data is provided in §II.F. Appendix II as indicated in the text. It is important to note that reported current densities in these experiments are calculated for 1 cm × 1 cm × 0.2 cm carbon felt working electrodes with a surface area of 226 ± 12 cm^2, as described in §II.F. Appendix II. This surface area is ~81-fold larger than had been previously reported for identical electrodes,[47] so current densities herein are accordingly ~81-fold smaller.

II.D. Results and Discussion

Figure II.1 displays the CA results as a function of time for the two types of reactors. Also shown are relevant timepoints in the course of the experiments; these are designated I to VI. The data from I to II (t = 0–20.4 h) compares the current generation for the two reactors, prior to DSSN+ addition to Type 2 reactors; during this time, one observes virtually identical behavior between the two biofilms. After the full medium change at II, all reactors typically reduce their current output to about 40% of the maximum observed between I and II. This is due to removal of planktonic cells and extracellular flavins that contribute to anodic current,[21,47] leaving only the biofilm to produce current.

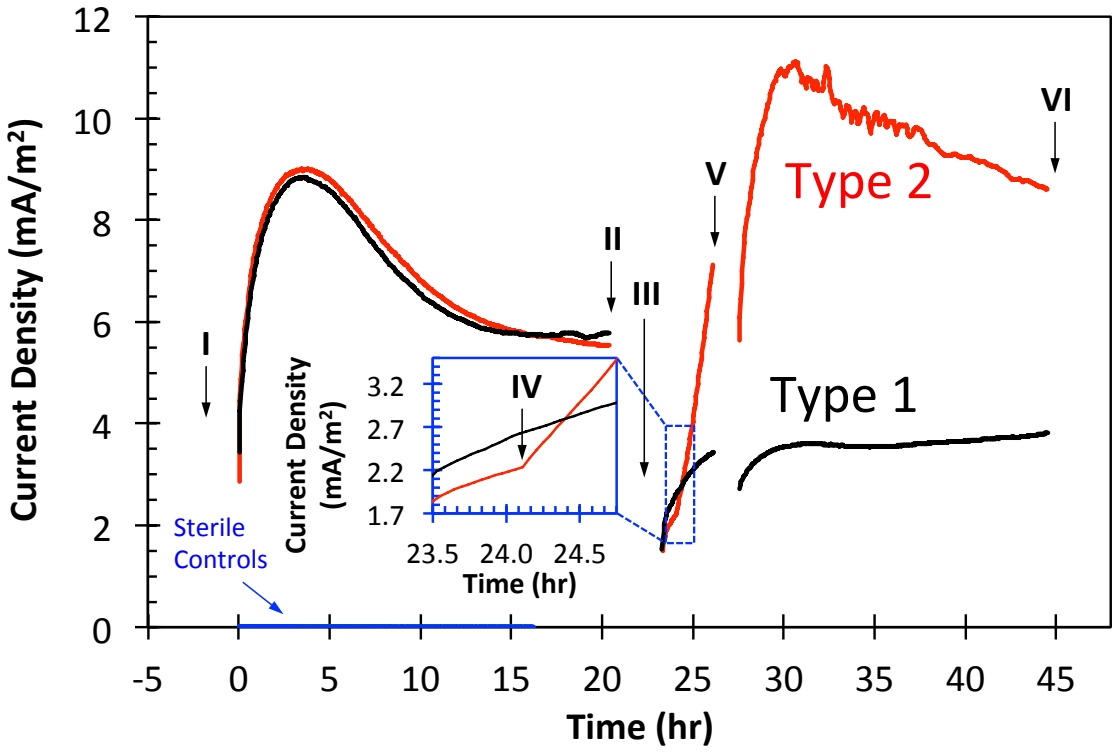

Figure II.2. Representative CA from one replicate of *S. oneidensis* in modified M1 minimal media at a poised potential of *E* = +0.2 V vs. Ag/AgCl. Note negligible current output from sterile controls (additional details may be found in §II.F. Appendix II). (**I**) Inoculation of reactors and initiation of current collection. (**II**) Full media change; reactor volume was replaced with fresh M1 media containing 30 mM Na-(L)-lactate. (**III**) HPLC sample, CV, and DPV after the full media change; CA resumed. (**IV, inset**) Addition of 5 µM DSSN+ to Type 2 reactor. (**V**) CV and DPV ~2 hours after DSSN+ addition to examine the electrochemical nature of the current acceleration. (**VI**) HPLC sample, CV, and DPV at the end of current collection, followed by chemical cell fixation and SEM of the fixed electrode.

Examination of Fig. II.2 from III (t = 23.2 h) to VI (t = 44.5 h) shows that when DSSN+ is added to Type 2 reactors at IV (t = 24.1 h), an acceleration in current production occurs within a short time (≤ 160 seconds), while Type 1 reactors remain stable. This ≤ 160 second response is much faster than the ~1.5 hour generation time of *S. oneidensis* in minimal media,[48] suggesting a boost in EET and not stimulated growth. After IV, current output from the Type 2 reactors remains ≥ 2-fold higher than Type 1 reactors, indicating the enhancement is sustained (see Fig. II.S1 for the other two replicates). From III to VI, DSSN+ addition also induces a statistically significant ~1.7 ± 0.3-fold increase in the CE (p = 0.010) from 51 ± 10% (Type 1 reactors) to 84 ± 7% (Type 2 reactors). The latter value is extraordinarily high for *S. oneidensis*-based devices.[49] Biofilm collected charge, $Q_{III\text{-}VI}$, also statistically significantly increases 2.2 ± 0.4-fold (p = 0.036) from 5.2 ± 0.9 C (Type 1) to 11.4 ± 2.7 C (Type 2) during this time. Table II.1 provides a summary of all data relevant to these measurements, including lactate concentration change, Δ[lac], and ideal charge collected from that lactate consumption, Q_{ideal}. Normalized ratios ± standard deviations as well as p-values for these parameters comparing Type 2 and Type 1 reactors are also provided, and indicate that not all measured parameters change statistically significantly with DSSN+ addition. It is also worth mentioning that in sterile reactors with poised electrodes containing growth media, DSSN+, and/or lactate, anodic current is negligibly small compared to reactors with *S. oneidensis* (this data is presented in Fig. II.2, but for clarity can also be found in Fig. II.S2). Therefore, addition of DSSN+ and lactate has no current-enhancing effect in the absence of cells.

At the end of operation, electrodes were removed, chemically fixed, and sliced with a razor for SEM imaging to estimate the electrode surface cell density, ρ (Fig. II.3 A and B).

Details of calculation of ρ are provided in §I.F.1. Methods, and SEM images from remaining replicate experiments are found in Fig. II.S3. For Type 1 reactors (Fig. II.3 A), triplicate average cell density is $\rho = 2.3 \pm 1.0 \times 10^7$ cells/cm^2, whereas for the Type 2 reactors (Fig. II.3 B) one observes $\rho = 7.0 \pm 2.5 \times 10^7$ cells/cm^2. These images thus demonstrate a 3.1 ± 0.6-fold increase in ρ for Type 2 reactors compared to Type 1 ($p = 0.120$). Such features are summarized in Fig. II.3 C and D and are provided in Table II.1.

This set of experiments demonstrates that DSSN+ promotes electrode colonization and confirms that the addition of 5 μM DSSN+ is not toxic to the developing biofilm. It is also notable that the planktonic turbidity remains undetectable during this time. Comparison of

Table II.1. Triplicate Mean Parameters and Normalized Ratios from Type 1 and Type 2 Reactors

Parameter	Expression	Type 1 Reactor	Type 2 Reactor	*p*-value[e]	Normalized Ratio (Type 2: Type 1)[f]
Biofilm Collected Charge (C)[a]	$Q_{III\text{-}VI} = \int I_{III\text{-}VI}(t)\mathrm{d}t$	5.2 ± 0.9	11.4 ± 2.7	0.036	2.2 ± 0.4
[lactate] Change (mM)[a]	Δ[lac]	−1.8 ± 0.2	−2.3 ± 0.4	0.251	1.3 ± 0.4
Ideal Charge Collected (C)[a,b]	$Q_{ideal} = -\Delta[\mathrm{lac}] \times VFn$	10.4 ± 1.2	13.5 ± 2.4	0.251	1.3 ± 0.4
Coulombic Efficiency (%)[a]	$CE = 100 \times Q_{III\text{-}VI}/Q_{ideal}$	51 ± 10	84 ± 7	0.01	1.7 ± 0.3
Electrode Cell Density (million/cm^2)[c]	$\rho = (1/K)\Sigma_k(N_k/\pi d_k h)$	23 ± 10	70 ± 25	0.12	3.1 ± 0.6
Max Current per Unit Dry Cell Mass (μA/mg)[d]	$I_{III\text{-}VI}(max)/\rho A_{electrode} m$	44 ± 9	34 ± 4	0.119	0.8 ± 0.2

[a] After media change to end of operation (between **III** and **VI**), thus deconvoluting the biofilm signal from bulk solution. [b] Calculated assuming 100% *CE* ($n = 4$ electrons/lactate); V = reactor volume (15 mL); F = Faraday constant = $N_A e$. [c] At the end of reactor operation (timepoint VI); values are mean ± std. dev. ($K = 12$ replicates for each of 3 electrodes of each type). [d] Surface area of the graphite felt electrodes, $A_{electrode}$, was determined to be 226 ± 12 cm^2 (24 replicates). The specific mass of 1×10^6 cells, m, was determined to be 4.4 ± 0.6 × 10^{-7} g (3 replicates). $I_{III\text{-}VI}$(max) was extracted from CA data. See §I.F.1. Methods, for details. [e] Calculated from 2-tailed *t*-tests. If four decimal places were retained, the p-value for *CE* is 0.0098 (i.e. > 99% significance). [f] Normalized Ratios are calculated by first dividing the parameter values for each reactor by $Q_{I\text{-}II}$ (i.e. integrated total charge collected between I and II) and then calculating the ratio. This treatment numerically corrects for possible confounding differences in the geometry and absolute number of cells on the electrode during biofilm establishment. For Electrode Cell Density, uncertainty was propagated by addition in quadrature to determine the std. dev.

the ρ-increase (3.1 ± 0.6) and the $Q_{III\text{-}VI}$-increase (2.2 ± 0.4) indicates that DSSN+ does not improve EET on a per-cell basis. However, one finds a linear relationship (Fig. II.3 D) between ρ and the normalized charge collected, $Q_{III\text{-}VI}/Q_{I\text{-}II}$, which shows that DSSN+-induced increases are not reactor-specific (see Table II.1 for normalization details).

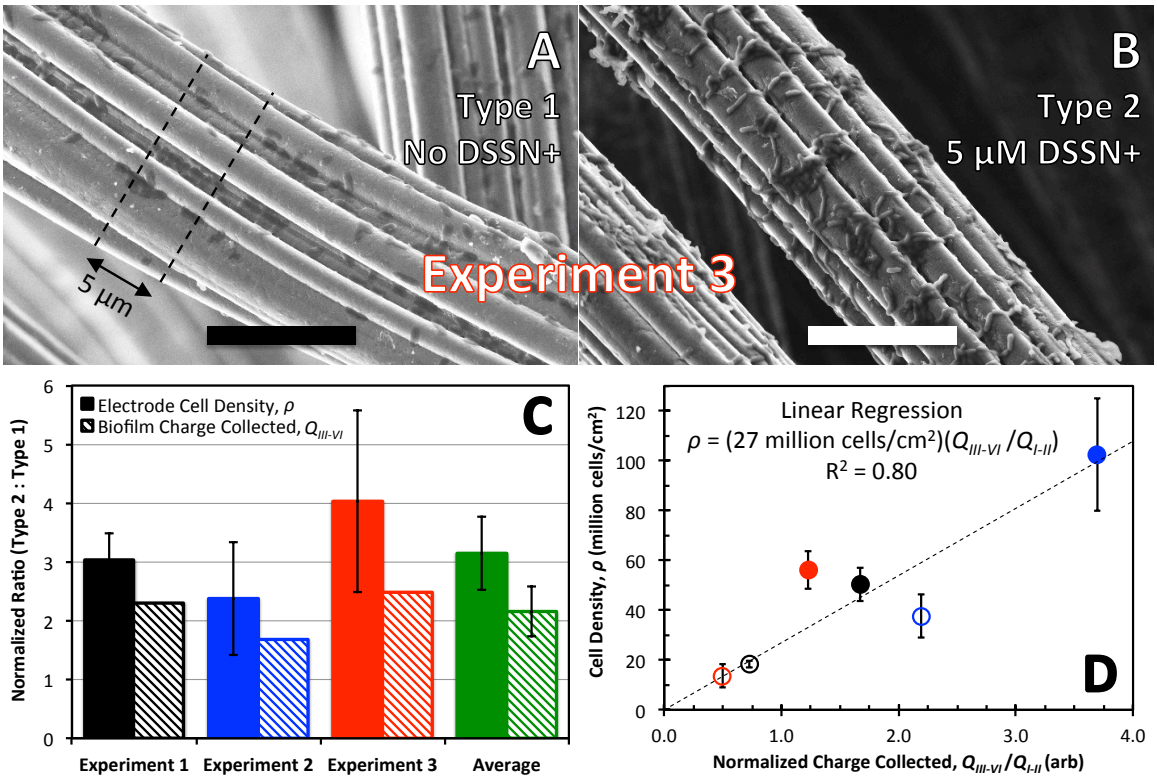

Figure II.3. Representative SEM images of chemically fixed graphite felt working electrodes, summary of resulting electrode cell density measurements, and correlation to biofilm collected charge. All six electrodes were imaged after timepoint VI, but only images from Experiment 3 are presented for clarity. Scale bars are 10 µm. (**A**) Fixed working electrode from Type 1 reactor. Dashed lines illustrate a possible geometric section utilized for cell counting. (**B**) Fixed working electrode from Type 2 reactor. (**C**) Normalized Ratios of Electrode Cell Density, ρ, and Biofilm Collected Charge, $Q_{III\text{-}VI}$, between all Type 2 and Type 1 reactors in this study. Green bars: average of Experiments 1, 2, and 3. Additional SEM images can be found in ESI, Fig. I.S3, and details of normalization can be found in Table I.1, *f.* (**D**) Plot of Electrode Cell Density, ρ, vs. Normalized Collected Charge, $Q_{III\text{-}VI}/Q_{I\text{-}II}$, for all six reactors in this work. Black, Experiment 1; Blue, Experiment 2; Red, Experiment 3; Open circles, Type 1 reactors; Closed circles, Type 2 Reactors; Dashed line, best-fit linear regression (equation inset).

At timepoints III, V, and VI in Fig. II.2, current collection was paused to conduct CV and DPV experiments. CV measurements at these timepoints (Fig. II.4 A and C) reveal two primary reversible catalytic electron transfer waves as the potential is swept past E = –0.42 V

and 0.05 V. That is, current output at these two potentials rises rapidly and begins to saturate at a limiting current, which is characteristic of redox species rapidly cycling back to a reduced state from metabolic turnover, thereby continuously supplying the electrode with electrons.[50,51] The absence of local maxima in the current response indicates no lactate mass transport limitations. Potentials of –0.42 V and +0.05 V are assigned to MET via flavins[21,22] and DET *via* cytochromes,[11,28,52] respectively. Additionally, it is worth noting that the current produced at the CV vertex potential (E = +0.2 V) at III, V, and VI in Fig. II.4 A and C is similar in amplitude to the CA current at the same timepoints in Fig. II.2, indicating that the electrochemical analyses accurately interrogate the respiring biofilms.

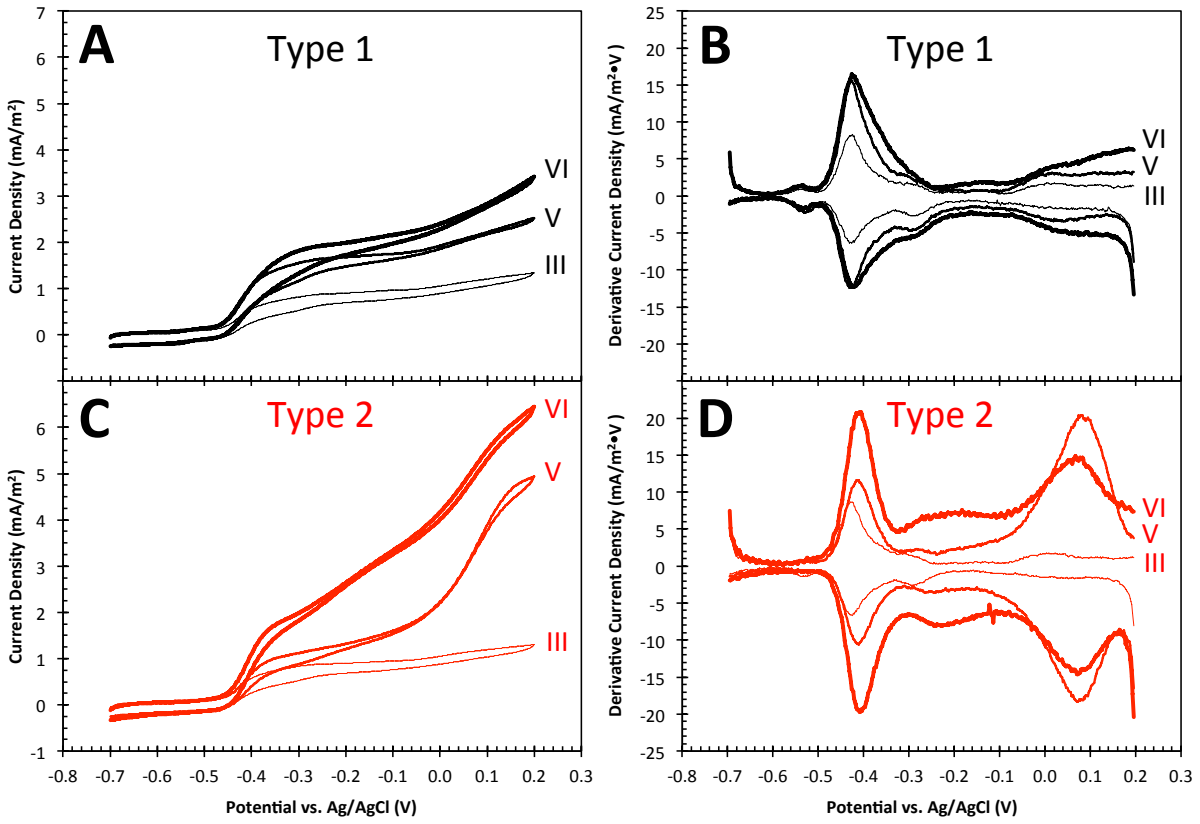

Figure II.4. Representative turnover CV and first derivative traces for Type 1 and Type 2 reactors to identify redox species affected by addition of DSSN+. All scans were conducted at 5 mV/s at timepoints III, V, and VI. The additional two replicate experiments are presented in Fig. S1. (**A**) CV traces from the Type 1 reactor. (**B**) 1st derivative of CV traces from the Type 1 reactor. (**C**) CV traces from the Type 2 reactor. (**D**) 1st derivative of CV traces from the Type 2 reactor.

From first derivative analysis of the CV traces (Fig. II.4 B and D), an additional catalytic wave can be detected near E = –0.3 V. This redox feature is tentatively assigned to flavin semiquinone based on the similarity to the previously reported biologically-stabilized flavin semiquinone peak position.[28,53] CV studies of sterile M1 media containing riboflavin, lactate, and/or DSSN+ (Fig. II.S4) lack this redox peak, further suggesting it is biologically-stabilized. Derivative analysis also reveals a redox feature at E = –0.54 V which does not contribute to catalytic electron transfer and is associated with the media (assigned by its presence in Fig. II.S4). Finally, Fig. II.S4 also indicates that DSSN+ is not redox active in the aqueous media in the potential window used for voltammetry (–0.7 V < E < +0.2 V) and therefore does not contribute to current.

In Fig. II.4, it becomes apparent that the EET increase from DSSN+ addition in the Type 2 reactor arises from current through the cytochrome DET machinery (E > –0.1 V[11]). This can be observed readily at timepoints V and VI by comparing the large-amplitude peak at E = +0.05 V in Fig. II.4 D to the same peak in Fig. II.4 B (the Type 1 reactor). Enhanced DET is consistent with the observed increase in CE, as DET is reported to be more efficient than MET due to diffusive loss of electrons in the latter.[49] Additionally, the elevated DET appears to cause a subsequent delayed increase of flavin signals over the same time period, seen by the increase in CV derivative peak amplitudes for flavin and flavin semiquinone at E = −0.42 V and −0.3 V, respectively, by timepoint VI (Fig. II.4 D).[28,29] An additional set of control CV experiments was conducted with the reactors' effluent after timepoint VI in freshly autoclaved identical reactors (Fig. II.S5). These experiments show essentially no faradaic current and hence indicate that nearly all of the electroactivity in Figs. II.1, II.2, and II.3 arises from electrode-associated cells. Thus, the media change at II is effective in

deconvoluting the biofilm signal from any bulk solution contributions.

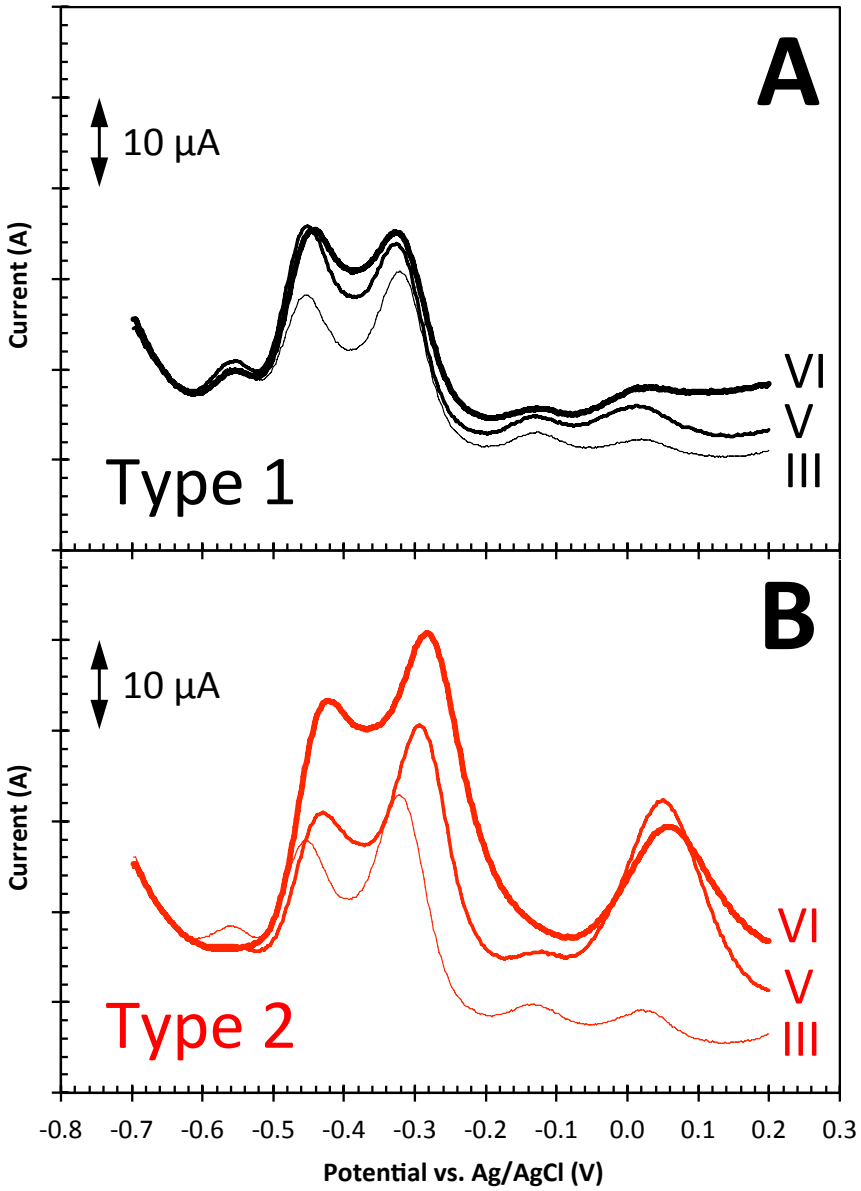

Figure II.5. DPV scans of working electrodes from representative Type 1 and Type 2 reactors show substantial increases in DET (and subsequently MET) redox activity due to DSSN+ addition. Scan rate matches CV at 5 mV/s for the most direct comparison. Note the 10 µA scaling arrow for the vertical axis (not current density). (**A**) Scans of the Type 1 reactor at timepoints III, V, and VI. (**B**) Scans of Type 2 reactor at timepoints III, V, and VI.

DPV measurements (Fig. II.5) were conducted immediately following CV analyses. These experiments are qualitatively similar to the first derivative CV analyses of the

electrodes, but DPV provides resolution by subtracting non-faradaic current from the redox signals.[54] Additionally, with mathematical modelling, peak areas empirically correlate to effective surface concentrations of redox species, and peak widths empirically correlate[54] to the number of electrons transferred per redox reaction, n (see §I.F.1. Methods for details).

Table II.2. Extracted Redox Parameters from Gaussian Fits to DPV from Representative Type 1 and Type 2 Reactors

			Type 1 Reactor			Type 2 Reactor		
Redox Species	Extracted DPV Redox Parameter	Variable	III	V	VI	III	V	VI
Flavin	Peak Center (V vs. Ag/AgCl)[a]	E_o	–0.428	–0.426	–0.416	–0.430	–0.404	–0.398
	Peak Height (μA)[a]	I_o	10.8	18.2	18.1	10.9	15.3	27.5
	Peak FWHM (mV)	2.35σ	71	71	71	71	71	94
	e^- Transferred per Redox Reaction[b]	$n = 2.30RT/\sigma F$	2	2	2	2	2	1.5
	Peak Area (μA•mV)	$\int I(E)dE$	814	1369	1363	820	1154	2754
	Normalized Concentration[c]	—	1	1.7	1.7	1	1.4	3.4
Flavin semi-quinone	Peak Center (V vs. Ag/AgCl)[a]	E_o	–0.298	–0.304	–0.304	–0.298	–0.270	–0.258
	Peak Height (μA)[a]	I_o	19.6	21	20.6	25.4	25.8	33.6
	Peak FWHM (mV)	2.35σ	94	94	94	94	94	118
	e^- Transferred per Redox Reaction[b]	$n = 2.30RT/\sigma F$	1.5	1.5	1.5	1.5	1.5	1.2
	Peak Area (μA•mV)	$\int I(E)dE$	1964	2104	2065	2548	2595	4220
	Normalized Concentration[c]	—	1	1.1	1.1	1	1	1.7
DET (cyto-chromes)	Peak Center (V vs. Ag/AgCl)[a]	E_o	0.047	0.037	0.061	0.047	0.075	0.083
	Peak Height (μA)[a]	I_o	2	3.5	3.5	3.8	21.1	12.7
	Peak FWHM (mV)	2.35σ	71	94	141	71	118	130
	e^- Transferred per Redox Reaction[b]	$n = 2.30RT/\sigma F$	2	1.5	1	2	1.2	1.1
	Peak Area (μA•mV)	$\int I(E)dE$	149	348	522	284	2645	1748
	Normalized Concentration[c]	—	1	2.3	3.5	1	9.3	6.2

[a] E_o values are corrected by one half the pulse height, $\Delta E/2$ = +25 mV, and I_o values are baseline subtracted (see §I.F.1. Methods for details). [b] Values of n are calibrated to the known 2-electron redox system of flavin using the FWHM (see §I.F.1. Methods for details). [c] In all cases, concentration is reported normalized to the DPV-determined value at timepoint III, and is thus unitless.

In this section, representative data from Experiment 3 is presented as well as numerically summarized in Table II.2. First, DPV redox peaks in the Type 1 reactor were analysed to establish values for an unmodified reactor (Fig. II.5 A). The area under the E = +0.05 V cytochrome peak increases over time. Fitting and integration of this peak (Fig. II.S6) reveals that the concentration increases by 2.3-fold ~3 hours after the media change (Fig. II.5 A, V) and continues to increase by up to 3.5-fold at the end of reactor operation (Fig. II.5 A, VI). Similar analysis of the E = −0.3 V (flavin semiquinone) and E = −0.42 V (flavin) peaks indicates that flavin semiquinone concentration increases only marginally (by 1.1-fold) ~3 hours after the media change (V) and stays at the same level (no obvious increase) until the end of reactor operation (VI). Flavin concentration increases by 1.7-fold approximately 3 hours after the media change (V), staying at the same level until the end of reactor operation (VI).

Next, DPV redox peaks in the Type 2 reactor (Fig. II.5 B) were analysed for comparison to the Type 1 reactor. Cytochrome concentration increases by 9.3-fold ~2 hours after DSSN+ addition (V), and then falls off to a 6.2-fold increase at the end of reactor operation (VI); the latter is nearly a 2-fold increase compared to the Type 1 reactor, and represents a quantitative measure of DSSN+ enhancing the rate of DET. Increases in concentrations of flavin semiquinone and flavin lag this increase in cytochrome signal. Flavin semiquinone increases negligibly ~2 hours after DSSN+ addition (V), but eventually increases by up to 1.7-fold at the end of reactor operation (VI)—much higher than the Type 1 reactor, and consistent with an increased rate of electron transfer.[28] Flavin increases by 1.4 fold ~2 hours after DSSN+ addition (V), which is reduced 0.3-fold compared to the Type 1 reactor at the same point. Ultimately, flavin increases 3.4-fold by the end of reactor operation (VI), which is a much

larger increase than is observed in the Type 1 reactor (1.7-fold). These DPV comparisons of the three redox species are consistent with the same trends in CV experiments in which DSSN+ increases cytochrome DET catalytic current in Type 2 reactors (Fig. II.4 A and C) and causes a subsequent delayed increase in the flavin-based MET catalytic currents. It is noteworthy that the rise in cytochrome DET signal is consistent with the observed growth in electrode-associated organisms in Type 2 reactors (Fig. II.3).

Okamoto et al[28] suggested that the number of transferred electrons per redox reaction, n, changes from 2 to 1 when flavins bind to cytochromes of *S. oneidensis* in the semiquinone state, and that this improves the rate of EET for the respiring organism. To explore whether such a phenomenon contributes to DSSN+'s electron transfer boost, the full width at half maximum of DPV current peaks was used to extract reasonable values for n. Specifically, DSSN+ causes the flavin peak to shift from $n = 2$ to $n = 1.5$, the flavin semiquinone peak to shift from $n = 1.5$ to $n = 1.2$, and the cytochrome peak to shift from $n = 2$ to $n = 1.2$, eventually reaching $n = 1.1$. These values are in contrast to the Type 1 reactor where flavin and flavin semiquinone remain constant at $n = 2$ and $n = 1.5$, respectively, and the cytochrome peak shifts from $n = 2$ to $n = 1.5$, eventually reaching a value of $n = 1$. Fractional values of n may be rationalized by the fact that measurements represent a bulk average. This analysis shows that DSSN+ causes n to shift towards 1 for flavins, flavin semiquinones, and cytochromes, as evidenced by broadening of respective DPV current peaks in the Type 2 reactors (see Table II.2). A smaller n is consistent with the proposed EET rate enhancement and thus is also directly consistent with the observed increase in anodic current.

In summary, the addition of 5 μM DSSN+ to poised *S. oneidensis* MR-1 bioreactors causes a rapid (≤ 160 seconds), sustained current increase which results in a >2-fold increase

in charge collected, a >3-fold increase in electrode colonization, and increases the CE of reactors from 51 ± 10% to 84 ± 7%—exceptionally high for a *S. oneidensis* device. Direct biofilm voltammetry indicates quantitatively that this EET increase from adding DSSN+ occurs *via* native cytochrome-based DET machinery and is consistent with respiration shifting towards a faster 1-electron process for all redox species involved. Because of their amphiphilic structure, COEs such as DSSN+ might physically access the comparably amphiphilic membrane-bound cytochromes OmcA and MtrC through electrically-insulating extracellular polymeric substances.[55,56] In this way, the aromatic core of the COE might effectively increase electronic surface area of the cytochromes and explain the rapid, sustainably-elevated rise in DET redox current.

II.E. References

1. Heidelberg, J. F. *et al.* Genome sequence of the dissimilatory metal ion-reducing bacterium Shewanella oneidensis. *Nat. Biotechnol.* **20,** 1118–23 (2002).
2. Coursolle, D. & Gralnick, J. A. Modularity of the Mtr respiratory pathway of Shewanella oneidensis strain MR-1. *Mol. Microbiol.* **77,** 995–1008 (2010).
3. Hartshorne, R. S. *et al.* Characterization of an electron conduit between bacteria and the extracellular environment. *Proc. Natl. Acad. Sci. U. S. A.* **106,** 22169–74 (2009).
4. Fredrickson, J. K. *et al.* Towards environmental systems biology of Shewanella. *Nat. Rev. Microbiol.* **6,** 592–603 (2008).
5. Park, D. H. & Kim, B. H. Growth Properties of the Iron-reducing Bacteria , Shewanella putrefaciens IR-1 and MR-1 Coupling to Reduction of Fe (III) to Fe (II). **39,** 273–278 (2001).
6. Richardson, D. J. *et al.* The 'porin-cytochrome' model for microbe-to-mineral electron transfer. *Mol. Microbiol.* **85,** 201–212 (2012).
7. Du, J., Catania, C. & Bazan, G. Modification of Abiotic–Biotic Interfaces with Small Molecules and Nanomaterials for Improved Bioelectronics. *Chem. Mater.* **26,** 686–697 (2013).
8. Lovley, D. R. Electromicrobiology. *Annu. Rev. Microbiol.* **66,** 391–409 (2012).
9. Logan, B. E. Exoelectrogenic bacteria that power microbial fuel cells. *Nat. Rev. Microbiol.* **7,** 375–81 (2009).
10. Franks, A. E. & Nevin, K. P. Microbial Fuel Cells, A Current Review. *Energies* **3,** 899–919 (2010).
11. Roy, J. N. *et al.* Catalytic biofilm formation by Shewanella oneidensis MR-1 and anode characterization by expanded uncertainty. *Electrochim. Acta* **126,** 3–10 (2014).

12. Myers, C. R. & Myers, J. M. Localization of Cytochromes to the Outer Membrane of Anaerobically Grown Shewanella putrefaciens MR-1. *J. Bacteriol.* **174,** 3429–3438 (1992).
13. Shi, L. *et al.* Isolation of a high-affinity functional protein complex between OmcA and MtrC: Two outer membrane decaheme c-type cytochromes of Shewanella oneidensis MR-1. *J. Bacteriol.* **188,** 4705–14 (2006).
14. Hartshorne, R. S. *et al.* Characterization of Shewanella oneidensis MtrC: a cell-surface decaheme cytochrome involved in respiratory electron transport to extracellular electron acceptors. *J. Biol. Inorg. Chem.* **12,** 1083–94 (2007).
15. Firer-Sherwood, M., Pulcu, G. S. & Elliott, S. J. Electrochemical interrogations of the Mtr cytochromes from Shewanella: opening a potential window. *J. Biol. Inorg. Chem.* **13,** 849–54 (2008).
16. Baron, D., LaBelle, E., Coursolle, D., Gralnick, J. A. & Bond, D. R. Electrochemical measurement of electron transfer kinetics by Shewanella oneidensis MR-1. *J. Biol. Chem.* **284,** 28865–73 (2009).
17. Shi, L. *et al.* The roles of outer membrane cytochromes of Shewanella and Geobacter in extracellular electron transfer. *Environ. Microbiol. Rep.* **1,** 220–227 (2009).
18. Okamoto, A., Nakamura, R. & Hashimoto, K. In-vivo identification of direct electron transfer from Shewanella oneidensis MR-1 to electrodes via outer-membrane OmcA–MtrCAB protein complexes. *Electrochim. Acta* **56,** 5526–5531 (2011).
19. Okamoto, A., Hashimoto, K. & Nakamura, R. Long-range electron conduction of Shewanella biofilms mediated by outer membrane C-type cytochromes. *Bioelectrochemistry* **85,** 61–65 (2012).
20. Marshall, M. J. *et al.* c-Type cytochrome-dependent formation of U(IV) nanoparticles by Shewanella oneidensis. *PLoS Biol.* **4,** e268 (2006).
21. Marsili, E. *et al.* Shewanella secretes flavins that mediate extracellular electron transfer. *Proc. Natl. Acad. Sci. U. S. A.* **105,** 3968–73 (2008).
22. von Canstein, H., Ogawa, J., Shimizu, S. & Lloyd, J. R. Secretion of flavins by Shewanella species and their role in extracellular electron transfer. *Appl. Environ. Microbiol.* **74,** 615–23 (2008).
23. Brutinel, E. D. & Gralnick, J. A. Shuttling happens: soluble flavin mediators of extracellular electron transfer in Shewanella. *Appl. Microbiol. Biotechnol.* **93,** 41–8 (2012).
24. Li, R., Tiedje, J. M., Chiu, C. & Worden, R. M. Soluble electron shuttles can mediate energy taxis toward insoluble electron acceptors. *Environ. Sci. Technol.* **46,** 2813–20 (2012).
25. Kotloski, N. J. & Gralnick, J. A. Flavin Electron Shuttles Dominate Extracellular Electron Transfer by Shewanella oneidensis. *MBio* **4,** 1–4 (2013).
26. Léger, C. & Bertrand, P. Direct electrochemistry of redox enzymes as a tool for mechanistic studies. *Chem. Rev.* **108,** 2379–438 (2008).
27. Ross, D. E., Brantley, S. L. & Tien, M. Kinetic characterization of OmcA and MtrC, terminal reductases involved in respiratory electron transfer for dissimilatory iron reduction in Shewanella oneidensis MR-1. *Appl. Environ. Microbiol.* **75,** 5218–26 (2009).
28. Okamoto, A., Hashimoto, K., Nealson, K. H. & Nakamura, R. Rate enhancement of bacterial extracellular electron transport involves bound flavin semiquinones. *Proc.*

Natl. Acad. Sci. **110,** 1–6 (2013).
29. Coursolle, D., Baron, D. B., Bond, D. R. & Gralnick, J. A. The Mtr respiratory pathway is essential for reducing flavins and electrodes in Shewanella oneidensis. *J. Bacteriol.* **192,** 467–74 (2010).
30. Gorby, Y. A. *et al.* Electrically conductive bacterial nanowires produced by Shewanella oneidensis strain MR-1 and other microorganisms. *Proc. Natl. Acad. Sci. U. S. A.* **103,** 11358–63 (2006).
31. El-Naggar, M. Y. *et al.* Electrical transport along bacterial nanowires from Shewanella oneidensis MR-1. *Proc. Natl. Acad. Sci. U. S. A.* **107,** 18127–31 (2010).
32. Strycharz-Glaven, S. M., Snider, R. M., Guiseppi-Elie, A. & Tender, L. M. On the electrical conductivity of microbial nanowires and biofilms. *Energy Environ. Sci.* **4,** 4366 (2011).
33. Polizzi, N. F., Skourtis, S. S. & Beratan, D. N. Physical constraints on charge transport through bacterial nanowires. *Faraday Discuss.* **155,** 43 (2012).
34. Pirbadian, S. & El-Naggar, M. Y. Multistep hopping and extracellular charge transfer in microbial redox chains. *Phys. Chem. Chem. Phys.* **14,** 13802–8 (2012).
35. Fitzgerald, L. A. *et al.* Shewanella oneidensis MR-1 Msh pilin proteins are involved in extracellular electron transfer in microbial fuel cells. *Process Biochem.* **47,** 170–174 (2012).
36. Malvankar, N. S. & Lovley, D. R. Microbial Nanowires: A New Paradigm for Biological Electron Transfer and Bioelectronics. *ChemSusChem* **5,** 1039–1046 (2012).
37. Malvankar, N. S., Tuominen, M. T. & Lovley, D. R. Comment on 'On electrical conductivity of microbial nanowires and biofilms' by S. M. Strycharz-Glaven, R. M. Snider, A. Guiseppi-Elie and L. M. Tender, Energy Environ. Sci., 2011, 4, 4366. *Energy Environ. Sci.* **5,** 6247 (2012).
38. Garner, L. E. *et al.* Modification of the optoelectronic properties of membranes via insertion of amphiphilic phenylenevinylene oligoelectrolytes. *J. Am. Chem. Soc.* **132,** 10042–52 (2010).
39. Hou, H. *et al.* Conjugated Oligoelectrolytes Increase Power Generation in E. coli Microbial Fuel Cells. *Adv. Mater.* **25,** 1593–7 (2013).
40. Wang, V. B. *et al.* Improving charge collection in Escherichia coli-carbon electrode devices with conjugated oligoelectrolytes. *Phys. Chem. Chem. Phys.* **15,** 5867–72 (2013).
41. Garner, L. E., Thomas, A. W., Sumner, J. J., Harvey, S. P. & Bazan, G. C. Conjugated oligoelectrolytes increase current response and organic contaminant removal in wastewater microbial fuel cells. *Energy Environ. Sci.* **5,** 9449–9452 (2012).
42. Thomas, A. W. *et al.* A lipid membrane intercalating conjugated oligoelectrolyte enables electrode driven succinate production in Shewanella. *Energy Environ. Sci.* **6,** 1761 (2013).
43. Woo, H. Y. *et al.* Solvent Effects on the Two-Photon Absorption of Distyrylbenzene Chromophores. *J. Am. Chem. Soc.* **127,** 14721–14729 (2005).
44. Lee, Y., Yang, I., Lee, J. & Hwang, S. Enhanced Photocurrent Generation by Forster Resonance Energy Transfer between Phospholipid-Assembled Conjugated Oligoelectrolytes and Nile Red. *J. Phys. Chem. C* **117,** 3298–3307 (2013).
45. Du, J. *et al.* Increased ion conductance across mammalian membranes modified with conjugated oligoelectrolytes. *Chem. Commun.* **49,** 9624–6 (2013).

46. Hinks, J. *et al.* Modeling the Membrane Insertion of Molecules Designed for Transmembrane Electron Transfer. *Langmuir* (2014).
47. Wang, V. B. *et al.* Comparison of flavins and a conjugated oligoelectrolyte in stimulating extracellular electron transport from Shewanella oneidensis MR-1. *Electrochem. commun.* **41,** 55–58 (2014).
48. Tang, Y. J., Meadows, A. L. & Keasling, J. D. A Kinetic Model Describing Shewanella oneidensis MR-1 Growth, Substrate Consumption, and Product Secretion. *Biotechnol. Bioeng.* **96,** 125–133 (2007).
49. Renslow, R. *et al.* Modeling biofilms with dual extracellular electron transfer mechanisms. *Phys. Chem. Chem. Phys.* **15,** 19262–83 (2013).
50. Armstrong, F. A., Heering, H. A. & Hirst, J. Reactions of complex metalloproteins studied by protein-film voltammetry. *Chem. Soc. Rev.* **26,** 169–179 (1997).
51. Marsili, E., Rollefson, J. B., Baron, D. B., Hozalski, R. M. & Bond, D. R. Microbial biofilm voltammetry: direct electrochemical characterization of catalytic electrode-attached biofilms. *Appl. Environ. Microbiol.* **74,** 7329–37 (2008).
52. Jain, A. *et al.* Electron transfer mechanism in Shewanella loihica PV-4 biofilms formed at graphite electrode. *Bioelectrochemistry* **87,** 28–32 (2012).
53. Zhou, Z. & Swenson, R. P. The Cumulative Electrostatic Effect of Aromatic Stacking Interactions and the Negative Electrostatic Environment of the Flavin Mononucleotide Binding Site Is a Major Determinant of the Reduction Potential for the Flavodoxin from Desulfovibrio vulgaris Hil. *Biochemistry* **35,** 15980–15988 (1996).
54. Bard, A. J. & Faulkner, L. R. *Electrochemical Methods: Fundamentals and Applications*. (2001).
55. Cao, B. *et al.* Extracellular polymeric substances from Shewanella sp. HRCR-1 biofilms: characterization by infrared spectroscopy and proteomics. *Environ. Microbiol.* **13,** 1018–31 (2011).
56. Lower, B. H. *et al.* Antibody recognition force microscopy shows that outer membrane cytochromes OmcA and MtrC are expressed on the exterior surface of Shewanella oneidensis MR-1. *Appl. Environ. Microbiol.* **75,** 2931–5 (2009).
57. Cao, B. *et al.* Biofilm shows spatially stratified metabolic responses to contaminant exposure. *Environ. Microbiol.* **14,** 2901–10 (2012).
58. Ji, E., Corbitt, T. S., Parthasarathy, A., Schanze, K. S. & Whitten, D. G. Light and dark-activated biocidal activity of conjugated polyelectrolytes. *ACS Appl. Mater. Interfaces* **3,** 2820–9 (2011).

II.F. Appendix II. Materials, Methods, and Supplementary Figures

II.F.1. Materials and Methods

II.F.1.a. Cell Culture and Inoculation

Initial cultures of *S. oneidensis* MR-1 were started from single colonies on LB agar plates, and cultivated at 30°C under an N_2 atmosphere in modified M1 medium[55,57] containing 20 mM Na-(L)-lactate as donor and 20 mM Na-fumarate as acceptor. After 48 hours of incubation, the culture reached a maximum OD_{600} of ~0.15. These stationary phase cultures (fumarate completely consumed) were then anaerobically transferred to potentiostat controlled 3-electrode-type electrochemical devices. At inoculation of the reactors (timepoint I, Fig. II.2), an additional dose of 10 mM Na-(L)-lactate was added to ensure no donor limitation.

II.F.1.b. Bioelectrochemical Reactors

3-electrode, batch-type, membraneless bioelectrochemical reactors were similar to those previously described,[51] with only minor differences as described here. In this work, the glass reactor vials had a 15 mL working volume and were sealed with rubber septa. Electrode specifications were as follows. Reference electrode: Ag/AgCl (3.5M KCl) with 3.2 mm Vycor frit (Gamry). Counter electrode: coiled 0.25 mm Ti wire (Aldrich), 10 turns. Working electrode: 1 cm × 1 cm × 0.2 cm graphite felt (Alfa Aesar), woven with Ti wire as the electrical lead. Anaerobic conditions were maintained through constant headspace degassing with humidified, deoxygenated N_2. Temperature was kept at 30°C by housing the reactors in a temperature regulated incubator.

II.F.1.c. Chronoamperometry (CA)

Using a Gamry potentiostat (Reference 600, Series G 300 or Series G 750 models) and multiplexer (model ECM8), graphite felt working electrodes were poised at +0.2 V vs. Ag/AgCl to serve as the sole terminal electron acceptor for the organisms. Freshly inoculated bioelectrochemical reactors were incubated in the dark[58] with 150 rpm magnetic stirring to promote growth of an electroactive biofilm. The current response was measured, recorded, and averaged for 20-second blocks (at 160 second intervals) with Gamry software (Framework Version 6.11, Build 2227, 2013). Time integration of the resulting current response determined the amount of charge transferred by the bacteria. After an initial overnight current collection (timepoints I to II, Fig. II.2), a full media change was undertaken (timepoint II, Fig. II.2) to replenish the lactate donor to 30 mM and deconvolute the biofilm from planktonic cell signals; this typically decreases the current output to about 40% of the maximum between I and II. Next, after electrochemical characterization with CV and DPV (timepoint III, Fig. II.2) and resuming CA at +0.2 V vs. Ag/AgCl for a period of ~1 hour, DSSN+ was added to Type 2 reactors (timepoint IV, Fig. II.2) and the system was allowed to operate for ~2 hours. After another brief pause in CA for CV and DPV analyses (timepoint V, Fig. II.2), current was continuously monitored until the end of reactor operation (timepoint VI, Fig. II.2).

II.F.1.d. High Performance Liquid Chromatography (HPLC)

HPLC analysis of reactor effluent was performed with a Shimadzu LC20AB instrument equipped with an organic acid compatible Aminex HPX-87H column (Bio-Rad). Samples from reactors were filtered through 0.22 μm PVDF filters (GSTek) to remove cells. The mobile phase was 0.004 M (0.008 N) H_2SO_4 flowing at 0.6 mL/min and UV detection was

set at 210 nm.

II.F.1.e. Coulombic Efficiency (CE) Determination

The efficiency of the bioelectronic system in converting lactate to electricity was calculated by first integrating the current response in Fig. II.2 between timepoints III and VI to obtain the total coulombs of charge collected:

$$Q_{III-VI} = \int_{III}^{VI} I(t)dt \; \mathrm{Q_{III\text{-}VI}} = \int_{\mathrm{III}}^{\mathrm{VI}} \mathrm{I(t)dt} \qquad \text{(II.1).}$$

For the same time period, the concentration of lactate was monitored in the reactor with HPLC to determine the change in molarity of lactate, Δ[lac]. By Eq. II.2,[49] each consumed lactate molecule should yield $n = 4\ e^-$, which represents 100% CE:

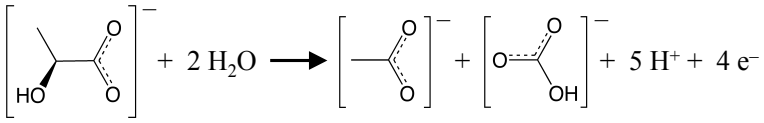

(II.2).

The charge equivalent (in Coulombs) of the consumed lactate is given by the expression

$$Q_{ideal} = -\Delta[\mathrm{lac}]VFn \qquad \text{(II.3),}$$

where V is the volume of the reactor (15 mL) and F is the Faraday constant (equal to $N_A e$ = 9.64853×10^4 C/mol). Finally, CE is the ratio of $Q_{III\text{-}VI}$ to Q_{ideal} in percent form:

$$\mathrm{CE} = 100(Q_{III\text{-}VI}/Q_{ideal})\mathrm{CE} = 100\left(\frac{\mathrm{Q_{III\text{-}VI}}}{\mathrm{Q_{ideal}}}\right) \quad \text{(II.4).}$$

II.F.1.f Electrochemistry (CV and DPV)

At various timepoints during the CA measurements (timepoints III, V, and VI, Fig. II.2), current monitoring and stirring were paused for CV and DPV analyses. Parameters for each were as follows. CV: $E_{initial} = E_{final} = -0.7$ V; $E_{vertex} = 0.2$ V; *scan rate* = 5 mV/s; *quiescent time* = 20 s. DPV: $E_{initial} = -0.7$ V; $E_{final} = 0.2$ V; *pulse height* = ΔE = 50 mV; *pulse width* = 200 ms; *sampling time* = last 10% of pulse; *step height* = 2 mV; *step time* = 400 ms; *scan rate* = 5 mV/s (scan rate is given by dividing step height by step time, 2 mV/400 ms = 5 mV/s, which was chosen to match the CV scan rate); *quiescent time* = 5 s.

II.F.1.g. Gaussian Fits to DPV Data and Parameter Extraction

For DPV redox peaks, the potentials at which maximum current occurs, E_{max}, are shifted from the actual redox potentials (peak centers) of the redox species, E_o, by a value of one half the pulse height, $\Delta E/2 = 25$ mV.[54] This may be corrected using the expression

$$\mathrm{E_o} = \mathrm{E_{max}} + \frac{\Delta \mathrm{E}}{2} E_o = E_{max} + \Delta E/2 \quad \text{(II.5),}$$

which was used to determine peak centers from the DPV current output. Using these values, redox current as a function of potential was then modeled using Gaussian functions of the form

$$I(E) = I_o \exp\left[\frac{-(E-E_o)^2}{2\sigma^2}\right] + I_{baseline} \mathrm{I(E)} = \mathrm{I_o} \exp\left[\frac{-(\mathrm{E-E_o})^2}{2\sigma^2}\right] + \mathrm{I_{baseline}} \quad \text{(II.6),}$$

where σ^2 is the variance of the function, I_o is the height of the peak, and the $I_{baseline}$ constant was used to subtract baseline current. Setting $I(E) = I_o/2$ after $I_{baseline}$ subtraction and solving yields two values for the potential at half maximum, $E_{\pm} = E_o \pm \sigma(2\ln2)^{1/2}$. The full width at half maximum (FWHM) of each redox peak is the difference in the two values and thus related to σ by the expression

$$\text{FWHM} = E_+ - E_- = 2\sigma(2\ln2)^{1/2} = 2.35\sigma \qquad \text{(II.7)}.$$

For DPV in particular, there is also a lower bound on the FWHM imposed in the limit of $\Delta E \rightarrow 0$, and this is represented by the inequality[54]

$$\text{FWHM} \geq 3.52RT/nF \qquad \text{(II.8)},$$

where n is the number of electrons transferred per redox reaction and RT/F = 26.1 mV is assumed constant (T = 303K) in this system. For n = 1, 2, 3, the limiting widths are thus FWHM ≥ 91.9 mV, 45.9 mV, and 30.6 mV, respectively. Combining Eqs. II.7 and II.8 and rearranging, it is possible to obtain an inequality for n in terms of the fitted variance parameter σ:

$$n \geq 1.49RT/\sigma F \qquad \text{(II.9)}.$$

Using this inequality and the known n = 2 redox system of flavin, σ was exactly

correlated to n. That is, for the experimental flavin redox peak at −0.42 V, σ was found to be 30 mV, meaning that the prefactor in Eq. II.9 is too small and the accurate expression is

$$n = 2.30RT/\sigma F \quad \text{(II.10)}.$$

This result was used with Eq. II.7 and experimental peak widths to determine the values of n in Table II.2.

II.F.1.h. Chemical Fixation of Electrodes

After all bioelectrochemical experiments, a final concentration of 2% (v/v) formaldehyde was added to reactors to fix electrode-associated cells. This was allowed to sit for 24 hours. After fixation, electrodes were sequentially rinsed with the following solutions twice each: 100 mM PBS, pH = 7 (10 min), deionized water (10 min), 70% ethanol in deionized water (10 min), 100% ethanol (30 min). Electrodes were then allowed to air dry for 24 hours and stored in glass scintillation vials for future study.

II.F.1.i. Scanning Electron Microscopy and Cell Counting

Images of the colonized graphite felt electrodes were obtained with an FEI XL40 SEM at an accelerating voltage of 5 kV, working distance of ~5 mm, and a spot size of 3. Post processing of images only involved increasing the brightness and/or contrast of the images by up to 40% in order to better visualize cells. Assuming a cylindrical geometry so that surface area of each graphite fiber could be approximated by $A_k = \pi d_k h_k$ (where d_i = diameter, h_k = height of cylinder), the SEM scale bar was used to determine d_i and divide the imaged graphite fiber into sections of equal height, h_k = 5 μm. An example of this method is shown

in the Type 1 reactor image in Fig. II.2. Twelve similar imaged sections (K = 12) were identified at random from SEM of each of the six reactors' electrodes (see Fig. II.S3); then the surface area A_k of each section was calculated, and the number of visible cells was counted in each section. It was assumed that the visible cells accounted for one half of the total number of cells on each fiber, so the counted number was multiplied by 2 to determine the total cells per cylindrical section, N_k. Finally, the number average cell density for each electrode, ρ, is:

$$\rho = \frac{1}{K}\sum_{k=1}^{K}(\rho_k) = \frac{1}{K}\sum_{k=1}^{K}\left(\frac{N_k}{A_k}\right) = \frac{1}{12}\sum_{i=1}^{12}\left(\frac{N_k}{\pi d_k h_k}\right) \quad \text{(II.11)},$$

where for k = 1, …, 12 and K = 12. Experimentally determined values of ρ for all reactors (see Fig. II.S3) are given in Table II.S1.

Table II.S1. Experimentally Determined Values of ρ

Experiment	Reactor Type	ρ (cells/cm^2)
1	1	$1.83 \pm 0.14 \times 10^7$
1	2	$5.02 \pm 0.66 \times 10^7$
2	1	$3.77 \pm 0.87 \times 10^7$
2	2	$1.03 \pm 0.23 \times 10^8$
3	1	$1.36 \pm 0.47 \times 10^7$
3	2	$5.62 \pm 0.76 \times 10^7$

II.F.1.j. Electrode Surface Area Determination and Max Current per Unit Protein Mass

Graphite felt electrode surface area was determined by measuring the mass of 24 identically prepared 1 cm × 1 cm × 0.2 cm electrode samples. These are the dimensions of all working electrodes used in this work. The average and standard deviation of the 24 measured values (22.6 ± 1.2 mg) were converted to surface area using the manufacturer's specification of 1 m^2/g to give a working electrode surface area of

$$A_{electrode} = 226 \pm 12 \text{ cm}^2 \quad \text{(II.12).}$$

Following this, three separate cultures of *S. oneidensis* MR-1 were grown to $OD_{600} = 0.20 \pm 0.01$. Then, 1 mL of each culture was removed and serial dilutions were plated out in 9 replicates each (for a total of 27 replicates) to determine the *S. oneidensis*-specific value of $1.0 \pm 0.1 \times 10^9$ cells/ml/OD. The same three cultures were then frozen in liquid nitrogen and lyophilized for 48 hours to remove all water content. The resulting dried cell pellets were massed on a microbalance to determine the *S. oneidensis*-specific value of $4.4 \pm 0.4 \times 10^{-4}$ g dry cell/ml/OD. Using these two conversion values, and addition in quadrature of the standard deviations, it was possible to calculate the specific mass of cells. Because ρ is expressed in units of million/cm^2, the specific mass of 1×10^6 was determined for subsequent calculations:

$$m = 4.4 \pm 0.6 \times 10^{-7} \text{ g dry mass}/10^6 \text{ cells} \quad \text{(II.13).}$$

Finally, the maximum current output from each reactor between timepoint III and VI, $I_{III\text{-}VI}(max)$, was determined numerically from the raw data (error was propagated by addition in quadrature). These values were used to calculate Maximum Current per Unit Dry Cell Mass for each reactor (which is a rough post-operation measure of the efficiency of the electron transfer process) by the following ratio:

$$I_{III\text{-}VI}(\text{max})/\rho A_{electrode} m \quad \text{(II.14).}$$

A numerical summary of $I_{III\text{-}VI}(max)$ and Maximum Current per Unit Dry Cell Mass by reactor type is provided in Table II.S2.

Table II.S2. Maximum Current per Unit Dry Cell Mass by Reactor Type

Experiment	Reactor Type	$I_{III\text{-}VI}(max)$ (μA)	$I_{III\text{-}VI}(max)/\rho A_{electrode}m$ (μA/mg)
1	1	73.0	39.9 ± 6.7
1	2	169.5	33.7 ± 6.7
2	1	114.0	30.2 ± 8.3
2	2	240.5	23.4 ± 6.2
3	1	86.2	63.0 ± 23.5
3	2	251.0	44.6 ± 8.9
Average	1	91 ± 21	44 ± 9
Average	2	220 ± 44	34 ± 4

II.F.2. Supplementary Figures with Discussion

As can be seen in the main text as well as Fig. II.S1 A and D, current output is consistently increased in the presence of DSSN+. Additionally, a pronounced catalytic wave at ~0.05 V arises upon DSSN+ addition to Type 2 reactors (Fig. II.S1 B and E), consistent across all three experiments. This can be visualized readily in the derivative CV traces (Fig. II.S1 C and F) as a peak centered at the same potential, and these derivative traces also provide affirmation that DSSN+ is not directly affecting flavin-based electron transfer.

Fig. II.S2 displays current outputs from sterile (negative control) reactors. For these experiments, the poised potential (+300 mV) as well as concentrations of lactate and DSSN+ were the same as when organisms were present (30 mM and 5 μM, respectively). These reactors show very little current production, indicating that DSSN+ and lactate do not contribute to current in the absence of *S. oneidensis*. Numerically, this may be rationalized. For the sake of argument, if it *is* assumed that (a) the collected charge arises from oxidation

of DSSN+ molecules at the electrode, (b) the terminal value from the red trace (2.64 mC) is

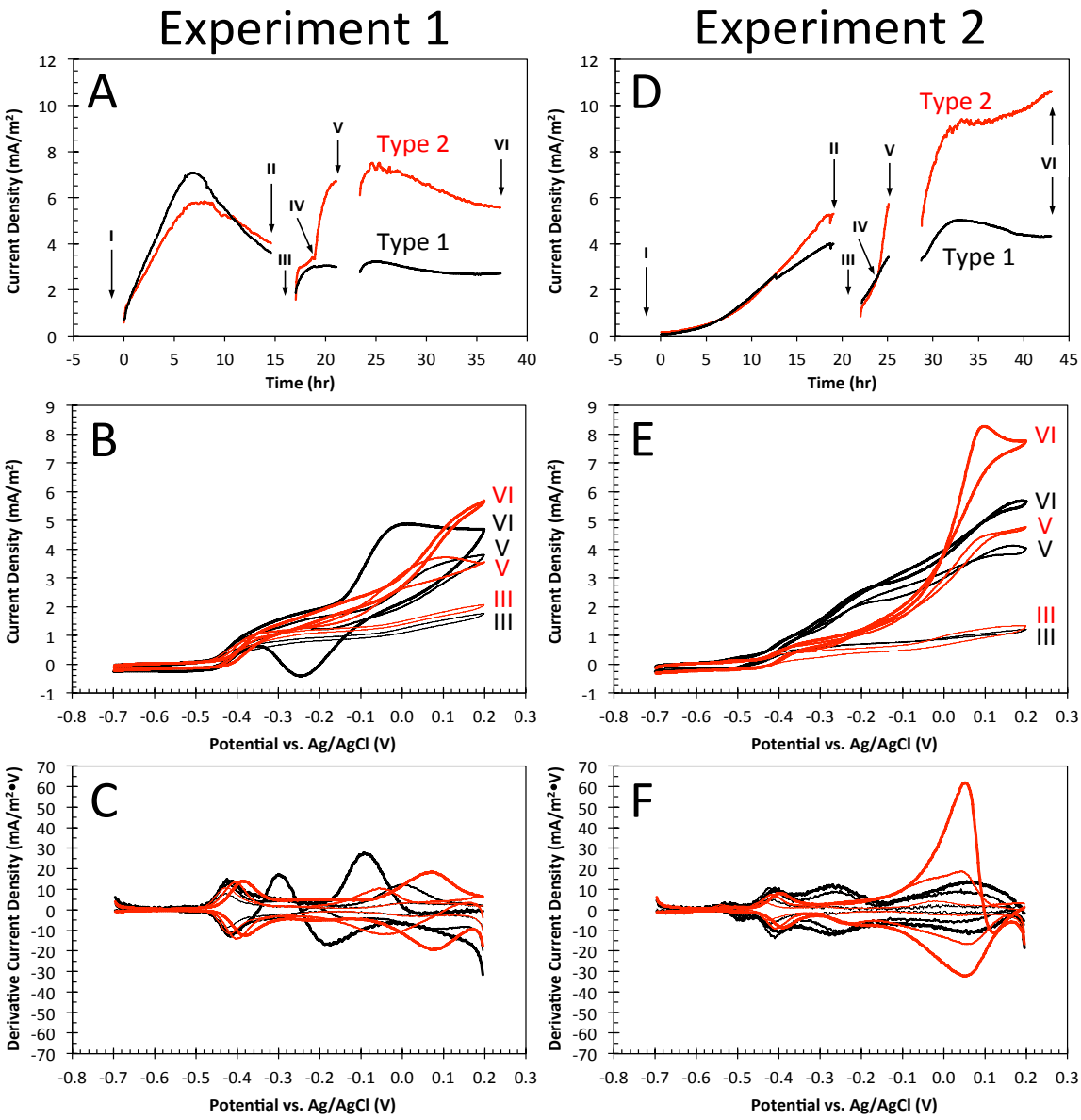

Figure II.S1. CA, CV, and derivative traces for remaining two replicate experiments. Note that experimental conditions are identical and timepoints are annotated in the same way as the representative replicate experiment in the main text. Specific timing of voltammetric analyses is different for each experiment (they were run on different days). For all plots, black traces represent Type 1 reactors and red traces represent Type 2 reactors which received a spike of 5 µM DSSN+ at timepoint IV. (**A**) CA for replicate Experiment 1. (**B**) CV traces for replicate Experiment 1. (**C**) Derivative CV traces for replicate Experiment 1. (**D**) CA for replicate Experiment 2. (**E**) CV traces for replicate Experiment 2. (**F**) Derivative CV traces for replicate Experiment 2.

the upper limit on charge collected over ~16 hours of operation, and (c) each DSSN+

molecule donates 1 electron to the electrode upon oxidation (such a 1:1 mole ratio is likely an underestimate were COE degradation *truly* occurring), then an upper limit of

$$\frac{Q/e}{[\mathrm{DSSN+}]VN_A} = \frac{(2.64\times10^{-3}\ \mathrm{C})(1\mathrm{e}^-/1.602\times10^{-19}\ \mathrm{C})}{(5\times10^{-6}\ \mathrm{mol\ COE/L})(0.015\ \mathrm{L})(6.02\times10^{23}\ \mathrm{molecules/mol\ COE})} = \frac{\mathbf{0.37\ electrons}}{\mathbf{COE\ molecule}}$$

are harvested at the electrode. This value does not account for complete oxidation of COE in solution, and it especially does not account for the much larger currents (on the order of ~1×10^{-4} A, corresponding to current densities of ~5 mA/m^2) and collected charge (on the order of ~10 C) generated in the presence of *S. oneidensis* MR-1 organisms.

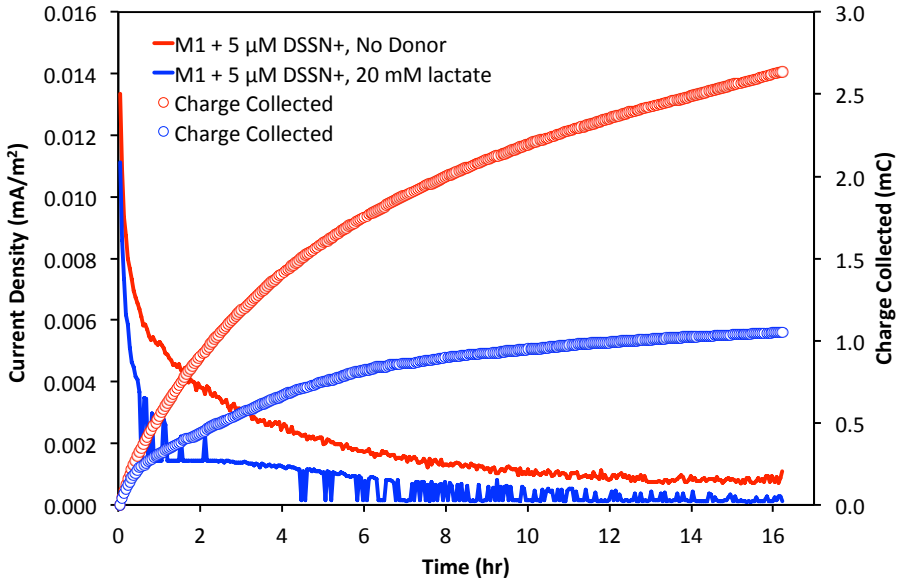

Figure II.S2. Sterile chronoamperometry (CA) of electrochemical reactors poised at +0.2 V vs. Ag/AgCl in M1 basal medium with DSSN+ or DSSN+ and lactate shows negligible current production. This is the same control data as is presented in Fig. 2 in the main text, but it is also presented here for additional discussion. (**Red Traces**) CA of M1 media with 5 µM DSSN+ as well as concomitant charge collected. (**Blue Traces**) CA of M1 media with 5 µM DSSN+ and 20 mM lactate as well as concomitant charge collected.

Together, then, these data and calculations affirm that *S. oneidensis* cells are necessary to catalyze lactate oxidation and concomitant current production in this system. DSSN+ is not

electrochemically degraded during operation at +200 mV vs. Ag/AgCl. Maintenance of the characteristic yellow color of DSSN+ molecules throughout device operation (not shown) is further evidence that DSSN+ is not degraded at the electrode.

Representative scanning electron micrographs of the remaining chemically fixed electrodes from the remaining two replicate experiments are displayed for reference in Fig. II.S3. These images qualitatively illustrate the quantitative trends observed in Table II.S1, where more cells colonize the electrodes in the presence of COE.

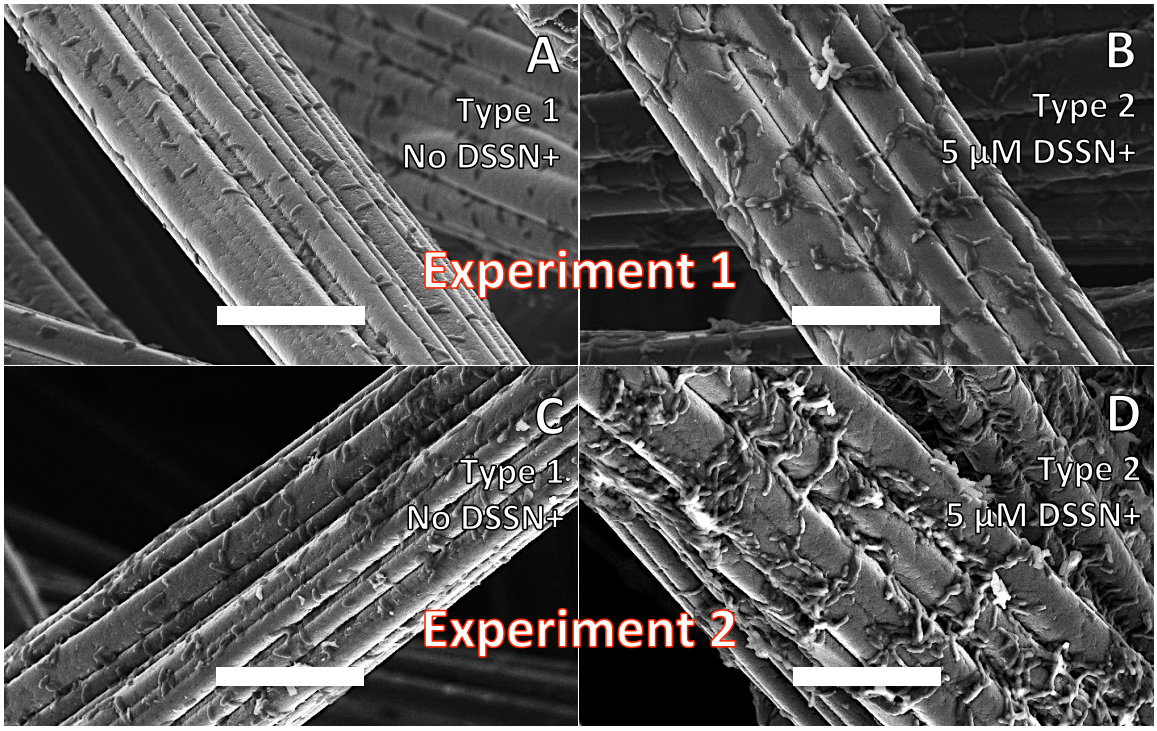

Figure II.S3. Representative SEM images of electrode surfaces from the remaining replicate experiments. Note that the corresponding numerical data for cell density, ρ, for each electrode can be found in Table I.S1. (**A**) Type 1 electrode from Experiment 1. (**B**) Type 2 electrode from Experiment 1. (**C**) Type 1 electrode from Experiment 2. (**D**) Type 2 electrode from Experiment 2.

Cyclic voltammetry was conducted in a 3-electrode reactor containing M1 media in the potential window –0.7 V to 0.2 V vs. Ag/AgCl, and these results are displayed in Fig. II.S4. To the basal M1 media the following were sequentially supplemented, with a CV trace

obtained after each addition (for clarity, only the initial media and final mixture are shown): 5 μM DSSN+, riboflavin at 5X concentration intervals (40 nM through 5 μM), and finally 20 mM lactate. In the basal media formulation, riboflavin exhibits the expected reversible oxidation/reduction centered at E = –0.42 V vs. Ag/AgCl. Importantly, the supplemented media shows essentially no redox current above baseline at any potential (other than that associated with the flavin) for any of these media additions. There is also no catalytic electron transfer associated with the riboflavin peak, indicating that reduced riboflavin is not provided to the electrode at an appreciable rate to sustain current (in contrast to the system catalyzed by *S. oneidensis*).

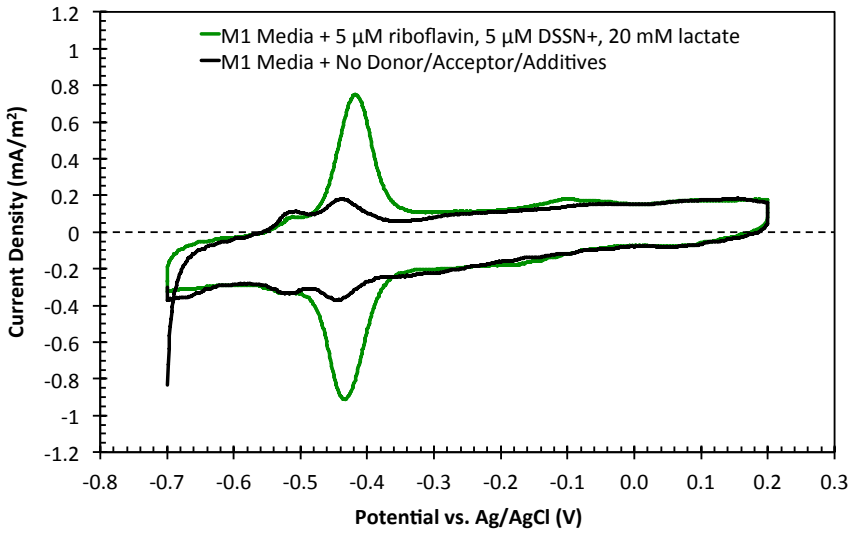

Figure II.S4. Sterile Cyclic Voltammetry (CV) demonstrates that M1 Media is inert and COEs are not redox active. Scan rate was 5 mV/s. (**Black Trace**) CV of M1 minimal media with no additives. (**Green Trace**) CV of M1 media supplemented with 5μM DSSN+, 5 μM riboflavin, and 20 mM lactate.

This control experiment also reaffirms that DSSN+ is not redox-active at the electrode during electrochemical reactor operation (neither alone nor in combination with riboflavin and/or lactate) and thus cannot solely account for the enhanced current production, as previously discussed. This ultimately indicates that the media is a sufficiently stable electrolyte solution for operation. Two small redox waves do arise at approximately –0.52 V

and –0.1 V, likely from trace vitamins, minerals, amino acids, or HEPES buffer in the M1 media formulation. These signals readily explain the consistent observation of the same peaks in the DPV data for Type 1 and Type 2 reactors (Fig. II.5), but the magnitudes of these peaks (~0.1 mA/m^2) strictly preclude them from implication in the much larger catalytic currents observed in the presence of organisms.

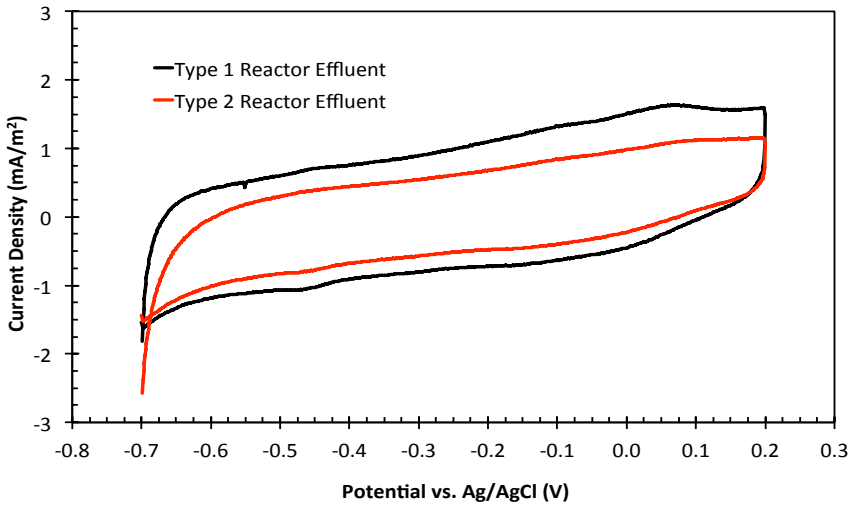

Figure II.S5. CV traces of effluent from Type 1 and Type 2 reactors at the end of operation show lack of catalytic activity. Scans were conducted at 5 mV/s. (**Black Trace**) CV from Type 1 reactor after timepoint VI. (**Red Trace**) CV from Type 2 reactor after timepoint VI.

The unaltered, anaerobic media from each reactor was removed with a sterile cannula at the end of operation (timepoint VI) and assayed with CV in a fresh 3-electrode electrochemical reactor (Fig. II.S5). Surprisingly, the effluent exhibits non-turnover behavior, producing no catalytic current. This suggests that current generated at the working electrode during reactor operation stems predominantly from cells at the electrode surface, and not from the bulk solution. This is expected because the media change at timepoint II deconvoluted the biofilm from the bulk solution. The small faradaic current from redox features present at $E \approx$ –0.44 V and +0.05 V are consistent with those seen in DPV and CV derivatives for flavin and DET, respectively (in the main text, Figs. II.3 and II.4), whereas

the peak from flavin semiquinone at $E \approx -0.33$ V is not apparent in these traces. The magnitudes of these faradaic currents is quite small, indicating that the effluent does not contribute significantly to the electrical output of these systems and that the media change at timepoint II is effective in deconvoluting the biofilm from the bulk solution.

Gaussian fits to represenatative DPV peaks are provided in Fig. II.S6.

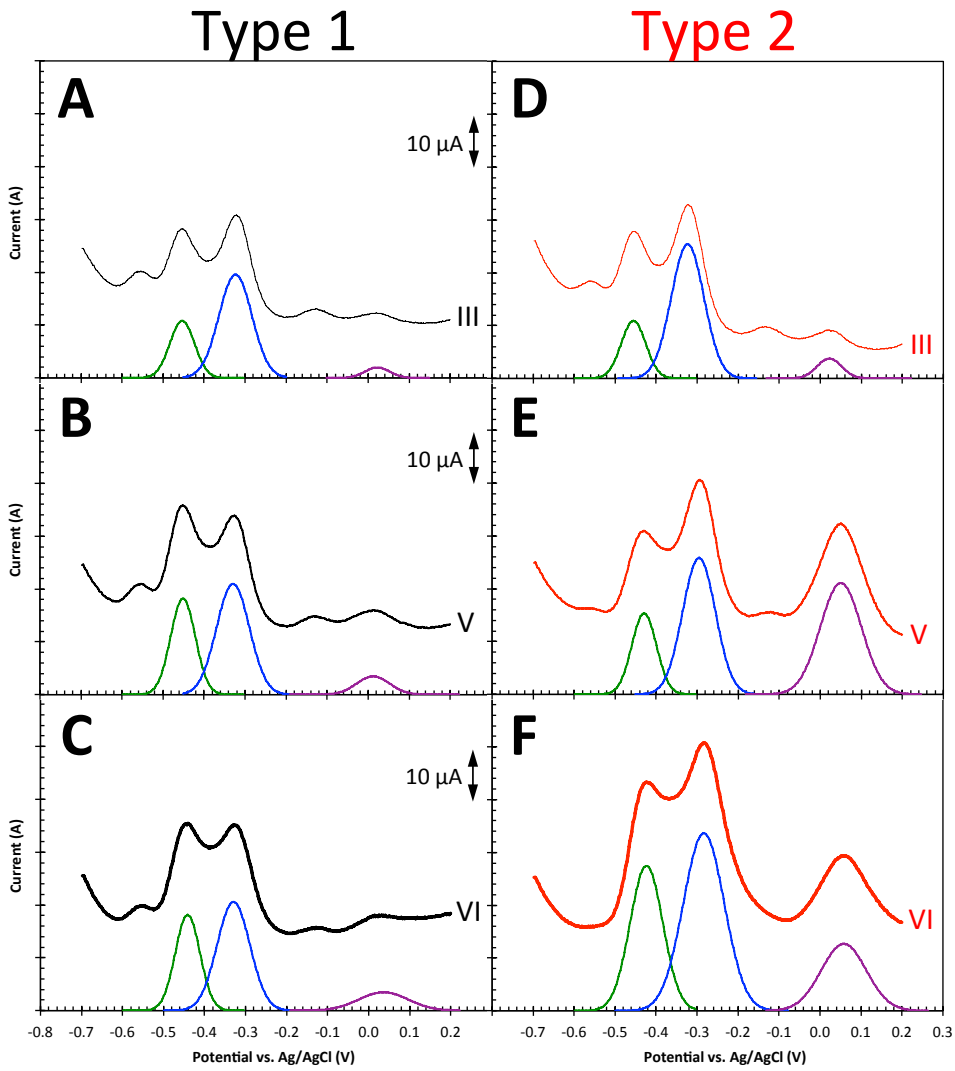

Figure II.S6. Gaussian modeling of representative DPV Data. Notice the provided 10 µA scale bar, which is the same for all plots. Scan rate was 5 mV/s, and other experimental parameters are provided in §I.F.1.g. Green traces represent fitted flavin signal peaks, blue traces are fitted flavin semiquinone signal peaks, and purple traces represent fitted cytochrome signal peaks. (**A**) DPV trace from Type 1 reactor at timepoint III. (**B**) DPV trace from Type 1 reactor at timepoint V. (**C**) DPV trace from Type 1 reactor at timepoint VI. (**D**) DPV trace from Type 2 reactor at timepoint III. (**E**) DPV trace from Type 2 reactor at timepoint V. (**F**) DPV trace from Type 2 reactor at timepoint VI.

Chapter III. Conjugated Oligoelectrolytes Accelerate Syntrophic Anaerobic Exchange of Reducing Equivalents

III.A. Abstract

Syntrophic metabolisms are typically rate-limited by diffusive exchange of reducing equivalents in the form of small energy-rich molecules, such as H_2. Certain syntrophic species reduce diffusion limitations by reducing cell-cell distances through cellular coaggregation, and a small subset have evolved the capacity for direct intercellular electron transfer (DIET), overriding the need for diffusive small molecule exchange. Due to its efficiency, DIET is an advantageous pathway for increasing the rate of syntrophic reactions, and yet it is currently restricted to species that possess cellular machinery appropriate for forming electrical connections. It is therefore of fundamental interest to enable DIET in syntrophic systems that utilize diffusion. Because *p*-phenylenevinylene-based conjugated oligoelectrolytes (PPV-COEs) have been reported to amplify bacteria-electrode electron exchange, we hypothesized that PPV-COEs may enable DIET. Therefore, PPV-COEs are used herein to modify the ethanol-consuming, H_2-exchanging syntrophy of *Pelobacter acetylenicus* and *Acetobacterium woodii* to examine the possibility of enabling DIET with PPV-COEs. Modification with PPV-COEs induces cellular coaggregation, provides up to a 95% increase in the rate of ethanol turnover, and enhances syntrophic output. Microscopy indicates that PPV-COEs modify both species' membranes without obvious toxicity or structural perturbations. Amperometric and voltammetric interrogations of PPV-COE-modified cultures show minimal faradaic current differences relative to unmodified controls, indicating that increased current flow (induced DIET) is not the mechanism of PPV-COE

action. Rather, results are consistent with aggregation being caused by reported changes in zeta potential from membrane-intercalated PPV-COEs.

III.B. Broader Impact

Syntrophic metabolism is one of the fundamental elements in global carbon cycling, bioremediation, and wastewater treatment. However, many syntrophic systems operate at the thermodynamic threshold for sustaining life, and their efficiency is limited by diffusive sharing of electron and energy equivalents. Strategies to overcome this limitation without obvious toxicity, such as by physically coupling syntrophic species together, are extremely valuable because they have the potential to enhance native interactions and override diffusive exchange. PPV-COEs electrostatically couple syntrophic bacteria together to enable accelerated substrate conversion, thus providing a foundation for these modifications using synthetic organic materials.

III.C. Introduction

Many microorganisms have evolved strategies to subsist in nutrient-limited anaerobic microenvironments that are often thermodynamically challenging for sustaining life.[1–7] Multiple species of microorganisms have co-evolved into syntrophic (obligately crossfeeding) communities that can collectively overcome thermodynamic limitations by distributing metabolic tasks.[8] While syntrophy has been recognized in the literature for nearly 60 years,[9–13] it is now recognized as a fundamental element in global carbon cycling, bioremediation, and organic waste conversion.[14–23]

Environmental syntrophy remains poorly understood due to the massive/undefined diversity of consortia involved,[24] the low available free energy of obligately syntrophic

anaerobic reactions that limits microorganism growth rates, and our (in)ability to isolate pure cultures of the species involved.[25–29] Discrete biochemical processes within environmental syntrophies therefore remain poorly understood, despite advances in computational methods.[30–41] Defined syntrophic cultures of isolated species are typically employed for mechanistic understanding and applied biocatalysis.

Syntrophies hinge upon an interspecies exchange of reducing equivalents. In many systems, this occurs by diffusion of reduced, electron-rich molecules such as H_2 or formate.[42,43] Evidence also exists that some syntrophic communities favor direct intercellular electron transfer (DIET).[5,17,44–48] Solid-state (semi)conductive materials that directly interface with microorganisms—such as iron oxide minerals,[49,50] biogenic sulfide-based mineral crusts,[51] and granular activated carbon[52]—appear to facilitate transmembrane electron transport (TET) *via* DIET. Enhancements to TET are observed in the presence of osmium redox polymers[53–55] and biogenic Pd^0 nanoparticles,[56] as well as in engineered artificial syntrophic systems.[57–61] Importantly, the strategy of adding (semi)conducting materials has only proven fruitful with organisms known to be capable of DIET and direct TET. Strictly-diffusive syntrophic species appear unable to directly couple to electroactive surfaces.[62]

There are examples of enhancing microbe-electrode/electrode-microbe electron exchange from the addition of membrane-intercalating *p*-phenylenevinylene-based conjugated oligoelectrolytes (PPV-COEs). When PPV-COEs modify such biotic-abiotic interfaces, the thermodynamic barrier for biological TET appears to be lowered: PPV-COEs increase power densities, current production, the coulombic efficiency of fuel consumption, and the rate of electrode-driven substrate reduction while decreasing internal resistance and enhancing direct TET in bioelectrochemical reactors.[63–69]

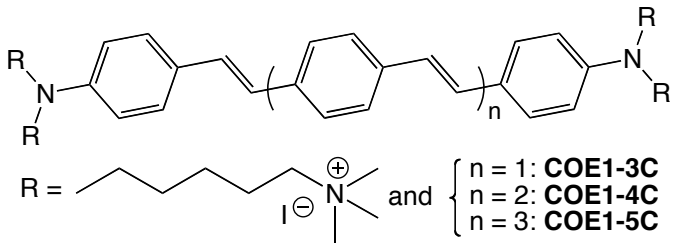

Figure III.1. Chemical structures of the PPV-COEs used in this work. Note that COE1-3C and COE1-4C may be respectively referred to as DSBN+ and DSSN+ in other references.

One might hypothesize that PPV-COEs would enrich syntrophic metabolism by boosting intercellular TET *via* DIET. PPV-COEs are an attractive class of materials to electronically modify organisms towards DIET due to their optoelectronic properties[63,70–74] and previously demonstrated bioelectrochemical utility. We therefore used the set of PPV-COEs with increasing molecular length in Fig. III.1 to investigate this possibility.

III.C.1. Details of the syntrophic metabolism

The strictly anaerobic, H_2-exchanging syntrophy of *Pelobacter acetylenicus* strain GhAcy 1 (DSM 3247) and *Acetobacterium woodii* strain WB1 (DSM 1030) was chosen as a model for investigating the effect of PPV-COEs on syntrophy and inducing DIET. The interactions of the two species are depicted in Fig. III.2. The two organisms have been well studied in pure culture and co-culture. There are no reported instances of DIET or cellular coaggregation between them, and there are no reports of augmenting them with synthetic materials. Each species can be selectively cultured with a modified Hungate technique[75] on characteristic substrates—acetoin for *P. acetylenicus*[26] and fructose for *A. woodii*.[76,77] The primary metabolic product from both organisms is aqueous acetate, which can be stoichiometrically quantified with high performance liquid chromatography (HPLC).

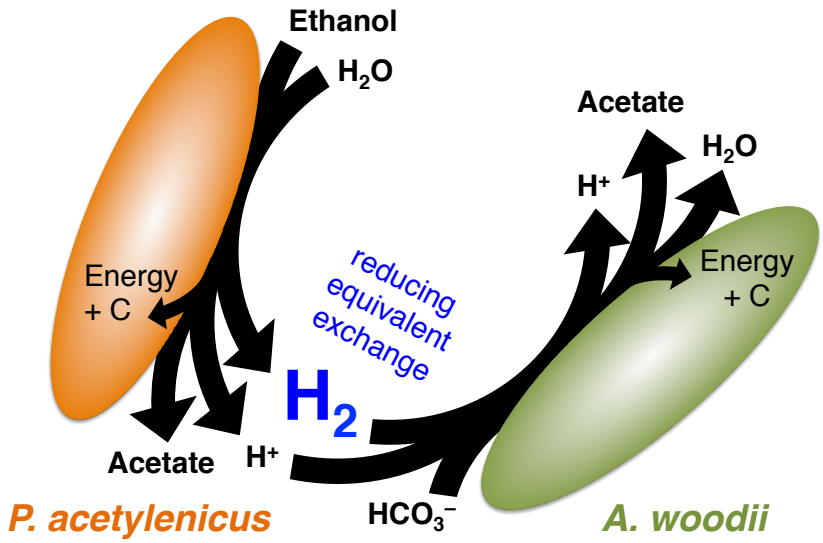

Figure III.2. A schematic of the native molecular features of the ethanol-degrading syntrophic metabolism of *P. acetylenicus* and *A. woodii*. Note that stoichiometry is not precise (see text for complete reactions), and the exchange of reducing equivalents occurs by diffusion of H_2. "C" indicates bio-assimilated carbon.

P. acetylenicus is a strictly anaerobic, mesophilic, gram negative, fermenting bacterium lacking several key genes normally encoding for complete oxidation of organic fuels, cytochrome production, and the capacity to reduce many external electron acceptors.[78] However, it does have high (de)hydrogenase activities,[79] permitting it to participate in syntrophic growth on primary aliphatic alcohols *via* electron confurcation[28] and interspecies H_2 transfer.[6,78–81] This metabolic functionality was first reported in the lost S-organism from "*Methanobacillus omelianskii*" mixed cultures,[10,82] and may also have played a key role in primordial earth.[83,84] The contemporary function of *P. acetylenicus* is likely ethanol degradation[78] (especially in marine sediments) by acid hydrolysis,

$$CH_3CH_2OH + H_2O \rightarrow CH_3COO^- + H^+ + 2\ H_2$$

$$\Delta G_0' = +4.8\ \text{kJ/mol}\ H_2 \qquad \text{(III.1)},$$

which is endergonic under standard conditions. Thus, this reaction only proceeds when

hydrogen partial pressure is low.

A. woodii is a strictly anaerobic, mesophilic, motile, gram positive, homoacetogenic bacterium[77,85] that effectively scavenges this excess hydrogen. As with all homoacetogens, its primary metabolite is acetate, which can be either fermentatively produced from hexose sugars or autotrophically synthesized from H_2 and CO_2/HCO_3^-.[76,86] In the latter case, the metabolic activity of *A. woodii* is regulated by the bicarbonate concentration of its growth medium[85] because CO_2 is in equilibrium with aqueous bicarbonate:

$$CO_2 + H_2O \rightleftharpoons H_2CO_3 \rightleftharpoons HCO_3^- + H^+ \qquad \text{(III.2).}$$

In pure culture, at high bicarbonate concentrations (> 60 mM), *A. woodii* can ferment ethanol to acetate[85] *via* the reaction

$$2\ CH_3CH_2OH + 2\ CO_2 \rightarrow 3\ CH_3COO^- + 3\ H^+$$

$$\Delta G_0' = -41.6\ \text{kJ/mol EtOH} \qquad \text{(III.3).}$$

Ethanol fermentation *via* Eq. III.3 by *A. woodii* is greatly limited when bicarbonate concentrations are low (~10 mM),[85] forcing the organism to revert to respiration on exogenous substrates such as CO_2/HCO_3^- or caffeate:[76,87–90]

$$4\ H_2 + 2\ HCO_3^- + 2\ H^+ \rightarrow CH_3COO^- + H^+ + 4\ H_2O$$

$$\Delta G_0' = -25.6\ \text{kJ/mol } H_2 \qquad \text{(III.4),}$$

H_2 + 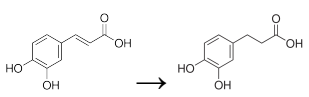 $\Delta G_0' = -85.5\ \text{kJ/mol } H_2$ (III.5).

Eqs. III.4 and III.5 represent means by which *A. woodii* may scavenge H_2 produced by *P. acetylenicus* to overcome the thermodynamic barrier to ethanol oxidation in Eq. III.1. In this way, *P. acetylenicus* and *A. woodii* syntrophically consume ethanol under strictly anaerobic conditions *via* H_2 exchange.[80,83,87,88,91] Combining Eqs. III.1 and III.4 or III.5, two possible total reactions for the syntrophic system are given by:

$$2\ CH_3CH_2OH + 2\ HCO_3^- + 2H^+ \rightarrow 3\ CH_3COO^- + 3H^+ + 2H_2O$$

(bicarbonate reduction) $\Delta G_0' = -76.8$ kJ/mol Ac (III.6),

$$2\ CH_3CH_2OH + 2\ H_2O + 4$$ 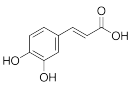 $$\rightarrow 2\ CH_3COO^- + 2\ H^+ + 4$$ 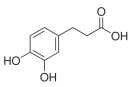

(caffeate reduction) $\Delta G_0' = -161.4$ kJ/mol Ac (III.7).

Increasing proximity between the two species facilitates syntrophic metabolism. The upper limit of efficiency is reached when the two species coaggregate.[44,45,51,92–94] Syntrophic performance may be measured *via* substrate turnover, growth rate, doubling time, and the visual and microscopic characterization of cellular aggregation.

III.D. Results and Discussion

Pure cultures of *P. acetylenicus* and *A. woodii* were started from lyophilized pellets and grown anaerobically in recommended media at 30 °C to stationary phase (see Materials and Methods for full details). Pressure tubes and microbial three-electrode electrochemical reactors (M3Cs) containing fresh media were then inoculated from these active cultures as desired, and appropriate volumes of degassed, sterile, 1 mM PPV-COE stock solutions were added to the inoculated media to final concentrations of 5 μM. Confocal fluorescence

microscopy (CFM) and scanning electron microscopy (SEM) characterization of PPV-COE-modified cells were conducted. Then, during growth phase, cultures were sampled to monitor turbidity (absorbance), $A(t)$, as well as [acetate]. Growth parameters were then extracted from numerical modelling of these data (see III.G.1 Materials and Methods). At the end of these experiments, cultures were first characterized with Gram stain and additional CFM, and then chemically fixed for SEM characterization of cellular aggregates. Finally, M3Cs containing PPV-COE-modified pure cultures were used to examine the bioelectrochemical effect of PPV-COE addition to the syntrophic species. These results are presented in the following sections.

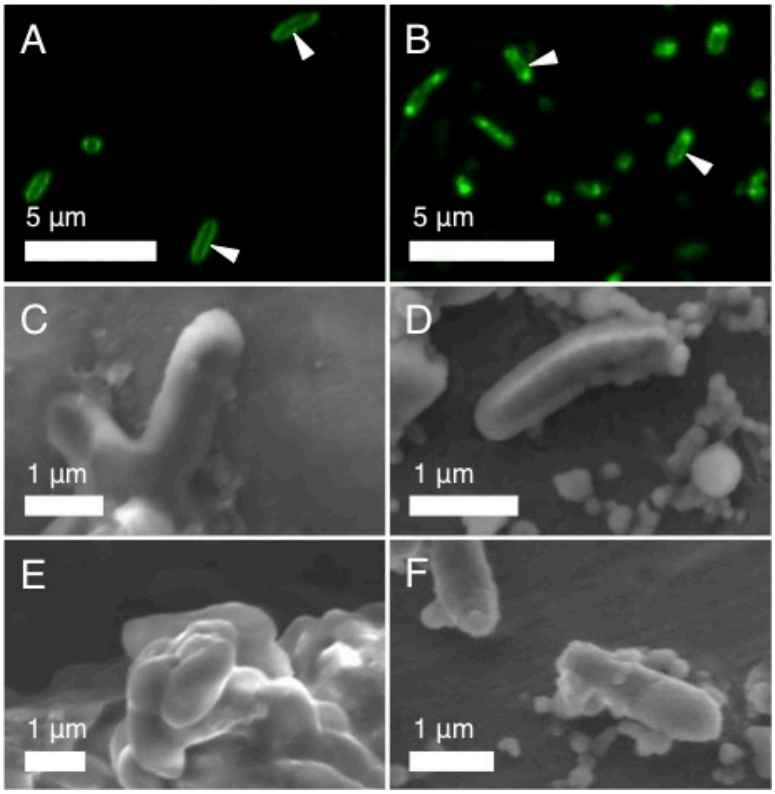

Figure III.3. Representative micrographs of *A. woodii* and *P. acetylenicus.* (**A**) Confocal fluorescence image of *A. woodii* stained with COE1-4C and (**B**) confocal fluorescence image of *P. acetylenicus* stained with COE1-4C showing membrane affinity of COE1-4C (white arrows). Laser excitation: 405 nm. (**C**) SEM image of chemically-fixed *A. woodii* stained with COE1-4C. (**D**) SEM image of chemically fixed *P. acetylenicus* stained with COE1-4C. (**E**) SEM image of chemically fixed unmodified *A. woodii*. (**F**) SEM image of chemically fixed unmodified *P. acetylenicus*. Smaller objects in C–F are remnant dehydrated salts from the growth media not removed in washing steps.

III.D.1. Microscopy of PPV-COE-modified cultures

Fig. III.3 A and B show CFM characterization of intense PPV-COE photoluminescence localized in the membranes of both organisms. This demonstrates that PPV-COEs spontaneously and selectively accumulate in both species' membranes from aqueous media. Chemical fixation of such modified cells and further characterization with SEM reveals that PPV-COEs impart no distinguishable differences in cell morphology between the two organisms, both relative to each other (Fig. III.3 C and D) and relative to unlabelled cultures (Fig. III.3 E and F).

III.D.2. Growth parameters of unmodified pure and syntrophic cultures

In growth medium containing 30 mM fructose as growth substrate, *A. woodii* achieved a growth rate of 0.037 ± 0.003 h^{-1} and a doubling time of 18.8 ± 1.4 h, reaching a maximum turbidity of 0.51 ± 0.07. In media containing 10 mM ethanol as growth substrate, *A. woodii* was able to grow fermentatively as in Eq. III.3, achieving a growth rate of 0.031 ± 0.008 h^{-1}, a doubling time of 23.4 ± 4.7 h, and a peak turbidity of 0.07 ± 0.01 (Fig. III.4 A, trace i); these data are consistent with extrapolations from literature data to 10 mM bicarbonate-buffered media.[85] The resultant production of acetate from *A. woodii* (~12 mM) is slightly below that expected (15 mM) from Eq. III.3. In a previous study, *A. woodii* metabolism was only monitored for 60 hours,[85] while here the experiment was extended to over 400 hours. One may conclude that *A. woodii* will grow on ethanol under low bicarbonate concentrations with sufficient incubation time, contrary to indications of inhibition under these conditions.[87,88]

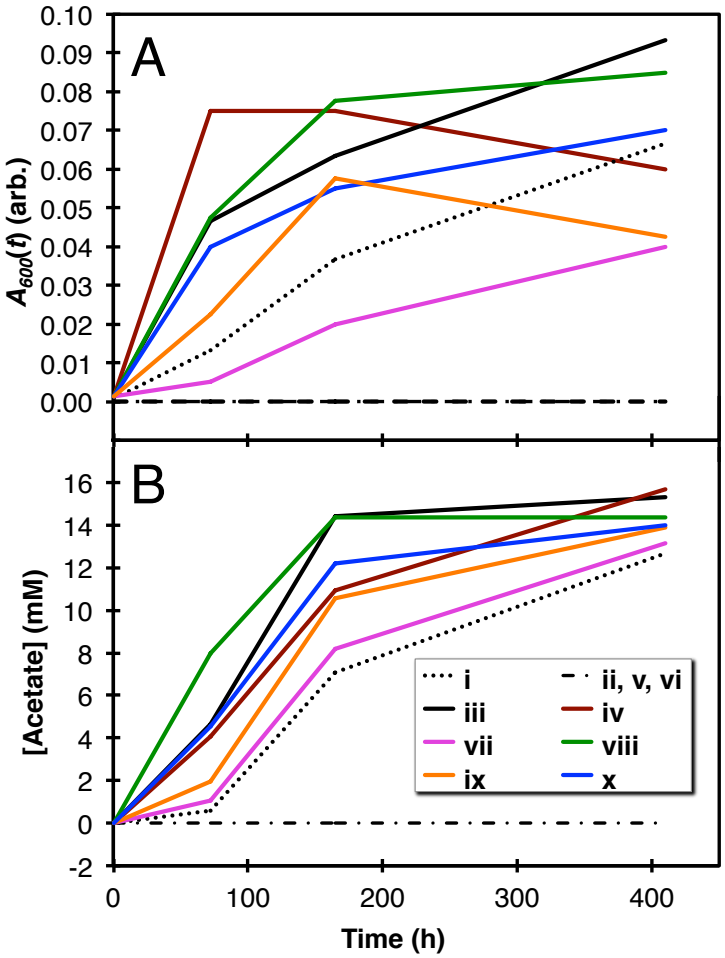

Figure III.4. Measurements of triplicate average culture turbidity and acetate production for pure cultures and syntrophic co-cultures grown on ethanol. Error bars are omitted for clarity. Roman numerals are consistent across other figures in the Chapter, and the legend applies to both panels of the figure, as follows: (**i**) *A. woodii* pure culture. (**ii**) *P. acetylenicus* pure culture, (**iii**) *P. acetylenicus/A. woodii* co-culture, no PPV-COE or caffeate. (**iv**) *P. acetylenicus/A. woodii* co-culture with 3 µM caffeate. (**v**) *P. acetylenicus/A. woodii* co-culture with 5 µM COE1-3C. (**vi**) *P. acetylenicus/A. woodii* co-culture with 5 µM COE1-4C. (**vii**) *P. acetylenicus/A. woodii* co-culture with 5 µM COE1-5C. (**viii**) *P. acetylenicus/A. woodii* co-culture with 3 µM caffeate and 5 µM COE1-3C. (**ix**) *P. acetylenicus/A. woodii* co-culture with 3 µM caffeate and 5 µM COE1-4C. (**x**) *P. acetylenicus/A. woodii* co-culture with 3 µM caffeate and 5 µM COE1-5C. (**A**) Planktonic culture turbidity measured at 600 nm over time. (**B**) Aqueous acetate production as a function of time concomitant with the culture turbidity traces in panel A.

In growth medium containing 11 mM acetoin as growth substrate, *P. acetylenicus* exhibited a growth rate of 0.027 ± 0.003 h^{-1} and a doubling time of 26.1 ± 3.4 h, achieving a maximum turbidity of 0.02 ± 0.01. In identical basal medium instead containing 10 mM ethanol as growth substrate, *P. acetylenicus* was unable to grow detectably over ~2 weeks of incubation (Fig. III.4 A, trace ii). This is consistent with the thermodynamic limitation on

ethanol fermentation described by Eq. III.1. Growth of pure cultures of both species on ethanol proceeds more slowly (or not at all) compared to growth on fructose (for *A. woodii*) or acetoin (for *P. acetylenicus*).

In order to compare the syntrophic metabolism with pure cultures, both species were co-inoculated in media similar to above containing 10 mM ethanol as substrate. Inoculum cell counts of each species were kept consistent with pure cultures by inoculating co-cultures at the same level as the pure cultures (1% inoculum of each species from an A = 0.01 OD culture). The overall cell count of the co-culture was thus 2-fold higher than either pure culture, but the cell count of either species remained constant—a necessary control to compare the growth rates of pure and co-cultures. Co-cultures exhibited a growth rate of 0.081 ± 0.024 h^{-1}, doubling times of 9.3 ± 2.7 h, and reached a peak turbidity of 0.12 ± 0.03 (see Fig. III.4 A, trace iii). Co-cultures thus exhibit an accelerated growth compared to the pure cultures that cannot be accounted for by simple summation of their growth rates or cell densities. This is strong evidence that the metabolism shifts to the more thermodynamically favorable syntrophic ethanol degradation pathway described by Eq. III.6. In the first 72 hours of growth, these co-cultures notably produced 4.6 ± 1.7 mM acetate as compared to *A. woodii* pure cultures that produced 0.6 ± 0.2 mM acetate, representing 7.9-fold more. The terminal value of [acetate] = 15.3 ± 1.3 mM at t = 405 h in the co-cultures is consistent with the expected 15 mM from the stoichiometry of Eq. III.6. These trends may be observed by comparing traces i-iii in Figs. III.4 and III.5, and are numerically presented in Table III.1.

III.D.3. Acceleration of syntrophy and cellular aggregation by addition of PPV-COE

Co-cultures governed by Eq. III.6 (ethanol donor and bicarbonate acceptor) that have been modified with PPV-COE achieve low final turbidities and low acetate production (Fig.

III.4, traces v-vii). At 5 μM, PPV-COEs are inhibitory in this system. In pure culture controls, 5 μM PPV-COE added to *A. woodii* and *P. acetylenicus* also completely inhibits growth (see Table III.1).

Table III.1. Extracted Culture Growth Parameters[a]

Index[b]	Species Present[c]	Growth Substrates[d]	5 μM PPV-COE Added	Maximum Turbidity, A_{max} (OD)	Growth Rate, μ (h^{-1})	Doubling Time, t_D (h)	[Acetate] at t = 72 h (μM)	[Acetate] at t = 405 h (μM)
—[e]	*A. w.*	30 mM fructose	—	0.51 ± 0.07	0.037 ± 0.003	18.8 ± 1.4	—	—
i	*A. w.*	10 mM EtOH	—	0.07 ± 0.01	0.031 ± 0.008	23.4 ± 4.7	0.6 ± 0.2	12.7 ± 1.5
—	*A. w.*	10 mM EtOH, 3 mM caff	—	n. d.[e]	n. d.	n. d.	n. d.	n. d.
—	*A. w.*	10 mM EtOH, 3 mM caff	Any	n. d.	n. d.	n. d.	n. d.	n. d.
—	*P. a.*	11 mM acetoin	—	0.02 ± 0.01	0.027 ± 0.003	26.1 ± 3.4	—	—
ii	*P. a.*	10 mM EtOH	—	n. d.	n. d.	n. d.	n. d.	n. d.
—	*P. a.*	10 mM EtOH, 3 mM caff	—	n. d.	n. d.	n. d.	n. d.	n. d.
—	*P. a.*	10 mM EtOH, 3 mM caff	Any	n. d.	n. d.	n. d.	n. d.	n. d.
iii	*A. w.* + *P. a.*	10 mM EtOH	—	0.12 ± 0.03	0.081 ± 0.024	9.3 ± 2.7	4.6 ± 1.7	15.3 ± 1.3
iv	*A. w.* + *P. a.*	10 mM EtOH, 3 mM caff	—	0.09 ± 0.05	0.047 ± 0.019	16.6 ± 6.1	4.1 ± 2.0	15.7 ± 0.6
v	*A. w.* + *P. a.*	10 mM EtOH	COE1-3C	n. d.	n. d.	n. d.	n. d.	n. d.
vi	*A. w.* + *P. a.*	10 mM EtOH	COE1-4C	n. d.	n. d.	n. d.	n. d.	n. d.
vii	*A. w.* + *P. a.*	10 mM EtOH	COE1-5C	0.05 ± 0.02	0.023 ± 0.014	36.4 ± 22.1	1.1 ± 0.9	13.1 ± 0.4
viii	*A. w.* + *P. a.*	10 mM EtOH, 3 mM caff	COE1-3C	0.09 ± 0.05	0.033 ± 0.006	21.0 ± 3.6	8.0 ± 1.8	14.4 ± 1.0
ix	*A. w.* + *P. a.*	10 mM EtOH, 3 mM caff	COE1-4C	0.09 ± 0.04	0.037 ± 0.002	18.8 ± 1.2	2.0 ± 1.5	13.9 ± 0.3
x	*A. w.* + *P. a.*	10 mM EtOH, 3 mM caff	COE1-5C	0.14 ± 0.02	0.039 ± 0.001	17.8 ± 0.6	4.5 ± 6.4	14.0 ± 1.0

[a] See the Appendix for mathematical details related to the extraction of these parameters. [b] Lowercase Roman numeral indices for experimental conditions are consistent across tables and figures. [c] *A. w.* = *Acetobacterium woodii*; *P. a.* = *Pelobacter acetylenicus*. [d] EtOH = ethanol, caff = caffeate. [e] — = Not applicable or not measured; n. d. = none detected.

This inhibition is puzzling in light of the general reported success of PPV-COEs in augmenting biological systems. One explanation is that the low free energy of ethanol oxidation and bicarbonate reduction[26,81,95] provides insufficient resources for the PPV-COE-stressed cells to adapt (and replicate).[81,95] To test this, prior to inoculation, the thermodynamically more-favorable acceptor 3,4-dihydroxycinnamate (caffeate) was supplemented at 3 mM into all previous culture conditions (see Eqs. III.5 and III.7). Each molecule of caffeate supports the two-electron oxidation of one molecule of H_2 (see Eq. III.5) as compared to two bicarbonate molecules supporting the oxidation of 4 H_2 to produce one acetate (see Eq. III.4). This concentration of caffeate may at most account for a 3 mM × (1 H_2 per caffeate/4 H_2 per acetate) = 0.75 mM decrease in acetate production while providing cells with more than three-fold more free energy per H_2 equivalent (compare Eqs. III.4 and III.5). Caffeate therefore also allows *A. woodii* to utilize lower concentrations of H_2.[96]

Control co-cultures supplemented with 3 mM caffeate and no PPV-COE (see Fig. III.4, traces iv) exhibit a planktonic growth rate of 0.047 ± 0.019 h^{-1}, doubling times of 16.6 ± 6.1 h, and a maximim turbidity of 0.09 ± 0.05—all of which are improved over pure cultures of *A. woodii* and *P. acetylenicus*. This is again compelling evidence of syntrophic association under these conditions. We note that the growth rate of caffeate-supplemented co-cultures is slightly reduced compared to non-supplemented co-cultures, consistent with a lag phase associated with the *de novo* synthesis of caffeate-reductase-type proteins.[90] Despite these subtle differences in growth, these co-cultures produce [acetate] = 15.7 ± 0.6 mM by t = 405 h, in good agreement with co-cultures not containing caffeate. This indicates that caffeate has little effect on the production of acetate, as expected from the above discussion.

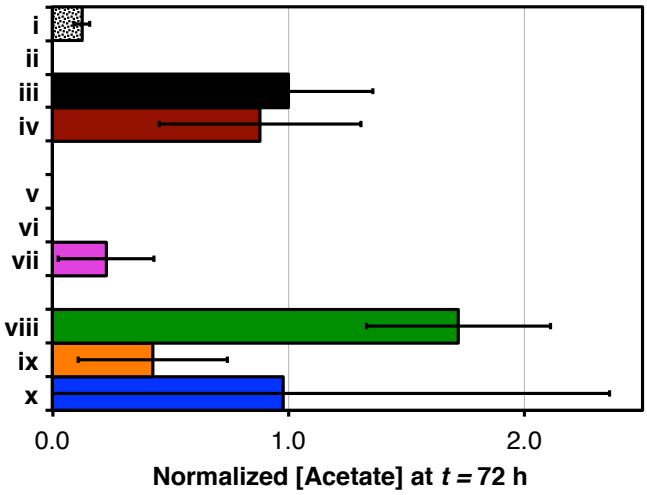

Figure III.5. Normalized triplicate average 72-hour acetate production from cultures modified with PPV-COEs. Colors and roman numerals correspond to the traces in Fig. III.4. Data are normalized to the acetate production of non-modified co-culture controls (**iii**, black bar equal to 1). Conditions **v–x** represent co-cultures modified with COE (note that **v–vii** contain no caffeate).

To test if caffeate might provide the means to overcome growth inhibition from PPV-COE, media supplemented with 3 mM caffeate was additionally supplemented with 5 µM PPV-COE prior to inoculation. Importantly, co-cultures inoculated into this media were able to grow (Fig. III.4, traces viii-x). The most striking trend is that cultures modified with COE1-3C exhibit a 95% (~2-fold) boost in acetate production, producing 8.0 ± 1.8 mM acetate by t = 72 h (Figs. III.4 and III.5, trace viii) as compared to 4.1 ± 2.0 mM acetate by t = 72 h in controls (Figs. III.4 and III.5, trace iv). The additional free energy provided by caffeate therefore appears to relieve PPV-COE growth inhibition.

Growth of these caffeate/PPV-COE-containing co-cultures also proceeds with macroscopic cellular coaggregation—in contrast to the purely-planktonic growth seen in cultures grown without PPV-COEs. As can be seen in Fig. III.6 A, these aggregates subsume much of the COE1-4C in the media. They are also structurally resilient to all but the most vigorous shaking. The retention of the yellow color in the aggregates argues that the organisms are not degrading PPV-COE molecules, as that would presumably break the

conjugation of the PPV backbone and result in decoloration of the material.

As a control for aggregation, PPV-COEs were added to (a) sterile media, (b) unmodified stationary-phase co-cultures, and (c) 1:1 optical density ratio mixtures of unmodified stationary phase pure cultures of *A. woodii* and *P. acetylenicus*. For condition (a), no aggregation was observed. For conditions (b) and (c), PPV-COEs were absorbed by cells in the cultures, and then the cells more readily settled out of solution, but in all cases, no aggregation occurred (gentle swirling was sufficient for resuspension even after > 100 hours of incubation). These experiments strongly suggest that physical aggregation of the two species from PPV-COEs occurs during growth phase.

Both cellular coaggregation and the observation of cells settling from solution are consistent with experiments showing that the PPV-COEs in Fig. III.1, which are cationic, will partially neutralize the net negative surface charge of bacteria.[97] As surface charge becomes less negative, the zeta potential of bacteria decreases in magnitude, presumably destabilizing the bacterial dispersion.

III.D.4. Morphological characterization of cellular aggregates

CFM, Gram stain protocols, and SEM were used to spatially map the PPV-COE-induced syntrophic aggregates. A representative aggregate is displayed in its growth media in a serum bottle in Fig. III.6 A, and a representative CFM image of an aggregate containing COE1-4C is presented in Fig. III.6 B. The uniform coloration and fluorescence in these images suggest that both PPV-COEs and organisms are distributed throughout the aggregates.

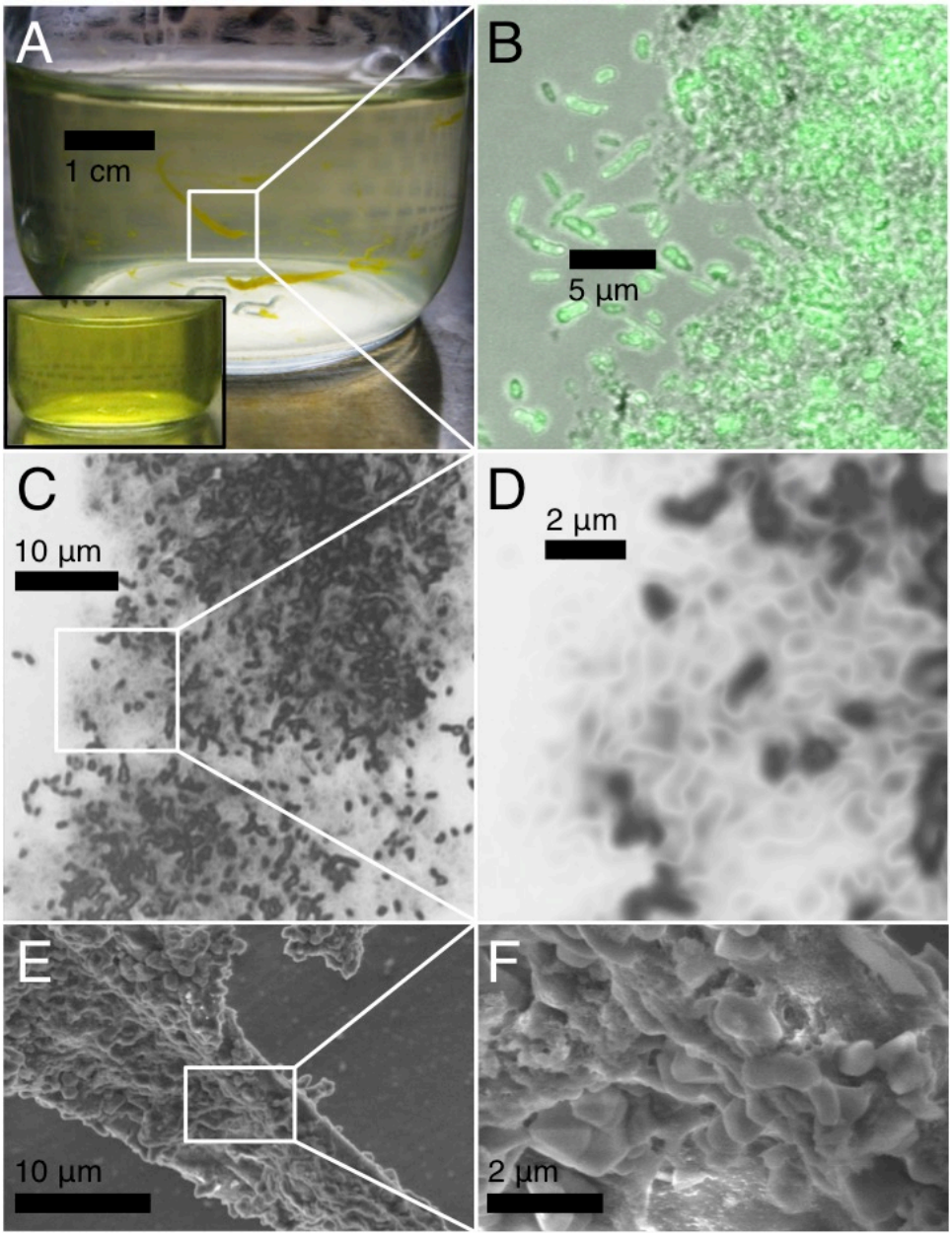

Figure III.6. Representative images of cellular aggregates. (**A**) Example of macroscopic aggregates of *P. acetylenicus* and *A. woodii* supplemented with caffeate and COE1-4C that have formed in COE1-4C-supplemented co-cultures. Note that some planktonic turbidity remains and the aggregates have visibly subsumed much of the COE1-4C (yellow) from solution. The culture was swirled to bring aggregates into suspension for imaging. (**A, inset**) Media prior to inoculation. (**B**) Composite overlay of brightfield image and confocal fluorescence emission (green, false color, 405 nm excitation) of the edge of a cellular aggregate formed in the presence of COE1-4C. Note the presence of cells in both planktonic and aggregate phases. (**C** and **D**) Brightfield image zoom series of a representative Gram-stained aggregate. *P. acetylenicus* cells are colored white while *A. woodii* cells are colored black. (**E** and **F**) A zoom series of two SEM images of a representative chemically-fixed aggregate which formed in the presence of COE1-4C. Note the fibrillar structure of the aggregate.

Gram staining was utilized to assay for the presence of both *P. acetylenicus* and *A. woodii* in the aggregates. As a control for false positives, pure cultures of each organism were Gram stained (not shown), and it was observed that *A. woodii* retained the dark purple crystal violet stain (Gram positive) while *P. acetylenicus* did not (Gram negative). Fig. III.6 C and D are images of representative Gram-stained PPV-COE/caffeate co-culture aggregates. Approximately equal fractions of Gram-positive and Gram-negative bacterial cells may be seen in these images, and this distribution of *A. woodii* and *P. acetylenicus* therefore rules out the possibility that PPV-COEs enabled selective enhancement of only one of the species. In previous reports of multi-species bacterial aggregates,[44,61] characteristic heterogeneously distributed "pockets" of each species define the aggregate morphology, but here, the aggregates appear to have a homogeneous mixing, consistent with the PPV-COEs providing a driving force for aggregation.

The traditional Safranin O counterstain is not used because the PPV-COEs function as sufficient counterstains. This may readily be seen in Fig. III.S1 in the Appendix, which shows true-color, brightfield, photoluminescence (PL), and brightfield/PL overlay images of a Gram-stained cellular aggregate formed from COE1-4C. By comparing the true-color image (Fig. III.S1 A) to the brightfield/PL overlay (Fig. III.S1 D), it is apparent that crystal violet stain is present in positions in the aggregate where PL from COE1-4C is quenched, confirming differentiation. Aggregates were also imaged with SEM (Fig. III.6 E and F) to resolve intercellular structures not visible with CFM. These micrographs show uniformly distributed intact cells in the aggregates. Some sub-cellular material is present within aggregates that has a noticeably fibrillar structure (Fig. III.6 E), suggesting that aggregates may be held together by extracellular polymeric substances.[98,99]

III.D.5. Electrochemical interrogation of PPV-COE-modified cultures

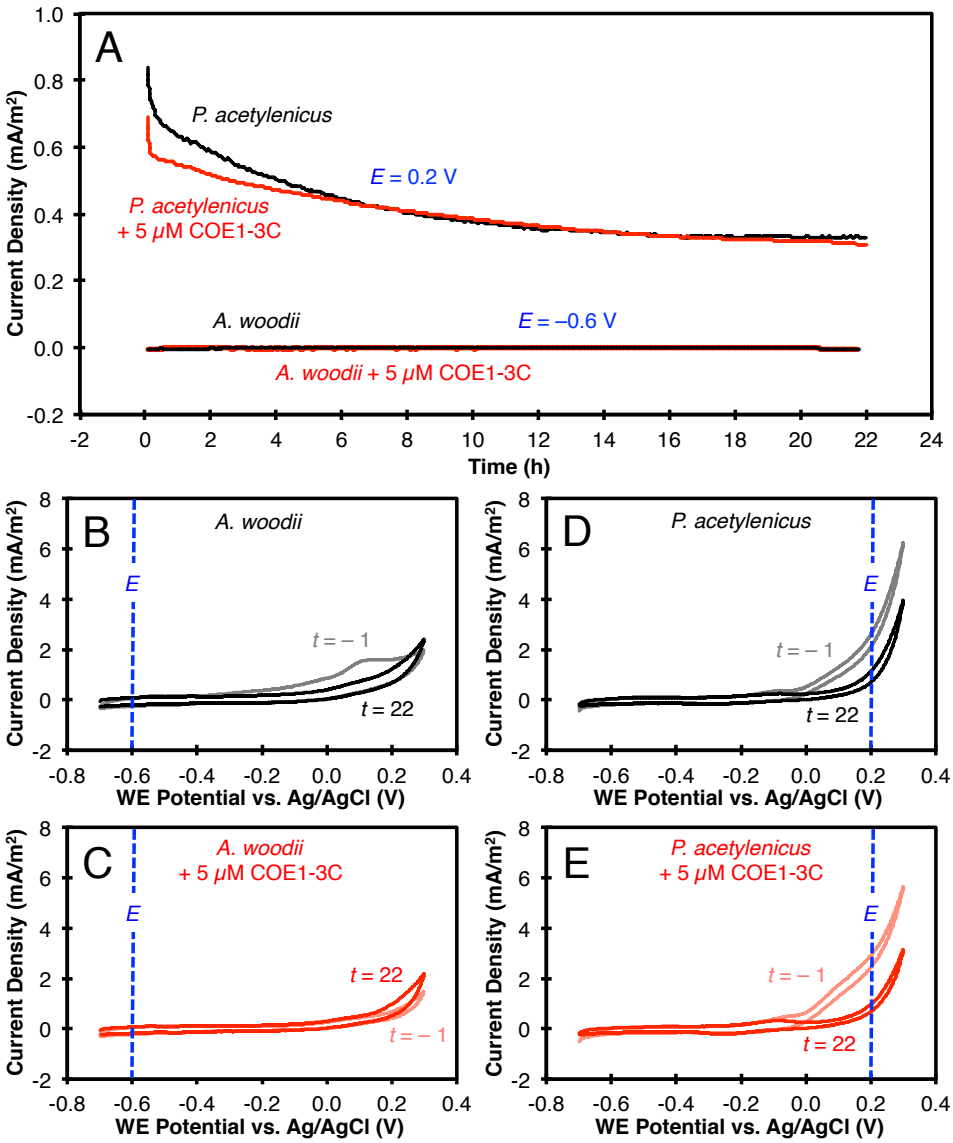

Figure III.7. Electrochemical measurements of cathodic *A. woodii* and anodic *P. acetylenicus* in M3Cs, both with and without 5 µM COE1-3C added. All plotted data are averages of duplicate experiments. Note that t = –1 h corresponds to one hour before the beginning of current collection, and t = 22 h corresponds to termination of current collection. CV measurements were conducted at 5 mV/s, and potentials are reported relative to the Ag/AgCl (sat. KCl) reference electrode. (**A**) CA traces for all four experimental conditions. Note that *A. woodii* M3C working electrodes were poised at E = –0.6 V (cathodic, reducing) while *P. acetylenicus* M3C working electrodes were poised at E = 0.2 V (anodic, oxidizing); these are depicted by blue text as well as dashed lines labelled "*E*" in the remaining figure panels. (**B**) CV measurements at t = –1 h and 22 h of unmodified *A. woodii*. (**C**) CV measurements at t = –1 h and 22 h of *A. woodii* modified with 5 µM COE1-3C. (**D**) CV measurements at t = –1 h and 22 h of unmodified *P. acetylenicus*. (**E**) CV measurements at t = –1 h and 22 h of *P. acetylenicus* modified with 5 µM COE1-3C.

To evaluate the potential role of DIET in the observed acceleration of syntrophic

metabolism afforded by COE1-3C, *P. acetylenicus* and *A. woodii* were cultured separately on graphite electrodes in microbial three-electrode electrochemical cells (M3Cs) where chronoamperometry (CA) and cyclic voltammetry (CV) measurements could be obtained. In these devices, if DIET is truly enabled by COE1-3C, then an appropriately poised electrode should be able to serve as an electrical proxy for the syntrophic partner organism for both species. This effect would be seen as an increase in electrochemical current output as compared to unmodified controls. The same basal BBM medium was used as in all prior experiments.

For *P. acetylenicus* M3Cs, 10 mM ethanol was supplied as the donor substrate in the media with an electrode poised as an anode at $E = 0.2$ V vs. Ag/AgCl (anodic) serving as the electron acceptor (to simulate an electrically connected *A. woodii* acceptor organism); devices were inoculated with 1% (v/v) acetoin-grown pure cultures. For *A. woodii* M3Cs, cells were initially grown autotrophically in BBM media (see Eqs. III.2 and III.4, and Materials and Methods) and then the full volume was inoculated into the devices with an electrode poised at $E = -0.6$ V vs. Ag/AgCl (cathodic) replacing H_2 as the electron donor (to simulate an electrically connected *P. acetylenicus* donor organism); 10 mM HCO_3^- and 3 mM caffeate were added as acceptors as in syntrophic cultures.

The duplicate-average measured CA current output from these M3Cs over 22 h is shown in Fig. III.7 A. In *A. woodii* M3Cs, cathodic current is negligible (~0 mA/m^2) under both unmodified and COE1-3C-modified conditions, indicating that COE1-3C has no measurable effect. The fact that *A. woodii* remains electrochemically inert is consistent with reports that it cannot consume current to partake in microbial electrosynthesis.[100] In *P. acetylenicus* M3Cs, anodic current is >0.6 mA/m^2 at $t = 0$ h and decays to ~0.3 mA/m^2 by $t = 22$ h for

both unmodified and COE1-3C-modified conditions; this signifies that COE1-3C has no current-amplifying effect. These current amplitudes are also negligible in comparison to current outputs from electrogenic species.[101,102] Because the current outputs are nearly congruent under both unmodified and COE1-3C-modified conditions, we conclude that COE1-3C modification does not alter either species' ability to electronically communicate with the electrode; because the electrode serves as a proxy for a syntrophic partner, this provides evidence that COE1-3C is not inducing DIET in the corresponding syntrophic culture. Rather, it seems that PPV-COEs enable aggregation that enhances diffusion-based syntrophies.

Before and after CA, M3Cs were analysed with CV to examine the potential dependence of current outputs. CV traces for *A. woodii* M3Cs, both unmodified (Fig. III.7 B) and modified with COE1-3C (Fig. III.7 C), are essentially featureless at E = –0.6 V and unchanged from t = –1 h to t = 22 h. This observation is consistent with the CA traces (Fig. III.7 A) and the inability of *A. woodii* to participate in cathodic processes. CV traces for *P. acetylenicus* M3Cs show an anodic current feature at t = –1 h with an onset at E = 0 V that is similar in magnitude and shape for both unmodified (Fig. III.7 D) and COE1-3C-modified (Fig. III.7 E) conditions. By t = 22 h, this feature has greatly diminished for both conditions. The magnitude and evolution of this anodic feature at E = 0.2 V helps explain the congruent non-zero decaying current outputs observed in Fig. III.7A. The general lack of differentiation of unmodified and COE1-3C-modified M3Cs containing *A. woodii* or *P. acetylenicus* provides additional supporting evidence that COE1-3C is not inducing DIET in these syntrophic cultures.

III.E. Conclusions

The syntrophy of *A. woodii* and *P. acetylenicus* investigated in this chapter operates near the thermodynamic limits of growth. The efficiency of this (and any) obligatory crossfeeding system may be increased as the species involved come into physical contact, as this reduces the distance that reducing equivalents must diffuse.

As PPV-COEs have seen much bioelectronic utility in bioelectrochemical devices, they were applied to this syntrophic system in an attempt to examine possible electron transfer between *A. woodii* and *P. acetylenicus*. This approach yielded several important conclusions. First, based on scanning electron and confocal fluorescence micrographs of cell morphology, PPV-COEs do not appear to be cytotoxic at the concentration tested (5 μM), nor do the organisms seem to degrade PPV-COEs. Neither growth rate nor metabolic product concentrations are increased from additions of 5 μM PPV-COEs to pure cultures of *A. woodii* and *P. acetylenicus*. PPV-COEs added to ethanol-consuming co-cultures of *A. woodii* and *P. acetylenicus* promote cellular aggregation, enabling formation of heterogeneous aggregates of the two species. This aggregation is consistent with reports of decreased cell zeta potential from addition of PPV-COEs. Aggregation decreases the apparent planktonic growth rate, but stimulates the rate of ethanol consumption under such conditions during mid-log growth by up to 95% specifically for COE1-3C. This suggests that COE1-3C improves syntrophic association of the two species by bringing them into physical proximity. During the course of experiments, we also observed that *A. woodii* in pure culture will ferment ethanol in the presence of bicarbonate concentrations ≤ 10 mM, given enough time (~2 weeks).

Subsequent electrochemical interrogation of the two species in M3Cs indicates that electrical communication with electrodes is not amplified by addition of COE1-3C. This

provides evidence that decreased diffusion length *via* aggregation appears to be the mechanism of PPV-COE enhancement in this system, as increased electron transfer by DIET would be detectable in the M3Cs as a faradaic current signal. While it is evident from this work that PPV-COEs favorably alter the syntrophic interaction, a chemical modifier that can induce DIET in a diffusion-based syntrophic system remains a desirable target.

III.F. References

1. Thauer, R. K., Jungermann, K. & Decker, K. Energy conservation in chemotrophic anaerobic bacteria. *Bacteriol. Rev.* **41,** 100–180 (1977).
2. Lovley, D. R., Phillips, E. J. & Lonergan, D. J. Hydrogen and Formate Oxidation Coupled to Dissimilatory Reduction of Iron or Manganese by Alteromonas putrefaciens. *Appl. Environ. Microbiol.* **55,** 700–6 (1989).
3. Lovley, D., Coates, J., Blunt-Harris, E., Phillips, E. & Woodward, J. Humic substances as electron acceptors for microbial respiration. *Lett. to Nat.* **382,** 445–448 (1996).
4. Heidelberg, J. F. *et al.* Genome sequence of the dissimilatory metal ion-reducing bacterium Shewanella oneidensis. *Nat. Biotechnol.* **20,** 1118–23 (2002).
5. Lovley, D. R. Extracellular electron transfer: wires, capacitors, iron lungs, and more. *Geobiology* **6,** 225–31 (2008).
6. Butler, J. E., Young, N. D. & Lovley, D. R. Evolution from a respiratory ancestor to fill syntrophic and fermentative niches: comparative genomics of six Geobacteraceae species. *BMC Genomics* **10,** 103 (2009).
7. Pfeffer, C. *et al.* Filamentous bacteria transport electrons over centimetre distances. *Nature* 10–13 (2012).
8. Schink, B. Synergistic interactions in the microbial world. *Antonie Van Leeuwenhoek* **81,** 257–61 (2002).
9. Postgate, J. R. On the Nutrition of Desulphovibrio desulphuricans: a correction. *J. Gen. Microbiol.* **9,** 440–444 (1958).
10. Bryant, M. P., Wolin, E. a, Wolin, M. J. & Wolfe, R. S. Methanobacillus omelianskii, a symbiotic association of two species of bacteria. *Arch. Mikrobiol.* **59,** 20–31 (1967).
11. Gray, B., Fowler, C., Nugent, N., Rigopoulos, N. & Fuller, R. Reevaluation of Chloropseudomonas ethylica strain 2-K. *Int. J. Syst. Bacteriol.* **23,** 256–264 (1973).
12. Pfennig, N. Desulfuromonas acetoxidans gen. nov. and sp. nov., a New Anaerobic, Sulfur-Reducing, Acetate-Oxidizing Bacterium. *Arch. Microbiol.* **2,** (1976).
13. Biebl, H. & Pfennig, N. Growth Yields of Green Sulfur Bacteria in Mixed Cultures with Sulfur and Sulfate Reducing Bacteria. *Arch. Microbiol.* **16,** 9–16 (1978).
14. McInerney, M. J. *et al.* Physiology, ecology, phylogeny, and genomics of microorganisms capable of syntrophic metabolism. *Ann. N. Y. Acad. Sci.* **1125,** 58–72 (2008).
15. McInerney, M. & Sieber, J. Microbial Syntrophy: Ecosystem-Level Biochemical Cooperation. *microbemagazine.org* **6,** 479–485 (2011).

16. Agler, M. T., Wrenn, B. a, Zinder, S. H. & Angenent, L. T. Waste to bioproduct conversion with undefined mixed cultures: the carboxylate platform. *Trends Biotechnol.* **29,** 70–8 (2011).
17. Morita, M., Malvankar, N., Franks, A. & Summers, Z. Potential for Direct Interspecies Electron Transfer in Methanogenic Wastewater Digester Aggregates. *MBio* **2,** 1–8 (2011).
18. Parameswaran, P., Torres, C. I., Lee, H.-S., Krajmalnik-Brown, R. & Rittmann, B. E. Syntrophic interactions among anode respiring bacteria (ARB) and Non-ARB in a biofilm anode: electron balances. *Biotechnol. Bioeng.* **103,** 513–23 (2009).
19. Parameswaran, P., Zhang, H., Torres, C. I., Rittmann, B. E. & Krajmalnik-Brown, R. Microbial community structure in a biofilm anode fed with a fermentable substrate: the significance of hydrogen scavengers. *Biotechnol. Bioeng.* **105,** 69–78 (2010).
20. Parameswaran, P., Torres, C. I., Lee, H.-S., Rittmann, B. E. & Krajmalnik-Brown, R. Hydrogen consumption in microbial electrochemical systems (MXCs): the role of homo-acetogenic bacteria. *Bioresour. Technol.* **102,** 263–71 (2011).
21. Dolfing, J. Syntrophy in microbial fuel cells. *ISME J.* **8,** 4–5 (2014).
22. Gieg, L. M., Fowler, S. J. & Berdugo-Clavijo, C. Syntrophic biodegradation of hydrocarbon contaminants. *Curr. Opin. Biotechnol.* **27,** 21–29 (2014).
23. Scheller, S., Yu, H., Chadwick, G. L. & Mcglynn, S. E. Artificial electron acceptors decouple archaeal methane oxidation from sulfate reduction. *Science.* **351,** 703–707 (2016).
24. Zengler, K. & Palsson, B. O. A road map for the development of community systems (CoSy) biology. *Nat. Rev. Microbiol.* **10,** 366–72 (2012).
25. Walker, C. B. *et al.* The electron transfer system of syntrophically grown Desulfovibrio vulgaris. *J. Bacteriol.* **191,** 5793–801 (2009).
26. Schink, B. & Stams, A. J. M. *The Prokaryotes, Chapter 1.11: Syntrophism among Prokaryotes*. (Springer New York, 2006).
27. McInerney, M. J. *et al.* The genome of Syntrophus aciditrophicus: life at the thermodynamic limit of microbial growth. *Proc. Natl. Acad. Sci. U. S. A.* **104,** 7600–5 (2007).
28. Sieber, J. R., McInerney, M. J. & Gunsalus, R. P. Genomic insights into syntrophy: the paradigm for anaerobic metabolic cooperation. *Annu. Rev. Microbiol.* **66,** 429–52 (2012).
29. Rinke, C. *et al.* Insights into the phylogeny and coding potential of microbial dark matter. *Nature* **499,** 431–437 (2013).
30. Stolyar, S. *et al.* Metabolic modeling of a mutualistic microbial community. *Mol. Syst. Biol.* **3,** 92 (2007).
31. Taffs, R. *et al.* In silico approaches to study mass and energy flows in microbial consortia: a syntrophic case study. *BMC Syst. Biol.* **3,** 114 (2009).
32. Wintermute, E. H. & Silver, P. A. Emergent cooperation in microbial metabolism. *Mol. Syst. Biol.* **6,** 407 (2010).
33. Klitgord, N. & Segre, D. Environments that Induce Synthetic Microbial Ecosystems. *PLoS Comput. Biol.* **6,** 1–17 (2010).
34. Zomorrodi, A. R. & Maranas, C. D. OptCom: A multi-level optimization framework for the metabolic modeling and analysis of microbial communities. *PLoS Comput. Biol.* **8,** (2012).

35. Lewis, N. E., Nagarajan, H. & Palsson, B. Ø. Constraining the metabolic genotype-phenotype relationship using a phylogeny of in silico methods. *Nat. Rev. Microbiol.* **10,** 291–305 (2012).
36. Nagarajan, H. *et al.* Characterization and modelling of interspecies electron transfer mechanisms and microbial community dynamics of a syntrophic association. *Nat. Commun.* **4,** 2809 (2013).
37. Molloy, S. Environmental microbiology: disentangling syntrophy. *Nat. Rev. Microbiol.* **12,** 7 (2014).
38. Zomorrodi, A. R., Islam, M. M. & Maranas, C. D. D-OptCom: Dynamic Multi-level and Multi-objective Metabolic Modeling of Microbial Communities. *ACS Synth. Biol.* **3,** 247–257 (2014).
39. O'Brien, E. J., Monk, J. M. & Palsson, B. O. Using Genome-scale Models to Predict Biological Capabilities. *Cell* **161,** 971–987 (2015).
40. Tan, J., Zuniga, C. & Zengler, K. Unraveling interactions in microbial communities - from co-cultures to microbiomes. *J. Microbiol.* **53,** 295–305 (2015).
41. Zomorrodi, A. R. & Segre, D. Synthetic Ecology of Microbes: Mathematical Models and Applications. *J. Mol. Biol.* **428**, 837-861 (2015).
42. McInerney, M. J., Sieber, J. R. & Gunsalus, R. P. Syntrophy in anaerobic global carbon cycles. *Curr. Opin. Biotechnol.* **20,** 623–32 (2009).
43. Stams, A. J. M. & Plugge, C. M. Electron transfer in syntrophic communities of anaerobic bacteria and archaea. *Nat. Rev. Microbiol.* **7,** 568–77 (2009).
44. Summers, Z. M. *et al.* Direct exchange of electrons within aggregates of an evolved syntrophic coculture of anaerobic bacteria. *Science.* **330,** 1413–5 (2010).
45. Lovley, D. R. Live wires: direct extracellular electron exchange for bioenergy and the bioremediation of energy-related contamination. *Energy Environ. Sci.* **4,** 4896 (2011).
46. Reguera, G. *et al.* Extracellular electron transfer via microbial nanowires. *Nature* **435,** 1098–1101 (2005).
47. Malvankar, N. S. & Lovley, D. R. Microbial Nanowires: A New Paradigm for Biological Electron Transfer and Bioelectronics. *ChemSusChem* **5,** 1039–1046 (2012).
48. Wegener, G., Krukenberg, V., Riedel, D., Tegetmeyer, H. E. & Boetius, A. Intercellular wiring enables electron transfer between methanotrophic archaea and bacteria. *Nature* **526,** 587–590 (2015).
49. Kato, S., Hashimoto, K. & Watanabe, K. Methanogenesis facilitated by electric syntrophy via (semi)conductive iron-oxide minerals. *Environ. Microbiol.* **14,** 1646–54 (2012).
50. Zhuang, L., Tang, J., Wang, Y., Hu, M. & Zhou, S. Conductive iron oxide minerals accelerate syntrophic cooperation in methanogenic benzoate degradation. *J. Hazard. Mater.* **293,** 37–45 (2015).
51. Enning, D. *et al.* Marine sulfate-reducing bacteria cause serious corrosion of iron under electroconductive biogenic mineral crust. *Environ. Microbiol.* **14,** 1772–87 (2012).
52. Liu, F. *et al.* Promoting direct interspecies electron transfer with activated carbon. *Energy Environ. Sci.* **5,** 8982 (2012).
53. Vostiar, I., Ferapontova, E. . & Gorton, L. Electrical 'wiring' of viable Gluconobacter oxydans cells with a flexible osmium-redox polyelectrolyte. *Electrochem. commun.* **6,** 621–626 (2004).
54. Timur, S. *et al.* Electrical wiring of Pseudomonas putida and Pseudomonas fluorescens

with osmium redox polymers. *Bioelectrochemistry* **71,** 38–45 (2007).
55. Coman, V. *et al.* Electrical wiring of live, metabolically enhanced Bacillus subtilis cells with flexible osmium-redox polymers. *J. Am. Chem. Soc.* **131,** 16171–6 (2009).
56. Wu, X. *et al.* A Role for Microbial Palladium Nanoparticles in Extracellular Electron Transfer. *Angew. Chemie* **123,** 447–450 (2011).
57. Waks, Z. & Silver, P. a. Engineering a synthetic dual-organism system for hydrogen production. *Appl. Environ. Microbiol.* **75,** 1867–75 (2009).
58. Hillesland, K. L. & Stahl, D. a. Rapid evolution of stability and productivity at the origin of a microbial mutualism. *Proc. Natl. Acad. Sci. U. S. A.* **107,** 2124–9 (2010).
59. Bernstein, H. C., Paulson, S. D. & Carlson, R. P. Synthetic Escherichia coli consortia engineered for syntrophy demonstrate enhanced biomass productivity. *J. Biotechnol.* **157,** 159–66 (2012).
60. Rosenbaum, M. A. *et al.* Shewanella oneidensis in a lactate-fed pure-culture and a glucose-fed co-culture with Lactococcus lactis with an electrode as electron acceptor. *Bioresour. Technol.* **102,** 2623–8 (2011).
61. Kim, H. J., Boedicker, J. Q., Choi, J. W. & Ismagilov, R. F. Defined spatial structure stabilizes a synthetic multispecies bacterial community. *Proc. Natl. Acad. Sci. U. S. A.* **105,** 18188–93 (2008).
62. Rotaru, A.-E. *et al.* Interspecies Electron Transfer via Hydrogen and Formate Rather than Direct Electrical Connections in Cocultures of Pelobacter carbinolicus and Geobacter sulfurreducens. *Appl. Environ. Microbiol.* **78,** 7645–51 (2012).
63. Garner, L. E. *et al.* Modification of the optoelectronic properties of membranes via insertion of amphiphilic phenylenevinylene oligoelectrolytes. *J. Am. Chem. Soc.* **132,** 10042–52 (2010).
64. Hou, H. *et al.* Conjugated oligoelectrolytes increase power generation in E. coli microbial fuel cells. *Adv. Mater.* **25,** 1593–7 (2013).
65. Garner, L. E., Thomas, A. W., Sumner, J. J., Harvey, S. P. & Bazan, G. C. Conjugated oligoelectrolytes increase current response and organic contaminant removal in wastewater microbial fuel cells. *Energy Environ. Sci.* **5,** 9449–9452 (2012).
66. Wang, V. B. *et al.* Comparison of flavins and a conjugated oligoelectrolyte in stimulating extracellular electron transport from Shewanella oneidensis MR-1. *Electrochem. commun.* **41,** 55–58 (2014).
67. Kirchhofer, N. D. *et al.* The conjugated oligoelectrolyte DSSN+ enables exceptional coulombic efficiency via direct electron transfer for anode-respiring Shewanella oneidensis MR-1-a mechanistic study. *Phys. Chem. Chem. Phys.* **16,** 20436–43 (2014).
68. Kirchhofer, N. D., Rasmussen, M. A., Dahlquist, F. W., Minteer, S. D. & Bazan, G. C. The photobioelectrochemical activity of thylakoid bioanodes is increased via photocurrent generation and improved contacts by membrane-intercalating conjugated oligoelectrolytes. *Energy Environ. Sci.* **8,** 2698–2706 (2015).
69. Thomas, A. W. *et al.* A lipid membrane intercalating conjugated oligoelectrolyte enables electrode driven succinate production in Shewanella. *Energy Environ. Sci.* **6,** 1761 (2013).
70. Davis, W., Svec, W., Ratner, M. & Wasielewski, M. Molecular-wire behaviour in p-phenylenevinylene oligomers. *Nature* **396,** 60–63 (1998).
71. Hoofman, R., Haas, M. De & Siebbeles, L. Highly mobile electrons and holes on isolated chains of the semiconducting polymer poly(phenylene vinylene). *Nature* **392,**

54–56 (1998).
72. Daniel, C. *et al.* Resonance energy transfer dynamics in hydrogen-bonded oligo-p-phenylenevinylene nanostructures. *Synth. Met.* **147,** 29–35 (2004).
73. Woo, H. Y. *et al.* Solvent Effects on the Two-Photon Absorption of Distyrylbenzene Chromophores. *J. Am. Chem. Soc.* **127,** 14721–14729 (2005).
74. Lloveras, V. *et al.* Tunneling versus hopping in mixed-valence oligo-p-phenylenevinylene polychlorinated bis(triphenylmethyl) radical anions. *J. Am. Chem. Soc.* **133,** 5818–33 (2011).
75. Hungate, R. *Methods of Microbiology, Chapter IV: A Roll Tube Method for Cultivation of Strict Anaerobes*. *Methods in microbiology* (1969).
76. Muller, V. Minireview: Energy Conservation in Acetogenic Bacteria. *Appl. Environ. Microbiol.* **69,** 6345–6353 (2003).
77. Balch, W. E. & Schoberth, S. Acetobacterium, a new genus of hydrogen-oxidizing, carbon dioxide-reducing, anaerobic bacteria. *Int. J. Syst. Bacteriol.* **27,** 355–361 (1977).
78. Schink, B. *The Prokaryotes, Chapter 3.4.1: The Genus Pelobacter*. (Springer New York, 2006).
79. Schink, B. Fermentation of acetylene by an obligate anaerobe, Pelobacter acetylenicus sp. nov.*. *Arch. Microbiol.* **142,** 295–301 (1985).
80. Seitz, H.-J., Schink, B. & Conrad, R. Thermodynamics of hydrogen metabolism in methanogenic cocultures degrading ethanol or lactate. *FEMS Microbiol. Lett.* **55,** 119–124 (1988).
81. Valentine, D. L., Reeburgh, W. S. & Blanton, D. C. A culture apparatus for maintaining H2 at sub-nanomolar concentrations. *J. Microbiol. Methods* **39,** 243–51 (2000).
82. Barker, H. A. Studies upon the methane fermentation. IV. The isolation and culture of methanobacterium omelianskii. *Antonie Van Leeuwenhoek* **6,** 201–220 (1940).
83. Seitz, H., Siheriz, F., Schink, B. & Conrad, R. Hydrogen production during fermentation of acetoin and acetylene by Pelobacter acetylenicus. *FEMS Microbiol. Lett.* **71,** 83–87 (1990).
84. Oremland, R. S. & Voytek, M. a. Acetylene as fast food: implications for development of life on anoxic primordial Earth and in the outer solar system. *Astrobiology* **8,** 45–58 (2008).
85. Buschhorn, H., Dürre, P. & Gottschalk, G. Production and Utilization of Ethanol by the Homoacetogen Acetobacterium woodii. *Appl. Environ. Microbiol.* **55,** 1835–40 (1989).
86. Ljungdahl, L. G. The Autotrophic Pathway of Acetate Synthesis in Acetogenic Bacteria. *Annu. Rev. Microbiol.* **40,** 415–450 (1986).
87. Seitz, H., Schink, B., Pfennig, N. & Conrad, R. Energetics of syntrophic ethanol oxidation in defined chemostat cocultures. 1. Energy requirement for H2 production and H2 oxidation. *Arch. Microbiol.* 82–88 (1990).
88. Seitz, H., Schink, B., Pfennig, N. & Conrad, R. Energetics of syntrophic ethanol oxidation in defined chemostat cocultures. 2. Energy sharing in biomass production. *Arch. Microbiol.* **155,** 89–93 (1990).
89. Imkamp, F. & Müller, V. Chemiosmotic Energy Conservation with Na+ as the Coupling Ion during Hydrogen-Dependent Caffeate Reduction by Acetobacterium woodii. *J. Bacteriol.* **184,** 1947–1951 (2002).
90. Dilling, S., Imkamp, F., Schmidt, S. & Müller, V. Regulation of caffeate respiration in the acetogenic bacterium Acetobacterium woodii. *Appl. Environ. Microbiol.* **73,** 3630–

6 (2007).
91. Stieb, M. & Schink, B. Cultivation of syntrophic anaerobic bacteria in membrane-separated culture devices. *FEMS Microbiol. Lett.* **45,** 71–76 (1987).
92. Ishii, S., Kosaka, T., Hori, K. & Hotta, Y. Coaggregation Facilitates Interspecies Hydrogen Transfer between Pelotomaculum thermopropionicum and Methanothermobacter thermautotrophicus. *Appl. Environ. Microbiol.* **71,** 7838–7845 (2005).
93. Shimoyama, T., Kato, S., Ishii, S. & Watanabe, K. Flagellum Mediates Symbiosis. *Science.* **323,** 2009–2009 (2009).
94. Felchner-Zwirello, M., Winter, J. & Gallert, C. Interspecies distances between propionic acid degraders and methanogens in syntrophic consortia for optimal hydrogen transfer. *Appl. Microbiol. Biotechnol.* **97,** 9193–205 (2013).
95. Schink, B. Energetics of Syntrophic Cooperation in Methanogenic Degradation. *Microbiol. Mol. Biol. Rev.* **61,** 262–280 (1997).
96. Cord-Ruwisch, R., Seitz, H.-J. & Conrad, R. The capacity of hydrogenotrophic anaerobic bacteria to compete for traces of hydrogen depends on the redox potential of the terminal electron acceptor. *Arch. Microbiol.* **149,** 350–357 (1988).
97. Catania, C., Thomas, A. W. & Bazan, G. C. Tuning cell surface charge in E. coli with conjugated oligoelectrolytes. *Chem. Sci.* **00,** 1–7 (2016).
98. Cao, B. *et al.* Extracellular polymeric substances from Shewanella sp. HRCR-1 biofilms: characterization by infrared spectroscopy and proteomics. *Environ. Microbiol.* **13,** 1018–31 (2011).
99. Borole, A. P. *et al.* Electroactive biofilms: Current status and future research needs. *Energy Environ. Sci.* **4,** 4813 (2011).
100. Nevin, K. P. *et al.* Electrosynthesis of organic compounds from carbon dioxide is catalyzed by a diversity of acetogenic microorganisms. *Appl. Environ. Microbiol.* **77,** 2882–6 (2011).
101. Marsili, E. *et al.* Shewanella secretes flavins that mediate extracellular electron transfer. *Proc. Natl. Acad. Sci. U. S. A.* **105,** 3968–73 (2008).
102. Marsili, E., Rollefson, J. B., Baron, D. B., Hozalski, R. M. & Bond, D. R. Microbial biofilm voltammetry: direct electrochemical characterization of catalytic electrode-attached biofilms. *Appl. Environ. Microbiol.* **74,** 7329–37 (2008).
103. Widdel, F. & Pfennig, N. Studies on dissimilatory sulfate-reducing bacteria that decompose fatty acids. *Arch. Microbiol.* 395–400 (1981).
104. Verhulst, P. Notice sur la loi que la population suit dans son accroissement. *Curr. Math. Phys* **10,** (1838).

III.G. Appendix III. Materials, Methods, and Supplementary Figures

III.G.1. Materials and Methods

III.G.1.a. Materials

PPV-COEs were synthesized according to literature procedures.[63,64] All other materials were used as received and purchased from Fisher Scientific or Sigma Aldrich unless indicated otherwise.

III.G.1.b. Cell culture and anaerobic technique

Pure cultures of *Acetobacterium woodii* strain WB1 (DSM 1030) and *Pelobacter acetylenicus* strain GhAcy 1 (DSM 3247) were anaerobically cultivated from lyophilized pellets in DSMZ recommended media (see composition in next subsection). For subculturing of these strains into test tubes, syntrophic cultures, and electrochemical reactors, an inoculation frequency equivalent to 1% (v/v) from an $A = 0.01$ culture was consistently used in bicarbonate buffered marine (BBM) medium (see composition below).

Unless stated otherwise, all cell culture media discussed below was degassed under 90%:10% N_2:CO_2 atmosphere, either with glass diffuser frits (for large volumes) or with cannulas inserted next to butyl rubber bungs (for pressure tubes and serum bottles). Stock gases were deoxygenated by passage through a sealed heated column of fine copper turnings, which may be regenerated by passing a 5% H_2 gas mixture through the turnings. A head pressure of ~5 psi in sealed media bottles/tubes was maintained to prevent inward diffusion of O_2.

Transfer of culture volumes was carefully kept anaerobic by the use of degassed syringes and butyl rubber bungs on all culture vessels. Syringes were made anaerobic by filling and

purging the barrel of the syringe at least 10 times with 90%:10% N_2:CO_2. The gas mixture was kept sterile by flowing through an autoclaved Micro-mate glass syringe barrel (Popper & Sons) filled with glass wool. Sterility of butyl rubber bungs was maintained by igniting 100% ethanol on the surface.

III.G.1.c. Anaerobic media preparation and composition

For cultivation of *A. woodii* from lyophilized pellets, DSMZ recommended media #135 was prepared with the following modifications: no resazurin (possible redox shuttle), trace element solution replaced with 100X trace element solution below, vitamin solution replaced with 100X vitamin solution below, and 0.50 g/L $Na_2S•9H_2O$ substituted with molar equivalent (2.1 mM) L-cysteine $HCl•H_2O$.

For autotrophic subcultures of *A. woodii* (relevant for M3Cs), the BBM media (composition below) was used, except that the standard gas mixture of 90%:10% N_2:CO_2 was replaced by a gas mixture of 80%:20% H_2:CO_2 as the carbon and energy source (see **Eq. III.4**).

For cultivation of *P. acetylenicus* from lyophilized pellets, DSMZ recommended media #293 was prepared with the following modifications: Na_2-succinate replaced with 1.0 g/L acetoin as the carbon source, no resazurin (possible redox shuttle), trace element solution SL-10 replaced with the 100X trace element solution below, and 0.36 g/L $Na_2S•9H_2O$ substituted with molar equivalent (1.5 mM) L-cysteine $HCl•H_2O$.

The basal BBM medium for growth studies, syntrophic growth, and use in electrochemical reactors was slightly modified from previously reported media[103] and has the following composition (values in g/L end volume): Na_2SO_4, 3.0; KH_2PO_4, 0.2; NH_4Cl, 0.25; KCl, 0.5; $CaCl_2•2H_20$, 0.15; NaC1, 20.0; $MgCl_2•6H_2O$, 3.0. This media was prepared in

deionized H_2O at 60% of the intended end volume (*e.g.* 600 mL for 1 L end volume) to allow for addition of further components, then autoclaved. Under constant degassing, the following volumes of additional sterile/degassed stock components were then added to the autoclaved, degassed BBM medium (values in mL of stock solution/L end volume): 100X trace element solution (see below), 10.0; 100X vitamin solution (see below), 10.0; 84 g/L $NaHCO_3$, 10.0; when applicable, caffeic acid (caffeate) solution (180.2 g/L, pH adjusted to 7.0 with Na_2CO_3), 30.0. Finally, pH was adjusted to ~7.1 with filter sterile 106 g/L Na_2CO_3 solution, and deionized water was added, leaving only room for electron donor (ethanol) and reducing agent (L-cysteine HCl) solutions.

Donor and reducing agent solutions were added immediately prior to inoculation in the following amounts, respectively (values in mL of stock solution/L end volume): aqueous 78.9 g/L (10% v/v) ethanol, 5.83; aqueous 26.3 g/L (150 mM) L-cysteine HCl•H_2O, 10.0.

The 100X trace element solution contains the following components (values in g/L): Nitrilotriacetic acid, 2.14; $MnCl_2$•$4H_2O$, 0.1; $FeSO_4$•$7H_2O$, 0.3; $CoCl_2$•$6H_2O$, 0.17; $ZnSO_4$•$7H_2O$, 0.2; $CuCl_2$•$2H_2O$, 0.03; $AlK(SO_4)_2$•$12H_2O$, 0.005; H_3BO_3, 0.005; Na_2MoO_4•$2H_2O$, 0.09; $NiSO_4$•$6H_2O$, 0.11; Na_2WO_4•$2H_2O$, 0.02. Sterility was achieved by filtration through a 0.20 μm pore filter (Fisherbrand).

The 100X vitamin solution contains the following components (values in g/L): biotin (vitamin B-7), 0.002; pantothenic acid (vitamin B-5), 0.005; cobalamin (vitamin B-12), 0.0001; *p*-aminobenzoic acid, 0.005; α-lipoic acid, 0.005; nicotinic acid (vitamin B-3), 0.005; thiamine (vitamin B-1), 0.005; riboflavin (vitamin B-2), 0.005; pyridoxine HCl (vitamin B-6), 0.01; folic acid (vitamin B-9), 0.002. Sterility was achieved by filtration through a 0.20 μm pore filter (Fisherbrand).

III.G.1.d.Culture turbidity measurements

Absorbance values of liquid cultures, $A(t)$, were measured with an Amersham Biosciences Ultrospec 10 Cell Density Meter at 600 nm in plastic cuvettes with 1 cm path length and 1 mL working volume. Sterile media was used as the blank.

III.G.1.e. Numerical extraction of growth parameters

In batch culture conditions such as those used in this study, the rate of turbidity change of the population, $dA(t)/dt$, is a function of the culture turbidity at a given time, $A(t)$, as well as the maximum culture turbidity, A_{max}, which represents the carrying capacity of the culture medium. This relationship is expressed by the logistic differential equation,[104]

$$\frac{dA(t)}{dt} = \mu A(t)\left(1 - \frac{A(t)}{A_{max}}\right) \quad (8),$$

where μ is the growth rate (h^{-1}) and t is the time elapsed after inoculation. The parenthetical term on the right hand side of Eq. III.8 represents negative feedback associated with consumption of growth substrate as the population saturates its environment. Solving this equation yields

$$A(t) = \frac{A_{max}A(0)e^{\mu t}}{A_{max}+A(0)(e^{\mu t}-1)} \quad (9),$$

where e is Euler's number and $A(0)$ is the turbidity of the population at $t = 0$ (inoculation). It should be noted that $A(0)$ is too small to be measured and must therefore be calculated by accounting for dilutions. Minor manipulation yields an expression for the growth rate of the

population:

$$\mu = \frac{1}{t}\ln\left(\frac{A_{max}A(t)-A(0)A(t)}{A_{max}A(0)-A(0)A(t)}\right) \quad (10).$$

Thus, by simply measuring $A(0)$, A_{max} and a time series $A(t_1, t_2, ...)$ of turbidity data and plugging these values into Eq. III.10, the intrinsic growth rate of a batch culture may be numerically extracted. Next, taking the limit of either very short growth times or very slow growth rate ($e^{\mu t} << 1$) in Eq. III.9, and noting that $A_{max} >> A(0)$, one obtains the expected exponential growth model:

$$A(t) = A(0)e^{\mu t} \quad (11).$$

Hence, Eq. III.11 is useful for extracting the growth rate for highly inhibited growth profiles (*i.e.* slow growth rate) as well as numerically calculating the doubling time (*i.e.* the short time for the population to double in size) of any population where the growth rate is known. For cultures in this study which grew slowly (*e.g. A. woodii* pure cultures), rearranging Eq. III.11 to

$$\mu = \frac{1}{t}\ln\left(\frac{A(t)}{A(0)}\right) \quad (12)$$

proves sufficient to extract the growth rate. It should be noted that using Eq. III.12 slightly underestimates the growth rate compared to using Eq. III.10 (the logistic model) because of an inherent assumption of no negative feedback in Eq. III.11. To calculate the doubling time

t_D, recognize that $A(t_D) = 2A(0)$, plug this into Eq. III.11, and solve for t_D:

$$t_D = \frac{\ln 2}{\mu} \quad (13),$$

where μ may come from Eqs. III.10 or III.12 as there is little difference in the short-time limit.

III.G.1.f. Confocal fluorescence microscopy (CFM)

Images were obtained by laser scanning confocal microscopy using an Olympus FluoView 1000S spectral scanning microscope equipped with a 60X 1.30 silicon oil immersion lens. Laser excitation at 405 nm was. Emission was collected between 480–580 nm. All images were processed using ImageJ.

III.G.1.g. Gram stain

Gram stain reagents were first prepared, followed by preparation of slide smears and then the Gram staining, as follows. *Crystal violet working solution*: 2.0 g of crystal violet was dissolved in 10 mL ethanol to make a crystal violet stock solution. 1.0 g ammonium oxalate was dissolved in 100 mL water to make a stock solution. Crystal violet working solution was obtained by mixing 1 mL crystal violet stock with 40 mL ammonium oxalate stock and 10 mL water. *Iodine solution*: 1.0 g I_2, 2.0 g KI, and 3.0 g $NaHCO_3$ were dissolved in 300 mL deionized H_2O. *Decolorizer solution*: Mix equal volumes ethanol and acetone. *Safranin O working solution*: 0.25 g Safranin O was dissolved in 10 mL ethanol to make a safranin O stock solution. Safranin O working solution was obtained by mixing 1 mL safranin O stock with 5 mL H_2O.

To prepare slide smears, microscope slides were first cleaned with ethanol and Kimwipes (Kimtech) to remove large debris. A drop of each relevant culture solution was obtained with a syringe and spread evenly in a spot of ~1.5 cm diameter on a clean microscope slide. Slides were placed on a hot plate set at 100 °C to drive off water and help adhere the cellular material for subsequent Gram stain and washing steps.

Enough crystal violet working solution was added to cover each adhered slide smear (~5 drops per smear) and left to stand for ~60 s. This solution was then gently rinsed away with deionized water with care in preserving the adhered smear. Enough iodine solution was then added to cover each adhered slide smear (~5 drops per smear) and left to stand for ~30 s. This solution was also gently rinsed away with deionized water, and excess water was shaken off. The next step was time sensitive: a few drops of decolorizer solution were added so the solution ran down the slide, and this was rinsed away with water after ~5 s—when the decolorizer no longer ran purple (excess decolorization defeats the purpose). If relevant, enough safranin O working solution (counterstain) was then added to cover each adhered slide smear (~5 drops per smear) and left to stand for ~20 s. This solution was gently rinsed away with deionized water, excess water was shaken off, and the slide was air dried for microscopy.

III.G.1.h. Chemical fixation of cultures

Desired volumes of relevant cultures were abstracted anaerobically from culture tubes using a degassed syringe and transferred to sterile, degassed pressure tubes sealed with butyl rubber stoppers. Degassed formaldehyde was added by syringe to a final concentration of 2% (v/v) and these mixtures were allowed to incubate at room temperature overnight. The pressure tubes were unsealed and a portion of the suspensions/aggregates under examination

were transferred to Al foil; these were heated on a hot plate at 100 °C to drive off water and adhere the biological components to the surface. These adhered/fixed samples were sequentially washed lightly with 10 mM phosphate buffered saline and deionized water (twice each) to remove precipitated salts. Finally, the adhered, fixed, washed samples were lyophilized overnight to remove any remaining water for imaging under high vacuum.

III.G.1.i. Scanning electron microscopy (SEM)

Images were obtained with a FEI XL40 SEM at 5.0 kV accelerating voltage, 3.0 spot size, and a working distance of 4.1 mm. No image post processing was used.

III.G.1.j. M3Cs, chronoamperometry (CA), and cyclic voltammetry (CV)

The microbial three-electrode electrochemical reactors (M3Cs) used herein are batch-type, membraneless glass vials with a 15 mL working volume that are sealed with rubber septa. The design is similar to those previously reported.[67] Electrode specifications are as follows. Reference electrode: Ag/AgCl (saturated KCl) bearing a 3.2 mm Vycor frit (Gamry). Counter electrode: coiled 0.25 mm Ti wire (Aldrich), 12 turns. Working electrode: 1 cm × 1 cm × 0.2 cm graphite felt (Alfa Aesar), woven with Ti wire as the electrical lead.

For CA experiments, a Gamry potentiostat (Reference 600, Series G 300 or Series G 750 models) and multiplexer (model ECM8), were used to poise M3C working electrodes at desired potentials. During CA, M3Cs were incubated in the dark at 30 °C with 100 rpm magnetic stirring, while the current outputs were recorded and averaged for 20-second blocks with Gamry software (Framework Version 6.11, Build 2227, 2013).

Before and after CA experiments, CV analyses of electrode-associated cells in M3Cs was conducted with the same hardware with the following parameters: $E_{initial} = E_{final} = -0.6$ V;

E_{vertex} = 0.4 V; scan rate = 0.005 V/s.

III.G.2. Supplementary Figures

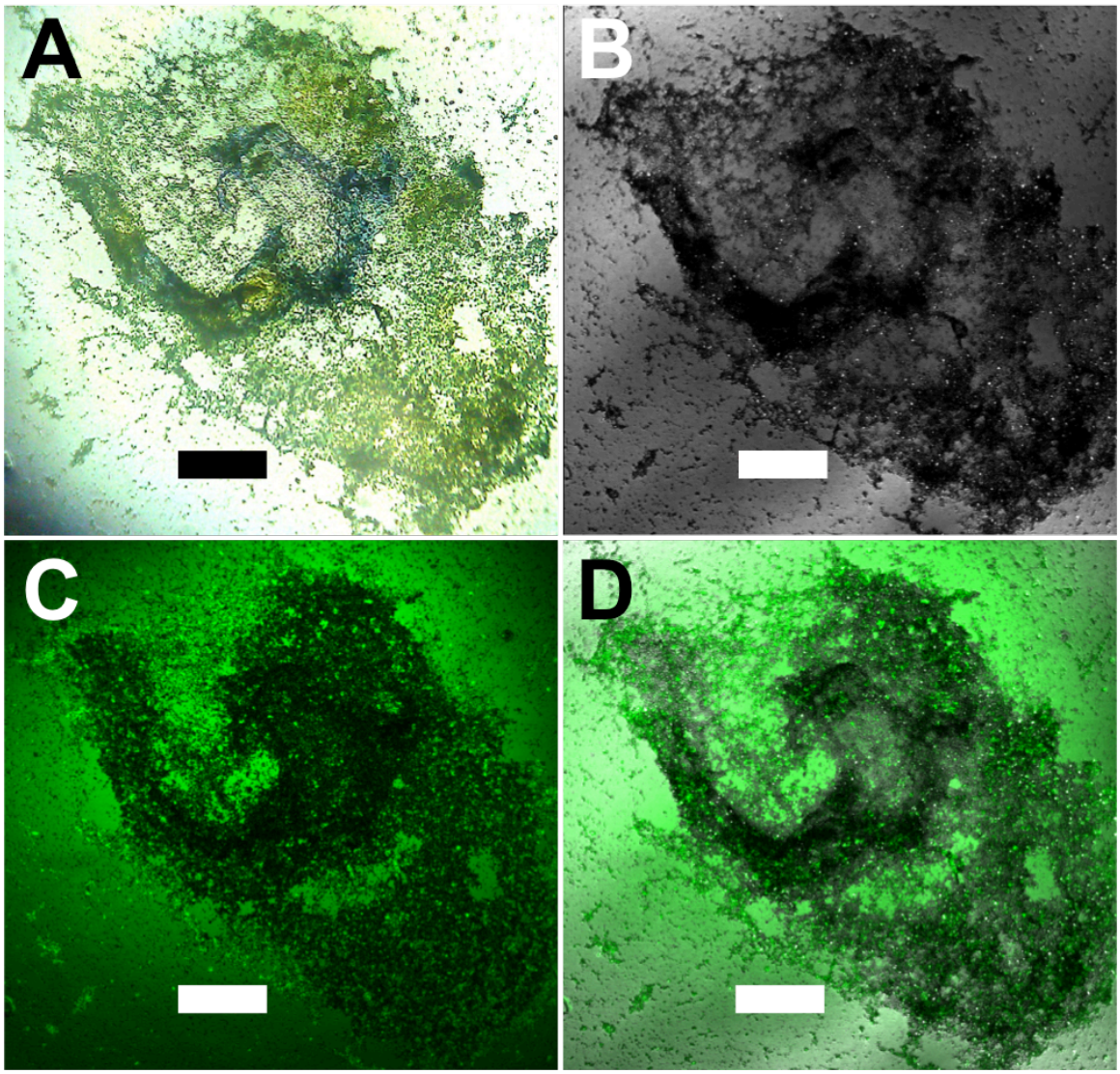

Figure III.S1. Images of a representative Gram-stained aggregate formed in the presence of COE1-4C. Scale bars are 100 μm. (**A**) True-color image. (**B**) Brightfield image. (**C**) Photoluminescence from COE1-4C. Laser excitation: 405 nm. (**D**) Composite overlay of brightfield and photoluminescence images in B and C.

Chapter IV. The Photobioelectrochemical Activity of Thylakoid Bioanodes is Increased *via* Photocurrent Generation and Improved Contacts by Membrane-Intercalating Conjugated Oligoelectrolytes

IV.A. Abstract

The photobioelectrochemical impact of a series of conjugated oligoelectrolytes (COEs) with a systematic progression of chemical structures was elucidated by their direct incorporation into thylakoid bioanodes. In both three-electrode electrochemical cells and bio-solar cell devices, significant anodic performance enhancements ($p < 0.1$) were observed when anodes were modified with certain COEs. Amperometric photocurrent densities increased by up to 2.3-fold for the best COE. In bio-solar cell devices, short-circuit photocurrent increased by up to 1.7-fold and short-circuit dark current increased by up to 1.4-fold, indicating that the best COEs enhance both photocurrent generation and interfacial electron transfer. Trends in these results indicate that the molecular length and pendant charge of COEs differentially contribute to photobioelectrochemical enhancements, and the optimal combination of these features is revealed. Control experiments indicate that COEs augment native thylakoid functionality, as COEs do not have redox activity or undergo chemical degradation

IV.B. Broader Impact

Conjugated oligoelectrolytes (COEs)—water soluble organic semiconducting oligomers with high membrane affinity—are able to modulate biocurrent in various dark-current microbial bioelectrochemical systems. In these systems, COE molecules boost native microbial transmembrane charge transfer processes. However, COEs have not been exploited

for energy harvesting/transfer purposes in practical light-driven biosystems such as thylakoid-based bio-solar cells, self-powered bio- or photo-sensors, and biotransistors. For the first time, we show that COE additives significantly enhance the performance of thylakoid-based devices. The best COEs improve both the dark- and photo-current output of thylakoid bioanodes, implicating a synergistic improvement of electrode contacts and photocurrent generation, and trends in these results reveal key structure-property relationships that guide future use.

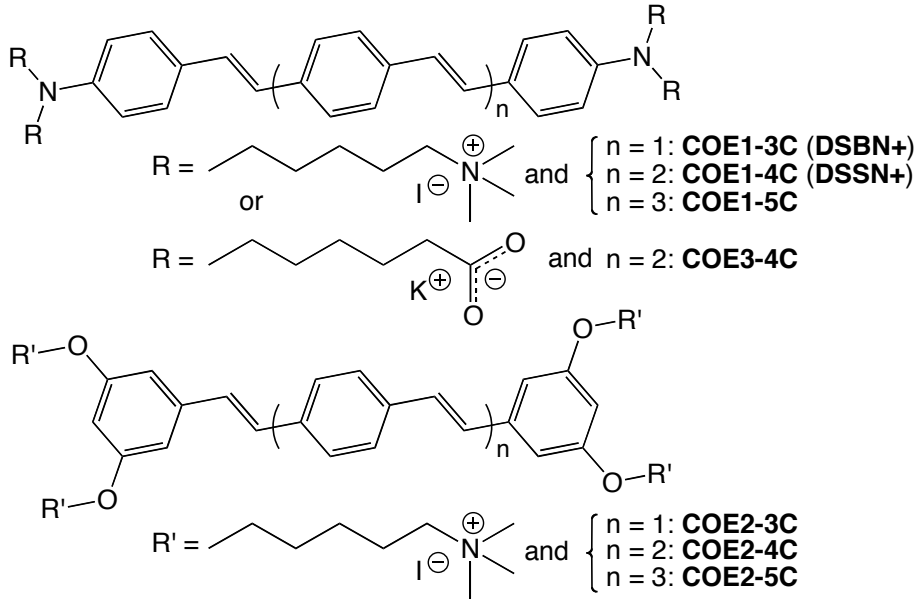

Figure IV.1. The seven COE derivatives used in this study. Note that COE1-3C and COE1-4C may also be referred to as DSBN+ and DSSN+, respectively, as seen previously in the literature.

IV.C. Introduction

Investigations[1–8] of membrane-intercalating conjugated oligoelectrolytes (COEs), such as those in Fig. IV.1, have largely focused on microbial bioelectrochemical systems in the absence of illumination. One study[9] with an illuminated synthetic photovoltaic system reported >93% efficient transmembrane Förster resonance energy transfer[10] (FRET) from

COE1-4C (a.k.a. DSSN+) to gold-electrode-tethered Nile red, and this enabled a 36% higher photocurrent density to be generated upon white light irradiation. COE1-4C was selected for its lipid-phase photoluminescence (PL) spectral overlap with Nile red's absorption; this is feasible because COE1-type molecules' absorption onset (optical gap) and PL are red-shifted relative to COE2-type analogues (Fig. IV.S1), due to D-A-D character.[11–13]

The Nile red synthetic photovoltaic system represents an analogue of the thylakoid membrane of green plants—the most abundant natural biological membrane—that is densely packed (~70% by area[14]) with photo- and electro-active protein complexes that convey energy *via* FRET.[15] One key thylakoid membrane protein complex is Photosystem II (PSII), a photosynthetic reaction center (RC) containing numerous antenna pigment molecules that absorb light and transfer photoexcitation energy to the P680 chlorophyll *a* (chl*a*) special pair at >90% efficiency.[16–21] This generates the P680* excited state (the primary electron donor in photosynthesis[16,22]) that is rapidly oxidized to $P680^+$ (the strongest naturally-occurring biological oxidant[16]) at near-unity quantum efficiency.[23] $P680^+$ drives water oxidation—evolving O_2, $4H^+$, and $4e^-$—in the metalloenzyme core of PSII,[15,18,21] so PSII is the primary source of usable electrons in thylakoid membranes.

In addition to PSII, Photosystem I (PSI) and the RCs from photosynthetic bacteria also exhibit quantum efficiencies approaching unity for photoexcitation energy transduction and charge separation.[24–27] There has therefore been keen effort in isolating these RCs and interfacing them with electrodes for photobioelectrochemical devices.[28–36] A related method (that is utilized in this chapter) is the electrode immobilization of whole thylakoid membranes that naturally contain PSI and PSII. This requires fewer purification steps and allows better RC stability at the expense of some charge transfer efficiency. Herein,

immobilization is accomplished *via* silica encapsulation with catalase,[37] though thylakoid membranes may also be "wired" to osmium redox polymers,[38] suspended with gold nanoparticles and quinones,[39] frozen in an albumin matrix,[40] incorporated in electrochemical cells with various mediators,[41] or tethered to multiwalled carbon nanotubes (MWCNTs).[42] These approaches, and more, have been critically reviewed.[43,44]

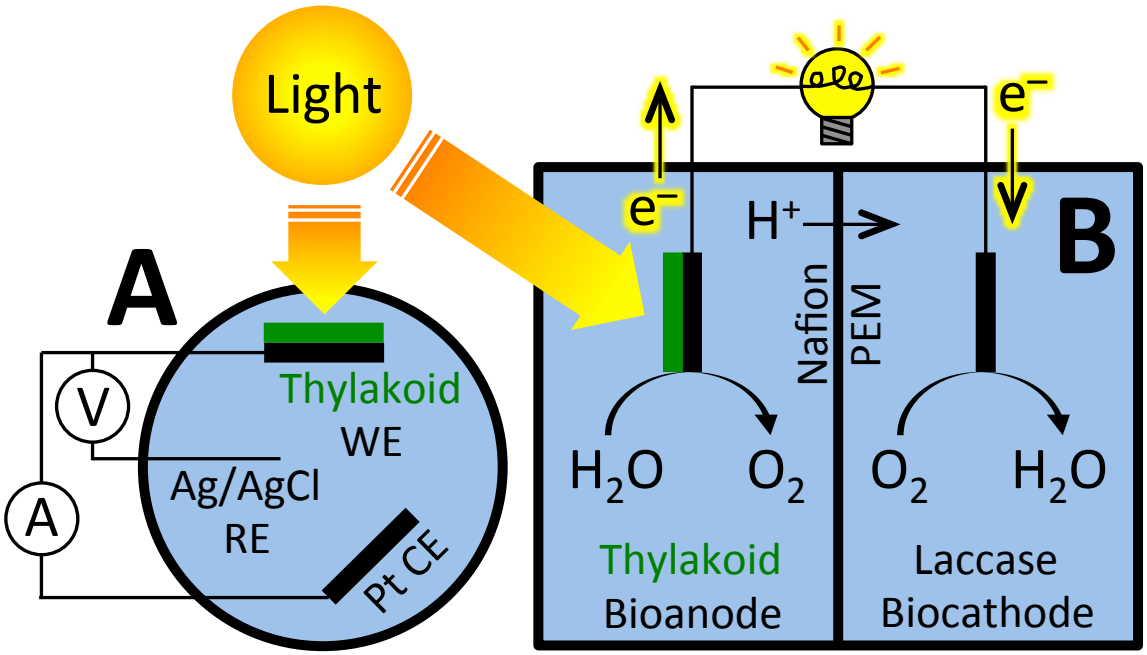

Figure IV.2. A schematic diagram of thylakoid-bioanode-based device architectures used for this work. (**A**) The three-electrode electrochemical cell. WE: Working electrode; RE: Reference electrode; CE: Counter electrode. Note that the WE and CE are analogous to an anode and cathode, respectively. Also note that a potential is poised between the WE and RE, while current is allowed to flow at the WE and CE, as controlled by a potentiostat (not pictured). (**B**) The two-chamber bio-solar cell. A Nafion® proton exchange membrane (PEM) allows for charge balance during electron flow. Note that the thylakoid bioanode is identical to the WE in the three-electrode device.

Two-compartment bio-solar cells constructed from spinach thylakoid bioanodes and laccase biocathodes were recently reported.[45,46] The thylakoid active layer absorbs light and generates electrons that are harvested as anodic photocurrent. This platform has been used to investigate additions of carbon quantum dots that sensitize thylakoid bio-solar cells[47] by increasing the direct electron transfer surface area of the electrode (increased current

collection) and increasing absorbance and photoluminescence intensities (enhanced light harvesting). These devices have also been modified with the discussed quinone derivatives[39] and MWCNTs.[48] The thylakoid bioanodes of these devices have practical utility in biosensors,[40,49–52] photosensors,[53] and biotransistors.[54] Thus, improving their electrochemical performance is anticipated to enhance their sensitivity and applicability across a wide range of applications.

Herein, thylakoid bioanodes have been modified with the seven derivatives in Fig. IV.1 by directly adding COEs to the thylakoid suspensions during electrode construction. The resulting thylakoid/COE electrodes were employed in both three-electrode electrochemical cells (Fig. IV.2 A) and bio-solar cells (Fig. IV.2 B). As can be seen in the Fig. IV.2 schematic, the two-compartment design of the bio-solar cells allows use of two solutions so that COEs are prevented by the PEM from interacting with the cathode.[45] Because of the strong affinity of COEs for lipid bilayers,[1,55] it is reasonable to expect that thylakoid membrane proteins (*e.g.* PSII) and their bound pigments may be spatially proximate[56] to intercalated COE molecules and experience COE-induced optoelectronic and/or diffusion-related[57] changes. However, due to the essential influence of light reactions in this novel thylakoid/COE-testing platform, COEs are not necessarily expected to evoke the same functionality or electrical outputs as have previously arisen in non-illuminated microbial systems.[1–8] Therefore, this study is an essential conceptual steppingstone towards understanding practical utility of COEs in light-driven systems.

The chapter is organized as follows. First, thylakoid/COE electrodes are characterized and optimized in a three-electrode device. Then, with all seven COE derivatives, optimized electrodes are used for photoamperometry in similar three-electrode devices and

subsequently employed in bio-solar cell devices. The resulting device outputs are then statistically compared to establish photobioelectrochemical structure-property relationships. These experiments offer insight into the ideal combination of molecular structure and pendant charge functionality of COEs for enhancing the performance of practical thylakoid-bioanode-based devices.

IV.D. Results and Discussion

IV.D.1. Electrochemical characterization of thylakoid bioanodes and optimization of COE concentration

In a three-electrode device (see Fig. IV.2 A, previous work,[46] and Experimental), thylakoid/COE electrodes containing 10 μM of each COE were first examined using cyclic voltammetry (CV) to identify electrochemical differences relative to unmodified thylakoid electrodes.

An example of the CV data is shown in Fig. IV.S2, specifically comparing the potential dependence of current output from an unmodified thylakoid electrode to a representative thylakoid/COE1-4C electrode. This was repeated for all tested COEs (not shown), and these data indicate that essentially no voltammetric difference exists between thylakoid/COE electrodes and unmodified thylakoid electrodes. Therefore, COEs are not contributing to anodic current *via* redox activity or chemical degradation. A small, reversible redox wave is identifiable in all CV traces at a central potential of ~0.35 V for thylakoid electrochemistry; all subsequent amperometric experiments were therefore conducted at E = 0.45 V to allow oxidation of this redox species.

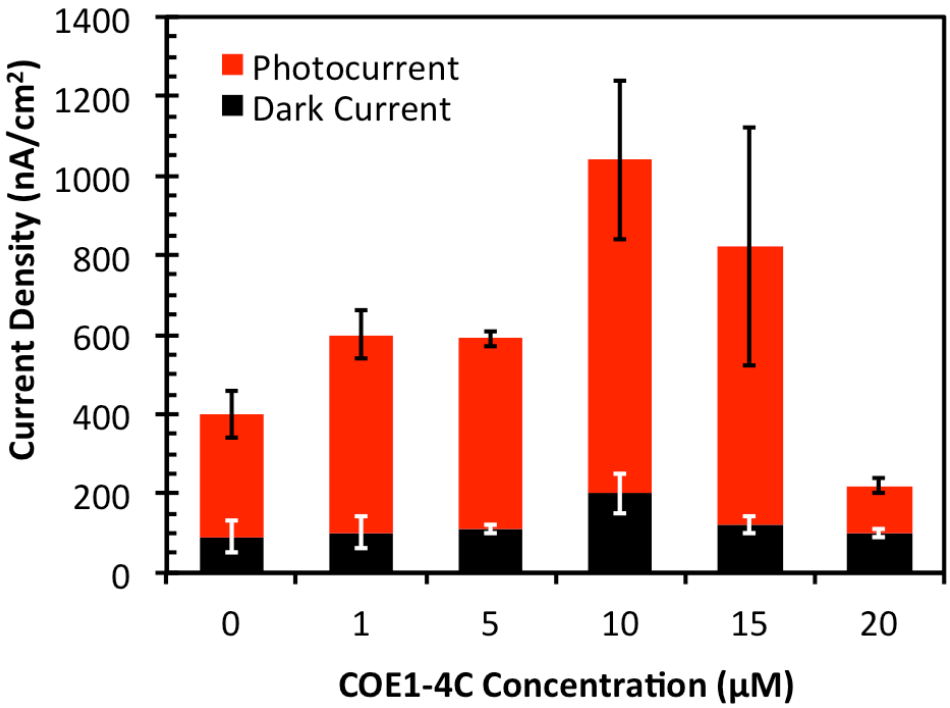

Figure IV.3. Optimization of COE concentration for maximal current output. Measurements were conducted by amperometry at a poised potential of E = 0.45 V vs. Ag/AgCl in 0.1 M, pH = 7.4 phosphate buffer. Photocurrent and dark current are presented stacked to illustrate the light current produced for each experimental condition (light current = dark current + photocurrent). Error bars represent ± 1 std. dev.

Using a similar three-electrode device, the COE concentration that maximizes current output from thylakoid/COE electrodes was identified amperometrically using COE1-4C. These experiments provide the current generated during a specific period of time (see Experimental). As can be seen in Fig. IV.3, a range of 1–20 μM COE1-4C was tested, which mimics the range typically explored in previous biological studies.[3–5,58] This range is equivalent to 50–1000 pmol COE per 50 μL solution, or 100–2000-fold less than the chlorophyll concentration in the thylakoid suspensions used for constructing the electrodes (see Experimental). The resulting amperometric light-, dark-, and photocurrent responses are summarized in Fig. IV.3. Dark current density is not significantly affected by the COE1-4C concentration, aside from a small increase at 10 μM COE1-4C. However, photocurrent density changes with COE1-4C concentration, as it increases slightly for 1 μM and 5 μM,

maximizes at 10 µM, remains elevated at 15 µM, and then at 20 µM falls below unmodified (0 µM) thylakoid electrodes. From these data, 10 µM was chosen as the standard concentration for subsequent experiments.

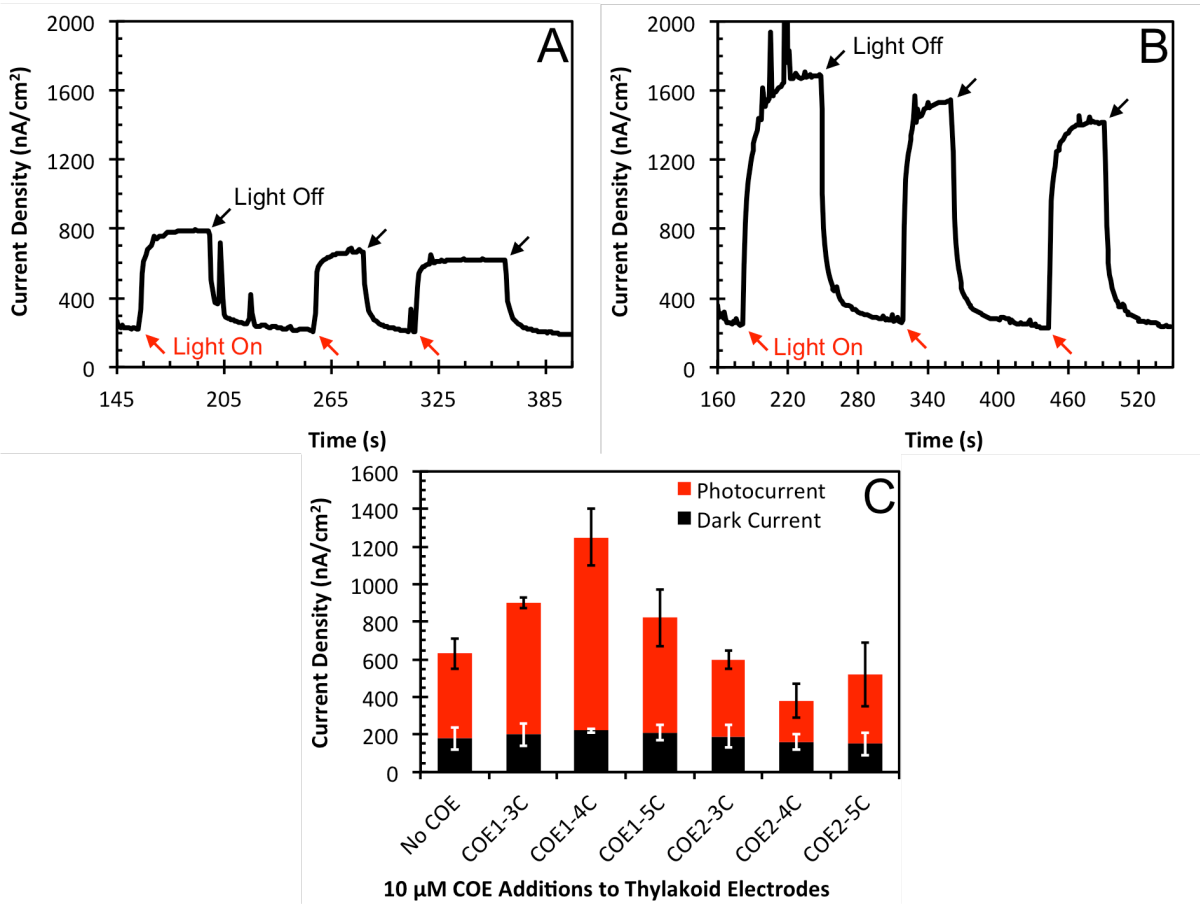

Figure IV.4. Amperometric current measurements. All data were collected at 0.45 V vs. Ag/AgCl in 0.1 M, pH = 7.4 phosphate buffer. Red arrows indicate when the light was turned on and black arrows when it was turned off. (A) Representative time course of current density output from an unmodified (No COE) thylakoid electrode under modulated illumination. (B) Representative time course of current density output from a thylakoid/COE1-4C electrode under modulated illumination. (C) Summary of triplicate average current density outputs from thylakoid and thylakoid/COE electrodes for all tested COEs. In all cases, light current is equivalent to the sum of photocurrent (red) and dark current (black). Error bars are ± 1 std. dev.

IV.D.2. Amperometry reveals COE-induced thylakoid photocurrent enhancements

In Fig. IV.4, a representative example of amperometric current output from a 3-electrode device for an unmodified thylakoid electrode (Fig. IV.4 A) is compared to the current output

from a representative electrode modified with COE1-4C (Fig. IV.4 B). The COE1-4C addition increases light current ("Light On" state) by approximately 2-fold, while dark current ("Light Off" state) is essentially unchanged; photocurrent is light minus dark current, so photocurrent increases about 3-fold in this specific instance. Triplicate average data and statistical significance for all COEs is summarized in Fig. IV.4 C and Table 1 and discussed below.

From Table 1, three COE derivatives have a statistically significant effect on thylakoid light current output (at > 90% significance): COE1-3C, COE1-4C, and COE2-4C. Relative to unmodified thylakoids, addition of COE1-3C provides a 1.4 ± 0.2-fold increase in light current (p = 0.061), and COE1-4C addition enables a 2.0 ± 0.5-fold increase in light current (p = 0.013). However, COE2-4C makes the device worse, decreasing light current to 0.6 ±

Table IV.1. Amperometric current density measurements at E = 0.45 V vs. Ag/AgCl with 10 µM COE additions in 0.1 M pH = 7.4 phosphate buffer

	Light current			Dark current			Photocurrent		
10 µM COE additions	Density (nA cm^{-2})	Fold change	p-Value[a]	Density (nA cm^{-2})	Fold change	p-Value [a]	Density (nA cm^{-2})	Fold change	p-Value[a]
No COE	630 ± 120	–	1.000	180 ± 60	–	1.000	450 ± 80	–	1.000
COE1-3C	900 ± 20	1.4 ± 0.2	0.061[b]	200 ± 60	1.1 ± 0.5	0.704	700 ± 30	1.6 ± 0.2	0.037[c]
COE1-4C	1250 ± 160	2.0 ± 0.5	0.013[c]	220 ± 10	1.2 ± 0.3	0.373	1030 ± 150	2.3 ± 0.8	0.009[d]
COE1-5C	820 ± 170	1.3 ± 0.4	0.212	210 ± 40	1.2 ± 0.4	0.523	610 ± 150	1.4 ± 0.5	0.202
COE2-3C	600 ± 100	1.0 ± 0.2	0.761	190 ± 60	1.1 ± 0.5	0.848	410 ± 50	0.9 ± 0.2	0.516
COE2-4C	390 ± 120	0.6 ± 0.2	0.070[b]	160 ± 40	0.9 ± 0.4	0.664	220 ± 90	0.5 ± 0.2	0.045[c]
COE2-5C	530 ± 200	0.8 ± 0.3	0.512	150 ± 60	0.8 ± 0.4	0.573	370 ± 170	0.8 ± 0.4	0.538
COE3-4C	790 ± 70	1.3 ± 0.2	0.140	240 ± 60	1.3 ± 0.6	0.288	540 ± 90	1.2 ± 0.3	0.286

[a] Calculated with 2-tailed unequal variance t-tests comparing mean current densities of thylakoid/COE electrodes to unmodified thylakoid electrodes. [b] Current density different than unmodified thylakoids at ≥ 90% significance (p < 0.1) [c] Current density different than unmodified thylakoids at ≥ 95% significance (p < 0.05) [d] Current density different than unmodified thylakoids at ≥ 99% significance (p < 0.01)

0.2-fold (p = 0.070). Dark current of thylakoid/COE electrodes is not statistically significantly different than the unmodified thylakoid electrodes for any tested COEs.

Photocurrent is statistically significantly higher (at ≥ 95% significance) with COE1-4C (2.3 ± 0.8-fold, p = 0.009) and COE1-3C (1.6 ± 0.2-fold, p = 0.037). This agrees with light current data because dark current is statistically unchanged. It is also noteworthy that by this 3-electrode technique, COE1-3C, COE1-4C, COE1-5C, and COE3-4C qualitatively increase the average measured photocurrent while COE2-3C, COE2-4C, and COE2-5C decrease it. This trend hints at COE molecular structural features playing a relevant photobioelectrochemical role that is further exposed in bio-solar cell experiments, below.

IV.D.3. Bio-solar cell experiments reveal statistically significant COE photobioelectrochemical structure-property relationships

The same bioanode electrodes were accordingly employed in two-compartment bio-solar cells[45] to further probe whether the amperometric trends hold and whether COEs improve (a) photocurrent generation within the thylakoids or (b) the thylakoid-electrode contact for current harvesting—or a combination of (a) and (b). An example of the obtained solar cell data is shown in Fig. IV.5, comparing linear polarization (LP) traces of unmodified thylakoid bio-solar cells (Fig. IV.5 A) to the best-performing thylakoid/COE1-4C devices (Fig. IV.5 B).

Four COE derivatives afford a statistically significant increase to the bio-solar cell short circuit light current (light-J_{sc}): COE1-3C, COE1-4C, COE1-5C, and COE2-5C. Light-J_{sc} is the sum of the contributions from short circuit dark current (dark-J_{sc}) and short circuit photocurrent (photo-J_{sc}). The best overall performance enhancement is afforded by COE1-4C, with a statistically significant 1.4-fold increase in each of light-J_{sc}, dark-J_{sc}, and photo-J_{sc}

(p = 0.003, 0.005, and 0.053, respectively). This indicates that COE1-4C enhances *both* photocurrent generation and the thylakoid-electrode contact.

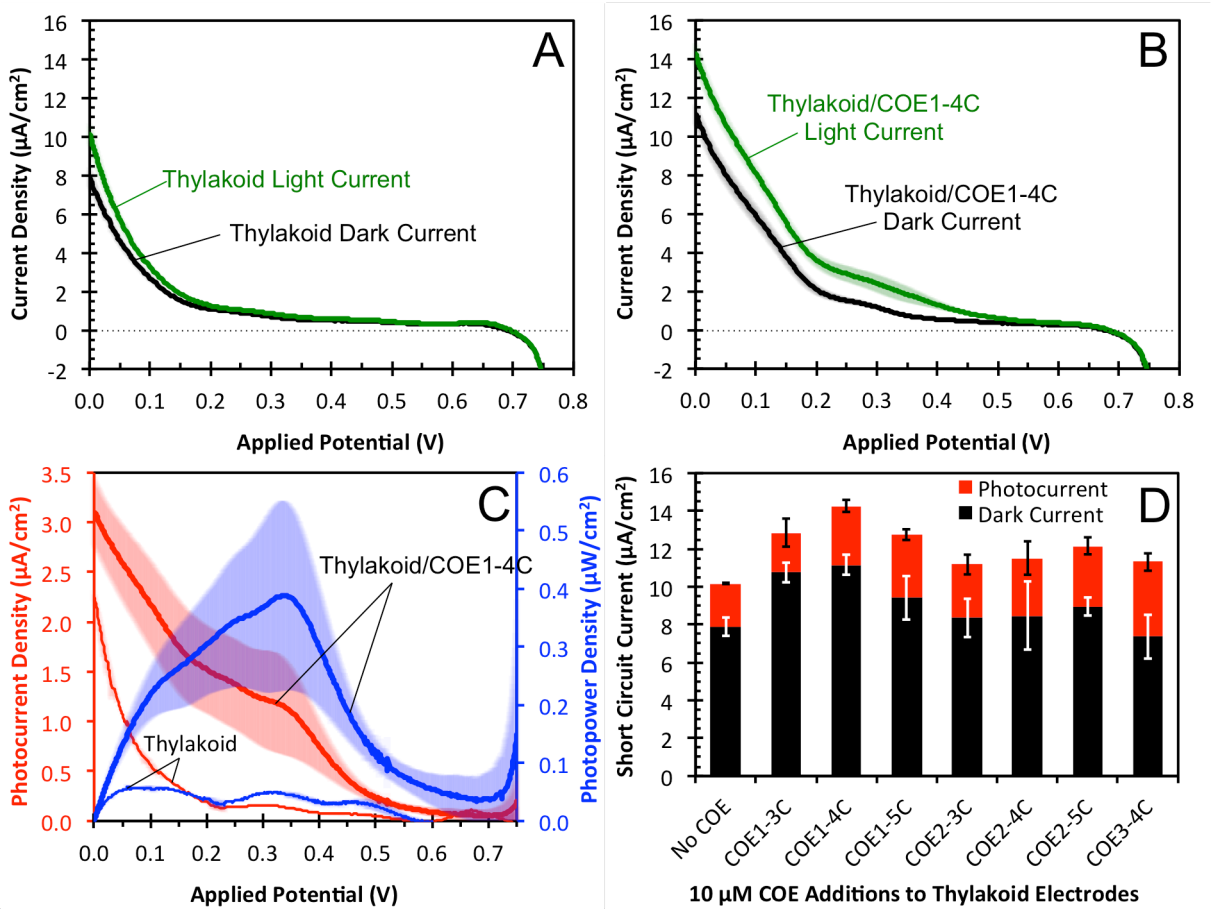

Figure IV.5. Bio-solar cell data from linear polarization. Devices were operated with 0.1 M pH = 7.4 phosphate buffer in the anode chamber and 0.1 M, pH = 5.5 Na-citrate buffer in the cathode chamber. Colored shaded regions surrounding plotted data represent ± 1 std. dev. at each potential (in some instances, the error is smaller than the width of the line). Potential was swept at 5 mV/s. (**A**) Average dark and light *J-V* curves for unmodified thylakoid bio-solar cells. (**B**) Average dark and light *J-V* curves for the highest-performing thylakoid/COE1-4C bio-solar cells. (**C**) Average photocurrent density (red) and photopower density (blue) measurements as a function of applied potential for devices in A and B. Here, photocurrent was calculated by subtracting dark current from light current for each of three devices and then taking the average. Photopower density is provided by $P = JV$. (**D**) Summary of dark-J_{sc} (black), photo-J_{sc} (red), and light-J_{sc} (red + black) for thylakoid and thylakoid/COE bio-solar cells for all tested COEs. Error bars represent ± 1 std. dev.

It is worth noting that the dark current in Fig. IV.5 B is also increased relative to the dark current in Fig. IV.5 A at intermediate potentials in the range 0 V < E ≤ 0.35 V. This increase in current indicates a decrease in device resistance that is consistent with the COE improving

the thylakoid-electrode electrical contact. Fig. IV.5 C displays photo-J_{sc} (red) and photo-power density (blue) for these representative devices, and in this instance, COE1-4C increases photopower about an order of magnitude at the maximum power point near +0.35 V applied potential. COE1-3C, COE1-5C, and COE2-5C also furnish statistically significant increases in light-J_{sc} of 1.3 ± 0.2-fold (p = 0.066), 1.3 ± 0.1-fold (p = 0.030), and 1.2 ± 0.1-fold (p = 0.022), respectively. J_{sc} data is summarized in Fig. IV.5 D, and a numerical summary with statistical significance of all data may be found in Table 2.

For COE1-3C, the increase in light-J_{sc} stems primarily from a 1.4 ± 0.1-fold (p = 0.006)

Table IV.2. Bio-solar cell *J-V* characteristics by linear polarization at 5 mV/s with 10 µM COE additions

		10 µM COE Additions to Thylakoids							
		No COE	COE1-3C	COE1-4C	COE1-5C	COE2-3C	COE2-4C	COE2-5C	COE3-4C
Light current	V_{oc} (mV)	699 ± 7	692 ± 6	691 ± 2	698 ± 4	684 ± 4	686 ± 1	682 ± 2	688 ± 7
	p-value[a]	1.000	0.280	0.197	0.844	0.048[c]	0.086[b]	0.056[b]	0.150
	J_{sc} (µA cm^{-2})	10.2 ± 0.5	12.9 ± 1.1	14.3 ± 0.6	12.7 ± 1.0	11.2 ± 1.2	11.5 ± 1.0	12.1 ± 0.6	11.3 ± 1.0
	Fold Change	-	1.3 ± 0.2	1.4 ± 0.1	1.3 ± 0.1	1.1 ± 0.1	1.1 ± 0.1	1.2 ± 0.1	1.1 ± 0.1
	p-value[a]	1.000	0.066[b]	0.003[d]	0.030[c]	0.309	0.138	0.022[c]	0.181
Dark current	V_{oc} (mV)	695 ± 11	687 ± 9	688 ± 4	695 ± 6	683 ± 5	671 ± 3	668 ± 17	674 ± 12
	p-value[a]	1.000	0.402	0.409	1.000	0.228	0.068[b]	0.104	0.112
	J_{sc} (µA cm^{-2})	7.9 ± 0.5	10.8 ± 0.5	11.2 ± 0.5	9.4 ± 1.2	8.4 ± 1.0	8.5 ± 1.8	9.0 ± 0.5	7.4 ± 1.2
	Fold Change	-	1.4 ± 0.1	1.4 ± 0.1	1.2 ± 0.2	1.1 ± 0.2	1.1 ± 0.3	1.1 ± 0.1	0.9 ± 0.2
	p-value[a]	1.000	0.006[d]	0.004[d]	0.168	0.541	0.649	0.053[b]	0.547
Photo-current	J_{sc} (µA cm^{-2})	2.3 ± 0.1	2.1 ± 0.8	3.1 ± 0.3	3.3 ± 0.3	2.8 ± 0.5	3.0 ± 0.9	3.2 ± 0.4	3.9 ± 0.5
	Fold Change	-	0.9 ± 0.3	1.4 ± 0.2	1.5 ± 0.2	1.2 ± 0.3	1.3 ± 0.5	1.4 ± 0.3	1.7 ± 0.4
	p-value[a]	1.000	0.716	0.053[b]	0.024[c]	0.218	0.269	0.069[b]	0.027[c]

[a] Calculated from 2-tailed unequal variance t-tests comparing thylakoid/COE electrodes to unmodified thylakoid electrodes. [b] J_{sc} or V_{oc} different than unmodified thylakoids at ≥ 90% significance ($p < 0.1$). [c] J_{sc} or V_{oc} different than unmodified thylakoids at ≥ 95% significance ($p < 0.05$). [c] J_{sc} or V_{oc} different than unmodified thylakoids at ≥ 99% significance ($p < 0.01$).

increase in dark-J_{sc} and no significant change in photo-J_{sc}; this implicates an improved electrode contact as the primary reason for current enhancement. For COE1-5C, the increase in light-J_{sc} arises from a 1.5 ± 0.2-fold (p = 0.024) increase in photo-J_{sc}, but no change to dark-J_{sc}. These results suggest that COE1-5C enables enhanced photocurrent generation. It is also worth noting that for these COE1-type derivatives, the open circuit voltage under illumination (light-V_{oc}) and in the dark (dark-V_{oc}) remain statistically indistinguishable. Finally, for COE2-5C, the 1.2 ± 0.1-fold (p = 0.022) light-J_{sc} increase results from a 1.4 ± 0.3-fold (p = 0.069) increase in photo-J_{sc}, and a 1.1 ± 0.1-fold (p = 0.053) increase in dark-J_{sc}, again implicating enhanced photocurrent generation and thylakoid-electrode contacts.

For COE2-3C and COE2-4C, average dark-J_{sc} and photo-J_{sc} increase slightly, but it is not statistically significant. For COE3-4C, the lack of change in light-J_{sc} appears to occur because of offsetting positive and negative effects: dark-J_{sc} decreases slightly, concomitant with a statistically significant 1.7 ± 0.4-fold (p = 0.027) increase in photo-J_{sc}, eliciting the highest photocurrent of any COE tested (3.9 ± 0.5 μA/cm^2).

From Table 2, three photobioelectrochemical structure-property relationships emerge: (i) COE1-3C, COE1-4C, and COE1-5C cause light-J_{sc} to increase at 95% significance. The key difference in these molecules is that the chromophore structures bear distal N heteroatoms (Fig. IV.1). The efficacy of COE1-type molecules over COE2-type points to a relevant photobioelectrochemical role for the N atoms. (ii) Shorter COEs (COE1-3C, COE1-4C) allow significantly better dark current collection by the bioanode, presumably by directly modifying the thylakoid-electrode interface (*via* membrane intercalation[55]), thereby improving the contact. Longer COEs (COE1-4C, COE1-5C, COE2-5C, COE3-4C) enhance photocurrent generation. COE1-4C appears to have the best mixture of these length-

dependent characteristics. (iii) Structurally, COE3-4C and COE1-4C differ only in their pendant charged groups. Whereas COE1-4C bears cationic groups and significantly increases thylakoid bioanode current outputs, COE3-4C bears anionic groups and only increases photocurrent outputs. This signifies that the pendant cationic moieties impact increased dark current outputs in this system.

IV.E. Conclusions

For the first time, certain COEs have been shown to improve electrical contacts and photocurrent generation in thylakoid-membrane-based photobioelectrochemical devices. The chemical features associated with these enhancements have been determined by systematic variation of the added COE molecules, and we imagine that these results have the potential to extend to other subcellular light-driven systems. COE1-4C appears to have the most ideal combination of molecular structure and pendant charge functionality, making it the recommended derivative for use in practical photobioelectrochemical devices. Amperometric and bio-solar cell data highlight several conclusions regarding these COE properties, as follows.

Within the class of compounds studied here, the molecular length of COE1-4C appears to be the most ideally suited to enhance thylakoid dark- and photo-current outputs, as compared to its shorter and longer counterparts (COE1-3C and COE1-5C, respectively). This agrees with similar observations in microbial systems that produce dark current.[1,4] Lipid bilayer modelling studies help rationalize this, suggesting that COE1-3C may aggregate and harmfully pinch a membrane to a greater degree than COE1-4C.[55] However, considerations of molecular length are insufficient as a direct design element for estimating biocurrent performance impact. Consider that COE1-4C and COE2-4C have similar lengths, and yet we

point out that their photobioelectrochemical effects on thylakoids are different. Due to optoelectronic differences in their chromophores, these molecules may have tendencies to accumulate in subtly different locations within the complex thylakoid membrane suspensions, thereby differentiating their ability to influence the thylakoid-electrode contact. An improved contact when using COE1-type molecules, as compared to COE2-type molecules, would aid in photocurrent collection, thus enabling the observed enhanced photobioelectrochemical energy conversion. The situation between COE1-4C and COE3-4C, which also have similar dimensions, is discussed in more detail below.

COE1-4C bears quaternary ammonium pendant groups, while COE3-4C bears carboxylate pendant groups, and both molecules have the same π-conjugated phenylenevinylene chromophore with distal N atoms. COE1-4C and COE3-4C will therefore have opposite coulombic interactions with charged surfaces, while keeping the conjugated segment constant. The thylakoid membrane surface carries a net negative charge from carboxylate moieties,[61] so thylakoid/COE3-4C coulombic repulsion should limit COE3-4C incorporation in the membrane. This reasoning is bolstered by new research showing that COE3-4C does not spontaneously intercalate into bacterial membranes (which are also negatively charged), nor does it enhance dark current extraction from bacteria, and these appear to be strongly correlated.[8] Indeed, in this present work, COE3-4C does not increase the thylakoid dark current (while COE1-4C does), and yet both COE1-4C and COE3-4C increase photocurrent. These results are consistent with the proposed differences in the location of accumulation in the thylakoid matrix as a function of molecular structure.

IV.F. References

1. Garner, L. E. *et al.* Modification of the optoelectronic properties of membranes via

insertion of amphiphilic phenylenevinylene oligoelectrolytes. *J. Am. Chem. Soc.* **132,** 10042–52 (2010).
2. Garner, L. E., Thomas, A. W., Sumner, J. J., Harvey, S. P. & Bazan, G. C. Conjugated oligoelectrolytes increase current response and organic contaminant removal in wastewater microbial fuel cells. *Energy Environ. Sci.* **5,** 9449–9452 (2012).
3. Wang, V. B. *et al.* Improving charge collection in Escherichia coli-carbon electrode devices with conjugated oligoelectrolytes. *Phys. Chem. Chem. Phys.* **15,** 5867–72 (2013).
4. Hou, H. *et al.* Conjugated Oligoelectrolytes Increase Power Generation in E. coli Microbial Fuel Cells. *Adv. Mater.* **25,** 1593–7 (2013).
5. Thomas, A. W. *et al.* A lipid membrane intercalating conjugated oligoelectrolyte enables electrode driven succinate production in Shewanella. *Energy Environ. Sci.* **6,** 1761 (2013).
6. Wang, V. B. *et al.* Comparison of flavins and a conjugated oligoelectrolyte in stimulating extracellular electron transport from Shewanella oneidensis MR-1. *Electrochem. commun.* **41,** 55–58 (2014).
7. Kirchhofer, N. D. *et al.* The conjugated oligoelectrolyte DSSN+ enables exceptional coulombic efficiency via direct electron transfer for anode-respiring Shewanella oneidensis MR-1-a mechanistic study. *Phys. Chem. Chem. Phys.* **16,** 20436–43 (2014).
8. Thomas, A. W., Catania, C., Garner, L. E. & Bazan, G. C. Pendant ionic groups of conjugated oligoelectrolytes govern their ability to intercalate into microbial membranes. *Chem. Commun.* **51,** 9294–9297 (2015).
9. Lee, Y., Yang, I., Lee, J. & Hwang, S. Enhanced Photocurrent Generation by Forster Resonance Energy Transfer between Phospholipid-Assembled Conjugated Oligoelectrolytes and Nile Red. *J. Phys. Chem. C* **117,** 3298–3307 (2013).
10. Förster, T. Zwischenmolekulare Energiewanderung und Fluoreszenz. *Ann. Phys.* **6,** 55–75 (1948).
11. Beaujuge, P., Amb, C. & Reynolds, J. R. Spectral engineering in π-conjugated polymers with intramolecular donor−acceptor interactions. *Acc. Chem. Res.* **43,** 1396–1407 (2010).
12. Choi, S. H. & Frisbie, C. D. Enhanced hopping conductivity in low band gap donor-acceptor molecular wires Up to 20 nm in length. *J. Am. Chem. Soc.* **132,** 16191–201 (2010).
13. Coughlin, J. E., Henson, Z. B., Welch, G. C. & Bazan, G. C. Design and synthesis of molecular donors for solution-processed high-efficiency organic solar cells. *Acc. Chem. Res.* **47,** 257–70 (2014).
14. Kirchhoff, H., Mukherjee, U. & Galla, H. Molecular Architecture of the Thylakoid Membrane: Lipid Diffusion Space for Plastoquinone. *Biochemistry* **41,** 4872–4882 (2002).
15. Dau, H. & Sauer, K. Exciton equilibration and Photosystem II exciton dynamics - a fluorescence study on Photosystem II membrane particles of spinach. *Biochim. Biophys. Acta - Bioenerg.* **1273,** 175–190 (1996).
16. Dau, H. & Zaharieva, I. Principles, efficiency, and blueprint character of solar-energy conversion in photosynthetic water oxidation. *Acc. Chem. Res.* **42,** 1861–70 (2009).
17. Krause, G. & Weis, E. Chlorophyll Fluorescence and Photosynthesis: The Basics. *Annu. Rev. Plant Physiol. Plant Mol. Biol.* **42,** 313–349 (1991).

18. Raszewski, G., Diner, B. A., Schlodder, E. & Renger, T. Spectroscopic properties of reaction center pigments in photosystem II core complexes: revision of the multimer model. *Biophys. J.* **95,** 105–19 (2008).
19. Kouřil, R., Dekker, J. P. & Boekema, E. J. Supramolecular organization of photosystem II in green plants. *Biochim. Biophys. Acta* **1817,** 2–12 (2012).
20. Standfuss, J., Terwisscha van Scheltinga, A. C., Lamborghini, M. & Kühlbrandt, W. Mechanisms of photoprotection and nonphotochemical quenching in pea light-harvesting complex at 2.5 A resolution. *EMBO J.* **24,** 919–28 (2005).
21. Renger, T. & Schlodder, E. Optical properties, excitation energy and primary charge transfer in photosystem II: theory meets experiment. *J. Photochem. Photobiol. B.* **104,** 126–41 (2011).
22. Grabolle, M. & Dau, H. Energetics of primary and secondary electron transfer in Photosystem II membrane particles of spinach revisited on basis of recombination-fluorescence measurements. *Biochim. Biophys. Acta* **1708,** 209–18 (2005).
23. Booth, P. J. *et al.* Observation of multiple radical pair states in photosystem 2 reaction centers. *Biochemistry* **30,** 7573–7586 (1991).
24. Wraight, C. A. & Clayton, R. K. The absolute quantum efficiency of bacteriochlorophyll photooxidation in reaction centres of Rhodopseudomonas spheroides. *Biochim. Biophys. Acta* **333,** 246–260 (1974).
25. Hoff, A. J. & Deisenhofer, J. Photophysics of photosynthesis. Structure and spectroscopy of reaction centers of purple bacteria. *Phys. Rep.* **287,** 1–247 (1997).
26. Pålsson, L. O. *et al.* Energy transfer and charge separation in photosystem I: P700 oxidation upon selective excitation of the long-wavelength antenna chlorophylls of Synechococcus elongatus. *Biophys. J.* **74,** 2611–2622 (1998).
27. Hogewoning, S. W. *et al.* Photosynthetic Quantum Yield Dynamics: From Photosystems to Leaves. *Plant Cell* **24,** 1921–1935 (2012).
28. LeBlanc, G., Gizzie, E., Yang, S., Cliffel, D. E. & Jennings, G. K. Photosystem I Protein Films at Electrode Surfaces for Solar Energy Conversion. *Langmuir* **30,** 10990–11001 (2014).
29. Yaghoubi, H. *et al.* The role of gold-adsorbed photosynthetic reaction centers and redox mediators in the charge transfer and photocurrent generation in a bio-photoelectrochemical cell. *J. Phys. Chem. C* **116,** 24868–24877 (2012).
30. Yaghoubi, H. *et al.* Hybrid Wiring of the Rhodobacter sphaeroides Reaction Center for Applications in Bio-photoelectrochemical Solar Cells. *J. Phys. Chem. C* **118,** 23509–23518 (2014).
31. Yaghoubi, H. *et al.* Large Photocurrent Response and External Quantum Efficiency in Biophotoelectrochemical Cells Incorporating Reaction Center Plus Light Harvesting Complexes. *Biomacromolecules* **16,** 1112–1118 (2015).
32. Das, R. *et al.* Complexes in Solid-State Electronic Devices Integration of Photosynthetic Protein Molecular Complexes in Solid-State Electronic Devices. *Nano Lett.* **4,** 1079–1083 (2004).
33. Saboe, P. O. *et al.* Two-Dimensional Protein Crystals for Solar Energy Conversion. *Adv. Mater.* **26,** 7064–7069 (2014).
34. Katz, E. Application of bifunctional reagents for immobilization of proteins on a carbon electrode surface: Oriented immobilization of photosynthetic reaction centers. *J. Electroanal. Chem.* **365,** 157–164 (1994).

35. Katz, E. Y., Shkuropatov, A. Y., Vagabova, O. I. & Shuvalov, V. A. Coupling of photoinduced charge separation in reaction centers of photosynthetic bacteria with electron transfer to a chemically modified electrode. *Biochim. Biophys. Acta - Bioenerg.* **976,** 121–128 (1989).
36. Caterino, R. *et al.* Photocurrent Generation in Diamond Electrodes Modified with Reaction Centers. *ACS Appl. Mater. Interfaces* **7,** 8099–8107 (2015).
37. Sjoholm, K. H., Rasmussen, M. & Minteer, S. D. Bio-Solar Cells Incorporating Catalase for Stabilization of Thylakoid Bioelectrodes during Direct Photoelectrocatalysis. *ECS Electrochem. Lett.* **1,** G7–G9 (2012).
38. Hamidi, H. *et al.* Photocurrent Generation from Thylakoid Membranes on Osmium-Redox-Polymer-Modified Electrodes. *ChemSusChem* **8,** 990–993 (2015).
39. Hasan, K. *et al.* Photoelectrochemical Communication between Thylakoid Membranes and Gold Electrodes through Different Quinone Derivatives. *ChemElectroChem* **1,** 131–139 (2014).
40. Purcell, M. & Carpentier, R. Immobilized plant thylakoid membranes as a biosensor for herbicides. *Biotechnol. Tech.* **4,** 363–368 (1990).
41. Mimeault, M. & Carpentier, R. Electrochemical monitoring of electron transfer in thylakoid membranes. *Enzyme Microb. Technol.* **10,** 691–694 (1988).
42. Calkins, J. O., Umasankar, Y., O'Neill, H. & Ramasamy, R. P. High photo-electrochemical activity of thylakoid–carbon nanotube composites for photosynthetic energy conversion. *Energy Environ. Sci.* **6,** 1891–1900 (2013).
43. Rasmussen, M. & Minteer, S. D. Photobioelectrochemistry: Solar Energy Conversion and Biofuel Production with Photosynthetic Catalysts. *J. Electrochem. Soc.* **161,** H647–H655 (2014).
44. Giardi, M. T. & Pace, E. Photosynthetic proteins for technological applications. *Trends Biotechnol.* **23,** 257–263 (2005).
45. Rasmussen, M., Shrier, A. & Minteer, S. D. High performance thylakoid bio-solar cell using laccase enzymatic biocathodes. *Phys. Chem. Chem. Phys.* **15,** 9062–5 (2013).
46. Rasmussen, M. & Minteer, S. D. Thylakoid direct photobioelectrocatalysis: utilizing stroma thylakoids to improve bio-solar cell performance. *Phys. Chem. Chem. Phys.* **16,** 17327–31 (2014).
47. Rasmussen, M., Wingersky, A. & Minteer, S. D. Improved Performance of a Thylakoid Bio-Solar Cell by Incorporation of Carbon Quantum Dots. *ECS Electrochem. Lett.* **3,** H1–H3 (2014).
48. Calkins, J. O., Umasankar, Y., O'Neill, H. & Ramasamy, R. P. High photo-electrochemical activity of thylakoid–carbon nanotube composites for photosynthetic energy conversion. *Energy Environ. Sci.* **6,** 1891 (2013).
49. Rasmussen, M. & Minteer, S. D. Self-powered herbicide biosensor utilizing thylakoid membranes. *Anal. Methods* **5,** 1140–1144 (2013).
50. Bettazzi, F., Laschi, S. & Mascini, M. One-shot screen-printed thylakoid membrane-based biosensor for the detection of photosynthetic inhibitors in discrete samples. *Anal. Chim. Acta* **589,** 14–21 (2007).
51. Giardi, M., Koblízek, M. & Masojídek, J. Photosystem II-based biosensors for the detection of pollutants. *Biosens. Bioelectron.* **16,** 1027–1033 (2001).
52. Carpentier, R., Loranger, C., Chartrand, J. & Purcell, M. Photoelectrochemical cell containing chloroplast membranes as a biosensor for phytotoxicity measurements. *Anal.*

Chim. Acta **249,** 55–60 (1991).
53. Terasaki, N. *et al.* Photosensor based on an FET utilizing a biocomponent of photosystem I for use in imaging devices. *Langmuir* **25,** 11969–74 (2009).
54. Fletcher, S. Discovery of a single molecule transistor in photosystem II. *J. Solid State Electrochem.* **19,** 241–250 (2015).
55. Hinks, J. *et al.* Modeling cell membrane perturbation by molecules designed for transmembrane electron transfer. *Langmuir* **30,** 2429–40 (2014).
56. Pribil, M., Labs, M. & Leister, D. Structure and dynamics of thylakoids in land plants. *J. Exp. Bot.* **65,** 1955–72 (2014).
57. Kirchhoff, H. Diffusion of molecules and macromolecules in thylakoid membranes. *Biochim. Biophys. Acta* **1837,** 495–502 (2014).
58. Gwozdzinska, P. *et al.* Phenylenevinylene conjugated oligoelectrolytes as fluorescent dyes for mammalian cell imaging. *Chem. Commun.* **50,** 14859–14861 (2014).
59. Cao, B. *et al.* Extracellular polymeric substances from Shewanella sp. HRCR-1 biofilms: characterization by infrared spectroscopy and proteomics. *Environ. Microbiol.* **13,** 1018–31 (2011).
60. Cao, B. *et al.* Biofilm shows spatially stratified metabolic responses to contaminant exposure. *Environ. Microbiol.* **14,** 2901–10 (2012).
61. Marsili, E., Rollefson, J. B., Baron, D. B., Hozalski, R. M. & Bond, D. R. Microbial biofilm voltammetry: direct electrochemical characterization of catalytic electrode-attached biofilms. *Appl. Environ. Microbiol.* **74,** 7329–37 (2008).
62. Ji, E., Corbitt, T. S., Parthasarathy, A., Schanze, K. S. & Whitten, D. G. Light and dark-activated biocidal activity of conjugated polyelectrolytes. *ACS Appl. Mater. Interfaces* **3,** 2820–9 (2011).
63. Renslow, R. *et al.* Modeling biofilms with dual extracellular electron transfer mechanisms. *Phys. Chem. Chem. Phys.* **15,** 19262–83 (2013).
64. Bard, A. J. & Faulkner, L. R. *Electrochemical Methods: Fundamentals and Applications*. (2001).

IV.G. Appendix IV. Materials, Methods, and Supplementary Figures

IV.G.1. Materials and Methods

IV.G.1.a. Thylakoid extraction, chlorophyll content, and photoactivity

For this work, thylakoid membrane suspensions were obtained from fresh organic spinach, evaluated for chlorophyll content, and validated as active by established protocols.[37,45,48] The entire procedure is explained here and was conducted at 4°C. Organic spinach from a local supermarket was washed with ultrapure water and dried. Three aqueous solutions were prepared for thylakoid extraction and electrode deposition: (1) Extraction buffer (5X) contained 300 g/L D-sorbitol, 62.5 g/L 2-[4-(2-hydroxyethyl)piperazin-1-yl]ethanesulfonic acid (HEPES), 2.9 g/L NaCl, 3.7 g/L ethylenediaminetetraacectic acid disodium dehydrate (EDTA), and 10 g/L $MgCl_2$; this was then diluted 5X to make a working extraction buffer. (2) Lysing solution contained 0.19 g/L $MgCl_2$. (3) Deposition buffer (pH = 7.8) contained 60 g/L D-sorbitol, 11.9 g/L HEPES, and 0.19 g/L $MgCl_2$, as well as 1 µL of a commercial 272.1 kU/mL (28.7 mg/mL) *Aspergillus niger* catalase suspension (Sigma Aldrich) per 100 µL of solution.

Spinach was deveined and blended for five pulses of 5 seconds in working extraction buffer. The resultant mixture was filtered through three layers of cheesecloth and supernatant was retained. Supernatant was centrifuged at 200×g for 3 minutes to remove cellular debris. Debris-free supernatant was transferred and centrifuged at 1000×g for 7 minutes to pellet chloroplasts. Supernatant was discarded, and chloroplasts were resuspended in a minimal volume of working extraction buffer; this was gently pipetted onto a 40% Percoll® density gradient (60% working extraction buffer) and centrifuged for 6 minutes at 1700×g. The

resulting pellet was lysed in lysing solution for 30 seconds to extract thylakoids and then immediately resuspended in deposition buffer. If not immediately used, these thylakoid suspensions were stored at −20°C.

By measuring the absorbances of the thylakoids in deposition buffer at 645 nm (A_{645}) and 663 nm (A_{663}), then using these values in a previously reported equation for chlorophyll *a* (chl*a*) concentration, given[48] [chl*a*] (mg/ml) = $(8.02A_{663} + 20.2A_{645})/10$, and finally multiplying by the molar mass of chl*a* (893.5 g/mol), chlorophyll content was determined to be ~100 nmol chlorophyll per 50 μL of thylakoid suspension, or ~2 mM. As discussed in the main text, this is 200-fold more concentrated than 10 μM COE additives.

In order to validate their photoactivity, extracted thylakoids were immobilized from deposition buffer onto a glass coverslip and oxygen production was measured using a micro-dissolved oxygen probe from Shelfscientific. The coverslip was immersed in 5 mL of 0.1 M phosphate buffer (pH = 7.4) containing 0.1 M nitrate, and oxygen concentration was measured in the dark until a stable value was obtained; the measurement was repeated while illuminating the coverslip-immobilized thylakoids. With confirmed thylakoid oxygen production (photoactivity), thylakoid electrodes were then fabricated according to previously reported procedures;[45] this is also described in the next section.

IV.G.1.b. Fabrication of thylakoid bioanodes and laccase biocathodes

3 cm × 1 cm pieces of Toray® carbon paper were first excised with a razor. A further 2 cm × 0.2 cm section was removed from the corner of each piece, and the retained 2 cm × 0.8 cm section was coated in wax to leave a 1 cm × 1 cm electroactive surface.

For thylakoid bioanodes, 50 μL of the thylakoid suspensions (in deposition buffer) were pipetted and spread onto one side of the 1 cm × 1 cm section and allowed to air dry for 30

minutes. Fig. IV.S3 A depicts several of these electrodes in the drying stage. In a fume hood, dried electrodes were placed with a thimbleful of tetramethyl orthosilicate and covered with a glass petri dish for 15 minutes to create a silica coating on the thylakoids.[37] These completed electrodes were stored at 4 °C overnight and used the next day. Thylakoid/COE electrodes were fabricated the same way, except that the desired COE concentration was added homogeneously with light agitation to 50 μL of the thylakoid suspension immediately prior to pipetting onto the carbon paper working electrode.

For laccase biocathodes, 15 mg of previously-prepared anthracene-modified multiwalled carbon nanotubes[59] were mixed with 150 mL purified laccase solution (Amano Enzyme, Inc.). This mixture was vortexed, then sonicated for 10 min, and this was repeated a second time. A 50 mL aliquot of tetrabutylammonium bromide-modified Nafion® from an established procedure[60] was then added to the mixture, followed by an additional 5 minutes of vortexation. The resulting thin black mixture was painted onto the 1 cm × 1 cm electroactive section and allowed to dry for ~30 min.

IV.G.1.c. Cyclic voltammetry

Scans were performed in a three-electrode electrochemical cell (Fig. IV.2 A and Fig. IV.S3 B), with each prepared electrode condition, in triplicate, in both the dark and the light. The electrolyte was 100 mM, pH = 7.4 phosphate buffer. Working electrodes were thylakoid electrodes, and electrical contact was made in the wax-coated section by clamping through the wax with an alligator clip; the reference electrode was Ag/AgCl (saturated KCl); the counter electrode was platinum mesh. Potential was swept twice from −100 mV to 650 mV at 5 mV/s, and the second sweep from each scan was recorded. All photoelectrochemical measurements of working electrodes were obtained with a CH Instruments CHI660

electrochemical workstation. Representative results from these experiments for unmodified thylakoids and COE1-4C-modified thylakoids are presented in Fig. IV.S2. Remaining traces of all other tested conditions are featureless and are essentially no different than these traces; therefore, they are omitted for the sake of clarity. The Toray® carbon paper working electrode has a very high surface area that leads to high capacitive currents, and this accounts for the large difference in current in forward and reverse scans (~2 $\mu A/cm^2$) in these CV experiments. The increase in current above E = 0.5 V is due to the electrochemistry of the electrode and not the thylakoids or COEs, which was confirmed by control CV scans of bare carbon electrodes (not shown).

IV.G.1.d. Amperometry

Current collection was performed at 0.45 V vs. Ag/AgCl in a three-electrode electrochemical cell (Fig. IV.S3 B) with 100 mM, pH = 7.4 phosphate buffer as the electrolyte. Working electrodes were thylakoid electrodes, and electrical contact was made in the wax-coated section by clamping through the wax with an alligator clip; the reference electrode was Ag/AgCl (saturated KCl); the counter electrode was platinum mesh. All photoelectrochemical measurements were obtained with a CH Instruments CHI660 electrochemical workstation. The current output from thylakoid (working) electrodes was monitored continuously, first in the dark until stable (~60 s) and then under illumination until stable (~60 s); this on-off switching was repeated three times in succession for each tested electrode and then averaged. The light current, dark current, and photocurrent densities were recorded as such and averaged for each experimental condition in triplicate. The light source was a 250 W (5200 lumen) halogen lamp positioned ~20 cm away from the electrode surface (see Fig. IV.S3C).

IV.G.1.e. Bio-solar cells

Two-chamber bio-solar cells were implemented with the thylakoid/COE electrodes, a laccase biocathode, and a Nafion® 212 proton exchange membrane, as previously reported.[45] Briefly, the solar cell device was constructed from four layered 5 cm × 5 cm × 0.5 cm pieces of poly(methyl methacrylate) bolted together. The two central pieces have a hole milled from the center and a slot milled outward from this hole at the top of the piece, allowing electrodes to be inserted into each (see Fig. IV.S3C). The two central pieces are separated by the Nafion®, which importantly allows for each compartment to be filled with different solutions, as each electrode operates optimally at a different pH in this device: the anode compartment was filled with ~3 mL of 100 mM, pH 7.4 phosphate buffer, while the cathode compartment contained ~3 mL of 150 mM, pH 5.5 citrate buffer. Anode-cathode separation was thus ~1 cm.

Linear polarization (LP) was used to obtain dark and light current-potential (*J*-*V*) curves for the solar cells, and the photocurrent was calculated from the difference in the curves. In LP (also commonly referred to as linear sweep voltammetry, or LSV), the potential between the anode and cathode is varied (without a reference electrode), while current is monitored, allowing for probing of light and dark *J*-*V* characteristics of the devices. LP experiments were performed using a Digi-IVY DY2023 potentiostat. Illumination was provided by a 250 W (5200 lumen) halogen lamp positioned ~20 cm away from the electrode. For each triplicate set of electrodes, the average short circuit current density and open circuit voltage were determined from the y- and x-intercepts of the *J*-*V* curves, respectively.

IV.G.1.f. Ultraviolet-visible (UV-vis) absorbance spectroscopy

In a quartz cuvette with 1 cm path length, aqueous absorbance measurements were

conducted at 1 nm wavelength intervals (20 nm/s) in the range 250–800 nm (Beckman Coulter DU 800 Spectrophotometer). An absorbance versus [COE] calibration curve was generated by measuring UV-vis spectra for the various COEs at a series of concentrations. By identifying the wavelength of maximal absorption (λ_{max}), plotting the absorbance intensity at λ_{max} as a function of the concentration, and fitting these data by least squares, a straight line through the origin was generated with slope equal to the extinction coefficient (ε) of each COE derivative. An example of this data for COE1-4C is provided in Fig. IV.S4.

IV.G.2. Supplementary Figures

COE	COE1-3C	COE1-4C	COE1-5C	COE2-3C	COE2-4C	COE2-5C	COE3-4C
λ_{max} (nm)	407	418	425	357	374	385	400
ε (M^{-1} cm^{-1})	85395	69430	76020	62582	29136	65060	37727
λ_{onset} (nm)	467	500	511	395	442	466	503
E_{gap} (eV)	2.66	2.48	2.43	3.14	2.81	2.66	2.47

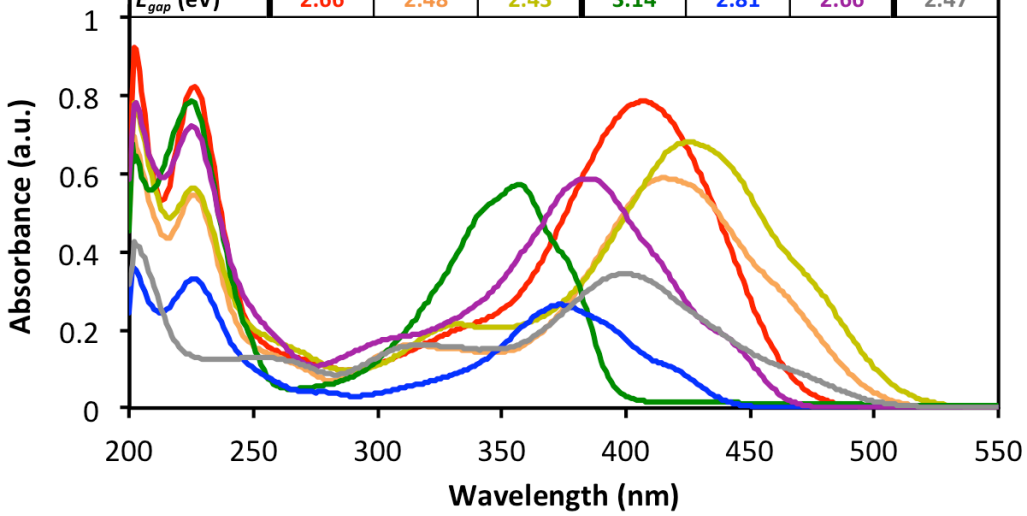

Figure IV.S1. Aqueous UV-vis absorbance spectra and optoelectronic properties of all seven COE molecules. Note the red-shifted spectra of COE-1 type molecules relative to COE-2 type.[1,2] [COE] = 9 µM in 100 mM, pH = 7.4 phosphate buffer. (Table, inset) A summary of the absorbance maxima (λ_{max}), extinction coefficient at λ_{max} (ε), absorbance onset (λ_{onset}), and optical gap (E_{gap}) for each of the COEs is displayed. Note that these spectra are not normalized, so ε is correlated to the peak height at λ_{max}.

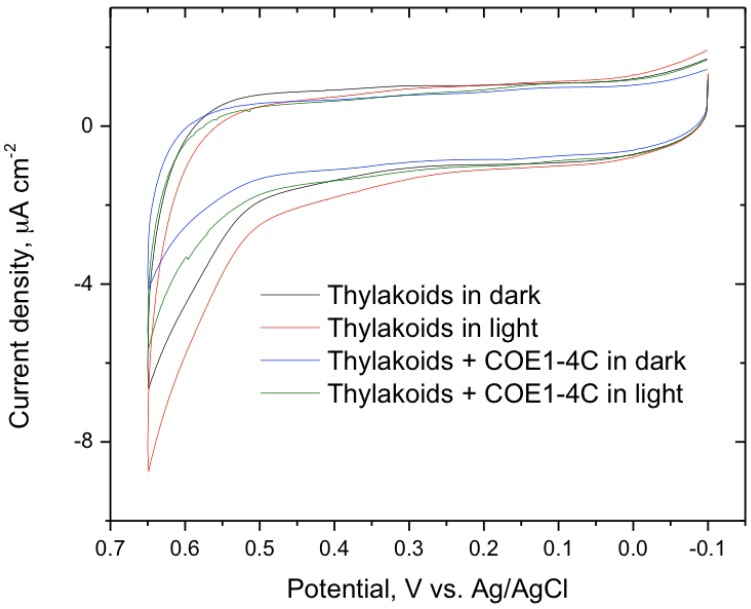

Figure IV.S2. Representative dark and light CV of thylakoid and thylakoid/COE electrodes. Buffer was 100 mM, pH 7.4 phosphate; scan rate = 10 mV/s.

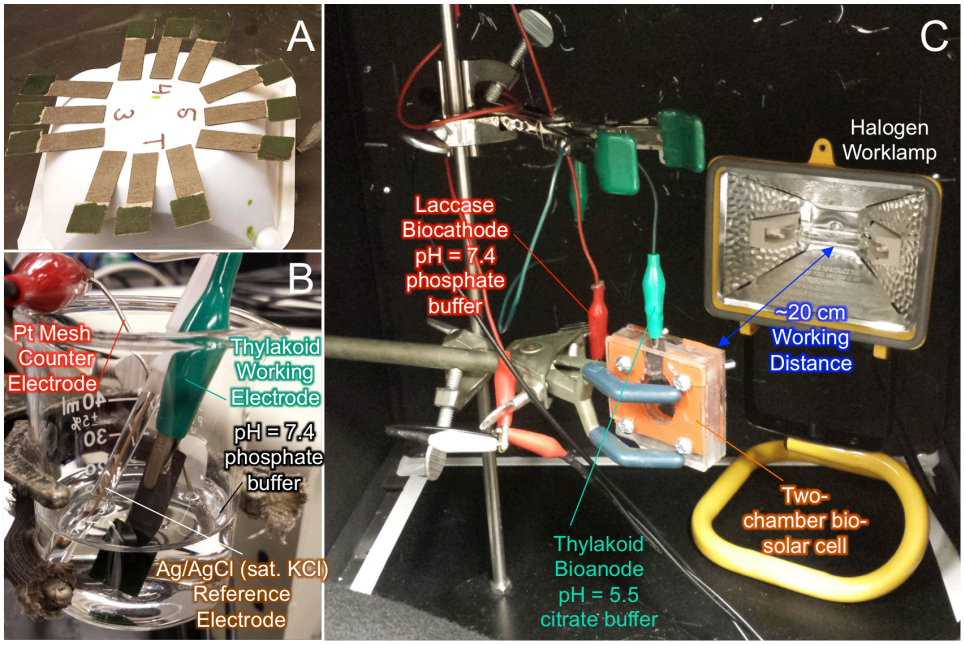

Figure IV.S3. Experimental Systems. (**A**) Drying working electrodes, constructed from 50 μL aliquots of thylakoids (unmodified and modified with COE1-3C, -4C, and -5C) drop cast on 1 cm × 1 cm Toray® carbon paper. This image was taken immediately prior to incubation with tetramethyl orthosilicate (silica layer deposition). (**B**) The three-electrode setup for electrochemical testing of the thyalkoid and thylakoid/COE working electrodes. (**C**) The chamber used for light- and dark-current measurements of thylakoid and thylakoid/COE working electrodes during amperometry and bio-solar cell testing. A two-chamber solar cell device[3] is pictured. The lamp is a 250 W halogen rated to 5200 lumens.

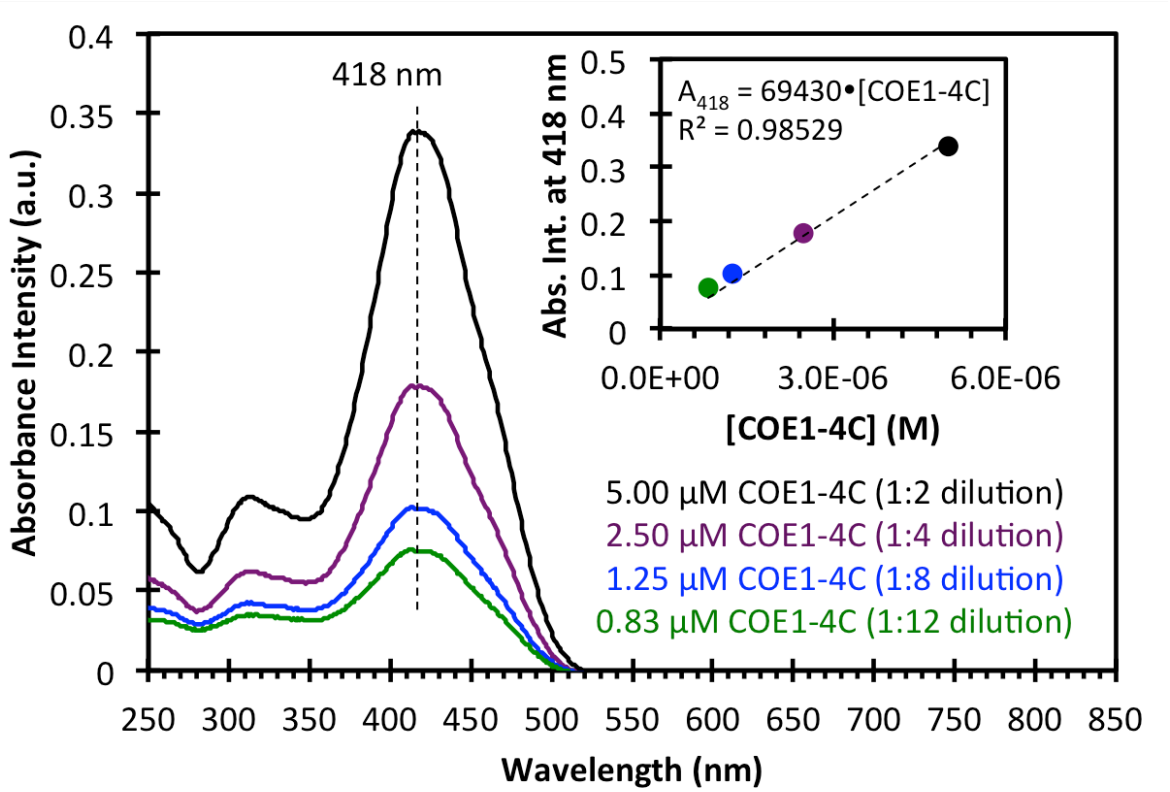

Figure IV.S4. Aqueous COE1-4C absorption concentration dependence. Solvent was 100 mM, pH = 7.4 phosphate buffer. The calibration curve (inset) at the absorbance maximum of 418 nm indicates an extinction coefficient of 69430 L mol^{-1} cm^{-1}.

Chapter V. DSFO+ as Molecular Respiratory Protein Prosthetic for Non-Electrogenic Mutants of *S. oneidensis* MR-1

V.A. Abstract

For emerging bioelectronic technologies, charge transfer processes remain rate-limited by poor contacts at biotic-abiotic interfaces. Direct chemical modification of these interfaces represents an under-developed approach for amplifying biocatalyzed current production. We present the synthesis and application of DSFO+, a redox-active conjugated oligoelectrolyte designed for membrane affinity that catalytically couples to biological respiratory transmembrane electron transport—much like a heme-containing protein. DSFO+ is employed with three strains of *Shewanella oneidensis* MR-1 (electrogenic wild type and two non-electrogenic knockout mutants) and amplifies anodic biocurrent in all strains without toxicity at a physiologically-relevant redox potential. This appears to be the first reported instance of such effects, and the first known partial rescue of respiratory biocurrent production in non-electrogenic bacterial phenotypes using a "protein prosthetic" electron conduit.

V.B. Introduction

Microbial bioenergy technologies take advantage of so-called "electrogenic" microorganisms[1–6] to catalyze the anaerobic conversion of organic fuels into usable electrical current. While *Geobacter* and *Shewanella* represent key electrogenic genera,[7] most microorganisms are ineffective electrocatalysts because they lack the native capacity to exchange electrons with extracellular solid-state conductors.[5] Genetic engineering provides one effective workaround[8,9] that is challenged by the lack of genetic manipulation tools for

many species.[10] Overcoming the scarcity of electrogenic microorganisms is conceivable, however, by using synthetic materials that improve the communication between biological entities and electronic components. Developing effective methods to modify living biotic/abiotic interfaces therefore provides a key materials challenge for advancing bioelectronic and bioelectrochemical technologies.[11,12] From this perspective, biocompatible organic conjugated and redox-active molecules or polymers are attractive, based on their previous applications ranging in bioelectrochemical and optoelectronic technologies.[13–15]

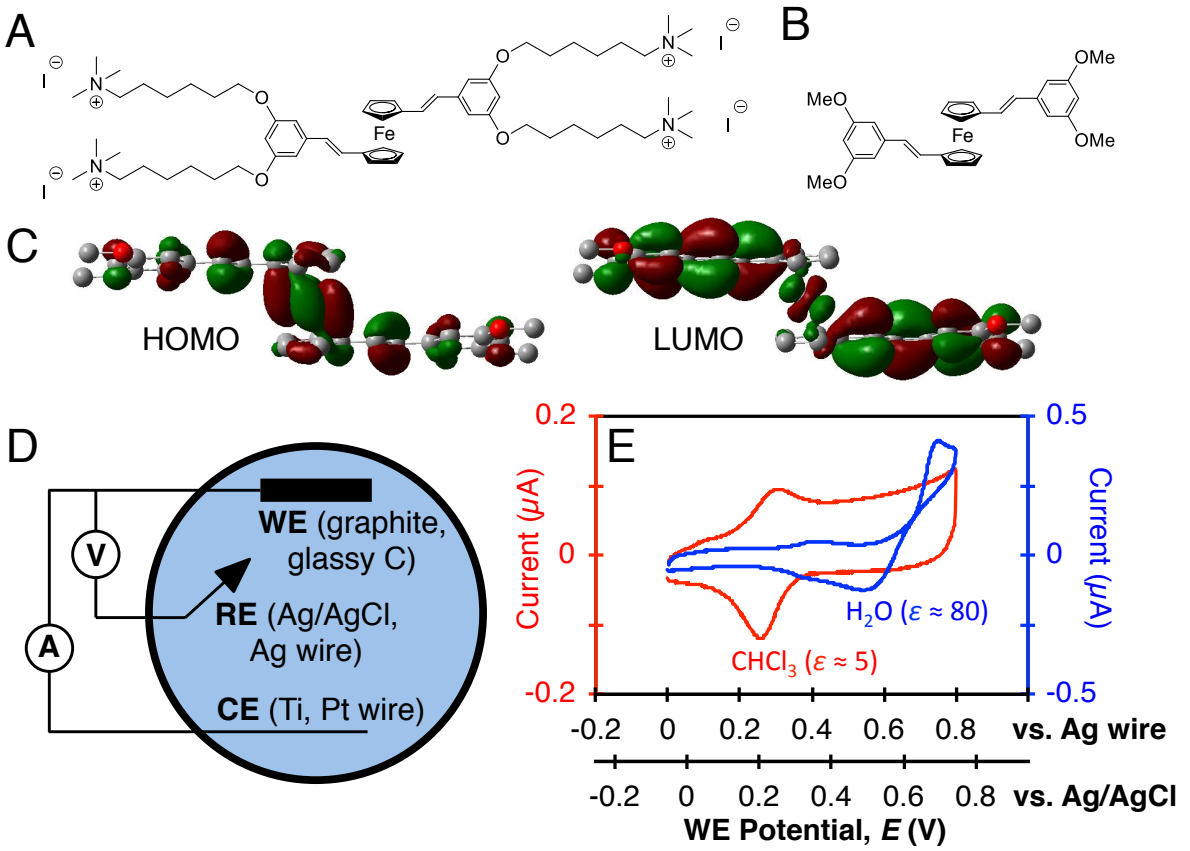

Figure V.1. Salient molecular and M3C details. (**A**) The molecular structure of water-soluble DSFO+. (**B**) The molecular structure of $DSFO(Me)_4$, the organic-soluble model compound. (**C**) DFT-calculated highest occupied and lowest unoccupied molecular orbitals (HOMO and LUMO) of the model compound $DSFO(Me)_4$. For clarity, hydrogen atoms are not displayed. (**D**) A schematic of the M3C device. Light blue represents the supporting electrolyte. WE, working electrode; RE, reference electrode; CE, counter electrode. Potential is poised between the WE and RE, as depicted by the "V," using a potentiostat and computer software (not depicted), while current flows at the WE and CE, as depicted by the "A." (**E**) CV traces of (blue) 10 μM DSFO+ in aqueous 100 mM pH = 7.4 phosphate buffer, and (red) 10 μM $DSFO(Me)_4$ in chloroform with 100 mM tetrabutylammonium hexafluorophosphate supporting electrolyte. Solvents and dielectric constants, ε, are indicated.

As a relevant example, membrane-intercalating *p*-phenylenevinyelene-based conjugated oligoelectrolytes (PPV-COEs) have been demonstrated to enhance voltage, dark current, photocurrent, power, electrode colonization, coulombic efficiency, and electrical contacts in (photo)bioelectrochemical systems with limited toxic side-effects.[16–24] One may initially surmise that PPV-COEs assist in transmembrane electron tunneling,[25,26] but this is less certain after accounting for molecular orbital/workfunction mismatching[21,23,24,27] and the absence of direct contacts.[28] However, emerging experimental evidence[29,30] and considerations of charge neutrality—which require monovalent cations to traverse a membrane to balance electrons—support the notion that PPV-COEs facilitate transmembrane ion conductance. This mechanism remains consistent with PPV-COEs enhancing the native direct electron transfer (DET) component of microbial electrode respiration[24] by alleviating a rate-limiting cation transfer bottleneck. While PPV-COEs demonstrably improve bioelectrochemical processes and have yielded insight, the challenge of creating a true "protein prosthetic" respiratory electron conduit remains.

We therefore designed and synthesized the COE *E,E*-1,1'-*bis*(2-(3,5-bis(6-trimethylammoniumhexyloxy)phenyl)ethenyl)ferrocene tetraiodide (DSFO+), shown in Fig. V.1 A. DSFO+ has the membrane-protein-like properties of amphiphilicity, a molecular length that can achieve lipid bilayer membrane thickness (~4 nm), and a biocompatible iron redox center—much like a mono-heme cytochrome. DSFO+ was further predicted to intercalate into a membrane from aqueous media because of its structural similarity to the membrane-intercalating PPV-COEs known as DSBN+ and COE2-3C.[16,19] One essential consideration remains: upon intercalation into a lipid bilayer membrane, the aromatic core of DSFO+ will reside in a nonpolar lipid environment. However, DSFO+ is only soluble for

electrochemical characterization in polar media, so the organic-soluble derivative *E,E*-1,1'-*bis*(2-(3,5-dimethoxyphenyl)ethenyl) ferrocene ($DSFO(Me)_4$), depicted in Fig. V.1 B, was also synthesized to permit electrochemical analyses in nonpolar organic solvents.

The redox potential of the ferrocene moiety (~0.21 V vs. Ag/AgCl)[31] is physiologically relevant because it falls between the redox potentials of organic fuels at pH = 7 ($E \leq -0.44$ V vs. Ag/AgCl) and oxygen reduction to water ($E = 0.62$ V vs. Ag/AgCl).[32–34] This unlocks the possibility of using DSFO+ as a redox intermediate akin to a "protein prosthetic" to amplify transmembrane electron transfer and establish (*i.e.* rescue) respiratory biocurrent in non-electrogenic mutants. By density functional theory calculations, it is also apparent that the frontier molecular wavefunctions are fully delocalized (Fig. V.1 C), which should aid in transmembrane electron motion. Successful respiratory biocurrent amplification or rescue *via* DSFO+ would be detectable as a catalytic electron transfer wave[35] centered at the redox potential of DSFO+ in a lipid bilayer. To our knowledge, such a mechanistic option for charge transport has not been achieved with a synthetic molecule.

In single-chamber microbial three-electrode electrochemical cells (M3Cs), schematically depicted in Fig. V.1 D, the metabolic activity of microorganisms is electrochemically coupled to an electrode, affording bioelectrochemical conversion with environmental control and potentiometric interrogation of electrode-associated microorganisms.[35,36] M3Cs thus provide an appealing reactor platform for measuring bioelectrochemical perturbations from modification with DSFO+. The present approach therefore utilizes bioanodic M3Cs employing genetic variants of the well-characterized model electrogenic organism *S. oneidensis* MR-1[37–39] and subsequent modification of these M3Cs with DSFO+. *S. oneidensis* MR-1 will partially oxidize one equivalent of lactate to theoretically yield one equivalent of

acetate and four equivalents of electrons for collection at an electrode[40]:

$$\text{Lactate}^- + 2\ H_2O \rightarrow \text{Acetate}^- + HCO_3^- + 5\ H^+ + 4\ e^- \quad \text{(V.1).}$$

These electrons ultimately depart the cell *via* the terminal MtrCAB-OmcA protein complex to enable respiration on an electrode, and thereby biocurrent production, by direct and mediated electron transfer (DET and MET) mechanisms.[24,41–43] Because of their structural interdependences,[44–46] genetic deletion of any of these proteins either partially inhibits (Δ*mtrC* and Δ*omcA*) or almost completely disables (Δ*mtrA* and Δ*mtrB*) respiratory current production on solid acceptors.[47] With these molecular features in mind, Δ*mtrA* and Δ*mtrB* strains were selected as non-electrogenic test cases for rescue with DSFO+, as well as for comparison against the electrogenic wild type (WT) strain in M3Cs.

Cyclic voltammetry (CV) was first used to characterize DSFO+ and $DSFO(Me)_4$ redox activity in a variety of solvents with different dielectric constants, ε. Then, *S. oneidensis* MR-1 growth inhibition by DSFO+ was assessed with minimum inhibitory concentration (MIC) assays. Chronoamperometry (CA) in M3Cs was used as a final control experiment to determine the optimal *in operando* concentration of DSFO+. With these data in hand, M3Cs were employed with WT, Δ*mtrA*, and Δ*mtrB* strains of *S. oneidensis* MR-1. Bacteria were modified in M3Cs *in operando* with solution additions of DSFO+ in order to examine biocurrent amplification in WT and rescue of biocurrent in the mutants. Using electrochemical measurements, coulombic efficiency (CE) analysis *via* high performance liquid chromatography (HPLC), live/dead confocal fluorescence microscopy (CFM), and scanning electron microscopy (SEM), the bioelectrochemical effect of DSFO+ was

characterized in these M3Cs, and these results are presented. The overall study is consistent with DSFO+ directly catalyzing respiratory biocurrent.

V.C. Results and Discussion

A brief description for the synthetic entry into DSFO+ and DSFO(Me)$_4$ is provided in Scheme V.1, and full details can be found in the Supporting Information. The key transformation involved a palladium-catalyzed Heck coupling employing 1,1'-divinylferrocene and 1-iodo-3,5-bis((6-iodohexyl)oxy)benzene[48–51] that selectively gave the desired trans olefin in 49% yield. After ionization of the neutral compound with trimethylamine, DSFO+ was afforded in quantitative yield. By instead employing 1-iodo-3,5-dimethoxybenzene in the Heck coupling reaction, the tetramethyl model compound DSFO(Me)$_4$ was afforded in a similar manner to DSFO+.

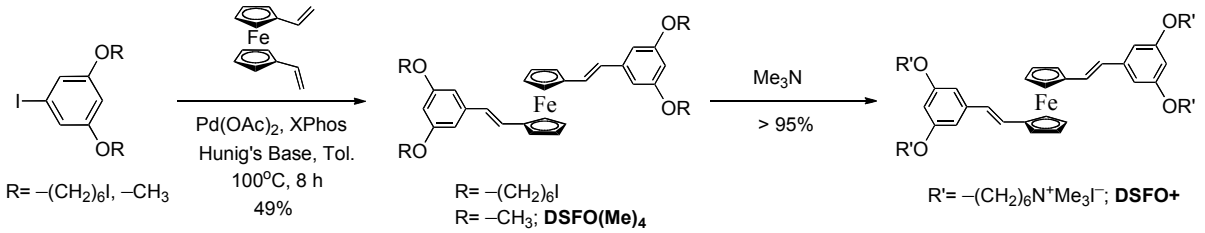

Scheme V.1. Synthetic approach for the preparation of DSFO+ and DSFO(Me)$_4$.

CV experiments were undertaken with DSFO+ and DSFO(Me)$_4$ in solvents with dielectric constants in the range $5 \leq \varepsilon \leq 80$. As can be seen in the resulting CV traces in Fig. V.1 E, DSFO(Me)$_4$ in chloroform ($\varepsilon \approx 5$) exhibits a reversible oxidation wave with an onset at 0.21 V vs. Ag (0.16 V vs. Ag/AgCl), while DSFO+ in water ($\varepsilon \approx 80$) exhibits a less-reversible oxidation wave with an onset at 0.68 V vs. Ag (0.62 V vs. Ag/AgCl); see Figs. V.S1 and V.S2 for complete details. It is worth pointing out that the redox potential-dielectric relationship is counterintuitive, as one may expect a decrease in the oxidation potential with

increasing dielectric constant.[52,53] Nonetheless, one can use these differences to probe the medium wherein the molecules have accumulated, particularly in view of the lack of useful optical differentiation between the molecules (Fig. V.S3).

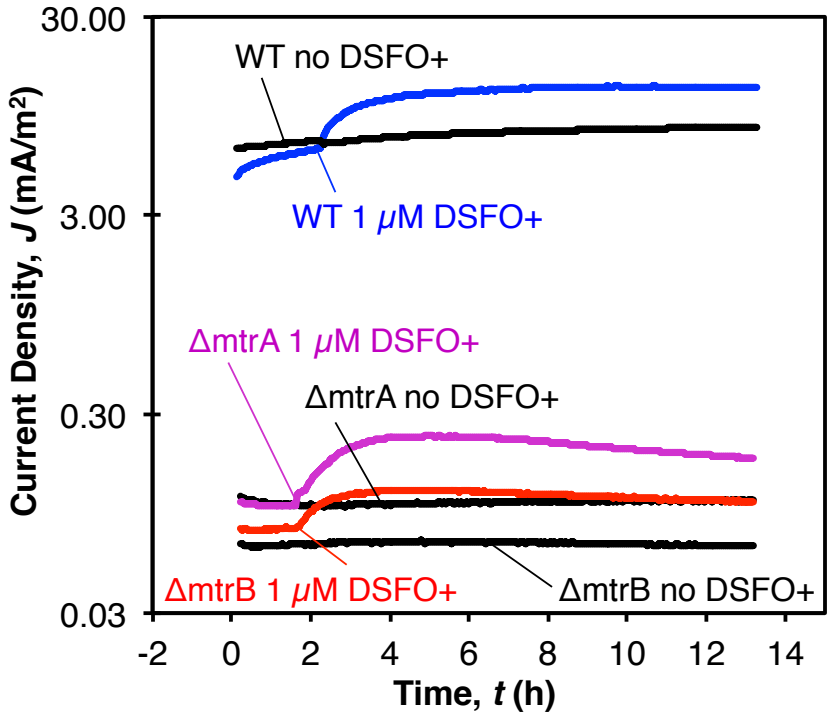

Figure. V.2. CA traces from representative M3C replicates operated at E = 0.27 V vs. Ag/AgCl with WT, Δ*mtrA*, and Δ*mtrB* strains. At t = 2 h, M3Cs were injected with (colored traces) 1 μM DSFO+ or (black traces) no DSFO+.

S. oneidensis MR-1 cultures were exposed in triplicate to a logarithmic series of DSFO+ concentrations, and the MIC of DSFO+ was determined to be 5 μM (see Fig. V.S4). This value agrees with inhibitory values measured for PPV-COEs.[16–24] Next, CA was used to establish biofilms for determination of $[DSFO+]_{optimal}$, the highest *in operando* concentration of DSFO+ without long-term negative effects on biocurrent. Briefly, biofilms of WT, Δ*mtrA*, and Δ*mtrB* strains were cultivated in M3Cs for 16 hours on graphite electrodes poised at E = 0.27 V vs. Ag/AgCl (the central redox potential of $DSFO(Me)_4$ in $CHCl_3$). The medium was then replaced to remove planktonic cells, thereby deconvoluting the electrical output of the

biofilm,[24] and CA was measured starting at t = 0 h. At t = 2 h, these active biofilms were then exposed to DSFO+ concentrations in the range $0 \leq [\text{DSFO+}] \leq 4$ μM and allowed to operate for 13 hours to determine $[\text{DSFO+}]_{\text{optimal}}$. Representative CA traces for these experiments with the WT reactors, found in Fig. V.S5, show that $[\text{DSFO+}]_{\text{optimal}} = 1$ μM. Therefore, all remaining experiments were conducted at this concentration.

Representative CA traces for WT, Δ*mtrA*, and Δ*mtrB* biofilms that were exposed to either 0 μM or 1 μM DSFO+ at t = 2 h are presented in Fig. V.2. These data qualitatively illustrate a key point: biofilms of all three strains exhibit an immediate, sustained amplification in respiratory biocurrent when DSFO+ is injected into the reactors. To our knowledge, this is the first reported instance of using a synthetic redox-active molecular protein prosthetic to partially rescue electrogenic character in non-electrogenic bacterial strains. In order to quantitatively explore this current amplification, eight biological replicate[54] biofilms of each of the three strains were established by identical methods. Similar CA experiments were then repeated; this time, four WT-M3Cs, four Δ*mtrA*-M3Cs, and four Δ*mtrB*-M3Cs received no modification (controls), while four of each type received a 1 μM dosage of DSFO+ at t = 1 h (test cases). The four replicate CA measurements were averaged for each of the six conditions, and these are presented in Fig. V.3 A, C, and E, where the breaks in the traces correspond to examination at key timepoints, as follows. At t = –1 h, *i.e.*, one hour before the beginning of CA measurements, CV analyses of the biofilms in fresh media were performed. At t = 0 h, HPLC samples were extracted and CA was recorded. At t = 1 h, DSFO+ was added into reactors. At t = 2 h, CA was paused for CV analyses that interrogated the bioelectrochemical effect of DSFO+ on the biofilms. At $t \approx 4$ h, CA was resumed and proceeded until termination at t = 19 h (WT-M3Cs), or t = 21 h (Δ*mtrA*-M3Cs, Δ*mtrB*-

M3Cs), when CV, HPLC sample extractions, live/dead CFM, and chemical fixation (for SEM) of bioanodes were undertaken.

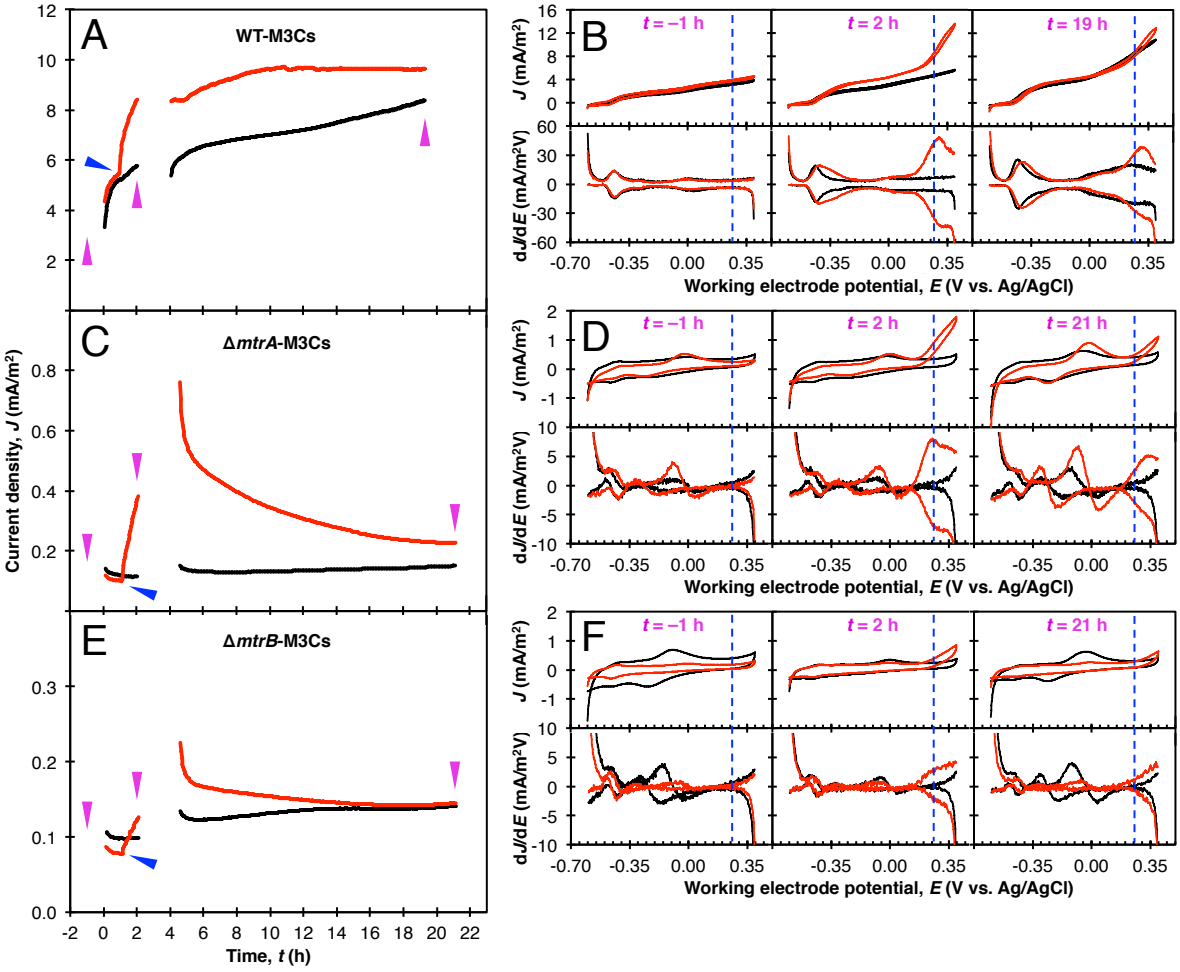

Figure V.3. Average CA and CV data for M3Cs containing the three *S. oneidensis* MR-1 strains, with and without DSFO+. Note that $t = -2$ h corresponds to the end of 16 h biofilm establishment. Black traces represent reactors containing no DSFO+, while red traces represent reactors modified with 1 µM DSFO+. Magenta arrows and times indicate timepoints when CV analysis was undertaken. Blue arrows indicate when DSFO+ was spiked in at $t = 1$ h. Vertical blue dashed lines in the CV and derivative data indicate the poised potential of $E = 0.27$ V used to collect the CA traces (this potential was chosen to match the expected formal potential of DSFO+ in lipid). (**A**) CA traces for WT-M3Cs. (**B**) CV and derivative traces for WT-M3Cs at the timepoints indicated in (A). (**C**) CA traces for Δ*mtrA*-M3Cs. (**D**) CV and derivative traces for Δ*mtrA*-M3Cs at the timepoints indicated in (C). (**E**) CA traces for Δ*mtrB*-M3Cs. (**F**) CV and derivative traces for Δ*mtrB*-M3Cs at the timepoints indicated in (E).

Injection of DSFO+ into WT-M3Cs at $t = 1$ h immediately stimulates biocurrent, which increases from ~5 mA/m^2 to >8 mA/m^2 by $t = 2$ h (Fig. V.3 A, red trace). This ~40% increase

in biocurrent compared to the positive control WT-M3Cs lacking DSFO+ (Fig. V.3 A, black trace) is sustained from t = 4 h to the end of operation at t = 19 h. These results are consistent with DSFO+ amplifying the electrode respiration of wild-type *S. oneidensis* MR-1. Examination of the CV traces and derivatives at t = –1, 2, and 19 h (Fig. V.3 B) implicates a catalytic electron transfer wave centered at ~0.27 V (oxidation onset at 0.20 V) as the source of increased current in test reactors. Comparison to the characteristic CVs in Figs. V.1 E and V.S1 A and B suggests that DSFO+ has incorporated into a low-dielectric environment because the onset potential is similar to the onset potential of $DSFO(Me)_4$ in chloroform. A lipid membrane has a dielectric constant of ε = ~2-3,[55,56] so this similarity in potential suggests that DSFO+ has intercalated; a point plotted at coordinates (E = 0.20 V, ε = 3) sits close to the regression line in the plot of ε vs. E in Fig. V.S1 C. The catalytic nature of the current signifies redox coupling of DSFO+ to respiratory transmembrane electron transfer, and this mechanistically distinguishes DSFO+ action from the paradigm of PPV-COEs that boost native *S. oneidensis* DET at $E \approx 0.05$ V in M3C devices.[24]

In similar experiments, adding DSFO+ to Δ*mtrA*-M3Cs at t = 1 h also rapidly boosts biocurrent production from ~0.10 mA/m^2 to ~0.40 mA/m^2 by t = 2 h (Fig. V.3 C, red trace). At t = 4 h, this current maximizes at ~0.75 mA/m^2—a ~400% increase compared to the ~0.15 mA/m^2 from the positive control (Fig. V.3 C, black trace)—and then exhibits a discharge presumably from charge buildup during the pause for CV. By t = 21 h, the biocurrent production remains elevated at ~50% above control Δ*mtrA*-M3Cs. CV traces and derivatives at t = –1, 2, and 21 h in Fig. V.3 D implicate the same DSFO+ catalytic electron transfer wave centered at E = 0.27 V as the source of increased current in test reactors, and this feature persists until the end of operation. This catalytic wave is also smaller in amplitude

than the same wave in the WT-M3Cs, consistent with the lower current density in Δ*mtrA*-M3Cs.

Table V.1. Quadruplicate average measured M3C device parameters[a]

Measured Parameter	Expression	WT-M3Cs		Δ*mtrA*-M3Cs		Δ*mtrB*-M3Cs	
		No DSFO+	1 μM DSFO+	No DSFO+	1 μM DSFO+	No DSFO+	1 μM DSFO+
Charge collected (C)[b]	$Q_{coll} = A\int J(t)\mathrm{d}t$	9.9 ± 1.7	12.8 ± 1.2	0.21 ± 0.08	0.48 ± 0.07	0.20 ± 0.11	0.22 ± 0.08
Lactate consumed (mM)[c]	$\Delta[\mathrm{lac}] = [\mathrm{lac}]_f - [\mathrm{lac}]_i$	−5.5 ± 1.7	−4.0 ± 0.9	−1.3 ± 0.3	−0.4 ± 0.2	−1.1 ± 0.8	−0.2 ± 0.1
Lactate charge equivalent (C)[d]	$Q_{lac} = -\Delta[\mathrm{lac}]VFn$	32 ± 10	23 ± 5	7.5 ± 2.0	2.3 ± 1.0	6.1 ± 4.7	1.3 ± 0.7
Lactate coulombic efficiency (%)	$CE_{lac} = 100 \times Q_{coll}/Q_{lac}$	31 ± 11	56 ± 14	3 ± 1	21 ± 10	3 ± 3	17 ± 11
Acetate produced (mM)[c]	$\Delta[\mathrm{ac}] = [\mathrm{ac}]_f - [\mathrm{ac}]_i$	3.4 ± 0.6	2.6 ± 0.5	1.0 ± 0.3	0.5 ± 0.3	0.6 ± 0.4	0.2 ± 0.1
Acetate charge equivalent (C)[d]	$Q_{ac} = \Delta[\mathrm{ac}]VFn$	20 ± 4	15 ± 3	5.8 ± 1.6	2.6 ± 1.8	3.5 ± 2.1	0.9 ± 0.3
Acetate coulombic efficiency (%)	$CE_{ac} = 100 \times Q_{coll}/Q_{ac}$	50 ± 12	85 ± 16	4 ± 1	18 ± 13	6 ± 5	26 ± 13
Electrode cell density (10^9 cells m^{-2})[e]	$\rho = (1/K)\Sigma_k(2N_k/\pi d_k h_k)$	107 ± 39	113 ± 46	63 ± 32	58 ± 21	67 ± 40	28 ± 13
Current density at t = 2 h (mA m^{-2})	J_2	5.8 ± 1.0	8.4 ± 0.8	0.11 ± 0.06	0.38 ± 0.14	0.10 ± 0.05	0.13 ± 0.04
Current per cell (fA $cell^{-1}$)	$I_{cell} = J_2/\rho$	54 ± 22	75 ± 31	1.8 ± 1.3	6.6 ± 3.3	1.5 ± 1.1	4.5 ± 2.5

[a] Quoted uncertainties represent ± 1 standard deviation (for measured values) or are propagated errors by addition of standard deviations in quadrature (for calculated values). [b] The surface area of working electrodes (average of 24 replicates) is A = 0.0226 ± 0.0012 m^2 [24]. [c] Note that Δ[lac] < 0 and Δ[ac] > 0 because the bacterial electrode reaction (Eq. V.1) converts lactate to acetate and electrons; this is why values for Q_{lac} and Q_{ac} have different signs. [d] Reactor volume is V = 15 mL. Faraday's constant is $F = eN_A \approx 96485$ C mol^{-1}, where $e = 1.602 \times 10^{-19}$ C and $N_A = 6.02 \times 10^{23}$ mol^{-1}. The electron equivalents produced per equivalent of substrate is n = 4 (Eq. V.1). [e] After M3C operation, ρ is determined from SEM images of the chemically fixed graphite electrode fibers by averaging counts per area of fiber-associated cells. For this, fibers are approximated as cylindrical and divided into K sections with diameters d_k and heights h_k (surface area is $\pi d_k h_k$). N_k is the number of cells counted on the kth cylindrical section; $2N_k$ is therefore used in the calculation of ρ to account for the fact that only half of any fiber cylinder may be imaged for cell counting. $K \geq 12$ in all cases.

Finally, adding DSFO+ to Δ*mtrB*-M3Cs at t = 1 h also immediately boosts biocurrent

production, which increases from ~0.08 mA/m^2 to ~0.12 mA/m^2 by t = 2 h (Fig. V.3 E, red trace). At t = 4 h, the biocurrent maximizes at ~0.23 mA/m^2—a ~65% increase in the biocurrent production compared to the ~0.14 mA/m^2 from positive control Δ*mtrB*-M3Cs lacking DSFO+ (Fig. V.3 E, black trace). By t = 21 h, the biocurrent returns to the level of control Δ*mtrB*-M3Cs. These results illustrate partial rescue of electrogenic character due to DSFO+ addition, though it is unsustained for Δ*mtrB*. The CV traces and derivatives at t = –1, 2, and 21 h in Fig. V.3 F implicate the same DSFO+ catalytic electron transfer wave centered at E = 0.27 V as the source of increased current in test reactors. For these reactors, this feature is again smaller than in WT-M3Cs and here does not persist until the end of operation, helping explain why the CA current returns to the level of the control reactor by the end of operation in Fig. V.3 E. Because DSFO+ does not sustainably rescue transmembrane electron transfer for the Δ*mtrB* strain, we speculate that an intact MtrB porin-barrel may play a more significant role for DSFO+ interaction than does the multi-heme MtrA protein. These data may also suggest that DSFO+ generally catalyzes wild-type bacterial electron transfer more effectively than mutant strains.

The CE of substrate conversion to current during CA may be determined by comparing the theoretical electron equivalents for the lactate consumed (Q_{lac}) and acetate produced (Q_{ac}) to the integrated charge collected from the bacteria, Q_{coll}. As can be seen in Table 1, in M3Cs with DSFO+ added, Q_{coll} increases during operation for all three strains, but the quantities of lactate consumed and acetate produced decrease for all three strains. For lactate consumption, unmodified WT-M3Cs had a CE of 31 ± 11%, which increased to 56 ± 14% with DSFO+ modification. For acetate production, the CE of WT-M3Cs increased from 50 ± 12% to 85 ± 16% with added DSFO+. Because lactate consumption not only yields current but also

provides electron and carbon equivalents for biosynthesis, it inherently has a lower CE. Acetate is produced during respiration (biocurrent production), so the greater percent increase in CE with respect to acetate production is consistent with ability of DSFO+ to improve electron transfer in *S. oneidensis* MR-1.

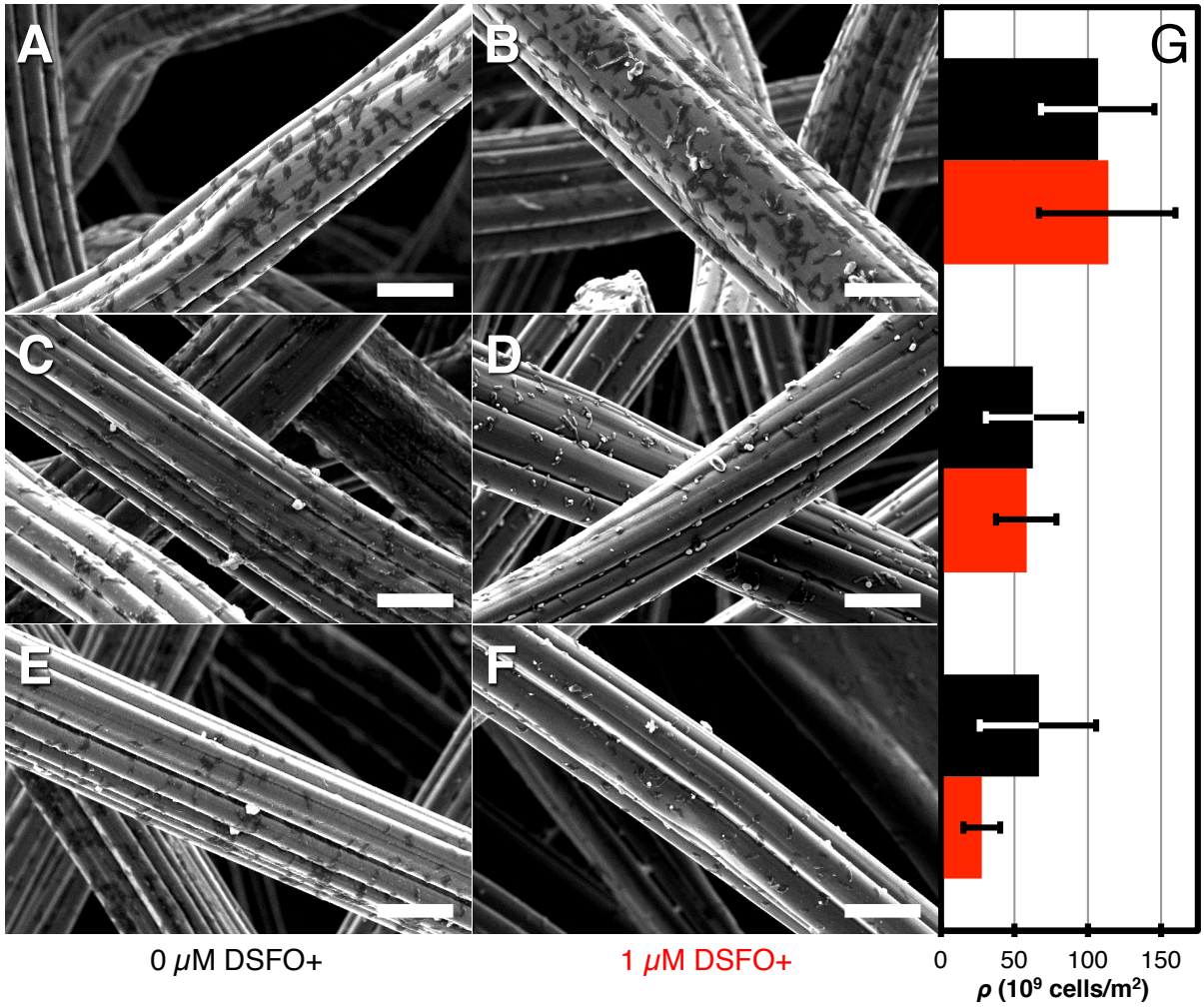

Figure V.4. Representative SEM images of graphite electrode fibers from all M3C conditions. Scale bars are 10 µm. (**A**) WT-M3Cs with 0 µM DSFO+. (**B**) WT-M3Cs with 1 µM DSFO+. (**C**) Δ*mtrA*-M3Cs with 0 µM DSFO+. (**D**) Δ*mtrA*-M3Cs with 1 µM DSFO+. (**E**) Δ*mtrB*-M3Cs with 0 µM DSFO+. (**F**) Δ*mtrB*-M3Cs with 1 µM DSFO+. (**G**) Graphical summary of electrode cell density by row (M3C type) for (black) 0 µM DSFO+ and (red) 1 µM DSFO+. Error bars represent ± 1 std. dev.

A similar trend was observed for Δ*mtrA*-M3Cs and Δ*mtrB*-M3Cs. For Δ*mtrA*-M3Cs, lactate CE increased from 3 ± 1% unmodified to 21 ± 10% with DSFO+ addition, and acetate

CE increased from 4 ± 1% unmodified to 18 ± 13% with DSFO+ addition. For Δ*mtrB*-M3Cs, lactate CE increased from 3 ± 3% unmodified to 17 ± 11% with DSFO+, and acetate CE increased from 6 ± 5% unmodified to 26 ± 13% with DSFO+. These global increases in CE suggest that incorporation of DSFO+ causes bacteria to produce more current per unit substrate. This feature has positive implications for DSFO+ in bioelectrochemical conversion: greater biocurrent production and more-efficient organic content removal are simultaneously allowed.

Once measurements were terminated, live/dead CFM was immediately performed to assess the toxicity of 1 μM DSFO+. The resulting images (Fig. V.S6) display sparse emission from propidium iodide (dead stain) relative to emission from DAPI (live stain), and there is no readily discernable difference in control and test reactors. This suggests low toxicity due to either DSFO+ or reactor conditions, consistent with the [DSFO+] = 1 μM < MIC determined earlier. Accordingly, the data in Figs. V.2 and V.3 and Table 1 appear to represent measurements of biologically-derived current.

After CFM characterization, electrodes were chemically fixed and dehydrated for imaging with SEM. Representative images obtained for each type of device are presented in Fig. V.4 A-F. Electrode surface cell density, ρ, is estimated from cell counts in such images. Values for ρ are summarized graphically in Fig. V.4 G and are presented numerically in Table 1. WT-M3Cs without DSFO+ support $\rho = 107 \pm 39 \times 10^9$ cells/m^2, while WT-M3Cs with 1 μM DSFO+ support $\rho = 113 \pm 46 \times 10^9$ cells/m^2, showing no significant difference in electrode association due to DSFO+. The Δ*mtrA*-M3Cs without DSFO+ support $\rho = 63 \pm 32 \times 10^9$ cells/m^2, while Δ*mtrA*-M3Cs with 1 μM DSFO+ support $\rho = 58 \pm 21 \times 10^9$ cells/m^2, also showing no significant difference in electrode association due to DSFO+. The Δ*mtrB*-

M3Cs without DSFO+ support $\rho = 67 \pm 40 \times 10^9$ cells/m^2, while Δ*mtrB*-M3Cs with 1 μM DSFO+ support $\rho = 28 \pm 13 \times 10^9$ cells/m^2, suggesting no significant difference in average electrode association due to DSFO+ (the mean values are different, but the standard deviations are large). The systematically lower values of ρ for Δ*mtrA*-M3Cs and Δ*mtrB*-M3Cs as compared to the WT-M3Cs are consistent with their lower current output (non-electrogenic phenotype) in Fig. V.3 C and E because electrode respiration (biocurrent production) is a driving force for electrode adhesion. Lower values of ρ are therefore also consistent with the accepted function of MtrB as the exposed docking site for the MtrC-OmcA proteins that are implicated in surface adhesion.[57,58] Because a reduction in electrode-associated cells limits the total M3C current output, this additionally agrees well with the CV traces in Fig. V.3 B, D and F that reveal smaller-amplitude biocatalytic current outputs from the DSFO+-modified mutant strains despite constant additions of 1 μM DSFO+. These consistencies further support the conclusion that current amplifications are biologically-derived.

Because there is no significant measured difference in ρ with and without DSFO+ for any of the strains, we conclude that biocurrent output per bacterial cell, I_{cell}, increases upon addition of DSFO+. One illustrative measure of I_{cell} is given by dividing the current density at $t = 2$ h, J_2, by the value of ρ for the same reactor conditions, given by

$$I_{cell} = J_2/\rho \qquad \text{(V.2)}.$$

Note that ρ is measured at $t \geq 19$ h, at which time it must be larger than it would have been at $t = 2$ h for any reactor conditions; I_{cell} is therefore a lower bound on the amperage

produced by each cell. These data are summarized in Table 1, and as can be seen, addition of DSFO+ to test reactors causes I_{cell} to increase 1.4-fold, 3.7-fold, and 3.0-fold for WT, Δ*mtrA*, and Δ*mtrB*, respectively. This contrasts with previously observed PPV-COE enhancements to *S. oneidensis* MR-1 M3Cs that show increased total current but decreased current on a per-cell basis.[24] These data therefore agree with the conclusion that the mechanism of enhancement from adding DSFO+ (respiratory redox coupling) is different than that from additions of PPV-COEs (native DET enhancement).

The possibilities that direct DSFO+ or lactate oxidation accounts for the current amplification or that DSFO+ directly catalyzes lactate-to-current conversion in the absence of bacteria are ruled out by three experiments. First, abiotic (negative control) M3Cs containing growth media and DSFO+ produce negligible current by CA under conditions identical to those in Figs. V.2 and V.3, indicating that neither DSFO+ nor lactate oxidation is the source of current (see Fig. V.S7 A). Moreover, a one-electron oxidation of 1 μM DSFO+ in these reactors (15 mL volume) could provide at most Q = [DSFO+]VFn = (1 μM)(15 mL)(96485 C/mol e^-)(1 e^-) = 0.0014 C of electrons to the working electrode. DSFO+ oxidation therefore cannot account for the increase in charge collected by >100-fold in even the lowest-current M3Cs in this work, which produce 0.20 ± 0.11 C. Second, the lactate concentration does not decrease for the same M3Cs during the CA experiments, confirming that lactate is not being oxidized in the absence of bacteria. Third, CV conducted in the potential range −0.6 V < E < 0.4 V on the same M3Cs (Fig. V.S7 B) lacks a faradaic current signal associated with DSFO+, further ruling out DSFO+ oxidation and remaining consistent with the E = 0.62 V onset of oxidation of aqueous DSFO+ determined in Fig. V.1 E.

These control experiments provide additional supporting evidence that the amplified

current observed upon addition of DSFO+ must be of biological origin. The data in this work are consistent with DSFO+ improving *S. oneidensis* MR-1 electrode respiration and partially rescuing electrogenic character in the non-electrogenic Δ*mtrA* and Δ*mtrB* mutant strains. This successful biocurrent amplification by direct biotic-abiotic interfacial modification broadly illuminates a new strategy in the field of bioelectronics. It is now apparent that incorporation of an appropriately designed synthetic redox-active molecular protein prosthetic is a valid approach for amplifying and rescuing catalytic biocurrent.

V.D. References

1. Bond, D. R., Holmes, D. E., Tender, L. M. & Lovley, D. R. Electrode-reducing microorganisms that harvest energy from marine sediments. *Science* **295,** 483–5 (2002).
2. Lovley, D. R. Bug juice: harvesting electricity with microorganisms. *Nat. Rev. Microbiol.* **4,** 497–508 (2006).
3. Lovley, D. R. Extracellular electron transfer: wires, capacitors, iron lungs, and more. *Geobiology* **6,** 225–31 (2008).
4. Torres, C. I. *et al.* Selecting anode-respiring bacteria based on anode potential: phylogenetic, electrochemical, and microscopic characterization. *Environ. Sci. Technol.* **43,** 9519–24 (2009).
5. Logan, B. E. Exoelectrogenic bacteria that power microbial fuel cells. *Nat. Rev. Microbiol.* **7,** 375–81 (2009).
6. Clarke, T. A. *et al.* Structure of a bacterial cell surface decaheme electron conduit. *Proc. Natl. Acad. Sci. U. S. A.* **108,** 9384–9 (2011).
7. Lovley, D. R. Electromicrobiology. *Annu. Rev. Microbiol.* **66,** 391–409 (2012).
8. Jensen, H. M. *et al.* Engineering of a synthetic electron conduit in living cells. *Proc. Natl. Acad. Sci.* **107,** 19213–19218 (2010).
9. Goldbeck, C. P. *et al.* Tuning Promoter Strengths for Improved Synthesis and Function of Electron Conduits in Escherichia coli. *ACS Synth. Biol.* **2,** 150–9 (2013).
10. Sydow, A., Krieg, T., Mayer, F., Schrader, J. & Holtmann, D. Electroactive bacteria-molecular mechanisms and genetic tools. *Appl. Microbiol. Biotechnol.* **98,** 8481–95 (2014).
11. Du, J., Catania, C. & Bazan, G. Modification of Abiotic–Biotic Interfaces with Small Molecules and Nanomaterials for Improved Bioelectronics. *Chem. Mater.* **26,** 686–697 (2013).
12. Malliaras, G. & Abidian, M. R. Organic Bioelectronic Materials and Devices. *Adv. Mater.* **27,** 7492–7492 (2015).
13. *Physics of Organic Semiconductors*. (John Wiley & Sons, 2012).
14. *Conjugated Polyelectrolytes: Fundamentals and Applications*. (John Wiley & Sons, 2013).

15. *Design and Synthesis of Conjugated Polymers*. (John Wiley & Sons, 2010).
16. Garner, L. E. *et al.* Modification of the optoelectronic properties of membranes via insertion of amphiphilic phenylenevinylene oligoelectrolytes. *J. Am. Chem. Soc.* **132,** 10042–52 (2010).
17. Garner, L. E., Thomas, A. W., Sumner, J. J., Harvey, S. P. & Bazan, G. C. Conjugated oligoelectrolytes increase current response and organic contaminant removal in wastewater microbial fuel cells. *Energy Environ. Sci.* **5,** 9449–9452 (2012).
18. Wang, V. B. *et al.* Improving charge collection in Escherichia coli-carbon electrode devices with conjugated oligoelectrolytes. *Phys. Chem. Chem. Phys.* **15,** 5867–72 (2013).
19. Hou, H. *et al.* Conjugated Oligoelectrolytes Increase Power Generation in E. coli Microbial Fuel Cells. *Adv. Mater.* **25,** 1593–7 (2013).
20. Thomas, A. W. *et al.* A lipid membrane intercalating conjugated oligoelectrolyte enables electrode driven succinate production in Shewanella. *Energy Environ. Sci.* **6,** 1761 (2013).
21. Wang, V. B. *et al.* Comparison of flavins and a conjugated oligoelectrolyte in stimulating extracellular electron transport from Shewanella oneidensis MR-1. *Electrochem. commun.* **41,** 55–58 (2014).
22. Thomas, A. W., Catania, C., Garner, L. E. & Bazan, G. C. Pendant ionic groups of conjugated oligoelectrolytes govern their ability to intercalate into microbial membranes. *Chem. Commun.* **51,** 9294–9297 (2015).
23. Kirchhofer, N. D., Rasmussen, M. A., Dahlquist, F. W., Minteer, S. D. & Bazan, G. C. The photobioelectrochemical activity of thylakoid bioanodes is increased via photocurrent generation and improved contacts by membrane-intercalating conjugated oligoelectrolytes. *Energy Environ. Sci.* **8,** 2698–2706 (2015).
24. Kirchhofer, N. D. *et al.* The conjugated oligoelectrolyte DSSN+ enables exceptional coulombic efficiency via direct electron transfer for anode-respiring Shewanella oneidensis MR-1-a mechanistic study. *Phys. Chem. Chem. Phys.* **16,** 20436–43 (2014).
25. Arrhenius, T. S., Blanchard-Desce, M., Dvolaitzky, M., Lehn, J. M. & Malthete, J. Molecular devices: Caroviologens as an approach to molecular wires-synthesis and incorporation into vesicle membranes. *Proc. Natl. Acad. Sci. U. S. A.* **83,** 5355–5359 (1986).
26. Davis, W., Svec, W., Ratner, M. & Wasielewski, M. Molecular-wire behaviour in p-phenylenevinylene oligomers. *Nature* **396,** 60–63 (1998).
27. Mujica, V., Kemp, M., Roitberg, A. & Ratner, M. Current-voltage characteristics of molecular wires: Eigenvalue staircase, Coulomb blockade, and rectification. *J. Chem. Phys.* **104,** 7296–7305 (1996).
28. Hipps, K. It's all about contacts. *Science.* **294,** 536–538 (2001).
29. Du, J. *et al.* Increased ion conductance across mammalian membranes modified with conjugated oligoelectrolytes. *Chem. Commun.* **49,** 9624–6 (2013).
30. Jahnke, J. P., Bazan, G. C. & Sumner, J. J. Effect of Modified Phospholipid Bilayers on the Electrochemical Activity of a Membrane-Spanning Conjugated Oligoelectrolyte. *Langmuir* **31,** 11613–11620 (2015).
31. Bond, A. M., McLennan, E. A., Stojanovic, R. S. & Thomas, F. G. Assessment of conditions under which the oxidation of ferrocene can be used as a standard voltammetric reference process in aqueous media. *Anal. Chem.* **50,** 2853–2860 (1987).

32. Cardona, C. M., Li, W., Kaifer, A. E., Stockdale, D. & Bazan, G. C. Electrochemical considerations for determining absolute frontier orbital energy levels of conjugated polymers for solar cell applications. *Adv. Mater.* **23,** 2367–71 (2011).
33. Connelly, N. G. & Geiger, W. E. Chemical Redox Agents for Organometallic Chemistry. *Chem. Rev.* **96,** 877–910 (1996).
34. Rabaey, K. & Rozendal, R. A. Microbial electrosynthesis -- revisiting the electrical route for microbial production. *Nat. Rev. Microbiol.* **8,** 706–16 (2010).
35. Marsili, E., Rollefson, J. B., Baron, D. B., Hozalski, R. M. & Bond, D. R. Microbial biofilm voltammetry: direct electrochemical characterization of catalytic electrode-attached biofilms. *Appl. Environ. Microbiol.* **74,** 7329–37 (2008).
36. Rosenbaum, M., Aulenta, F., Villano, M. & Angenent, L. T. Cathodes as electron donors for microbial metabolism: which extracellular electron transfer mechanisms are involved? *Bioresour. Technol.* **102,** 324–33 (2011).
37. Marsili, E. *et al.* Shewanella secretes flavins that mediate extracellular electron transfer. *Proc. Natl. Acad. Sci. U. S. A.* **105,** 3968–73 (2008).
38. Fredrickson, J. K. *et al.* Towards environmental systems biology of Shewanella. *Nat. Rev. Microbiol.* **6,** 592–603 (2008).
39. Hau, H. H. & Gralnick, J. A. Ecology and biotechnology of the genus Shewanella. *Annu. Rev. Microbiol.* **61,** 237–258 (2007).
40. Renslow, R. *et al.* Modeling biofilms with dual extracellular electron transfer mechanisms. *Phys. Chem. Chem. Phys.* **15,** 19262–83 (2013).
41. White, G. F. *et al.* Rapid electron exchange between surface-exposed bacterial cytochromes and Fe(III) minerals. *Proc. Natl. Acad. Sci. U. S. A.* **110,** 6346–51 (2013).
42. Baron, D., LaBelle, E., Coursolle, D., Gralnick, J. A. & Bond, D. R. Electrochemical measurement of electron transfer kinetics by Shewanella oneidensis MR-1. *J. Biol. Chem.* **284,** 28865–73 (2009).
43. Roy, J. N. *et al.* Catalytic biofilm formation by Shewanella oneidensis MR-1 and anode characterization by expanded uncertainty. *Electrochim. Acta* **126,** 3–10 (2014).
44. Hartshorne, R. S. *et al.* Characterization of an electron conduit between bacteria and the extracellular environment. *Proc. Natl. Acad. Sci. U. S. A.* **106,** 22169–74 (2009).
45. Richardson, D. J. *et al.* The 'porin-cytochrome' model for microbe-to-mineral electron transfer. *Mol. Microbiol.* **85,** 201–212 (2012).
46. Shi, L. *et al.* Isolation of a high-affinity functional protein complex between OmcA and MtrC: Two outer membrane decaheme c-type cytochromes of Shewanella oneidensis MR-1. *J. Bacteriol.* **188,** 4705–14 (2006).
47. Coursolle, D., Baron, D. B., Bond, D. R. & Gralnick, J. A. The Mtr respiratory pathway is essential for reducing flavins and electrodes in Shewanella oneidensis. *J. Bacteriol.* **192,** 467–74 (2010).
48. Barry, K. P. & Nataro, C. A new synthesis and electrochemistry of 1,1'-bis(beta-hydroxyethyl)ferrocene. *Inorganica Chim. Acta* **362,** 2068–2070 (2009).
49. Patwa, A. N., Gonnade, R. G., Kumar, V. A., Bhadbhade, M. M. & Ganesh, K. N. Ferrocene-bis(thymine/uracil) conjugates: Base pairing directed, spacer dependent self-assembly and supramolecular packing. *J. Org. Chem.* **75,** 8705–8708 (2010).
50. Lin, A., Willis, A. C. & Banwell, M. G. A chemoenzymatic and enantioselective total synthesis of the resorcylic acid lactone L-783,290, the trans-isomer of L-783,277. *Tetrahedron Lett.* **51,** 1044–1047 (2010).

51. Mertz, E. & Zimmerman, S. C. Cross-linked dendrimer hosts containing reporter groups for amine guests. *J. Am. Chem. Soc.* **125,** 3424–3425 (2003).
52. Kassner, R. J. Effects of Nonpolar Environments on the Redox Potentials of Heme Complexes. *Proc. Natl. Acad. Sci. U. S. A.* **69,** 2263–2267 (1972).
53. Marsh, B. J., Hampton, L., Goggins, S. & Frost, C. G. Fine-tuning of ferrocene redox potentials towards multiplex DNA detection. *New J. Chem.* **38,** 5260–5263 (2014).
54. Blainey, P., Krzywinski, M. & Altman, N. Points of Significance: Replication. *Nat. Methods* **11,** 879–880 (2014).
55. Dilger, J. P., McLaughlin, S. G., McIntosh, T. J. & Simon, S. A. The dielectric constant of phospholipid bilayers and the permeability of membranes to ions. *Science* **206,** 1196–1198 (1979).
56. Gramse, G., Dols-Perez, A., Edwards, M. A., Fumagalli, L. & Gomila, G. Nanoscale measurement of the dielectric constant of supported lipid bilayers in aqueous solutions with electrostatic force microscopy. *Biophys. J.* **104,** 1257–1262 (2013).
57. Myers, C. R. & Myers, J. M. MtrB is required for proper incorporation of the cytochromes OmcA and OmcB into the outer membrane of Shewanella putrefaciens MR-1. *Appl. Environ. Microbiol.* **68,** 5585–5594 (2002).
58. Coursolle, D. & Gralnick, J. A. Modularity of the Mtr respiratory pathway of Shewanella oneidensis strain MR-1. *Mol. Microbiol.* **77,** 995–1008 (2010).
59. Cao, B. *et al.* Biofilm shows spatially stratified metabolic responses to contaminant exposure. *Environ. Microbiol.* **14,** 2901–10 (2012).
60. Cao, B. *et al.* Extracellular polymeric substances from Shewanella sp. HRCR-1 biofilms: characterization by infrared spectroscopy and proteomics. *Environ. Microbiol.* **13,** 1018–31 (2011).
61. Andrews, J. M. Determination of minimum inhibitory concentrations. *J. Antimicrob. Chemother.* **48,** 5–16 (2001).
62. Ji, E., Corbitt, T. S., Parthasarathy, A., Schanze, K. S. & Whitten, D. G. Light and dark-activated biocidal activity of conjugated polyelectrolytes. *ACS Appl. Mater. Interfaces* **3,** 2820–9 (2011).

V.E. Appendix V. Materials, Methods, and Supplementary Figures

V.E.1. Materials and Methods

V.E.1.a General information for the synthesis of DSFO(Me)$_4$ and DSFO+

The full synthetic route to the compounds of interest is provided in Scheme V.S1, and preparations of intermediate compounds are provided below. Unless otherwise noted, materials were purchased from suppliers (Sigma Aldrich, Acros, Strem, and TCI) and were used without further purification. ^{1}H and ^{13}C NMR spectra were recorded on either a Bruker DMX 500 MHz or Varian VNMRS 600 MHz spectrometer and all chemical shifts are reported in ppm values (δ) versus tetramethylsilane. Dry toluene and dry, inhibitor-free THF were taken from a solvent purification system, using packed alumina columns under Argon. Silica gel column chromatography was purchased from Dynamic Adsorbents Inc. and had particle size of 32-64 μM. Compounds 2 and 3 were synthesized according to literature procedures.[50,51]

V.E.1.b. Preparation of 1,3-bis((6-bromohexyl)oxy)-5-iodobenzene (4)

1 g of 1-iodo-3,5-dihydroxybenzene (3) (1 eq., 4.24 mmol), 6.5 mL of 1,6-dibromohexane (10 eq., 42.4 mmol), and 1.758 g of K_2CO_3 (3 eq., 12.72 mmol) were charged into a 50 mL round bottom flask. Then, 10 mL of dry acetone was added and the flask equipped with a reflux condenser and an argon line was attached. The solution was allowed to reflux for 18 hours and cooled to room temperature. The resulting solution was diluted with dichloromethane and filtered through a celite plug. The solvent was removed *in vacuo* and the resulting yellow oil was purified using silica gel chromatography with 20%

(v/v) dichloromethane in hexane to give a clear oil, which was the desired product contaminated with excess 1,6-dibromohexane. The oil was triturated with methanol (~10 mL) three times to give 1.471 (62% yield) of a white powder. ^{1}H NMR (500 MHz, $CDCl_3$) δ = 6.86 (d, *J*=2.5, 2H), 6.41 (t, *J*=2.7, 1H), 3.93 (t, *J*=6.4, 4H), 3.45 (t, *J*=6.8, 4H), 1.92 (p, *J*=6.7, 4H), 1.79 (p, *J*=6.8, 4H), 1.51 (m, *J*=10.8, 5.5, 8H). ^{13}C NMR (600 MHz, $CDCl_3$) δ 160.49, 116.24, 101.42, 94.05, 67.95, 33.74, 32.63, 28.93, 27.85, 25.22.

V.E.1.c. Preparation of 1,3-bis((6-iodohexyl)oxy)-5-iodobenzene (5)

500 mg (1 eq., 0.89 mmol) of 1-iodo-3,5-bis((6-bromohexyl)oxy)benzene, 738 mg of sodium iodide (5 eq., 4.45 mmol) and 20 mL of dry acetone were charged into a 50 mL 3-neck round bottom flask. The solution was heated to reflux under an inert atmosphere for 6 hours. The solution was cooled to room temperature, diluted with dichloromethane, and filtered through a silica plug. After the removal of solvent, the product was purified using a short silica gel column with 20% (v/v) dichloromethane in hexane to give 581 mg (98% yield) of a light yellow oil that solidifies to a white powder. ^{1}H NMR (500 MHz, $CDCl_3$) δ = 6.86 (d, *J*=2.2, 2H), 6.41 (t, *J*=2.2, 1H), 3.92 (t, *J*=6.3, 4H), 3.23 (t, *J*=6.9, 4H), 1.88 (m, *J*=7.7, 3.9, 3.4, 4H), 1.79 (m, *J*=10.0, 8.3, 5.2, 4H), 1.50 (p, *J*=3.6, 8H). ^{13}C NMR (600 MHz, $CDCl_3$) δ 160.53, 116.30, 101.50, 94.07, 67.99, 33.37, 30.20, 28.91, 25.02, 6.88.

V.E.1.d. Preparation of E-1,1'-bis(2-(3,5-((6-iodohexyl)oxy)phenyl)ethenyl)ferrocene (6)

In a nitrogen filled glovebox, 317 mg of 1-iodo-3,5-bis((6-iodohexyl)oxy)benzene (2.3 eq., 0.48 mmol), 50 mg of 1,1'-divinylferrocene (1 eq., 0.21 mmol), 3 mg palladium acetate (5 mol %, 0.011 mmol), 10 mg XPhos (10 mol %, 0.021 mmol), 0.15 mL diisopropylethylamine (4 eq., 0.84 mmol), and 1.5 mL of toluene were charged into a 0.5-2

mL microwave tube. This tube was sealed and heated at 100 ^{o}C in a pre-heated oil bath for 8 hours. The solution was allowed to cool to room temperature and was directly loaded onto a silica gel column using 19% (v/v) toluene and 1% (v/v) ethyl acetate in hexane to give 130 mg (48% yield) of a deep red oil. ^{1}H NMR (500 MHz, $CDCl_3$) δ = 6.76 (d, *J*=16.1, 2H), 6.58 (d, *J*=16.1, 2H), 6.49 (d, *J*=2.1, 4H), 6.34 (t, *J*=2.1, 2H), 4.42 (t, *J*=1.7, 4H), 4.28 (t, *J*=1.8, 4H), 3.91 (t, *J*=6.4, 8H), 3.25 (t, *J*=7.0, 0.7, 8H), 1.96 – 1.85 (m, 8H), 1.81 (m, 8H), 1.55 – 1.43 (m, 16H). ^{13}C NMR (600 MHz, CD_2Cl_2) δ 160.35, 139.61, 126.49, 126.40, 104.05, 100.15, 83.95, 70.21, 67.96, 67.70, 33.52, 30.28, 29.12, 25.05, 7.21.

V.E.1.e. Preparation of E-1,1'-bis(2-(3,5-dimethoxyphenyl)ethenyl)ferrocene (DSFO(Me)$_4$) (7)

In a nitrogen filled glovebox, 238 mg of 1-iodo-3,5-dimethypxy)benzene (2) (2.3 eq., 0.97 mmol), 100 mg of 1,1'-divinylferrocene (1 eq., 0.42 mmol), 5 mg palladium acetate (5 mol %, 0.021 mmol), 20 mg XPhos (10 mol %, 0.042 mmol), 0.44 mL diisopropylethylamine (6 eq., 0.84 mmol), and 1.5 mL of toluene were charged into a 0.5-2 mL microwave tube. This tube was sealed and heated at 100 ^{o}C in a pre-heated oil bath for 8 hours. The solution was allowed to cool to room temperature and was directly loaded onto a silica gel column using 5% (v/v) dichloromethane and 10% (v/v) ethyl acetate in hexane. After completion of the column, the desired product crystallized out of solution in the collection test tubes and was collected by filtration to give 104 mg (49% yield) of a deep red crystalline solid. ^{1}H NMR (500 MHz, $CDCl_3$) δ = 6.73 (d, *J*=16.1, 1H), 6.57 (d, *J*=16.1, 1H), 6.48 (d, *J*=2.2, 2H), 6.34 (t, *J*=2.2, 1H), 4.43 (t, *J*=2.0, 2H), 4.29 (t, *J*=1.9, 2H), 3.78 (s, 6H). ^{13}C NMR (600 MHz, $CDCl_3$) δ 160.49, 116.24, 101.45, 94.04, 68.02, 67.95, 33.73, 32.63, 29.03, 28.93, 27.85, 25.22.

V.E.1.f. Preparation of E-1,1'-bis(2-(3,5-((6-trimethylammoniumhexyl)oxy)phenyl) ethenyl)ferrocene tetraiodide (DSFO+) (8)

50 mg (1 eq., 38.6 μmol) of E-1,1'-bis(2-(3,5-((6-iodohexyl)oxy)phenyl) ethenyl)ferrocene was weighed into a 10 mL round bottom flask and 5 mL of dry, inhibitor-free THF was added via syringe and the flask sealed with a septum. Then, 0.3 mL (20 eq., 0.772 mmol) of 3.2 M trimethylamine solution in methanol was added via syringe. The solution was allowed to stir for 24 hours, at which time a red semi-solid precipitate remains. The THF was removed *in vacuo* and the resulting semi-solid was dissolved in methanol and another 0.3 mL of trimethylamine solution was added. After stirring for another 24 hours, the solvent was removed *in vacuo* and the resulting semi-solid was dissolved in deionized water and lyophilized to give a deep red, fluffy solid of mass 59 mg (quantitative yield). 1H NMR (500 MHz, D2O, 340K) δ = 7.04 (d, *J*=16.2, 2H), 6.86 (d, *J*=16.1, 2H), 6.78 (d, *J*=2.2, 4H), 6.73 (t, *J*=2.1, 2H), 4.84 (t, *J*= 1.3, 4H), 4.63 (t, *J*= 1.3, 4H), 4.22 (t, *J*=6.5, 8H), 3.61 – 3.57 (m, 8H), 3.41 (s, 36H), 2.11 – 2.02 (m, 16H), 1.85 – 1.77 (m, 8H), 1.73 (m, 8H). ^{13}C NMR (600 MHz, D_2O, 313K) δ 160.20, 139.64, 127.09, 126.14, 104.77, 100.49, 68.41, 67.56, 66.69, 53.50, 32.88, 29.03, 25.87, 25.45, 23.09, 22.81.

V.E.1.g. Density Functional Theory (DFT) Calculations

All DFT calculations were performed using Gaussian09 software suite with GuassView5. The geometry optimizations and frontier orbital visualizations utilized the B3LYP/6-311G** functional/basis set.

V.E.1.h. Cell Culture and Inoculation

Strains of *Shewanella oneidensis* MR-1 were struck out on LB agar plates from frozen

bacterial stock and incubated at 30 °C for ~24 hours to isolate single colonies. Biological replicate cultures were grown by selecting morphologically similar colonies with a sterile loop to inoculate anaerobic (actively bubbling with N_2 gas) modified M1 medium[59,60] containing 20 mM Na-(L)-lactate as donor and 20 mM Na-fumarate as acceptor. After 24 hours of incubation with shaking at 30 °C, such cultures consistently reach a maximum OD_{600} of ~0.16 (or 1.6×10^8 cfu/mL, as *Shewanella oneidensis* MR-1 was previously determined to be $\sim 1 \times 10^9$ cfu/mL/OD.[24] These stationary phase cultures (fumarate completely consumed) may then be used to inoculate separate replicate M3Cs or MIC assay tubes as described.

V.E.1.i. Microbial 3-electrode electrochemical cells (M3Cs)

The 3-electrode, batch-type, membraneless bioelectrochemical reactors used herein (M3Cs) were similar to those previously reported;[24] key components are described here. Glass M3C vials had a 15 mL working volume and were sealed with rubber septa. Electrode specifications were as follows. Reference electrode: Ag/AgCl (saturated KCl) with 3.2 mm Vycor frit (Gamry). Counter electrode: coiled 0.25 mm Ti wire (Aldrich), 10 turns. Working electrode: 1 cm × 1 cm × 0.2 cm graphite felt (Alfa Aesar), woven with Ti wire as the electrical lead. Anaerobic conditions were maintained through constant headspace degassing with humidified, deoxygenated N_2. Temperature was kept at 30 °C by housing the M3Cs in a temperature regulated incubator.

V.E.1.j. Cyclic Voltammetry (CV)

For characterization of $DSFO(Me)_4$, the working electrode potential was swept twice from $E_{initial} = E_{final} = 0$ V to $E_{vertex} = 0.8$ V and back at a scan rate of 0.01 V/s, and the second

trace was used for analysis. The concentration of $DSFO(Me)_4$ was kept constant at 10 μM and the supporting electrolyte, tetrabutylammonium hexafluorophosphate, was also invariant at 100 mM. $DSFO(Me)_4$ was investigated in chloroform, acetonitrile, and dimethyl sulfoxide as solvents (Fig. V.S1 A). For characterization of DSFO+, the potential was also swept twice from $E_{initial} = E_{final} = 0$ V to $E_{vertex} = 0.8$ V and back at a scan rate of 0.01 V/s, and the second trace was kept for analysis. The concentration of DSFO+ remained constant at 10 μM and the supporting electrolyte was invariant at 100 mM. DSFO+ was investigated in water with 100 mM phosphate buffer (pH = 7.2) as electrolyte (Fig. V.S2), in Ethanol/methanol (1:1 volume/volume) with 100 mM sodium perchlorate as electrolyte, and dimethyl sulfoxide with 100 mM tetrabutylammonium hexafluorophosphate as electrolyte (Fig. V.S1 B). The different supporting electrolytes used were chosen for their electrochemical inertness and their solubility in the desired solvent, as it was not possible to find a single electrolyte soluble in all of the desired solvents.

At various timepoints during CA measurements, current monitoring was paused for CV analyses of the electrode-respiring biofilms. For such experiments, CV parameters were as follows: $E_{initial} = E_{final} = -0.6$ V; $E_{vertex} = 0.4$ V; scan rate = 0.005 V/s.

V.E.1.k. Ultraviolet-Visible Absorbance Spectroscopy

Solutions were illuminated at 1 nm wavelength intervals at a scan rate of 20 nm/s (Beckman Coulter DU 800 Spectrophotometer) in a quartz cuvette with 1 cm path length. DSFO+ and $DSFO(Me)_4$ spectra may be found in Fig. V.S3.

V.E.1.l. DSFO+ Minimum Inhibitory Concentration (MIC) Determination

A filter-sterile 1 mM stock solution of DSFO+ was prepared in M1 medium. M1 was

used so that upon additions of varying volumes of this stock to test conditions, the basal composition of the growth medium was invariant. Triplicate 10 mL volumes of M1 medium containing 20 mM Na-(L)-lactate as donor and 20 mM Na-fumarate as acceptor were then prepared in capped anaerobic test tubes with the following concentrations of DSFO+ (volume of 1 mM stock added to 10 mL provided in parenthesis): 0 μM (0 μL), 0.1 μM (1 μL), 0.2 μM (2 μL), 0.5 μM (5 μL), 1 μM (10 μL), 2.25 μM (22.5 μL), 5 μM (50 μL), 11.25 μM (112.5 μL), 25 μM (250 μL). These concentrations were selected for two reasons. They contain previously tested COE concentrations of 1.0 μM, 5.0 μM, and 25.0 μM, and the remaining values fall between those on a base-5 logarithmic scale in approximately half-order of magnitude increments. Finally, 0.5% additions (50 μL per 10 mL test volume) of triplicate bacterial cultures were inoculated into corresponding triplicate test replicates for starting cell loadings of ~8 × 10^6 cfu/mL (this has an undetectable OD_{600} with the spectrometer and by eye). Test tubes were incubated at 30 °C for 72 hours without stirring, and the MIC was read as the lowest concentration that completely inhibited growth.[61] Results are summarized in Fig. V.S4.

V.E.1.m. Chronoamperometry (CA)

Using a Gamry potentiostat (Reference 600, Series G 300 or Series G 750 models) and multiplexer (model ECM8), M3C graphite felt working electrodes were poised at E = 0.27 V vs. Ag/AgCl to serve as the sole terminal electron acceptor for the organisms. Freshly inoculated M3Cs were incubated in the dark[62] with 100 rpm magnetic stirring for 16 hours to promote growth of an electroactive biofilm. Then a full media change was undertaken to replenish the lactate donor to 20 mM and deconvolute the biofilm from planktonic cell signals. Electrochemical characterization with CV was immediately used to characterize the

biofilm. Steps following this CV are different depending on the nature of the ensuing experiment, as follows.

For determination of the optimal *in operando* concentration of DSFO+ (Fig. V.S5), CA was then resumed at E = 0.27 V and DSFO+ was injected ~2 hours later at a series of concentrations below the MIC determined above. These M3Cs then operated for an additional 11 hours and were terminated.

For mechanistic experiments (Fig. V.2 in the main text), CA was then resumed at E = 0.27 V and DSFO+ was injected ~1 hour later at 1 μM. The system was allowed to operate for an additional ~1 hour, and then CA was paused for CV analyses. Then CA was resumed and current was continuously monitored until the end of M3C operation.

The current response was measured, recorded, and averaged for 20-second blocks (at 160 second intervals) with Gamry software (Framework Version 6.11, Build 2227, 2013). Time integration of the resulting current response determined the amount of charge transferred by the bacteria, Q_{coll} (Table 1).

V.E.1.n. Preparation of Confocal Microscopy Samples

Immediately after the completion of M3C operation, the anode containing the biofilm was blotted dry using a Kimwipe. Then, the electrode was immersed in a water solution containing 10 μM 4',6-diamidino-2-phenylindole (DAPI, live stain) and 5 μM propidium iodide (PI, dead stain) for 30 minutes. The electrode was next blotted dry, briefly immersed in deionized water to remove excess dye, and blotted dry again in two consecutive cycles. Next, a small portion of the electrode was cut off, placed on a microscope cover slip, covered in Type B immersion oil, and a piece of tape was placed on top to prevent movement of the sample. These samples were immediately taken to the confocal microscope and imaged

within 1 hour of sample preparation.

V.E.1.o. Confocal Microscope Images of M3C Electrodes

Fluorescence emission images and concomitant co-localized bright field images were acquired on an inverted Olympus IX81 instrument equipped with a 60X objective. In order to separately image the emission from each chromophore, the instrument was set to the proper excitation wavelength maxima for DAPI ($\lambda_{abs.\ max.}$ = 358 nm) and PI ($\lambda_{abs.\ max.}$ = 535 nm), and separate emission spectra were collected for DAPI ($\lambda_{em.\ max}$ = 461 nm) and PI ($\lambda_{em.\ max}$ = 617 nm). The confocal images are presented as a 4×4 set of images for each condition, as shown in Fig. V.S6. In each panel of that figure, the upper left image is the DAPI emission channel, the upper right image is the PI emission channel, the lower left image is the overlay of DAPI and PI emission channels, and the bottom right image is brightfield transmittance to image the electrode (this image is black due to the opaque nature of the electrode).

V.E.1.p. High Performance Liquid Chromatography (HPLC)

HPLC analysis of M3C effluent was performed with a Shimadzu LC20AB instrument equipped with an organic acid compatible Aminex HPX-87H column (Bio-Rad). Samples from M3Cs were filtered through 0.22 μm PVDF filters (GSTek) to remove cells, and diluted 10-fold into mobile phase prior to analysis. The mobile phase was 0.004 M (0.008 N) aqueous H_2SO_4 flowing at 0.6 mL/min, and UV detection was set at 210 nm.

V.E.1.q. Coulombic Efficiency (CE) Determination

The efficiency of the bioelectronic system in converting lactate to electricity was calculated by first integrating the current density response in Fig. V.3 A, C, and E (main text) from t = 0 to t = 21 to obtain the total charge collected, Q_{coll} (in Coulombs):

$$Q_{coll} = A \int_0^{21} J(t)dt \quad \text{(V.S1)},$$

where A is the surface area of the electrode, previously determined to be A = 0.0226 ± 0.0012 m^2 [24]. For the same time period, the concentrations of lactate and acetate were monitored in the M3C with HPLC to determine the decrease in lactate concentration, Δ[lac], and increase in acetate concentration, Δ[ac]. By Eq. V.1 (main text) each consumed lactate molecule should yield 4 e^-, representing 100% CE:[40]

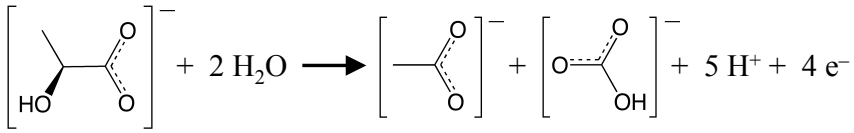

(V.S2).

The charge equivalent (in Coulombs) of the consumed lactate and produced acetate is given by the expression

$$Q_{ideal} = -\Delta[\text{lac}]VFn \quad \text{(V.S3)},$$

where V is the volume of the M3C (15 mL), F is the Faraday constant (equal to eN_A = 9.64853 × 10^4 C/mol), and n = 4 is the number of electrons theoretically produced per lactate molecule consumed (Eq. V.S2). Finally, CE is the ratio of Q_{coll} to either Q_{lac} or Q_{ac} in percent form:

$$CE_{lac/ac} = 100\left(\frac{Q_{coll}}{Q_{lac/ac}}\right) \quad \text{(V.S4)}.$$

V.E.1.r. Chemical Fixation of Electrodes

After all bioelectrochemical and confocal microscopy experiments, M3C working electrodes were submerged in 100 mM PBS, pH = 7 containing 2% (v/v) formaldehyde to fix electrode-associated cells. This was allowed to sit for 24 hours. After fixation, electrodes were sequentially rinsed with the following solutions twice each: 100 mM PBS, pH = 7 (10 min), deionized water (10 min), 70% ethanol in deionized water (10 min), 100% ethanol (30 min). Electrodes were then allowed to air dry for 24 hours and stored in glass scintillation vials for future study.

V.E.1.s. Scanning Electron Microscopy and Cell Counting

Images of chemically fixed graphite felt electrodes were obtained with an FEI XL40 SEM at an accelerating voltage of 5 kV, working distance of ~5 mm, and a spot size of 3. Post processing of images only involved increasing the brightness and/or contrast of the images by up to 40% in order to better visualize cells. Assuming a cylindrical geometry so that surface area of each graphite fiber could be approximated by $\pi d_k h_k$ (where d_k = diameter, h_k = height of cylinder), the SEM scale bar was used to determine d_k and divide the imaged graphite fiber into K sections of height h_k. Then the number of visible cells was counted in each section. It was assumed that the visible cells accounted for one half of the total number of cells on a given fiber, so the counted number was multiplied by 2 to determine the total cells per cylindrical section, N_i. The expression for the number average cell density for each electrode, ρ, is given in Eq. V.S5. An example of this method has been previously reported.[24]

$$\rho = \frac{1}{K}\sum_{k=1}^{K}(\rho_k) = \frac{1}{K}\sum_{i=1}^{K}\left(\frac{N_k}{\pi d_k h_k}\right) \quad \text{(V.S5).}$$

V.E.2. Supplementary Figures

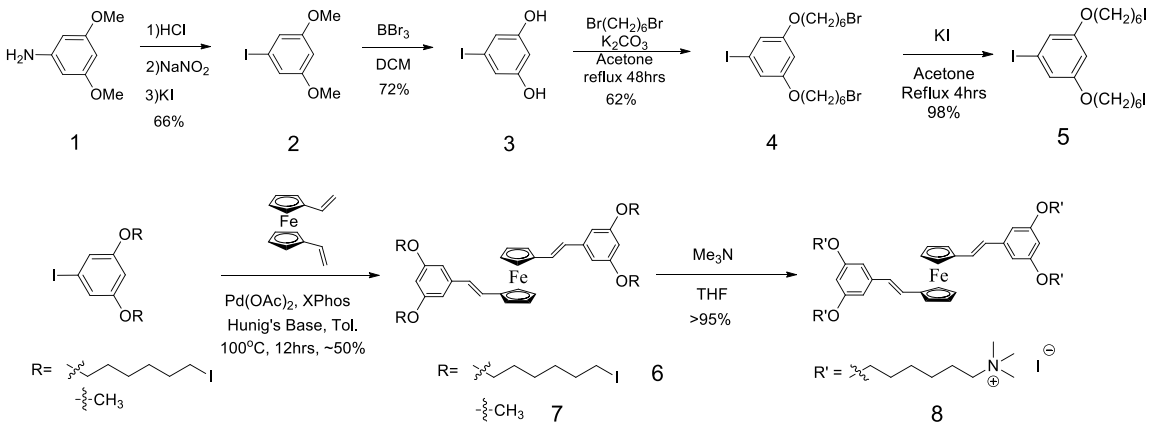

Scheme V.S1. Synthetic route to DSFO(Me)$_4$ (7) and DSFO+ (8).

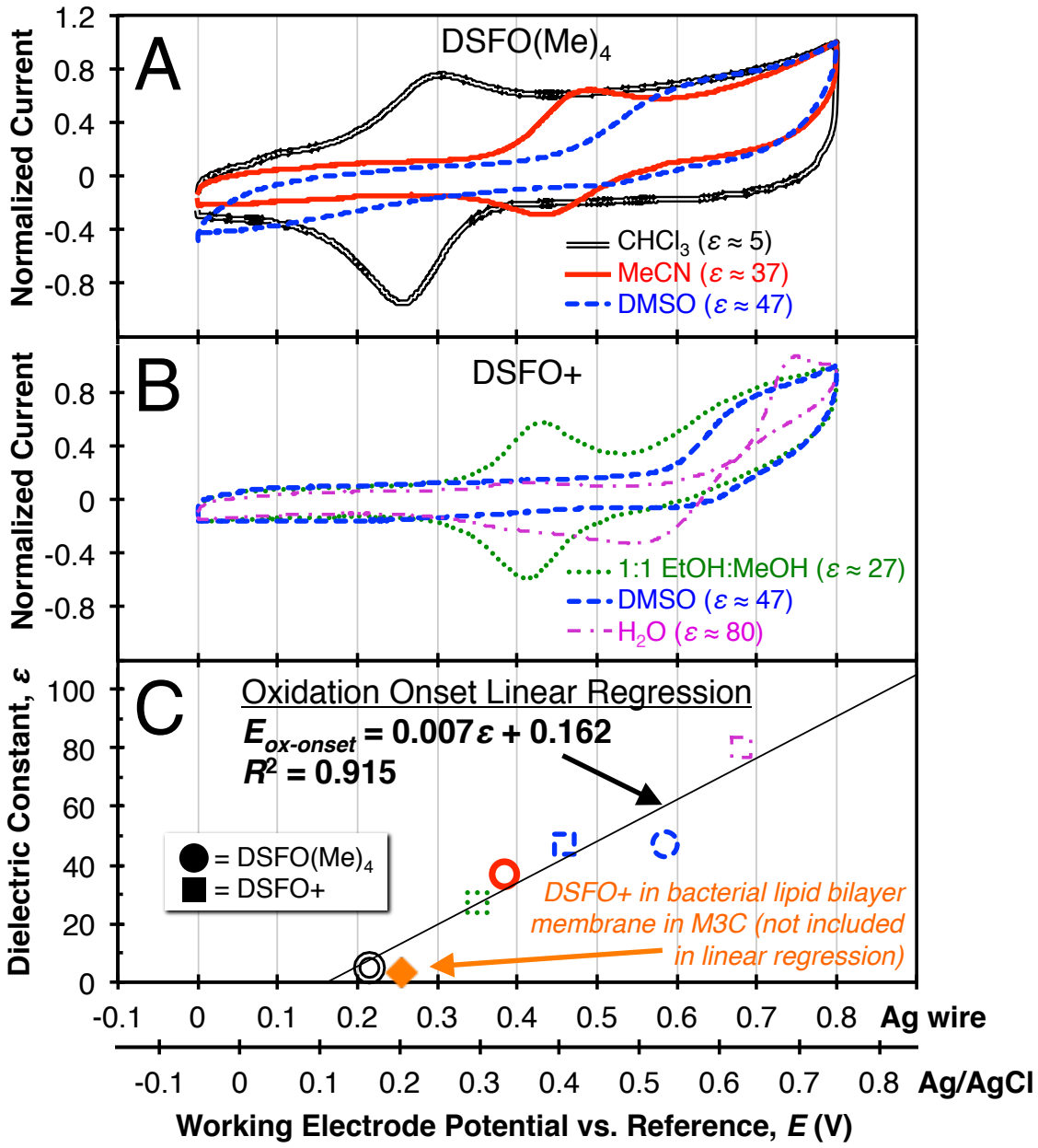

Figure V.S1. CV traces of DSFO(Me)$_4$ and DSFO+ in varying solvents, and summary of oxidation onset potentials. All solutions were made with 100 mM supporting electrolyte. The working electrode was glassy carbon, the reference electrode was Ag wire, and the counter electrode was Pt wire. The Ag/AgCl axis has been provided for reference. (**A**) CVs of DSFO(Me)$_4$ in solvents with low-to-intermediate dielectric constant. (**B**) CVs of DSFO+ in solvents with intermediate-to-high dielectric constants. (**C**) Summary of extracted oxidation onset potentials (HOMO redox potentials) from the traces in (A) and (B). Note the addition of the orange diamond data point, corresponding to the oxidation onset potential of DSFO+ in a lipid bilayer.

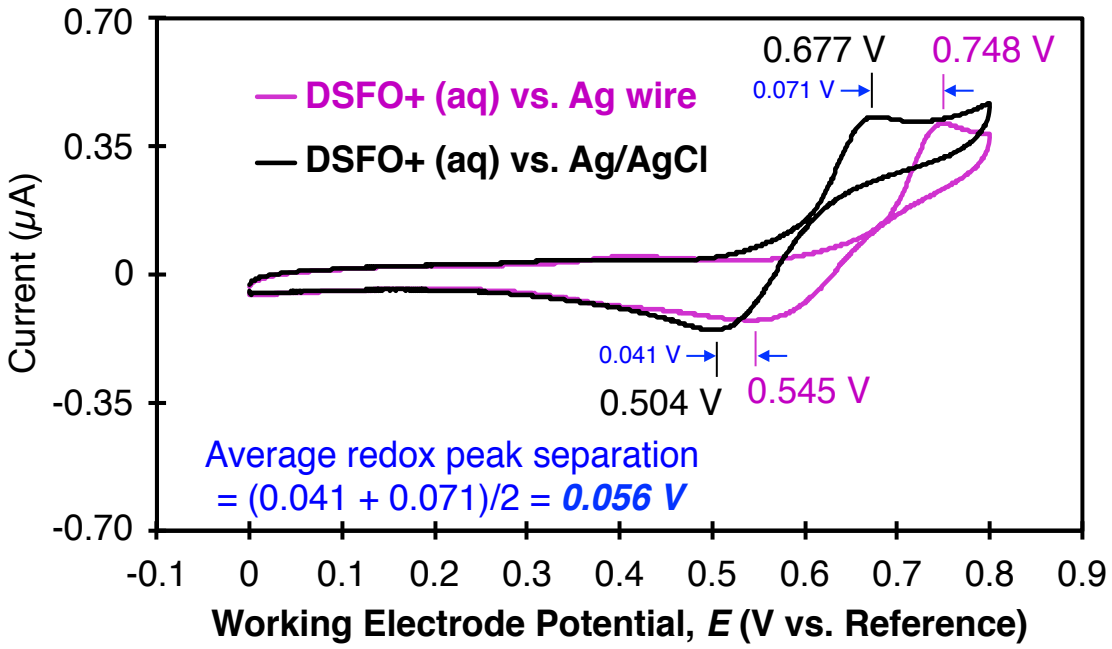

Figure V.S2. CV traces of DSFO+ in 100 mM aqueous phosphate buffer versus the Ag reference electrode and the Ag/AgCl (saturated KCl) reference electrode. Here, DSFO+ acts as an internal standard that allows direct comparison of the two reference electrodes in identical solution. The formal difference in the redox potential of DSFO+ is taken as the average separation between oxidation and reduction waves (0.056 V) in the two media. Therefore, because DSFO+ redox is 0.056 V more negative versus Ag/AgCl than versus Ag wire, Ag/AgCl is formally +0.056 V vs. Ag (or equivalently, Ag wire is formally –0.056 V vs. Ag/AgCl).

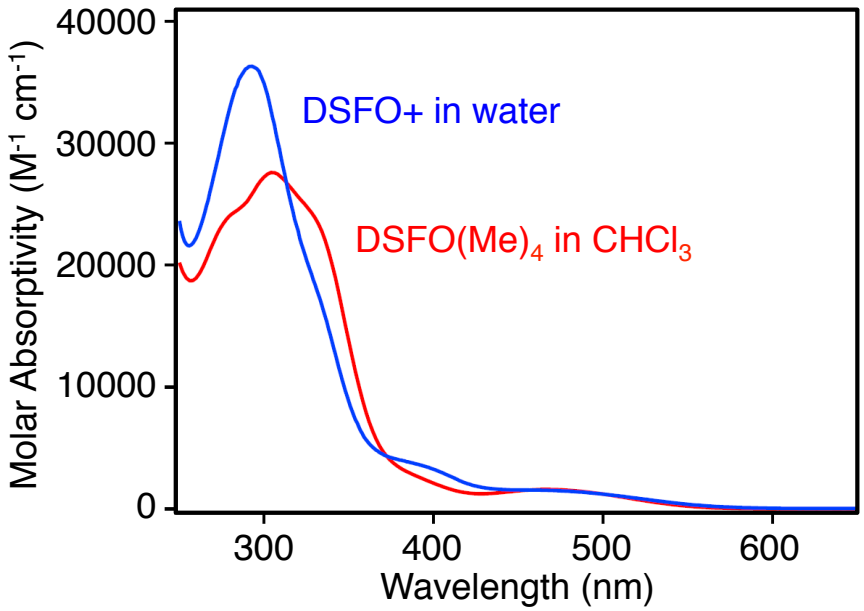

Figure V.S3. Solution UV-vis spectra for DSFO+ and DSFO(Me)$_4$. (**Blue**) DSFO+ in 100 mM aqueous phosphate buffer at pH = 7.4 and (**Red**) DSFO(Me)$_4$ in chloroform with 100 mM tetrabutylammonium hexafluorophosphate as supporting electrolyte.

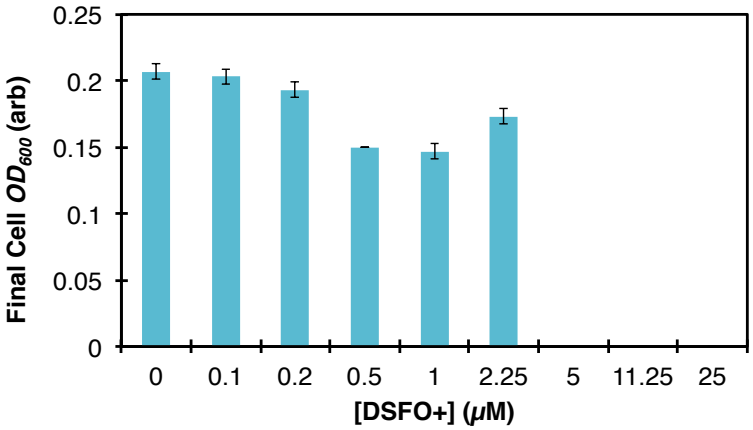

Figure V.S4. Determination of the MIC of DSFO+ for *S. oneidensis* MR-1. Triplicate average cell culture optical density at t = 72 h was measured at 600 nm as a function of logarithmic DSFO+ concentrations. The MIC is read as the lowest concentration that completely inhibits growth [61] of the target organism (here detected as 5 μM).

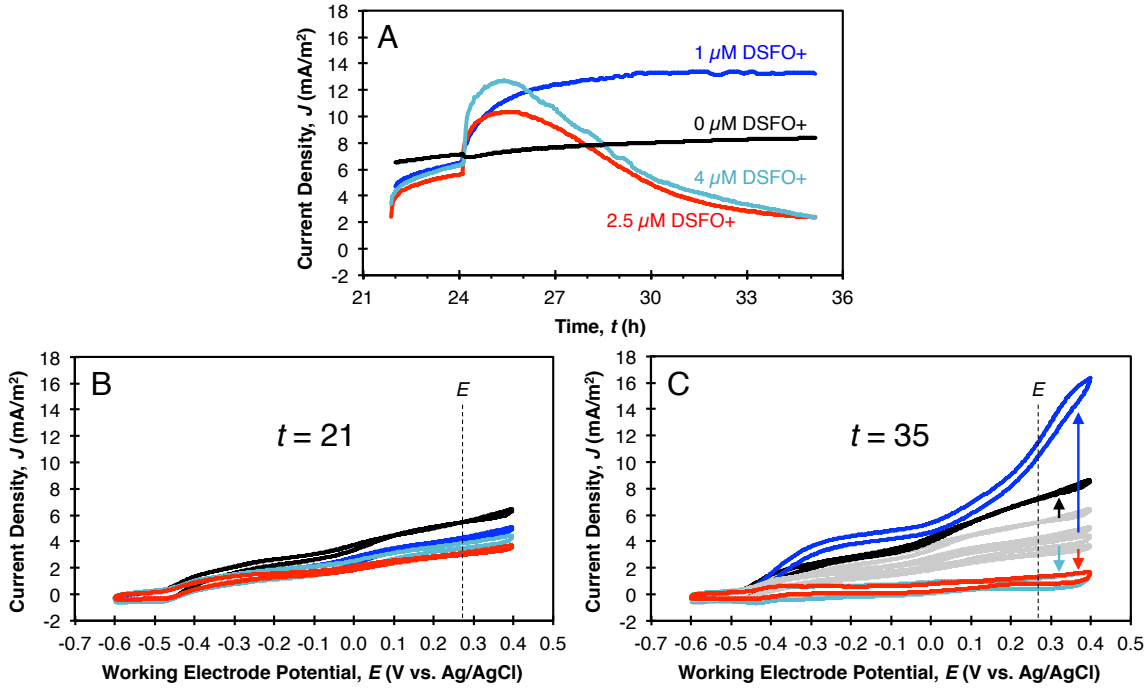

Figure V.S5. CA and CV traces for representative single replicate *S. oneidensis* MR-1 M3Cs operated at E = 0.27 V to determine $[DSFO]_{optimal}$, the optimal sub-MIC concentration of DSFO+. Note that t = 4–20 h (16 h total time) were used for potentiostatic establishment of stable electroactive biofilms at E = 0.27 V, and a full media change was conducted at t = 20 h that removed planktonic cells to deconvolute the biofilm signal from planktonic cells. (**A**) Biofilm current density over time (CA traces) as a function of added DSFO+ concentration (annotated on plot). Note that DSFO+ was added 2 h after CA started. (**B**) Biofilm CV at t = 21 h for all M3Cs, immediately after the media change (and 3 h prior to addition of DSFO+). The vertical dashed line labeled "E" corresponds to a potential of E = 0.27 V. Note that all M3Cs have similar voltammograms. (**C**) Biofilm CV at t = 35 h for all M3Cs, immediately after CA data collection ended. The vertical dashed line corresponds to a potential of E = 0.27 V. Note the arrows displaying the trends in the voltammograms for each device. 1 μM DSFO+ appropriately shows the largest current at E = 0.27 V, due to the catalytic wave from DSFO+.

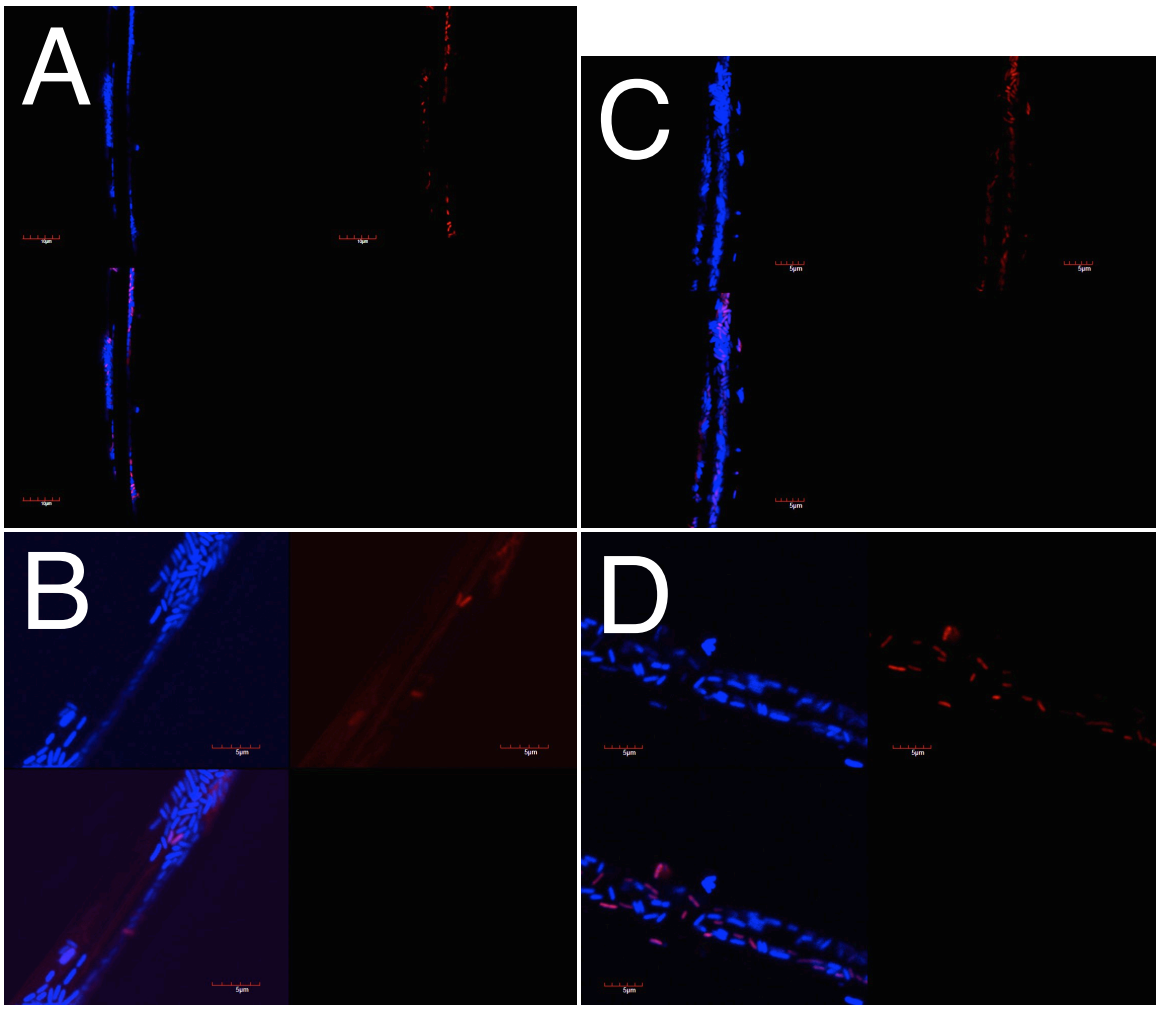

Figure V.S6. Representative CFM images of M3C working electrodes immediately after CA measurements to assess for *in operando* toxicity of 1 µM DSFO+. Electrodes were simultaneously stained with 4',6-diamidino-2-phenylindole (DAPI, live stain) and propidium iodide (PI, dead stain). Note that images are false-color. Each panel is divided into four quadrants as follows: upper left, emission from DAPI (blue); upper right, emission from PI (red); lower left, overlay of DAPI emission (blue) and PI emission (red); lower right, bright field transmittance showing complete occlusion due to the graphite electrode. In all images, scale bars are 5 µm. (**A**) WT-M3C electrode with 0 µM DSFO+. (**B**) WT-M3C electrode with 1 µM DSFO+. (**C**) ΔmtrA-M3C electrode with 1 µM DSFO+. (**D**) ΔmtrB-M3C electrode with 1 µM DSFO+.

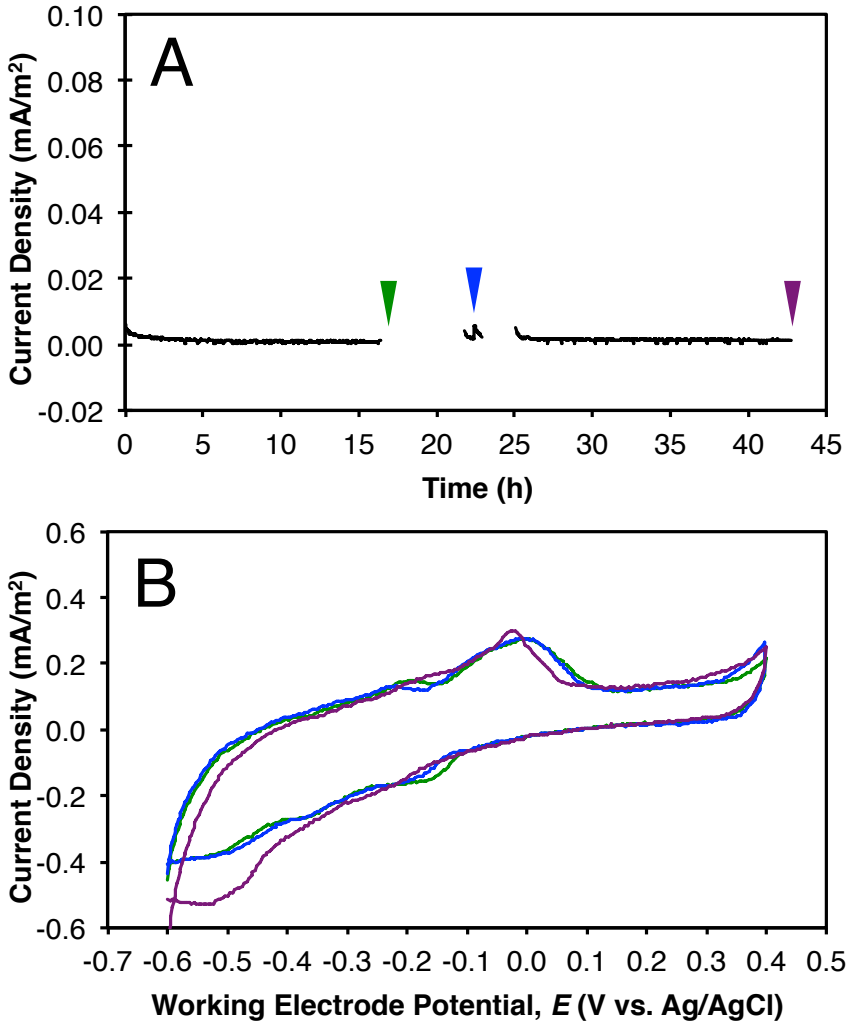

Figure V.S7. Abiotic (negative control) M3C CA and CV traces. The M3Cs contain only buffered growth media and DSFO+. The experiments were conducted as single replicates concomitant with the M3Cs in Fig. V.2 in the main text. (**A**) CA trace collected at E = 0.27 V showing current density over time. Salient timepoints during M3C operation are as follows. At t = 0 h, current collection begins. At t = 17 h (green arrow), current collection is paused for CV analysis. At t = 22, current collection is resumed so that 5 µM DSFO+ may be spiked in during current collection at t = 22.5 h (blue arrow). At t = 23 h, current collection is again paused for CV analysis to discern the effects of DSFO+ addition. At t = 25 h, current collection is resumed. At t = 43 h (purple arrow), current collection is terminated and CV analysis is undertaken. (**B**) CV traces corresponding to the timepoints in (A) where CA was paused at t = 17 h (green trace), t = 23 h (blue trace), and t = 43 h (purple trace).

Chapter VI. Amplification of Bacterial Anode Respiration by a Self-Doped p-Type pH-Neutral Conjugated Polyelectrolyte (CPE)

VI.A. Abstract

Poor abiotic-biotic interfacial contacts remain a limiting feature in the performance of bioelectronic devices. Conducting polymers have increasingly been used for improving the interfaces of electrical and biological components. Conjugated polyelectrolytes (CPEs) represent an under-explored class of pH-neutral polymeric materials for further improving these contacts. A set of four CPEs with varying backbone structures, pendant ionic functionalities, and the ability to remain doped in pH-neutral aqueous media were therefore employed to evaluate the impact of these molecular features on biocurrent outputs. CPEs were added to anaerobic microbial three electrode electrochemical cells (M3Cs) containing lactate-consuming, anode-respiring *Shewanella oneidensis* MR-1 at a poised potential of 0.3 V vs. Ag/AgCl. CPE-K, a p-type, self-doped anionic CPE, notably amplifies steady-state biocurrent output from *S. oneidensis* MR-1 by 2.7 ± 0.7-fold relative to positive controls at >99.5% significance ($P = 0.002$). Having anionic pendant groups present on CPE-K appears to be necessary but not sufficient for biocurrent amplification because the anionic polymer CPE-2 does not statistically significantly alter steady-state current density ($P = 0.174$) and the cationic CPE derivatives CPE-3 and CPE-4 respectively inhibit steady-state current density relative to controls by 0.3 ± 0.2-fold and 0.5 ± 0.1-fold at >95% significance ($P = 0.022$ and $P = 0.042$, respectively). Charge collected as a function of added CPE tracks with these trends in current density. After accounting for electrode bacterial colonization, we conclude that individual bacteria produce statistically similar current with and without CPE-K; the coulombic efficiency of the process is also statistically unaffected. Electrochemical

characterization indicates that increased direct electron transfer is the mechanism of biocurrent amplification, while changes in mediated electron transfer are not implicated. By absorbance spectroscopy, *S. oneidensis* MR-1 appears to donate metabolic electrons to CPE-K, thereby de-doping (neutralizing) the polymer chains in analogy to respiration on metal oxides. We surmise that CPE-K acts as a conductive extension of the electrode, as it is re-doped (re-oxidized) at the electrode surface for additional acceptance of metabolic electrons. This rationalizes both the amplified biocurrent relative to controls and the observed increase in cell coverage of the electrode surface not observed for the other CPEs, and indicates that CPE-K may have immediate utility in practical bioelectrochemical systems.

VI.B. Introduction

Conventional electronic components, such as metals, metal oxides, carbon nanotubes, and graphenes, are often inherently toxic to biological cells.[1–12] Yet, there is growing interest in bioelectronics—interfacing biological and electronic elements—for applications in bioenergy conversion and catalysis,[13] biosensing,[14] medical diagnostics and drug delivery,[15] neural and tissue interrogation,[16] and more. Continued progress in these bioelectronic application areas therefore necessitates continued materials advances, and organic electronic materials may provide a solution. Herein, the scope is specifically narrowed to organic electronic materials that may *in situ* chemically modify microorganism-electrode bioelectrocatalytic electron transfer processes occurring in microbial bioelectrochemical systems.[17] Such processes are relevant both in bioconversion of organic fuels to electrical current[18–20] and in bioelectrosynthesis of organic fuels from electrical current.[21–23] New materials continue to emerge for amplifying these processes,[24] with membrane-intercalating conjugated oligoelectrolytes (COEs) representing a notable family of organic semiconducting

compounds reported to achieve biological-electrode electrical enhancement.[25–38] The organic conducting polymers polyaniline (PANI), polypyrrole (PPy), and poly(3,4-ethylenedioxythiophene) (PEDOT) have also been used to directly modify electrodes for bioelectronic applications,[15,39,40] and yet even these materials remain hindered by their low pH (acidity), which is bio-incompatible and known to be corrosive to metal contacts in electronic devices. Materials that exhibit similar capacities to improve biological-electrode contacts, conversion efficiencies, reaction rates, signal transduction, and electrical outputs—while remaining affordably synthesized, easy to work with, and pH-neutral—are extremely valuable.

Conjugated polyelectrolytes (CPEs)[43] are a class of pH-neutral semiconducting polymeric materials that fit these requirements and remain underutilized in bioelectronic applications, despite their apparent utility as interfacial modifying agents in organic electronic[44–50] and thermoelectric[51,52] devices. CPEs contain π-conjugated molecular backbones and bear ionic pendant functionalities for solubility in polar solvents. Their extended molecular lengths, dispersion of molecular weights, and the ability to undergo doping to afford conductivity are features akin to those of PANI, PPy, and PEDOT. One may thus imagine that a biocompatible, conductive matrix of CPEs co-interfaced with microorganisms and electrodes will improve contacts, increase conversion efficiencies and reaction rates, and amplify biocurrent outputs. This hypothesis is reasonable in view of the similar strategy that certain bacterial genera (*e.g. Geobacter* and *Shewanella*) natively undertake in which conductive matrices of putative "nanowires" are constructed *in situ*.[53–70] Direct electron transfer through such matrices represents the only adequate physical explanation for the high kinetic rates of electron transfer and conversion of organic fuel to current exhibited by these bacteria.[71]

Accordingly, the set of four CPEs depicted in Fig. VI.1 (CPE-K, CPE-2, CPE-3, and CPE-4) are employed herein at 10 μM (by monomer) in microbial three-electrode electrochemical cells (M3Cs)[72] in an effort to amplify biocurrent outputs from anode-respiring cultures of the model electrogenic bacterium *Shewanella oneidensis* MR-1.[73–75] Molecular properties of the CPEs are summarized in Table VI.1. Synthetic batches of CPEs were selected that have a similar average number of repeat units per polymer chain (X_n = 7–12) in an effort to control for effects governed by molecular length. The variations in the π-conjugated backbones and polar functionalities produce the CPE absorbance spectra displayed in Fig. VI.2 (also see Fig. VI.S1 for molar absorptivity plots).

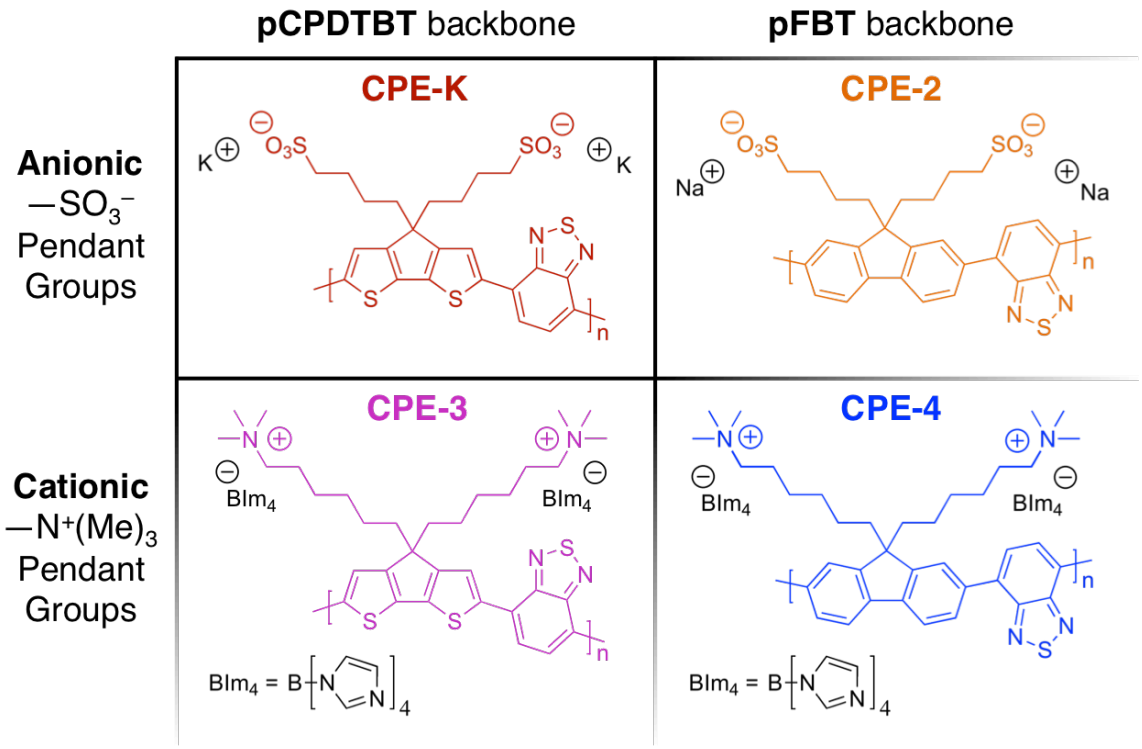

Figure VI.1. CPE molecular structures and backbone/pendant group interrelationships of the CPEs used in this study. The color scheme assigned to the four derivatives in this figure is maintained throughout the text and across figures for ease of comparison. For CPE-K and CPE-2, note that the countercations are different, but this is negligible in this work as they dissociate upon solvation in aqueous media. The alkyl chains of CPE-K and CPE-2 are slightly shorter than CPE-3 and CPE-4 due to considerations for synthesis (see Materials and Methods). For CPE-3 and CPE-4, "BIm_4" indicates the tetrakis(1-imidazolyl)borate counterion.

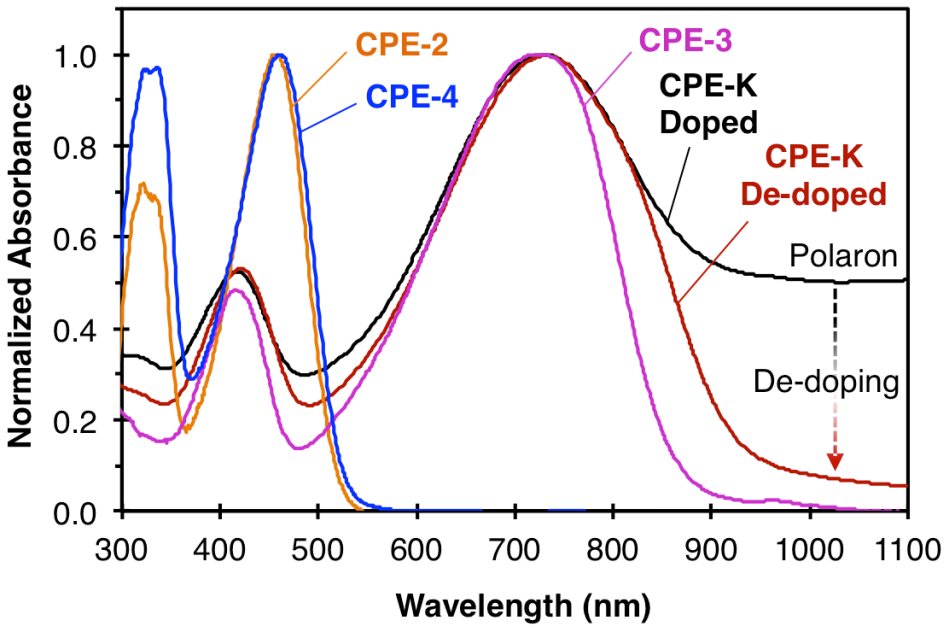

Figure VI.2. Normalized absorbance spectra of CPEs in pH-neutral aqueous M3C culture media. Numerical analysis of absorption maxima and onsets is provided in the text and tables.

Differences in these molecular features are anticipated to facilitate different interactions with the bacteria. For instance, consider anionic CPE-K (pendant sulfonate groups) and cationic CPE-3 (pendant trimethylammonium groups) derivatives that contain an identical poly[cyclopenta-(2,1-b;3,4-b')-dithiophene-*alt*-4,7-(2,1,3-benzothiadiazole)] (pCPDTBT) backbone. Reports indicate that CPE-3 exhibits a coulombic attraction with the negatively charged cell surface, affording a cell binding affinity dramatically higher than that of CPE-K, and thus, CPE-3 may reverse the zeta potential polarity of a bacterial suspension while CPE-K will not.[76] Similar electrostatic considerations pertain to the anionic CPE-2 (pendant sulfonate groups) and cationic CPE-4 (pendant trimethylammonium groups) derivatives that share a common poly[fluorine-*alt*-4,7-(2,1,3-benzothiadiazole)] (pFBT) backbone. Bacteria modified with cationic derivatives CPE-3 and CPE-4 will presumably bear a more-positive zeta potential and experience less electrostatic driving force for adhering to the positively

charged anode in M3Cs, while anionic derivatives CPE-K and CPE-2 will induce no such response. It bears emphasizing that hydrophobic interactions do not appear to play a role in these CPE-bacteria binding interactions.[76] CPE-K is p-type, self-doped, and remains stably p-doped in water[77] (*i.e.* pH-neutral aqueous culture media), meaning that CPE-K will be more conductive in M3C conditions than its counterparts in Fig. VI.1. This has positive implications for its ability to participate in biocurrent transmission, possibly by a reversible doping mechanism. An illustration of the predicted electrostatic interactions and electron transfer pathways due to the differences in these molecular features is provided in Fig. VI.3. Experiments testing these predictions are discussed below. Throughout the remainder of the chapter, all discussed experiments are conducted in triplicate, all potentials are reported relative to the Ag/AgCl (saturated KCl) reference electrode, and error bars represent ± one standard deviation from the mean.

Chronoamperometry (CA) and cyclic voltammetry (CV) experiments are first undertaken to correlate changes in current density outputs to the variations in conjugated backbone and pendant ionic groups of the CPEs, affording a window into the impact that these features individually have on time- and potential-dependent bacteria-electrode electronic interactions. *S. oneidensis* MR-1 is understood to have electrochemically distinguishable mediated (MET) and direct electron transfer (DET) pathways in M3Cs,[32,78–80] so the mechanism of perturbations to extracellular electron transfer (EET) from CPEs is revealed by CV characterization. *S. oneidensis* MR-1 catalyzes partial oxidation of lactate to acetate, theoretically liberating four electrons per lactate by the reaction[80]

$$\text{Lactate}^- + 2\ H_2O \rightarrow \text{Acetate}^- + HCO_3^- + 5\ H^+ + 4\ e^- \qquad \text{(VI.1)}.$$

The coulombic efficiency (*CE*) of substrate conversion as measured by high performance liquid chromatography may accordingly be calculated by dividing integrated charge from CA measurements, Q_j (j = +, –, K, 2, 3, and 4, corresponding to controls and CPE labels), by the charge equivalent of lactate consumed, Q_{lac}. These data are correlated to electrochemical changes as a function of added CPE. The doping state of CPE-K may be measured by optical spectroscopy, wherein the presence of polarons (unpaired electrons on the backbone) contribute to a near-IR absorbance band at ~1100 nm[77] (Fig. VI.2). Absorbance spectroscopy is therefore used to test the prediction in Fig. VI.3 that *S. oneidensis* MR-1 will de-dope CPE-K (*i.e.* use the holes on the backbone as electron acceptors) as an electron transfer relay for amplified biocurrent. Following electrochemical measurements, M3C working electrodes are chemically fixed and imaged with scanning electron microscopy (SEM) for counting of electrode-associated cells (see Materials and Methods) to quantify surface cell density, ρ_j,

Table VI.1. Molecular properties of CPEs[a]

CPE	M_o (g/mol)[b]	M_n (×10^3 g/mol)[c]	PDI[d]	X_n[e]	λ_{max} (nm)	$\varepsilon(\lambda_{max})$ (×10^3 M^{-1} cm^{-1})[f]	λ_{onset} (nm)[g]	E_g (eV)[h]	E_{HOMO} (V vs. Fc/Fc$^+$)[i]	E_{HOMO} (V vs. Ag/AgCl)[j]	$HOMO$ (eV)[k]	EA (eV)[l]
K	658.9	7.7	1.1	12	735	20.4	929	1.33	−0.05	0.26	−5.05	−3.72
2	614.7	6.1	1.1	10	457	5.9	515	2.41	0.88	1.09	−5.98	−3.57
3	1153.1	7.9	1.8	7	724	15.2	858	1.45	−0.10	0.11	−5.00	−3.55
4	1141.1	12.8	2.3	11	460	18.1	521	2.38	0.66	0.87	−5.76	−3.38

[a] Optical properties of CPEs were determined in buffered pH = 7.1 M1 growth medium in the undoped state, while physical and electronic properties were measured with undoped neutral derivatives of the CPEs in organic solvents (see Materials and Methods). [b] Monomer molecular weight. [c] Number average molecular weight, determined by gel permeation chromatography (see Mateirals and Methods). [d] Polydispersity index, determined by gel permeation chromatography (see Materials and Methods). [e] Number average degree of polymerization, calculated as $X_n = M_n/M_o$. [f] Molar absorptivity at the absorbance maximum. [g] For each CPE, λ_{onset} is determined from the red side of the most redshifted absorption band (Fig. VI.2) by extending a line tangent to the linear portion of the trace to its point of intersection with the wavelength axis. [h] Optical energy gap, calculated by E_g = 1240 eV nm / λ_{onset}. [i] Oxidation onset potential of the highest occupied molecular orbital (HOMO), determined by cyclic voltammetry relative to an internal Fc/Fc$^+$ standard and silver wire pseudoreference electrode. [j] Oxidation onset potential of the HOMO, calculated assuming 0 V vs. Fc/Fc$^+$ is equivalent to 0.21 V vs. Ag/AgCl in aqueous solution from Ref. #70. [k] HOMO energy relative to the vacuum level, numerically determined from E_{HOMO} by the procedure in Ref. #71 assuming that 0 V vs. Fc/Fc$^+$ is equivalent to –5.10 eV on the Fermi scale and 0.40 V vs. SCE. [l] Electron affinity relative to the vacuum level, $EA = HOMO + E_g$, serves as a proxy for the lowest unoccupied molecular orbital (LUMO) energy.

which is correlated to the current density output. Unmodified *S. oneidensis* MR-1 is known to form sparse biofilms,[32,81] suggesting that increasing ρ may increase current outputs.

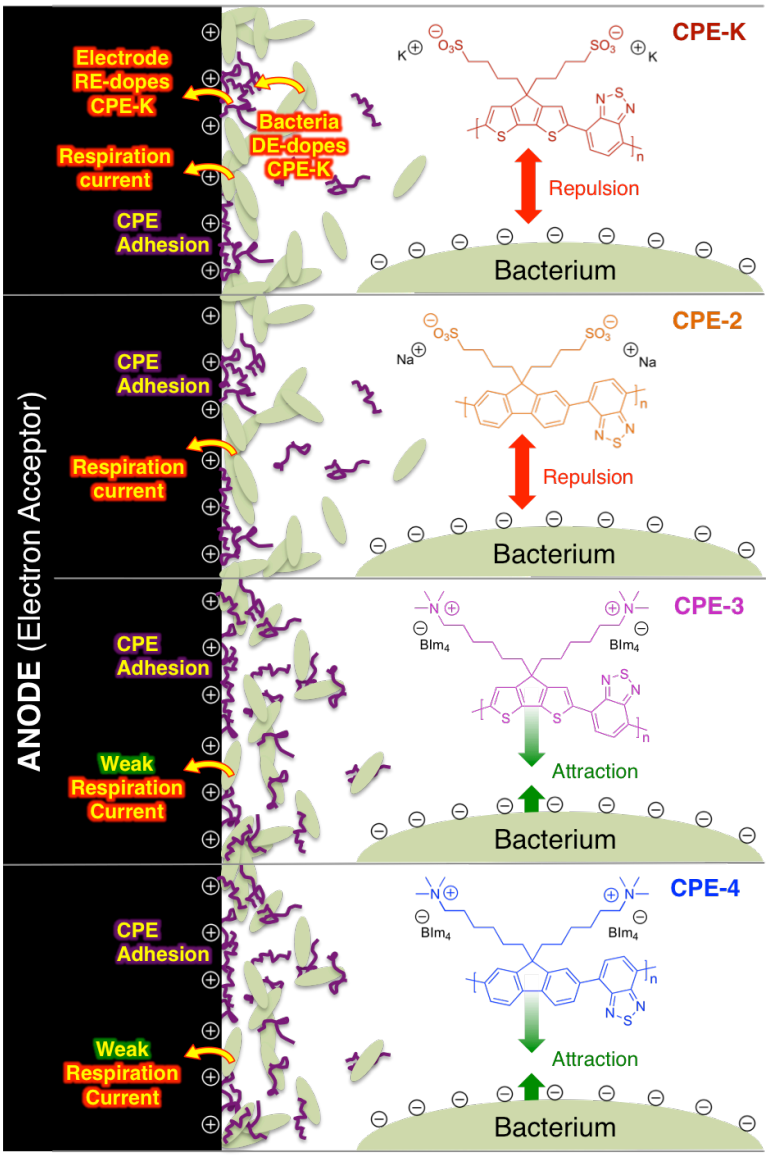

Figure VI.3. An illustration of bacteria-CPE-anode surface adhesion interactions and putative electron transfer processes. Green arrows represent attractive electrostatic forces, while red arrows represent repulsive electrostatic forces. Curved yellow arrows with red borders represent putative electron transfer processes. Light green ovals represent bacteria, while dark purple twisted lines represent CPE polymer chains. Note that the CPE, bacteria, and anode surface interactions due to electrostatics, van der Waals interactions, and/or the hydrophobic effect is a cartoon representation.

CPEs have been shown to act as dispersants for carbon nanotubes due to a hydrophobic interaction of the conjugated backbones with graphene-like surfaces.[46,52] A hydrophobic

interaction of CPEs may therefore occur with the M3C graphite felt working electrode fibers (which have graphene-like surfaces), even though CPE-bacteria hydrophobic interactions appear nonexistent.[76] In order to deconvolute contributions of this effect from the bacteria-electrode interaction, CA experiments were conducted with additional M3Cs without bacteria to allow CPE-electrode interactions to occur *in situ*; absorbance spectroscopy was conducted on the media after CA to quantify the CPE concentration adsorbed, $[CPE]_{ads}$.

VI.C. Results and Discussion

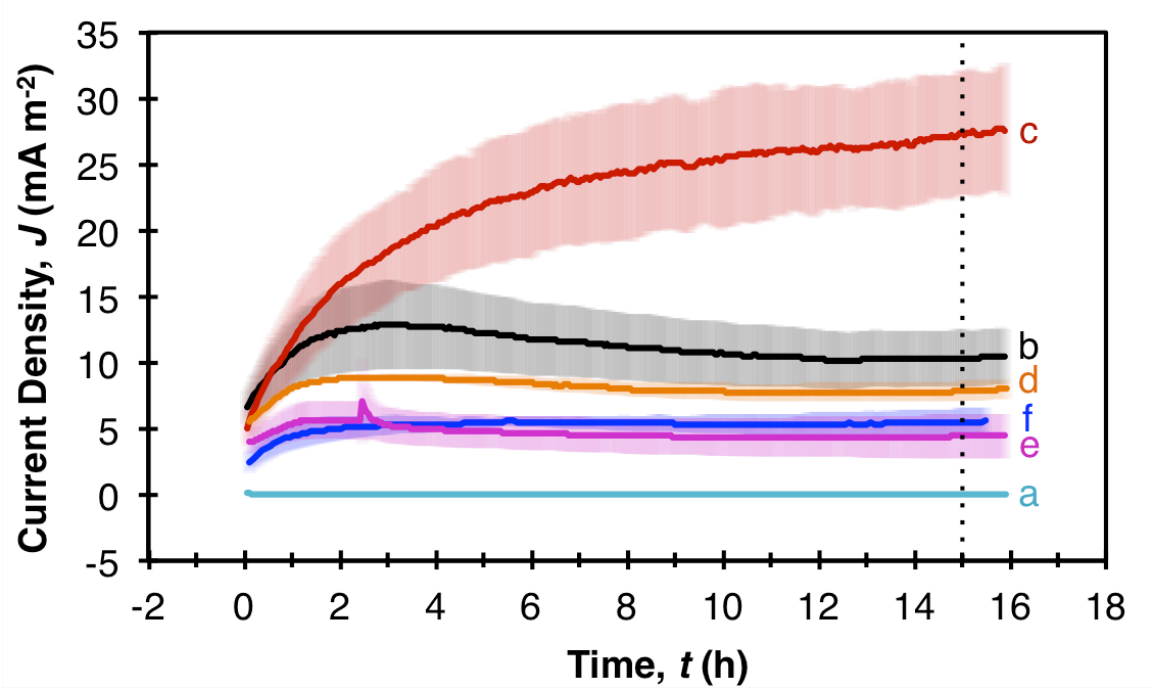

Figure VI.4. Average current density as a function of time (CA traces) for M3Cs modified with CPEs. Shaded areas above and below the traces represent ± 1 std. dev. from the mean. The dotted line indicates t = 15 h, taken as the point of steady-state (~0 slope) current for each type of device. (**a**) Negative control: M3Cs containing CPEs in culture medium with no cells; 11 replicates. (**b**) Positive control: M3Cs containing *S. oneidensis* MR-1 and no CPEs; 3 replicates. (**c**) M3Cs containing 10 µM CPE-K and *S. oneidensis* MR-1; 4 replicates. (**d**) M3Cs containing 10 µM CPE-2 and *S. oneidensis* MR-1; 3 replicates. (**e**) M3Cs containing 10 µM CPE-3 and *S. oneidensis* MR-1; 3 replicates. Note that the current spike at $t \approx 2.5$ h is within the standard deviation of measurements and was caused by an air bubble dislodging from the reference electrode frit in one of the replicate reactors. (**f**) M3Cs containing 10 µM CPE-4 and *S. oneidensis* MR-1; 3 replicates.

The current response of *S. oneidensis* MR-1 was first monitored by CA at 0.3 V in M3Cs modified with each of the CPE derivatives, and these were compared against positive control M3Cs receiving no CPE modification as well as negative control reactors containing CPEs with no bacteria. The average current density output as a function of time over the course of 16 h for all conditions is plotted in Fig. VI.4. As can be seen, by t = 15 h, a steady-state (~0 slope) current density, $J_{SS,j}$, is reached for each of the j experimental conditions (*i.e.* j = +, –, K, 2, 3, and 4, corresponding to the controls and CPE labels). The negative control M3C (Fig. VI.4 a) produces a negligible steady-state current of $J_{SS,-}$ = 0.01 ± 0.02 mA m^{-2}, statistically distinct at >95% significance from the positive control M3C (Fig. VI.4 b) that produces $J_{SS,+}$ = 10.3 ± 2.1 mA m^{-2} (P = 0.014). These control data show that CPEs do not act as the source of generated current in the absence of bacteria, and the current density for the positive controls is comparable to that previously measured[32] in similar devices poised at 0.2 V.

M3C modification with anionic CPE-K (Fig. VI.4 c) provides a notable 2.7 ± 0.7-fold increase in steady-state current over the positive control to $J_{SS,K}$ = 27.5 ± 4.7 mA m^{-2} at >99.5% significance (P = 0.002), while modification with the other anionic CPE-2 (Fig. VI.4 d) has no statistically significant effect but does slightly decrease the average steady-state current by 0.8 ± 0.2-fold to $J_{SS,2}$ = 7.9 ± 0.8 mA m^{-2} (P = 0.174). Modification with cationic derivatives CPE-3 (Fig. VI.4 e) and CPE-4 (Fig. VI.4 f) respectively decreases average steady-state current output at >95% significance by 0.3 ± 0.2-fold to $J_{SS,3}$ = 4.4 ± 1.7 mA m^{-2} (P = 0.022) and 0.5 ± 0.1-fold to $J_{SS,4}$ = 5.5 ± 1.0 mA m^{-2} (P = 0.042). These trends are summarized in Table VI.2.

Table VI.2. Measured and calculated parameters from M3Cs

Parameter	Expression	Positive Control (No CPE)	Negative Control (No Cells)	10 μM additions (by monomer mass) to M3Cs			
				CPE-K	CPE-2	CPE-3	CPE-4
Steady-state current density (mA m^{-2})	$J_{SS,j} = J_j(t)\|_{t = 15\ h}$	10.3 ± 2.1	0.01 ± 0.02	27.5 ± 4.7	7.9 ± 0.8	4.4 ± 1.7	5.5 ± 1.0
Fold change from positive control	—[h]	—	0.001 ± 0.003	2.7 ± 0.7	0.8 ± 0.2	0.3 ± 0.2	0.5 ± 0.1
P-value[b] for $J_{SS,j}$	—	$P = 1.000$	$P = 0.014$	$P = 0.002$	$P = 0.174$	$P = 0.022$	$P = 0.042$
Integrated charge (C)[c]	$Q_j = A\int J(t)dt$	14.3 ± 3.2	0.02 ± 0.04	29.0 ± 5.8	10.5 ± 0.6	6.1 ± 1.8	6.6 ± 0.6
Fold change from positive control	—	—	0.001 ± 0.002	2.0 ± 0.6	0.7 ± 0.2	0.4 ± 0.2	0.4 ± 0.1
P-value[b] for Q_j	—	$P = 1.000$	$P = 0.016$	$P = 0.009$	$P = 0.165$	$P = 0.027$	$P = 0.047$
Lactate consumed (mM)[d]	$\Delta[lac] = [lac]_f - [lac]_i$	–2.8 ± 0.3	0.0 ± 0.0	–7.0 ± 3.2	–2.5 ± 0.3	–1.7 ± 0.2	–1.7 ± 0.5
Lactate charge equivalent (C)[e]	$Q_{lac} = -\Delta[lac]VFn$	16.4 ± 3.5	0.0 ± 0.0	40.7 ± 18.4	14.5 ± 2.0	10.0 ± 1.2	9.6 ± 2.9
P-value[b] for $\Delta[lac]$ and Q_{lac}	—	$P = 1.000$	—	$P = 0.078$	$P = 0.289$	$P = 0.009$	$P = 0.041$
Coulombic efficiency (%)	$CE_j = 100 \times Q_j / Q_{lac}$	88 ± 10	—	76 ± 15	73 ± 7	59 ± 12	69 ± 24
P-value[b] for CE_j	—	$P = 1.000$	—	$P = 0.261$	$P = 0.108$	$P = 0.034$	$P = 0.305$
Electrode cell coverage fraction[f]	$X_j = A_{biofilm}/A_{total}$	0.12 ± 0.04	0.00 ± 0.00	0.53 ± 0.16	0.12 ± 0.06	0.12 ± 0.02	0.08 ± 0.02
Electrode cell density (×10^9 m^{-2})[g]	$\rho_j = X_j/A_{cell}$	214 ± 76	0 ± 0	960 ± 298	216 ± 108	215 ± 40	151 ± 30
P-value[b] for X_j and ρ_j	—	$P = 1.000$	—	$P = 0.011$	$P = 0.981$	$P = 0.985$	$P = 0.221$
Steady-state current per cell (fA/cell)	$I_{cell,j} = J_{SS,j}/\rho_j$	48 ± 20	—	29 ± 10	37 ± 19	21 ± 9	36 ± 10
P-value[b] for $I_{cell,j}$	—	$P = 1.000$	—	$P = 0.236$	$P = 0.523$	$P = 0.130$	$P = 0.422$

[a] Measured values are averages from the replicate M3Cs as discussed in the text and figures, while calculated parameters follow the provided expressions; quoted uncertainties represent ± 1 standard deviation (for measured values) or are propagated errors by addition of standard deviations in quadrature (for calculated values). The index j is used to designate the experimental conditions (j = +, –, K, 2, 3, and 4, corresponding to the controls and CPE labels). [b] Calculated from two-tailed unequal variance *t*-tests comparing mean values of the positive control to mean values from other conditions. By convention, $P < 0.05$ is taken to indicate "statistically different at >95% significance." [c] The surface area of working electrodes (average of 24 replicates) is $A = 0.0226 \pm 0.0012$ m^2 as determined in Ref. #32. [d] Note that $\Delta[lac] < 0$ because lactate consumption produces electrons in Eq. 1; this is why the expression for Q_{lac} contains a negative sign. [e] $V = 15$ mL; $F = eN_A \approx 96485$ C mol^{-1}, where $e = 1.602 \times 10^{-19}$ C and $N_A = 6.02 \times 10^{23}$ mol^{-1}; $n = 4$ from Eq. 1. [f] The value of $A_{biofilm}$ and A_{total} were determined from SEM images using ImageJ (see Materials and Methods), where $A_{biofilm}$ is the electrode area covered by bacterial cells and A_{total} is the area of the electrode surface in a given image. [g] Using ImageJ and SEM images, the cross-sectional area of a single bacterium was determined to be $A_{cell} = 5.57 \pm 0.39 \times 10^{-13}$ m^2 (0.557 ± 0.039 μm^2); by virtue of *S. oneidensis* MR-1 only growing as a monolayer of cells (see Ref. #84), this sets an upper bound on cell coverage of $\rho \leq 1/A_{cell} = 1.80 \pm 0.13 \times 10^{12}$ cells/m^2. [h] Not applicable or undefined.

Pendant anionic groups consequently appear necessary but not sufficient for a CPE to amplify the current density response of *S. oneidensis* MR-1 above that of the unmodified positive control. The narrow-bandgap alternating donor-acceptor[82,83] pCPDTBT molecular backbone found in CPE-K and CPE-3 also appears necessary but not sufficient for current amplification, particularly in view of the strong donor character (low ionization potential) of the CPDT moiety that allows CPE-K to be p-doped in neutral ambient conditions.[44] As can also be seen in Table VI.2, trends in charge collected (Q_j) as a function of the CPE derivative added track almost identically with trends in steady-state current in terms of fold changes and statistical significance; the same conclusions may thus be drawn from the data and therefore discussion is omitted for redundancy. Instead, a discussion of the lactate consumption and coulombic efficiency of lactate-to-current conversion, CE_j, which is related to Q_j, is provided next.

Negative control M3Cs consume 0 mM lactate (so CE_- is undefined), ruling out the possibility that CPEs catalyze lactate-to-current conversion in the absence of bacteria. Bacteria in positive control M3Cs consume –2.8 ± 0.3 mM lactate at CE_+ = 88 ± 10% conversion to current—the highest CE_j obtained for any tested condition. This value of CE_+ is notably higher than the 51 ± 10% observed for positive control M3Cs poised at 0.2 V in previous studies.[32] This increase in efficiency is likely an effect of the 0.3 V poised potential that provides a higher driving force for electron transport through the more-efficient[80] native *S. oneidensis* MR-1 DET pathway.

CPE-K modification enables removal of –7.0 ± 3.2 mM lactate (P = 0.078) at CE_K = 76 ± 15% (P = 0.261). This elevated substrate consumption at >90% significance is consistent with the increased current and charge outputs from CPE-K and signifies amplified electrode

respiration. M3C modification with CPE-2 has no statistically significant effect on substrate removal or conversion efficiency, permitting –2.5 ± 0.3 mM lactate removal (P = 0.289) at CE_2 = 73 ± 7% (P = 0.108). This implies that CPE-2 has no impact on electrode respiration, which is consistent with the observed lack of significant effect on current and charge outputs. M3C modification with cationic derivatives CPE-3 and CPE-4 decreases lactate consumption (at >95% significance) to, respectively, –1.7 ± 0.2 mM (P = 0.009) and –1.7 ± 0.5 mM (P = 0.041) at CE_3 = 59 ± 12% (P = 0.034) and CE_4 = 69 ± 24% (P = 0.305). The combination of decreased substrate consumption and lowered efficiency suggests that the bacteria modified with CPE-3 and CPE-4 are inhibited in their ability to respire on the electrode, rationalizing the corresponding observed decreases in current and charge outputs. These data are largely consistent with the CPE-bacteria-electrode adhesion interactions predicted in Fig. VI.3.

For all M3C conditions, CV was undertaken at t = −1 h (*i.e.* one hour before CA current collection was initiated in Fig. VI.4) and t = 16 h (*i.e.* immediately after CA current collection ended in Fig. VI.4) to characterize the potential dependence of current—and changes to that dependence—during device operation. The potential range of −0.6 V ≤ E ≤ 0.4 V used for CV is chosen to encompass three voltammetric features: (a) the native flavin-based MET catalytic current wave centered at ~−0.4 V,[73,84] (b) the native cytochrome-based DET catalytic current wave centered at ~0 V,[78,85,86] and (c) the M3C poised potential of E = 0.3 V. For both timepoints, the resulting CV traces and their derivatives (dJ/dE) are presented in Fig. VI.5 and discussed here.

Negative control M3Cs exhibit featureless, unchanging CV and dJ/dE traces, as can be seen in Fig. VI.5 a and g, indicating an absence of faradaic processes that would contribute to current production. This is consistent with the lack of CA current produced from these

devices and reinforces the observation that CPEs do not generate current in the absence of bacteria. In CV traces for positive control M3Cs (Fig. VI.5 b), the current response increases at E = 0.3 V from ~5 mA m^{-2} (t = −1 h) to ~10 mA m^{-2} (t = 16 h), in accord with the same increase in current density during CA (Fig. VI.4 b). The corresponding positive control dJ/dE trace in Fig. VI.5 g highlights two potential ranges for native catalytic electron transfer: the MET pathway is observed at −0.5 V ≤ E ≤ −0.3 V with the expected flavin peak at ~−0.4 V, while DET is observed at E ≥ −0.1 V with a peak at ~0 V. These peaks remain approximately equivalent to each other in magnitude over time, and both increase during device operation from ~±12 mA m^{-2} V^{-1} (t = −1 h) to ~±21 mA m^{-2} V^{-1} (t = 16 h) (see Table VI.3). These data indicate that for unmodified *S. oneidensis* MR-1, MET and DET contribute approximately equally to the catalytic current measured by CA, and these control experiments form the mechanistic basis for comparison of bacterial processes in the CPE-modified M3Cs as follows.

In the CV traces at t = −1 h, one observes the following M3C current density outputs at E = 0.3 V for each of the CPEs: ~4 mA m^{-2} for CPE-K M3Cs (Fig. VI.5 c), ~4 mA m^{-2} for CPE-2 M3Cs (Fig. VI.5 d), ~3 mA m^{-2} for CPE-3 M3Cs (Fig. VI.5 e), and ~2 mA m^{-2} for CPE-4 M3Cs (Fig. VI.5 f). These data broadly suggest that CPEs cause an initial reduction in bacterial current output at E = 0.3 V relative to the positive control (~5 mA m^{-2}), consistent with the initial values of $J(t)$ seen in CA traces in Fig. VI.4. However, the situation changes with device operation, as CV traces at t = 16 h reveal the following current density outputs at E = 0.3 V: ~21 mA m^{-2} for CPE-K M3Cs (Fig. VI.5 c), ~7 mA m^{-2} for CPE-2 M3Cs (Fig. VI.5 d), ~3 mA m^{-2} for CPE-3 M3Cs (Fig. VI.5 e), and ~4 mA m^{-2} for CPE-4 M3Cs (Fig. VI.5 f). Thus, relative to positive controls at t = 16 h (~10 mA m^{-2}), CPE-K enhances

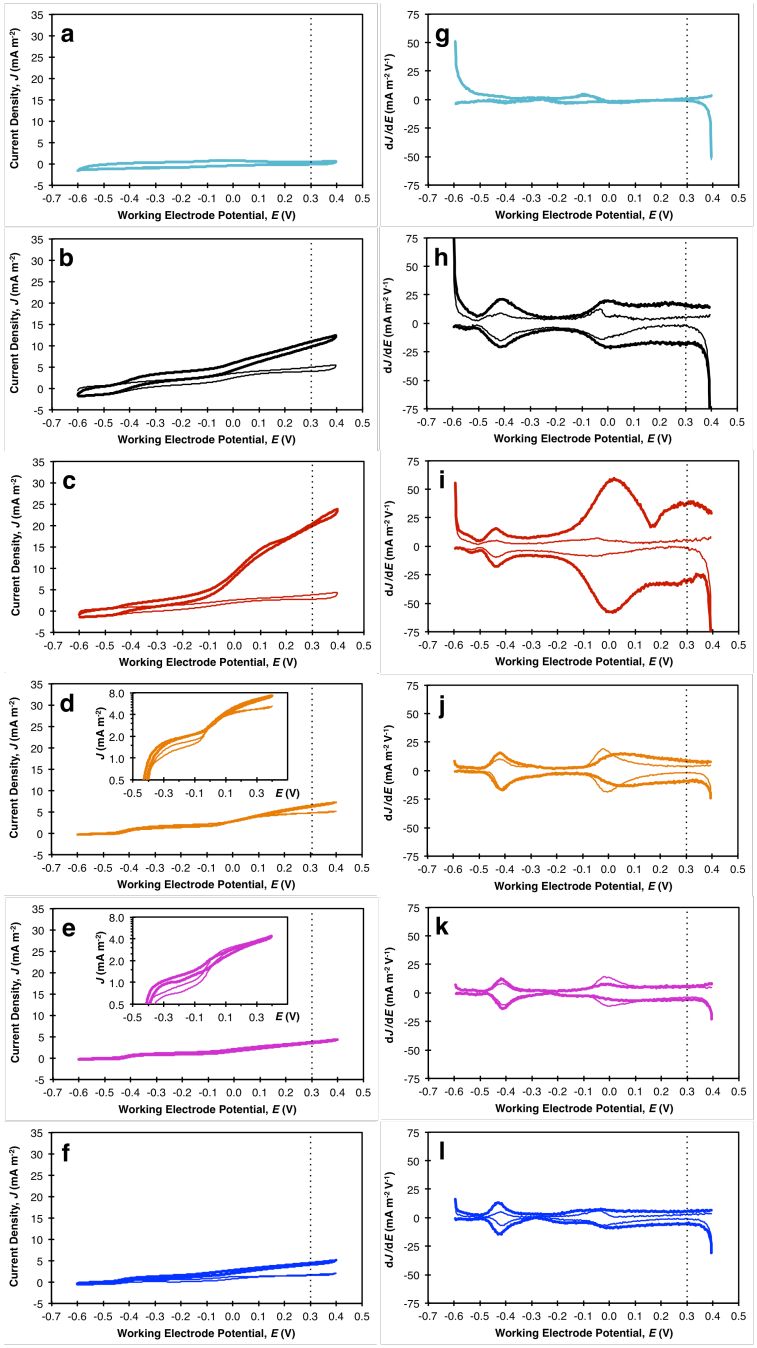

Figure VI.5. Average outputs from cyclic voltammetry (CV) and CV derivative (d*J*/d*E*) characterization of the potential dependence of EET for *S. oneidensis* MR-1 modified with CPEs in M3Cs. For each figure panel, the thin trace corresponds to $t = -1$ h (*i.e.* one hour before CA current collection) and the heavy trace corresponds to $t = 16$ h (*i.e.* immediately after CA current collection). Dotted lines in CV and d*J*/d*E* traces designate the working electrode poised potential of $E = 0.3$ V used for CA. Note that traces of the same color are used to indicate corresponding experimental conditions in (**a–f**) CV data and (**g–l**) d*J*/d*E* data. Each plotted trace is the average of ≥ 3 replicates, as indicated in the following labels. (**a, g**) Negative control: CPEs (any of the four tested) in culture medium with no cells; 11 replicates. (**b, h**) Positive control: *S. oneidensis* MR-1 and no CPEs; 3 replicates. (**c, i**) 10 µM CPE-K and *S. oneidensis* MR-1; 4 replicates. (**d, j**) 10 µM CPE-2 and *S. oneidensis* MR-1; 3 replicates. (**d, inset**) *J* plotted on a logarithmic scale vs. *E* for curve differentiation. (**e, k**) 10 µM CPE-3 and *S. oneidensis* MR-1; 3 replicates. (**e, inset**) *J* plotted on a logarithmic scale vs. *E* for curve differentiation. (**f, l**) 10 µM CPE-4 and *S. oneidensis* MR-1; 3 replicates.

catalytic current output, CPE-2 has a slightly inhibitory effect on catalytic current, and the cationic derivatives CPE-3 and CPE-4 inhibit catalytic current. The trend in these data matches that for measured steady-state current densities and charge collected (Table VI.2).

The MET and DET signals in the dJ/dE traces corresponding to these data help mechanistically rationalize the electrochemical effect of the CPEs. These data are summarized in Table VI.3 and discussed here. Relative to the positive control MET peak amplitude at t = −1 h (~±12 mA m^{-2} V^{-1}), the MET signal is suppressed to ~±7 mA m^{-2} V^{-1} for CPE-K (Fig. VI.5 i), increased to ~±14 mA m^{-2} V^{-1} for CPE-2 (Fig. VI.5 j), suppressed to ~±9 mA m^{-2} V^{-1} for CPE-3 (Fig. VI.5 k), and suppressed to ~±6 mA m^{-2} V^{-1} for CPE-4 (Fig. VI.5 l). Relative to the positive control DET signal at t = −1 h (~±12 mA m^{-2} V^{-1}), the DET signal is suppressed to ~±7 mA m^{-2} V^{-1} for CPE-K (Fig. VI.5 i), increased to ~±19 mA m^{-2} V^{-1} for CPE-2 (Fig. VI.5 j), increased to ~±13 mA m^{-2} V^{-1} for CPE-3 (Fig. VI.5 k), and suppressed to ~±6 mA m^{-2} V^{-1} for CPE-4 (Fig. VI.5 l). Relative to the positive control MET peak amplitude at t = 16 h (~±21 mA m^{-2} V^{-1}), the MET signal is suppressed to ~±16 mA m^{-2} V^{-1} for CPE-K (Fig. VI.5 i), suppressed to ~±16 mA m^{-2} V^{-1} for CPE-2 (Fig. VI.5 j), suppressed to ~±13 mA m^{-2} V^{-1} for CPE-3 (Fig. VI.5 k), and suppressed to ~±14 mA m^{-2} V^{-1} for CPE-4 (Fig. VI.5 l). Relative to the positive control DET signal at t = 16 h (~±21 mA m^{-2} V^{-1}), the DET signal is dramatically increased to ~±60 mA m^{-2} V^{-1} for CPE-K (Fig. VI.5 i), suppressed to ~±14 mA m^{-2} V^{-1} for CPE-2 (Fig. VI.5 j), suppressed to ~±7 mA m^{-2} V^{-1} for CPE-3 (Fig. VI.5 k), and suppressed to ~±8 mA m^{-2} V^{-1} for CPE-4 (Fig. VI.5 l). One may first broadly conclude that CPEs slightly inhibit the MET pathway relative to the native MET activity from *S. oneidensis* MR-1, as the only M3Cs exhibiting an MET signal higher than the control are those modified with CPE-2 at t = –1 h (this disappears by t = 16 h). One may

next conclude that CPEs generally inhibit the DET pathway relative to the native DET activity from *S. oneidensis* MR-1: the only M3Cs exhibiting a DET signal higher than the control are those modified with CPE-2 at $t = -1$ h (this also disappears by $t = 16$ h) and CPE-K at $t = 16$ h. For CPE-K, that DET signal (~±60 mA m^{-2} V^{-1}) is ~3-fold higher than positive controls and suggests that CPE-K serves as an extension of the electrode providing direct electrochemical contact because MET is not simultaneously increased. The DET increases in the presence of anionic derivatives CPE-K and CPE-2 combined with the ~3-fold DET suppression from cationic derivatives CPE-3 and CPE-4 compared to the positive control is further evidence supporting the predicted adhesion interactions in Fig. VI.3.

Table VI.3. Approximate MET (–0.4 V) and DET (0 V) d*J*/d*E* peak amplitudes before and after CA

	d*J*/d*E* (mA m^2 V^{-1}) at $t = -1$ (before CA)			d*J*/d*E* (mA m^2 V^{-1}) at $t = 16$ (after CA)		
CPE added	MET (–0.4 V)	DET (0 V)	MET:DET	MET (–0.4 V)	DET (0 V)	MET:DET
None (+ control)	±12	±12	1:1	±21	±21	1:1
CPE-K	±7	±7	1:1	±16	±60	1:3.75
CPE-2	±14	±19	1:1.36	±16	±14	1:0.88
CPE-3	±9	±13	1:1.44	±13	±7	1:0.54
CPE-4	±6	±6	1:1	±14	±8	1:0.57

The claim that CPE-K serves as an extension of the electrode is bolstered by absorbance spectroscopy. When an aqueous solution of doped CPE-K is added at 10 μM end concentration to an anaerobic suspension of electrochemically active *S. oneidensis* MR-1 (*i.e.* the conditions in an M3C), the polaronic ~1100 nm absorption band rapidly disappears, yielding the black trace in Fig. VI.2. As can be seen in Fig. VI.S1, the oscillator strength associated with the polaronic band shifts to the optical transition at 735 nm during this de-doping, consistent with previous reports.[44] Even if bacteria are removed from suspension by centrifugation, CPE-K remains de-doped from this process (Fig. VI.S2). These data suggest that the bacteria are able to donate metabolic electrons to CPE-K, de-doping the polymer by

filling the holes on the backbone. Of relevance is the notable additional catalytic electron transfer signal apparent at 0.15 V ≤ E ≤ 0.4 V in the t = 16 h CPE-K dJ/dE data (Fig. VI.5 i) that is not observed with any other CPEs. Considering that the frontier orbital potential (E_{HOMO} = 0.26 V) for CPE-K (Table VI.1) falls in this range, we conjecture that this catalytic signal arises from the electrode re-doping (oxidizing) bacterially de-doped CPE-K at the electrode surface, enabling a catalytic doping cycle for electron transfer (as predicted in Fig. VI.3). We note that E_{HOMO} = 0.11 V for CPE-3, and yet its inability to undergo doping under these conditions is consistent with its lack of catalytic contribution to electron transfer.

In view of the above data indicating that some CPEs suppress electron transfer while CPE-K increases it, it is relevant to quantify (a) the bacterial colonization of the electrode as a function of added CPE and (b) the concentration of CPEs adsorbed to the electrode during device operation. In regards to (a), electrode respiration provides a driving force for surface colonization,[32] meaning that increased electron transfer typically increases the surface density of cells, ρ_j. Therefore, after current collection and electrochemical characterization, SEM images of chemically fixed electrodes were obtained, and image processing was used to quantify the fraction of the electrode surface covered with bacteria, X_j, that enables calculation of ρ_j (see Materials and Methods). Representative images obtained for each condition are displayed in Fig. VI.6, and a quantitative summary is provided in Table VI.2. As can be seen, negative control M3Cs support no bacterial colonization (Fig. VI.6 a), while positive control M3Cs support X_+ = 0.12 ± 0.04 and ρ_+ = 214 ± 76 × 10^9 cells m^{-2} (Fig. VI.6 b). CPE-K modification supports statistically higher colonization than the positive control (at >95% significance), with X_K = 0.53 ± 0.16 and ρ_K = 960 ± 298 × 10^9 cells m^{-2} (P = 0.011) (Fig. VI.6 c). CPE-2 modification supports X_2 = 0.12 ± 0.06 and ρ_2 = 216 ± 108 × 10^9 cells

m^{-2} ($P = 0.981$) (Fig. VI.6 d), CPE-3 modification supports $X_3 = 0.12 \pm 0.02$ and $\rho_3 = 215 \pm 40 \times 10^9$ cells m^{-2} ($P = 0.985$) (Fig. VI.6 e), and CPE-4 modification supports $X_4 = 0.08 \pm 0.02$ and $\rho_4 = 151 \pm 30 \times 10^9$ cells m^{-2} ($P = 221$) (Fig. VI.6 f); none of these are statistically distinct from the positive control. Calculation of the current output on a per-cell basis, $I_{cell,j}$, reveals that it is statistically unaffected by the additions of CPEs (see Table VI.2), in contrast to the *reduction* in per-cell current observed in previous studies with COEs.[32]

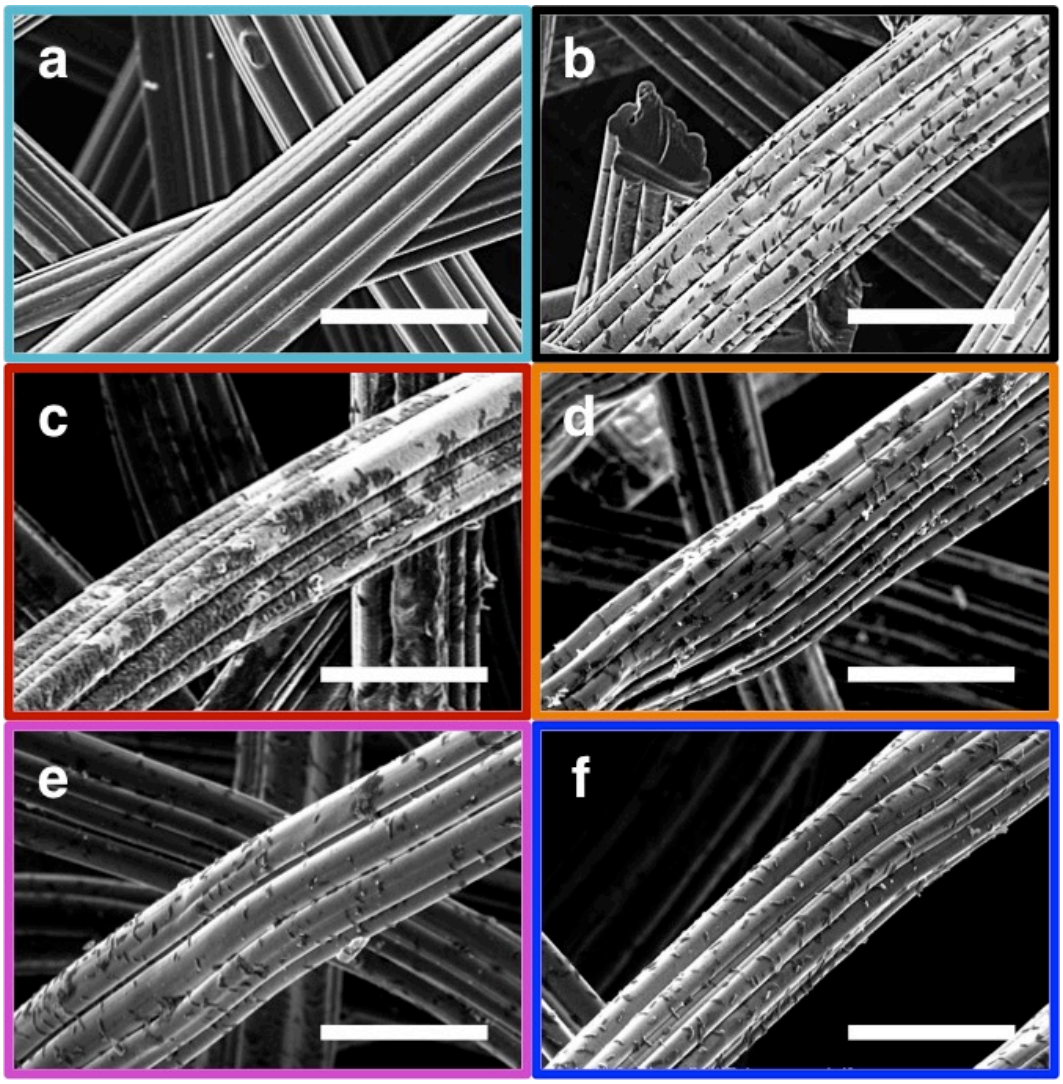

Figure VI.6. Representative SEM images of chemically-fixed M3C working electrodes. Chemical fixation (see Materials and Methods) was undertaken after termination of all bioelectrochemical measurements, followed by SEM imaging. Scale bars are 20 µm. (**a**) Negative control: CPEs in culture medium with no cells. (**b**) Positive control: *S. oneidensis* MR-1, no CPEs. (**c**) *S. oneidensis* MR-1 + 10 µM CPE-K. (**d**) *S. oneidensis* MR-1 + 10 µM CPE-2. (**e**) *S. oneidensis* MR-1 + 10 µM CPE-3. (**f**) *S. oneidensis* MR-1 + 10 µM CPE-4.

For (b), additional M3C CA experiments were conducted using CPEs without bacteria to allow CPEs to adsorb to the electrode *in situ*. Briefly, optical absorbance spectroscopy was conducted on the media after CA to quantify the CPE concentrations retained in solution, $[CPE]_{ret}$. Then, the difference in $[CPE]_{ret}$ and the original 10 μM solutions is taken as the concentration adsorbed to the electrode, given by

$$[CPE]_{ads} = 10\ \mu M - [CPE]_{ret} \quad \text{(VI.2)}.$$

It stands to reason that CPEs may electrostatically bind to the polar SiO_2 surface of the M3C vials, thereby decreasing the measured value of $[CPE]_{ret}$, so the measured value of $[CPE]_{ads}$ represents an upper bound. As can be seen in Table VI.4, $[CPE]_{ads}$ is 2.9 ± 0.7 mM for CPE-K, 1.8 ± 0.4 mM for CPE-2, 2.7 ± 0.8 mM for CPE-3, and 6.1 ± 0.9 mM for CPE-4. These data do not appear to correlate with the CPE molecular structures or pendant charges. Rather, by comparison to the molecular properties presented in Table VI.2, $[CPE]_{ads}$ appears to correlate to the molecular weight (M_n) of the CPEs. This suggests that CPEs adsorb to the electrode due to a hydrophobic interaction, not by an electrostatic force.

Table VI.4. Quantification of CPE electrode adsorption in the absence of bacteria

		CPEs			
Parameter	Expression	CPE-K	CPE-2	CPE-3	CPE-4
[CPE] retained in solution after CA (μM)[a]	$[CPE]_{ret} = A(\lambda_{max})/\varepsilon(\lambda_{max})l$	7.1 ± 0.7	8.2 ± 0.4	7.3 ± 0.8	3.9 ± 0.9
[CPE] adsorbed to electrode after CA (μM)	$[CPE]_{ads} = 10 - [CPE]_{ret}$	2.9 ± 0.7	1.8 ± 0.4	2.7 ± 0.8	6.1 ± 0.9

[a] Calculated using the Beer-Lambert law for absorbance, $A(\lambda) = \varepsilon(\lambda)cl$, where $A(\lambda)$ is absorption at a given wavelength (unitless), $\varepsilon(\lambda)$ is the molar absorptivity (M^{-1} cm^{-1}) at a given wavelength, c is the concentration of the absorbing species (M), and l is the path length of the cuvette (cm); $A(\lambda)$ and $\varepsilon(\lambda)$ are evaluated at the absorbance maxima, λ_{max}, of each CPE (see Table VI.1), l = 1 cm, and $c = [CPE]_{ret}$.

VI.D. Conclusions

Considering cell colonization and CPE-electrode adsorption results in view of the electrochemical and optical characterization presented here, one may surmise that cationic CPEs (CPE-3 and CPE-4)—and to a lesser extent, anionic CPE-2—passivate the electrode surface against bacterial electron transfer, while only self-doped, anionic CPE-K creates a conductive extension of the electrode by virtue of being cyclically de-doped (reduced) by metabolic electrons and doped (oxidized) by the electrode. For CPE-3 and CPE-4, this passivation is exacerbated by electrostatic CPE-cell binding that decreases cell zeta potential and electrostatic electrode affinity. Mechanistically, CPE-K appears to enhance the native DET pathway of the bacteria by enabling greater electrode colonization, but MET is not enhanced. These conclusions are consistent with (a) trends in steady-state biocurrent outputs relative to controls indicating that CPE-K amplifies current, CPE-2 has minimal effect, and CPE-3 and CPE-4 inhibit current, as well as (b) the observed increase in electrode cell coverage from CPE-K not observed for the other CPEs. More broadly, the efficacy of CPE-K and the ease of its implementation from aqueous solution suggest that it may find immediate use as a biotic-abiotic interfacial modifier in a variety of bioelectrochemical devices, while specific practical device conditions will no doubt require optimization.

VI.E. References

1. Borenfreund, E. & Puerner, J. A. Cytotoxicity of metals, metal-metal and metal-chelator combinations assayed in vitro. *Toxicology* **39,** 121–134 (1986).
2. Gans, J., Wolinsky, M. & Dunbar, J. Computational improvements reveal great bacterial diversity and high metal toxicity in soil. *Science* **309,** 1387–1390 (2005).
3. Simon-Deckers, A. *et al.* Size-, composition- and shape-dependent toxicological impact of metal oxide nanoparticles and carbon nanotubes toward bacteria. *Environ. Sci. Technol.* **43,** 8423–8429 (2009).
4. Jones, D. L. & Kochian, L. V. Aluminum interaction with plasma membrane lipids and enzyme metal binding sites and its potential role in Al cytotoxicity. *FEBS Lett.* **400,**

51–57 (1997).
5. Baek, Y. W. & An, Y. J. Microbial toxicity of metal oxide nanoparticles (CuO, NiO, ZnO, and Sb2O3) to Escherichia coli, Bacillus subtilis, and Streptococcus aureus. *Sci. Total Environ.* **409,** 1603–1608 (2011).
6. Heinlaan, M., Ivask, A., Blinova, I., Dubourguier, H. C. & Kahru, A. Toxicity of nanosized and bulk ZnO, CuO and TiO2 to bacteria Vibrio fischeri and crustaceans Daphnia magna and Thamnocephalus platyurus. *Chemosphere* **71,** 1308–1316 (2008).
7. Karlsson, H. L., Cronholm, P., Gustafsson, J. & Möller, L. Copper oxide nanoparticles are highly toxic: A comparison between metal oxide nanoparticles and carbon nanotubes. *Chem. Res. Toxicol.* **21,** 1726–1732 (2008).
8. Kang, S., Mauter, M. S. & Elimelech, M. Physicochemical Determinants of Multiwalled Carbon Nanotube Bacterial Cytotoxicity Physicochemical Determinants of Multiwalled Carbon Nanotube Bacterial Cytotoxicity. **42,** 7528–7534 (2008).
9. Kang, S., Pinault, M., Pfefferle, L. D. & Elimelech, M. Single-walled carbon nanotubes exhibit strong antimicrobial activity. *Langmuir* **23,** 8670–8673 (2007).
10. Kostarelos, K. The long and short of carbon nanotube toxicity. *Nat. Biotechnol.* **26,** 774–776 (2008).
11. Lam, C.-W., James, J. T., McCluskey, R., Arepalli, S. & Hunter, R. L. A review of carbon nanotube toxicity and assessment of potential occupational and environmental health risks. *Crit. Rev. Toxicol.* **36,** 189–217 (2006).
12. Akhavan, O. & Ghaderi, E. Toxicity of graphene and graphene oxide nanowalls against bacteria. *ACS Nano* **4,** 5731–5736 (2010).
13. Hill, H. A. O. & Higgins, I. J. Bioelectrocatalysis. *Philos. Trans. R. Soc. A Math. Phys. Eng. Sci.* **302,** 267–273 (1981).
14. Magliulo, M., Manoli, K., Macchia, E., Palazzo, G. & Torsi, L. Tailoring Functional Interlayers in Organic Field-Effect Transistor Biosensors. *Adv. Mater.* 1–24 (2014).
15. Park, S., Kang, Y. J. & Majd, S. A Review of Patterned Organic Bioelectronic Materials and their Biomedical Applications. *Adv. Mater.* **27,** 7583–7619 (2015).
16. Green, R. & Abidian, M. R. Conducting Polymers for Neural Prosthetic and Neural Interface Applications. 1–18 (2015).
17. Rosenbaum, M. A. & Franks, A. E. Microbial catalysis in bioelectrochemical technologies: status quo, challenges and perspectives. *Appl. Microbiol. Biotechnol.* **98,** 509–18 (2014).
18. Logan, B. E. Exoelectrogenic bacteria that power microbial fuel cells. *Nat. Rev. Microbiol.* **7,** 375–81 (2009).
19. Borole, A. P. *et al.* Electroactive biofilms: Current status and future research needs. *Energy Environ. Sci.* **4,** 4813 (2011).
20. Logan, B. E. & Rabaey, K. Conversion of wastes into bioelectricity and chemicals by using microbial electrochemical technologies. *Science.* **337,** 686–90 (2012).
21. Nevin, K., Woodard, T., Franks, A., Summers, Z. & Lovley, D. Microbial Electrosynthesis: Feeding Microbes Electricity To Convert Carbon Dioxide and Water to Multicarbon Extracellular Organic Compounds. *MBio* **1,** 1–4 (2010).
22. Rabaey, K. & Rozendal, R. A. Microbial electrosynthesis - revisiting the electrical route for microbial production. *Nat. Rev. Microbiol.* **8,** 706–16 (2010).
23. Cheng, S., Xing, D., Call, D. F. & Logan, B. E. Direct Biological Conversion of Electrical Current into Methane by Electromethanogenesis. *Environ. Sci. Technol.* **43,**

3953–3958 (2009).
24. Du, J., Catania, C. & Bazan, G. Modification of Abiotic−Biotic Interfaces with Small Molecules and Nanomaterials for Improved Bioelectronics. *Chem. Mater.* (2013).
25. Garner, L. E. *et al.* Modification of the optoelectronic properties of membranes via insertion of amphiphilic phenylenevinylene oligoelectrolytes. *J. Am. Chem. Soc.* **132,** 10042–52 (2010).
26. Garner, L. E., Thomas, A. W., Sumner, J. J., Harvey, S. P. & Bazan, G. C. Conjugated oligoelectrolytes increase current response and organic contaminant removal in wastewater microbial fuel cells. *Energy Environ. Sci.* **5,** 9449–9452 (2012).
27. Hou, H. *et al.* Conjugated Oligoelectrolytes Increase Power Generation in E. coli Microbial Fuel Cells. *Adv. Mater.* **25,** 1593–7 (2013).
28. Du, J. *et al.* Increased ion conductance across mammalian membranes modified with conjugated oligoelectrolytes. *Chem. Commun.* **49,** 9624–6 (2013).
29. Thomas, A. W. *et al.* A lipid membrane intercalating conjugated oligoelectrolyte enables electrode driven succinate production in Shewanella. *Energy Environ. Sci.* **6,** 1761 (2013).
30. Wang, V. B. *et al.* Improving charge collection in Escherichia coli-carbon electrode devices with conjugated oligoelectrolytes. *Phys. Chem. Chem. Phys.* **15,** 5867–72 (2013).
31. Wang, V. B. *et al.* Comparison of flavins and a conjugated oligoelectrolyte in stimulating extracellular electron transport from Shewanella oneidensis MR-1. *Electrochem. commun.* **41,** 55–58 (2014).
32. Kirchhofer, N. D. *et al.* The conjugated oligoelectrolyte DSSN+ enables exceptional coulombic efficiency via direct electron transfer for anode-respiring Shewanella oneidensis MR-1-a mechanistic study. *Phys. Chem. Chem. Phys.* **16,** 20436–43 (2014).
33. Thomas, A. W., Henson, Z. B., Du., J., Vandenberg C. A., & Bazan, G. C. Synthesis, Characterization, and Biological Affinity of a Near-Infrared-Emitting Conjugated Oligoelectrolyte. *J. Am. Chem. Soc.* **136,** 3736–3739 (2014).
34. Hinks, J. *et al.* Modeling cell membrane perturbation by molecules designed for transmembrane electron transfer. *Langmuir* **30,** 2429–40 (2014).
35. Thomas, A. W., Catania, C., Garner, L. E. & Bazan, G. C. Pendant ionic groups of conjugated oligoelectrolytes govern their ability to intercalate into microbial membranes. *Chem. Commun.* **51,** 9294–9297 (2015).
36. Kirchhofer, N. D., Rasmussen, M. A., Dahlquist, F. W., Minteer, S. D. & Bazan, G. C. The photobioelectrochemical activity of thylakoid bioanodes is increased via photocurrent generation and improved contacts by membrane-intercalating conjugated oligoelectrolytes. *Energy Environ. Sci.* **8,** 2698–2706 (2015).
37. Yan, H., Catania, C. & Bazan, G. C. Membrane-Intercalating Conjugated Oligoelectrolytes: Impact on Bioelectrochemical Systems. *Adv. Mater.* **27,** 2958–2973 (2015).
38. Jahnke, J. P., Bazan, G. C. & Sumner, J. J. Effect of Modified Phospholipid Bilayers on the Electrochemical Activity of a Membrane-Spanning Conjugated Oligoelectrolyte. *Langmuir* **31,** 11613–11620 (2015).
39. Liu, D., Lei, L., Yang, B., Yu, Q. & Li, Z. Direct electron transfer from electrode to electrochemically active bacteria in a bioelectrochemical dechlorination system. *Bioresour. Technol.* **148,** 9–14 (2013).

40. Yu, Y.-Y., Chen, H., Yong, Y.-C., Kim, D.-H. & Song, H. Conductive artificial biofilm dramatically enhances bioelectricity production in Shewanella-inoculated microbial fuel cells. *Chem. Commun.* **47,** 12825 (2011).
41. Bond, A. M., McLennan, E. A., Stojanovic, R. S. & Thomas, F. G. Assessment of conditions under which the oxidation of ferrocene can be used as a standard voltammetric reference process in aqueous media. *Anal. Chem.* **50,** 2853–2860 (1987).
42. Cardona, C. M., Li, W., Kaifer, A. E., Stockdale, D. & Bazan, G. C. Electrochemical considerations for determining absolute frontier orbital energy levels of conjugated polymers for solar cell applications. *Adv. Mater.* **23,** 2367–2371 (2011).
43. *Conjugated Polyelectrolytes: Fundamentals and Applications*. (John Wiley & Sons, 2013).
44. Mai, C.-K. *et al.* Facile Doping of Anionic Narrow-Band-Gap Conjugated Polyelectrolytes During Dialysis. *Angew. Chemie Int. Ed.* **52,** 12874–12878 (2013).
45. Zhou, H. *et al.* Conductive Conjugated Polyelectrolyte as Hole-Transporting Layer for Organic Bulk Heterojunction Solar Cells. *Adv. Mater.* **26,** 780–785 (2014).
46. Li, Y. *et al.* Electronic Properties of Conjugated Polyelectrolyte/Single-Walled Carbon Nanotube Composites. *Adv. Mater.* **26**, 4697-4703 (2014).
47. Zhou, H. *et al.* Polymer Homo-Tandem Solar Cells with Best Efficiency of 11.3%. *Adv. Mater.* **27,** 1767–1773 (2015).
48. Mai, C.-K. *et al.* Electrical properties of doped conjugated polyelectrolytes with modulated density of the ionic functionalities. *Chem. Commun.* **51,** 17607–17610 (2015).
49. Choi, H. *et al.* Conjugated polyelectrolyte hole transport layer for inverted-type perovskite solar cells. *Nat. Commun.* **6,** 7348 (2015).
50. Zhou, H. *et al.* Solution-Processed pH-Neutral Conjugated Polyelectrolyte Improves Interfacial Contact in Organic Solar Cells. *ACS Nano* **9,** 371–377 (2015).
51. Mai, C. *et al.* Side-Chain Effects on the Conductivity, Morphology, and Thermoelectric Properties of Self-Doped Narrow-Band-Gap Conjugated Polyelectrolytes. *J. Am. Chem. Soc.* **136**, 13478-13481 (2014).
52. Mai, C.-K. *et al.* Varying the ionic functionalities of conjugated polyelectrolytes leads to both p- and n-type carbon nanotube composites for flexible thermoelectrics. *Energy Environ. Sci.* **8,** 2341–2346 (2015).
53. Reguera, G. *et al.* Extracellular electron transfer via microbial nanowires. *Nature* **435,** 1098–1101 (2005).
54. Reguera, G. *et al.* Biofilm and nanowire production leads to increased current in Geobacter sulfurreducens fuel cells. *Appl. Environ. Microbiol.* **72,** 7345–8 (2006).
55. Gorby, Y. A. *et al.* Electrically conductive bacterial nanowires produced by Shewanella oneidensis strain MR-1 and other microorganisms. *Proc. Natl. Acad. Sci. U. S. A.* **103,** 11358–63 (2006).
56. El-Naggar, M. Y. *et al.* Electrical transport along bacterial nanowires from Shewanella oneidensis MR-1. *Proc. Natl. Acad. Sci. U. S. A.* **107,** 18127–31 (2010).
57. Strycharz-Glaven, S. M., Snider, R. M., Guiseppi-Elie, A. & Tender, L. M. On the electrical conductivity of microbial nanowires and biofilms. *Energy Environ. Sci.* **4,** 4366 (2011).
58. Malvankar, N. S. *et al.* Tunable metallic-like conductivity in microbial nanowire networks. *Nat. Nanotechnol.* **6,** 573–9 (2011).

59. Veazey, J. P., Reguera, G. & Tessmer, S. H. Electronic properties of conductive pili of the metal-reducing bacterium Geobacter sulfurreducens probed by scanning tunneling microscopy. *Phys. Rev. E - Stat. Nonlinear, Soft Matter Phys.* **84,** 1–4 (2011).
60. Bond, D. R., Strycharz-Glaven, S. M., Tender, L. M. & Torres, C. I. On Electron Transport through Geobacter Biofilms. *ChemSusChem* **5,** 1099–1105 (2012).
61. Malvankar, N. S., Tuominen, M. T. & Lovley, D. R. Comment on 'On electrical conductivity of microbial nanowires and biofilms' by S. M. Strycharz-Glaven, R. M. Snider, A. Guiseppi-Elie and L. M. Tender, Energy Environ. Sci., 2011, 4, 4366. *Energy Environ. Sci.* **5,** 6247 (2012).
62. Strycharz-Glaven, S. M. & Tender, L. M. Reply to the 'Comment on "'On electrical conductivity of microbial nanowires and biofilms"' by N. S. Malvankar, M. T. Tuominen and D. R. Lovley, Energy Environ. Sci., 2012, 5, DOI: 10.1039/c2ee02613a. *Energy Environ. Sci.* **5,** 6250–6255 (2012).
63. Malvankar, N. S. & Lovley, D. R. Microbial Nanowires: A New Paradigm for Biological Electron Transfer and Bioelectronics. *ChemSusChem* **5,** 1039–1046 (2012).
64. Malvankar, N. S., Tuominen, M. T. & Lovley, D. R. Lack of cytochrome involvement in long-range electron transport through conductive biofilms and nanowires of Geobacter sulfurreducens. *Energy Environ. Sci.* **5,** 8651 (2012).
65. Leung, K. M. *et al.* Shewanella oneidensis MR-1 bacterial nanowires exhibit p-type, tunable electronic behavior. *Nano Lett.* **13,** 2407–11 (2013).
66. Reardon, P. N. & Mueller, K. T. Structure of the type IVa major pilin from the electrically conductive bacterial nanowires of geobacter sulfurreducens. *J. Biol. Chem.* **288,** 29260–29266 (2013).
67. Malvankar, N. S. & Lovley, D. R. Microbial nanowires for bioenergy applications. *Curr. Opin. Biotechnol.* **27,** 88–95 (2014).
68. Pirbadian, S. *et al.* Shewanella oneidensis MR-1 nanowires are outer membrane and periplasmic extensions of the extracellular electron transport components. *Proc. Natl. Acad. Sci.* **111,** 1–6 (2014).
69. Malvankar, N. S. *et al.* Structural Basis for Metallic-Like Conductivity in Microbial Nanowires. *MBio* **6,** 1–10 (2015).
70. Yan, H. *et al.* Inter-Aromatic Distances in Geobacter Sulfurreducens Pili Relevant to Biofilm Charge Transport. *Adv. Mater.* **27,** 1908–1911 (2015).
71. Torres, C. I. *et al.* A kinetic perspective on extracellular electron transfer by anode-respiring bacteria. *FEMS Microbiol. Rev.* **34,** 3–17 (2010).
72. Marsili, E., Rollefson, J. B., Baron, D. B., Hozalski, R. M. & Bond, D. R. Microbial biofilm voltammetry: direct electrochemical characterization of catalytic electrode-attached biofilms. *Appl. Environ. Microbiol.* **74,** 7329–37 (2008).
73. Marsili, E. *et al.* Shewanella secretes flavins that mediate extracellular electron transfer. *Proc. Natl. Acad. Sci. U. S. A.* **105,** 3968–73 (2008).
74. Fredrickson, J. K. *et al.* Towards environmental systems biology of Shewanella. *Nat. Rev. Microbiol.* **6,** 592–603 (2008).
75. Hau, H. H. & Gralnick, J. A. Ecology and biotechnology of the genus Shewanella. *Annu. Rev. Microbiol.* **61,** 237–258 (2007).
76. Feng, G., Mai, C.-K., Zhan, R., Bazan, G. C. & Liu, B. Narrow band gap conjugated polyelectrolytes for photothermal killing of bacteria. *J. Mater. Chem. B* **3,** 7340–7346 (2015).

77. Mai, C. K. *et al.* Facile doping of anionic narrow-band-gap conjugated polyelectrolytes during dialysis. *Angew. Chemie - Int. Ed.* **52,** 12874–12878 (2013).
78. Roy, J. N. *et al.* Catalytic biofilm formation by Shewanella oneidensis MR-1 and anode characterization by expanded uncertainty. *Electrochim. Acta* **126,** 3–10 (2014).
79. Babanova, S. *et al.* Innovative statistical interpretation of Shewanella oneidensis microbial fuel cells data. *Phys. Chem. Chem. Phys.* **16,** 8956–69 (2014).
80. Renslow, R. *et al.* Modeling biofilms with dual extracellular electron transfer mechanisms. *Phys. Chem. Chem. Phys.* **15,** 19262–83 (2013).
81. Rosenbaum, M., Cotta, M. A. & Angenent, L. T. Aerated Shewanella oneidensis in continuously fed bioelectrochemical systems for power and hydrogen production. *Biotechnol. Bioeng.* **105,** 880–888 (2010).
82. Beaujuge, P., Amb, C. & Reynolds, J. R. Spectral engineering in π-conjugated polymers with intramolecular donor−acceptor interactions. *Acc. Chem. Res.* **43,** 1396–1407 (2010).
83. Coughlin, J. E., Henson, Z. B., Welch, G. C. & Bazan, G. C. Design and synthesis of molecular donors for solution-processed high-efficiency organic solar cells. *Acc. Chem. Res.* **47,** 257–70 (2014).
84. von Canstein, H., Ogawa, J., Shimizu, S. & Lloyd, J. R. Secretion of flavins by Shewanella species and their role in extracellular electron transfer. *Appl. Environ. Microbiol.* **74,** 615–23 (2008).
85. Okamoto, A., Hashimoto, K., Nealson, K. H. & Nakamura, R. Rate enhancement of bacterial extracellular electron transport involves bound flavin semiquinones. *Proc. Natl. Acad. Sci.* **110,** 1–6 (2013).
86. Jain, A. *et al.* Electron transfer mechanism in Shewanella loihica PV-4 biofilms formed at graphite electrode. *Bioelectrochemistry* **87,** 28–32 (2012).
87. Blainey, P., Krzywinski, M. & Altman, N. Points of Significance: Replication. *Nat. Methods* **11,** 879–880 (2014).
88. Cao, B. *et al.* Biofilm shows spatially stratified metabolic responses to contaminant exposure. *Environ. Microbiol.* **14,** 2901–10 (2012).
89. Cao, B. *et al.* Extracellular polymeric substances from Shewanella sp. HRCR-1 biofilms: characterization by infrared spectroscopy and proteomics. *Environ. Microbiol.* **13,** 1018–31 (2011).
90. Kirchhofer, N. D. *et al.* The conjugated oligoelectrolyte DSSN+ enables exceptional coulombic efficiency via direct electron transfer for anode-respiring Shewanella oneidensis MR-1-a mechanistic study. *Phys. Chem. Chem. Phys.* **16,** 20436–43 (2014).
91. Ji, E., Corbitt, T. S., Parthasarathy, A., Schanze, K. S. & Whitten, D. G. Light and dark-activated biocidal activity of conjugated polyelectrolytes. *ACS Appl. Mater. Interfaces* **3,** 2820–9 (2011).

VI.F. Appendix VI. Materials, Methods, and Supplementary Figures

VI.F.1. Materials and Methods

VI.F.1.a. Materials

All chemicals were purchased from Fisher Scientific or Sigma Aldrich and used as received unless otherwise indicated. CPE-K and CPE-2 were synthesized according to literature procedures.[44] The molecular weights of CPE-K and CPE-2 were determined by gel permeation chromatography (GPC) in DMF of their derivatives, which were obtained after ion exchange with excess tetrabutylammonium bromide followed by dialysis.[44] CPE-3 and CPE-4 were prepared from the corresponding neutral polymer CPE-C6Br and PFBT-C6Br, respectively. The syntheses involve quaternization with trimethylamine followed by ion exchange with excess $NaBIm_4$, as described in the next subsection.

VI.F.1.b. General information for the synthesis of CPE-3

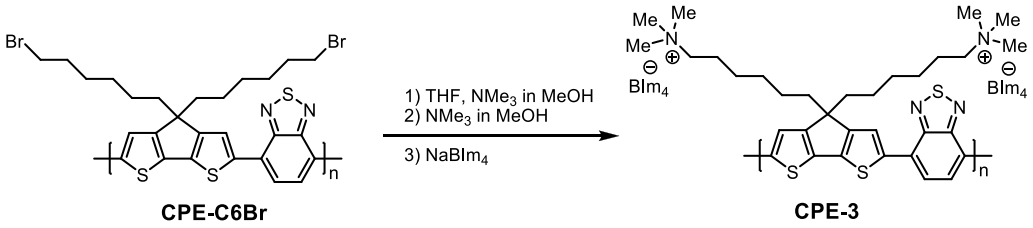

Scheme VI.S1. Preparation of CPE-3.

CPE-3 was synthesized from the neutral polymer precursor (CPE-C6Br).[44] CPE-C6Br (95 mg) was dissolved in THF (10 mL), and excess NMe_3 in MeOH (3.2 M, 1.9 mL, 20 equivalences of Br) was added. Some polymer was precipitated in ~5 minutes. The reaction mixture was allowed to stir at room temperature for 5 h, and concentrated. The residue was redissolved in MeOH (10 mL) and NMe_3 in MeOH (3.2 M, 1.6 mL) was added. The mixture

was stirred overnight. Concentration and drying under vacuum provided the intermediate as an orange solid (101 mg, 90%). The intermediate (36 mg) was dissolved in MeOH (5 mL), and $NaBIm_4$ (144 mg, 10 equivalences of Br) was added. The mixture was stirred at RT for 1 hr, concentrated and cold water was added (40 mL). The aqueous suspension was centrifuged, and the supernatant was removed. The residue was redissolved in MeOH (5 mL) followed by addition of $NaBIm_4$. The mixing and removal of excess $NaBIm_4$ were repeated twice, and the final product was dried under vacuum to provide CPE-3 (30 mg, 62%). ^{1}H NMR (600 MHz, CD_3OD) δ 8.30 – 7.80 (m, 4H), 7.19 (s, 8H), 7.01 (s, 8H), 6.82 (s, 8H), 3.25 – 2.70 (m, 22H), 2.28 – 0.68 (m, 20H).

VI.F.1.c. General information for the synthesis of CPE-4

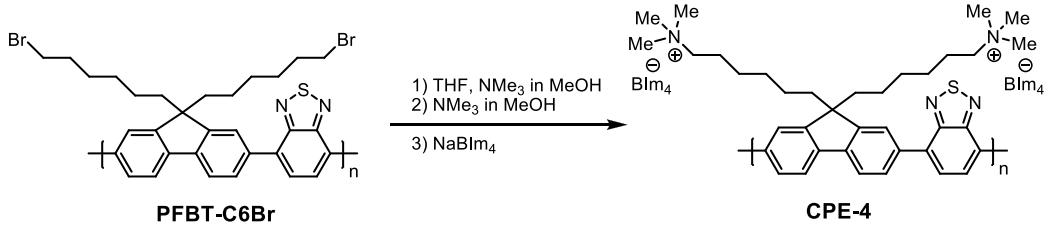

Scheme VI.S2. Preparation of CPE-4.

CPE-4 was synthesized from the neutral polymer precursor (PFBT-C6Br)[52] using a similar procedure as CPE-3 (52% overall yield). ^{1}H NMR (600 MHz, CD_3OD) δ 8.30 – 7.90 (m, 8H), 7.21 (s, 8H), 7.02 (s, 8H), 6.85 (s, 8H), 3.13 (br s, 4H), 3.06 – 2.84 (m, 18H), 1.73 – 1.42 (br s, 4H), 1.42 – 1.04 (m, 4H), 0.95 – 0.60 (br s, 4H).

VI.F.1.d. Cell culture, inoculation, and growth medium

Shewanella oneidensis MR-1 was struck out on LB agar plates from frozen bacterial stock and incubated at 30 °C for ~24 hours to isolate single colonies. Biological replicate[87]

cultures were grown by selecting morphologically similar colonies with a sterile loop to inoculate anaerobic (actively bubbling with N_2 gas) modified M1 medium[88,89] containing 20 mM Na-(L)-lactate as donor and 20 mM Na-fumarate as acceptor. After 24 hours of incubation with shaking at 30 °C, such cultures consistently reach a maximum OD_{600} of ~0.16 (or 1.6×10^8 cfu/mL, as *Shewanella oneidensis* MR-1 was previously determined to be ~1×10^9 cfu/mL/OD.[32] These stationary phase cultures (fumarate completely consumed) may then be used to inoculate separate replicate M3Cs as described, as most of the lactate remains.

VI.F.1.e. Bioelectrochemical reactors

The 3-electrode, batch-type, membraneless bioelectrochemical reactors used herein (M3Cs) were similar to those previously reported[90] and key components are described here. Glass M3C vials had a 15 mL working volume and were sealed with rubber septa. Electrode specifications were as follows. Reference electrode: Ag/AgCl (saturated KCl) with 3.2 mm Vycor frit (Gamry). Counter electrode: coiled 0.25 mm Ti wire (Aldrich), 10 turns. Working electrode: 1 cm × 1 cm × 0.2 cm graphite felt (Alfa Aesar), woven with Ti wire as the electrical lead. Anaerobic conditions were maintained through constant headspace degassing with humidified, deoxygenated N_2. Temperature was kept at 30 °C by housing the M3Cs in a temperature regulated incubator. CPEs were added to stationary cultures (previous subsection) at 10 μM end concentration by first making concentrated aqueous solutions (200–1000 μM) and then adding the necessary negligible volume of these solutions to achieve the correct CPE concentration. The mixtures were subsequently used to inoculate M3Cs.

VI.F.1.f. Ultraviolet-Visible Absorbance Spectroscopy

Solutions were illuminated at 1 nm wavelength intervals at a scan rate of 20 nm/s (Beckman Coulter DU 800 Spectrophotometer) in a quartz cuvette with 1 cm path length.

VI.F.1.g. Chronoamperometry (CA)

Using a Gamry potentiostat (Reference 600, Series G 300 or Series G 750 models) and multiplexer (model ECM8), M3C graphite felt working electrodes were poised at E = 0.3 V vs. Ag/AgCl to serve as the sole terminal electron acceptor for bacteria. M3Cs were inoculated from stationary bacteria-CPE mixtures (see above) and incubated in the dark[91] with 100 rpm magnetic stirring for 16 hours to cultivate an electroactive biofilm and measure current responses. The current response was measured, recorded, and averaged for 20-second blocks (at 160 second intervals) with Gamry software (Framework Version 6.11, Build 2227, 2013). Time integration of the resulting current response determined the amount of charge transferred by the bacteria, Q_{coll} (Table VI.1).

VI.F.1.h. Cyclic voltammetry (CV)

Electrochemical characterization with CV was undertaken with a Gamry potentiostat (Reference 600, Series G 300 or Series G 750 models) and multiplexer (model ECM8) immediately before and after CA to characterize the CPE-bacteria-electrode interactions. For these experiments, the working electrode potential was swept from $E_{initial}$ = –0.6 V to E_{vertex} = 0.4 V and back to E_{final} = –0.6 V at a scan rate of 0.005 V/s.

VI.F.1.i. High performance liquid chromatography (HPLC)

HPLC analysis of M3C effluent was performed with a Shimadzu LC20AB instrument equipped with an organic acid compatible Aminex HPX-87H column (Bio-Rad). Samples

from M3Cs were filtered through 0.22 μm PVDF filters (GSTek) to remove cells, and diluted 10-fold into mobile phase prior to analysis. The mobile phase was 0.004 M (0.008 N) aqueous H_2SO_4 flowing at 0.6 mL/min, and UV detection was set at 210 nm.

VI.F.1.j. Scanning electron microscopy (SEM)

Images of chemically fixed graphite felt electrodes were obtained with an FEI XL40 SEM at an accelerating voltage of 5 kV, working distance of ~5 mm, and a spot size of 3. Post processing of images only involved increasing the brightness and/or contrast of the images by up to 40% in order to better visualize cells.

VI.F.1.k. Cell counting

To find electrode cell density, ρ_j, for the M3Cs, SEM images were analyzed using ImageJ. Each SEM image was originally obtained in 8-bit grey scale (see Fig. VI.S3 a). All images were then spatially calibrated by using the line tool to trace the scale bars. Images were thresholded (Image > Adjust > Threshold) to segment out the microbes from the electrode background (Fig. VI.S3 b). The polygon selection tool was then used to outline the predominant electrode fiber as the region of interest in the image. In order to discount stray pixels that fell within the threshold range, the minimum particle size was set to 15 pixels, and the area fraction of microbes on the electrode region of interest was calculated (Analyze > Analyze Particles). The option "Show Outlines" was used to check that all desired features were included in the results (Fig. VI.S3 c). Area fraction results (Fig. VI.S3 d) were averaged across multiple SEM images of each M3C type. By a similar method using small segments of the SEM images containing single bacterial cells, the average area of a single cell was determined to be A_{cell} = 5.57 ± 0.39 × 10^{-13} m^2 (or 0.557 ± 0.039 μm^2). ρ_j was finally

calculated by dividing the average area fraction by A_{cell} as described in Table VI.2 in the main text.

VI.F.1.l. Chemical fixation of cells

After all bioelectrochemical and confocal microscopy experiments, M3C working electrodes were submerged in 100 mM PBS, pH = 7 containing 2% (v/v) formaldehyde to fix electrode-associated cells for 24 hours. After fixation, electrodes were sequentially rinsed with the following solutions twice each: 100 mM PBS, pH = 7 (10 min), deionized water (10 min), 70% ethanol in deionized water (10 min), 100% ethanol (30 min). Electrodes were then allowed to air dry for 24 hours and stored in glass scintillation vials for future study.

VI.F.2. Supplementary Figures

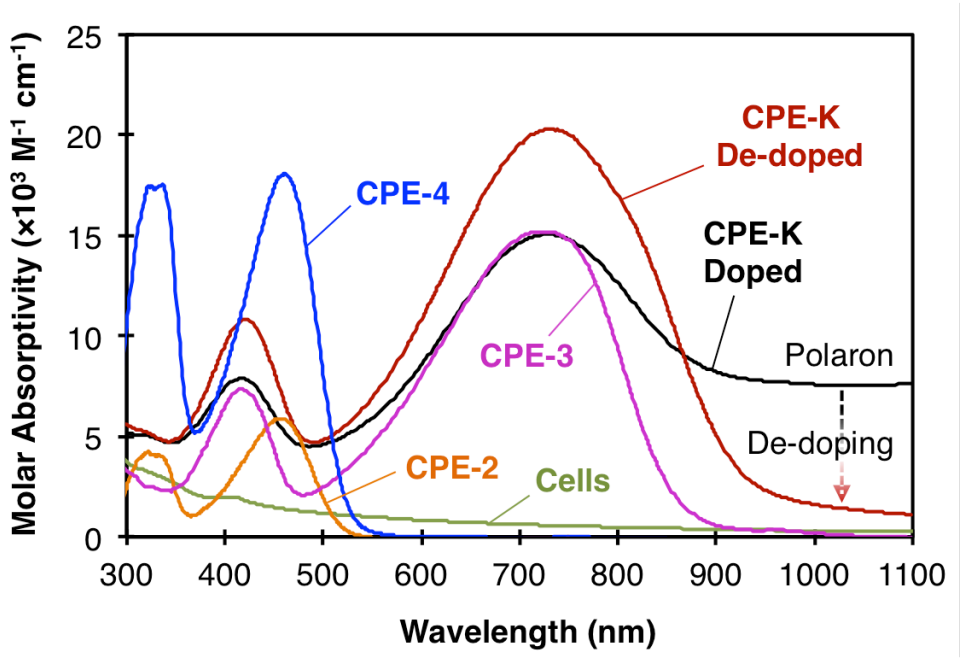

Figure VI.S1. Non-normalized molar absorptivity of CPEs by monomer molecular weight. The green trace corresponds to absorbance of the OD = 0.16 bacterial cultures used for inoculation, scaled as it would have contributed to these spectra.

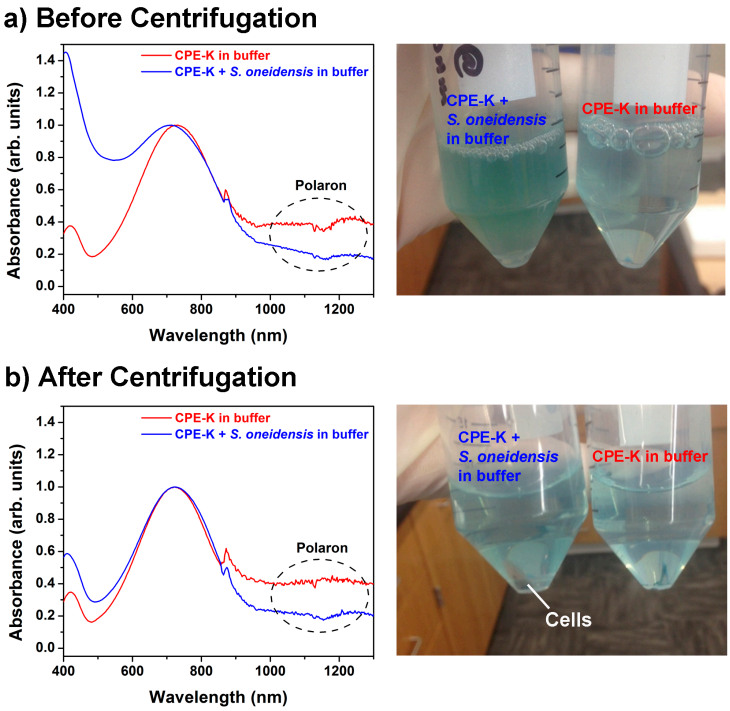

Figure VI.S2. Normalized absorbance spectra of equimolar CPE-K solutions with and without *S. oneidensis* MR-1 (a) before and (b) after centrifugation. Dashed oval: polaron absorption decreases in the presence of bacteria. Dashed arrow: shorter wavelength absorbance in the blue trace decreases as the suspension of bacteria is removed from solution by centrifugation.

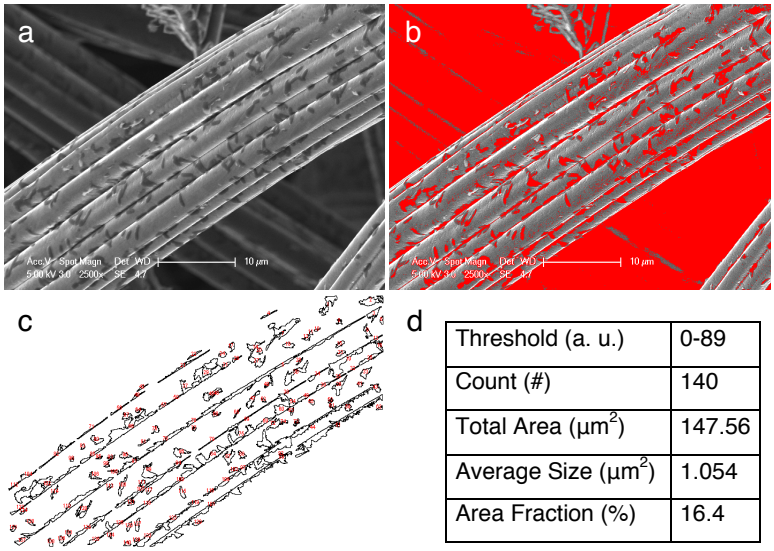

Threshold (a. u.)	0-89
Count (#)	140
Total Area (μm^2)	147.56
Average Size (μm^2)	1.054
Area Fraction (%)	16.4

Figure VI.S3. Example cell counting with ImageJ on a representative image. (**a**) Original 8-bit (.tif) SEM image showcasing bacteria on an electrode fiber. (**b**) Thresholded image identifying bacteria (red blobs on electrode fiber). (**c**) Outlines of identified bacteria in the area of interest (the electrode fiber). Red markings are number annotations for counted objects. (**d**) Parameters used and identified in the cell counting process. Threshold is related to the shading level; count represents the number of objects identified with closed outlines (cells); total area is the area of identified cells; average size is the average area of identified cells; area fraction is the percentage of the area of interest covered by the identified cells.